

UC San Diego

UC San Diego Electronic Theses and Dissertations

Title

Bulk metallic glasses and their composites : composition optimization, thermal stability, and microstructural tunability

Permalink

<https://escholarship.org/uc/item/2j20070s>

Author

Khalifa, Hesham Ezzat

Publication Date

2009

Peer reviewed|Thesis/dissertation

UNIVERSITY OF CALIFORNIA, SAN DIEGO

Bulk Metallic Glasses and their Composites: Composition Optimization, Thermal Stability, and Microstructural Tunability

A dissertation submitted in partial satisfaction of the requirements
for the degree of Doctor of Philosophy

in

Materials Science and Engineering

by

Hesham Ezzat Khalifa

Committee in charge:

Professor Kenneth S. Vecchio, Chair
Professor Gaurav Arya
Professor Prabhakar Bandaru
Professor Vlado Lubarda
Professor Michael Sailor

2009

Copyright

Hesham Ezzat Khalifa, 2009

All right reserved

The Dissertation of Hesham Ezzat Khalifa is approved, and it is acceptable in quality and form for publication on microfilm and electronically:

Chair

University of California, San Diego

2009

Dedicated to my family.

Ezzat, Shadia, and Kareem Khalifa

Table of Contents

Signature Page	iii
Dedication	iv
Table of Contents	v
List of Figures	viii
List of Tables	xix
Acknowledgements.....	xxi
Vita.....	xxiii
Abstract of the Dissertation	xxv
Chapter 1: Motivation and Objectives	1
Chapter 2: Background	8
2.1 Metallic Glass and Glass Formation	8
2.2 Factors effecting metallic glass formation.....	9
2.2.1 Miracle Packing Model.....	11
2.2.2 Chemical Short Range Order (CSRO) Model.....	14
2.2.3 Liquidus Model.....	15
2.3 Characterization of Metallic Glass.....	18
2.4 Properties of BMG.....	34
2.4.1 Mechanical Properties.....	34
2.4.2 Corrosion resistance in BMG.....	56
2.4.3 Magnetic features of BMGs.....	59

Chapter 3: Experimental Methods	64
3.1 Alloy Melting and Processing Methods.....	64
3.2 X-Ray Diffractometry	69
3.3 Thermal Analysis	69
3.4 Corrosion Testing.....	69
3.5 Mechanical Testing.....	70
3.6 Microstructural and Chemical Characterization	70
Chapter 4: Iron-based Bulk Metallic Glasses and BMG-derived Composites	71
4.1 Effect of Mo-Fe Substitution on Glass Forming Ability and Thermal Stability of Fe-C-B-Mo-Cr-W Bulk Amorphous Alloys.....	71
4.1.1 Abstract.....	71
4.1.2 Introduction.....	71
4.1.3 Results and Discussion	75
4.1.4 Conclusion	96
4.2 Devitrification and cooling rate effects on microstructure and mechanical properties in $\text{Fe}_{57}\text{C}_9\text{B}_{11}\text{Mo}_{12}\text{Cr}_8\text{W}_3$ metallic glass.....	98
4.2.1 Abstract.....	98
4.2.2 Introduction.....	98
4.2.3 Results and Discussion	100
4.2.4 Conclusion	122
Chapter 5: Titanium-based Bulk Metallic Glass Composites.....	124
5.1 Thermal Stability and Crystallization Phenomena of Low Cost Ti-based Bulk Metallic Glass	124
5.1.1 Abstract.....	124
5.1.2 Introduction.....	124
5.1.3 Results and Discussion	126
5.1.4 Conclusions.....	140
5.2 High Strength $(\text{Ti}_{58}\text{Ni}_{28}\text{Cu}_8\text{Si}_4\text{Sn}_2)_{100-x}\text{Mo}_x$ nanoeutectic matrix- \square -Ti dendrite BMG-derived composites with enhanced ductility and corrosion resistance	142
5.2.1 Abstract.....	142
5.2.2 Introduction.....	142
5.2.3 Results and Discussion	145

5.2.4 Conclusions	160
5.3 Development of tough Ti-based bulk metallic glass matrix composites without the use of beryllium	162
5.3.1 Abstract	162
5.3.2 Introduction	162
5.3.3 Results and Discussion	165
5.3.4 Conclusion	188
Chapter 6: Conclusion	190
Chapter 7: References	193

List of Figures

Figure 2.3.1. Differential Scanning Calorimetry for $\text{Pd}_{43}\text{Ni}_{10}\text{Cu}_{27}\text{P}_{20}$ indicating a dependence of T_g onset on heating rate. Endotherms are upwards [34].....	19
Figure 2.3.2. DSC curves for cast amorphous $\text{Fe}_{61}\text{Co}_7\text{Ni}_7\text{Zr}_8\text{Nb}_2\text{B}_{15}$, $\text{Fe}_{56}\text{Co}_7\text{Ni}_7\text{Zr}_8\text{Ta}_2\text{B}_{20}$, $\text{Fe}_{60}\text{Co}_8\text{Zr}_8\text{Nb}_2\text{Mo}_5\text{W}_2\text{B}_{15}$, and $\text{Fe}_{60}\text{Co}_8\text{Zr}_{10}\text{Mo}_5\text{W}_2\text{B}_{15}$ cylinders with diameters of 1 and 3 mm. T_g and T_x are clearly labeled.	19
Figure 2.3.3. A comparison of critical cooling rate and reduced glass transition for conventional metallic glass, BMG, and silicate glass [5]	23
Figure 2.3.4. Relationship between R_c , t_{\max} , and SCLR for various bulk amorphous alloys [20]	23
Figure 2.3.5. Free energy curve governing crystallization	25
Figure 2.3.6. A comparison of viscosity of various glass forming liquids. Metallic Glass forming liquids fall intermediate between strong and fragile [5]	30
Figure 2.3.7. Schematic diagram for the entropy changes on cooling a liquid from T_m to T_K for fragile and strong liquids [48].....	30
Figure 2.3.8. Kissinger plot of DTA data for $\text{Fe}_{61}\text{Co}_5\text{Zr}_8\text{Y}_2\text{Cr}_2\text{Mo}_7\text{B}_{15}$ rod and ribbon amorphous alloys [53].....	34
Figure 2.4.1. The relations between mechanical properties of typical BMGs: (a) tensile fracture strength ($\sigma_{t,f}$) with Young's modulus (E); (b) Vickers hardness (H_v) with Young's modulus (E) [20]	36
Figure 2.4.2. (a) Cup and cone failure surface of Zr-based BMG tested in tension indicating localized melting under high strain rate condition. (b) Vein	

pattern fracture surface in fracture toughness experiment of Zr-based BMG.	
The vein pattern suggests a decrease in glass viscosity resulting in highly localized flow process on the crack plane [5]	39
Figure 2.4.3. (a) Multiple shear bands in Zr-based Vitreloy 1 tested at a strain rate of 5×10^{-2} . (b) True stress-True strain curve indicating the development of plasticity above a critical strain rate in Vitreloy 1 [62]	40
Figure 2.4.4. (a) Representative optical micrograph of semi-circular shear bands around a pyramidal Vickers indentation in a bulk metallic glass. (b) Zoomed in image of semi-circular shear bands from same sample highlighting the step-like nature of the shear bands.....	41
Figure 2.4.5. Complex micro gear fabricated by superplastic forming of BMG[65]	42
Figure 2.4.6. (a) Quasi-static compression stress-strain curves of Vit 106 and composites reinforced with WC, SiC, W, and Ta. (b) Quasi-static tensile stress-strain curves of Vit 106 and composites reinforced with WC, SiC, W, and Ta [59]	46
Figure 2.4.7. Optical micrographs of polished surfaces of (a) $Zr_{57}Nb_5Al_{10}Cu_{15.4}Ni_{12.6}$ alloy (Vit 106)/WC composites, (b) Vit 106/SiC composites, and (c) Vit 106/W composites, showing a uniform distribution of particles in the Vit 106 matrix [59]	47
Figure 2.4.8. a) SEM image of lathy phase. (I: dendritic phase; II: XRD pattern of the alloy), b) Bright-field TEM image of alloy. (I: HRTEM image of the lathy phase, and II: HRTEM image of the amorphous matrix), c) HRTEM image	

of nanostructured grains embedded in the amorphous matrix, d) Schematic illustration of hierarchical microstructure for the Fe-based alloy [79]	49
Figure 2.4.9. Compressive stress-strain curve for $\text{Fe}_{42}\text{Co}_{7.3}\text{Ni}_{16}\text{Cr}_{11.8}\text{Cu}_{6.3}\text{C}_{14.8}\text{Y}_{1.8}$ at ambient temperature with inset of true stress-true strain [79].	50
Figure 2.4.10. Fracture behavior and deformation mechanisms of the failed alloy: (a) SEM image of the fractured surface; b) SEM images showing magnified regions marked by I, II, III and IV in a); c), Bright field TEM image of the deformed sample; d) HRTEM image exhibiting numerous stacking faults in the deformed sample [79]	52
Figure 2.4.11. (a) SEM micrograph of microstructure achieved in Zr-Ti-Nb-Cu-Be BMG composite. (b) HRTEM micrograph of glass/crystal interface, SADP insets indicate b.c.c. structure in crystalline phase and amorphous structure in glassy matrix [81].	54
Figure 2.4.12. (a) Engineering stress-strain curves for Vitreloy1 and 3 different Vitreloy1-derived BMG composites. (b) High magnification SEM image of microstructure-shear band interaction [81].	55
Figure 2.4.13. Corrosion rates of amorphous $\text{Fe}_{50-x}\text{Cr}_{16}\text{Mo}_{16}\text{C}_{18}\text{B}_x$ rods 1.2 mm in diameter in HCl solutions open to air for 168 h at 298K [83]	57
Figure 2.4.14. SEM micrographs of the surfaces of glassy $\text{Fe}_{50-x}\text{Cr}_{16}\text{Mo}_{16}\text{C}_{18}\text{B}_x$ 1.2 mm rods in 12 M HCl for 168 h at 298 K [83]	58
Figure 2.4.15 Comparison of I-H hysteresis loops for ring shaped Fe-based BMG with stacked melt spun ribbons making the same shape.	60

Figure 2.4.16 XRD spectra for $\text{Fe}_{61}\text{Co}_7\text{Zr}_{9.5}\text{Mo}_5\text{W}_2\text{B}_{15.5}$ annealed for 2h at 873, 908, 933, 968, and 983K.....	62
Figure 2.4.17 Dependence of M_s and H_c with annealing temperature. Inset shows hysteresis loops for as-cast and annealed samples [16]	63
Figure 3.1. Assembly for splat-quenching alloys.	66
Figure 3.2. Copper mold featuring several different rod diameters.....	66
Figure 3.3. (a) Parallel pipe copper mold assembly heating 10 g sample of Ti-based BMG composite, (b) parallel plates in opened and closed positions, (c) a Ti-based BMG-derived composite cast using the parallel plate copper mold assembly. This set-up is capable of melting 15 g samples.	66
Figure 3.4. Schematic of semi-solid processing with parallel plate copper mold and induction coil. Blue and red represent ingoing and outgoing cooling water, respectively. (a) an ingot is prepared by arc melting for the two part cylindrical mold piece. Each copper plate has a semi-cylinder mold machined into it. The brass posts in the bottom plate ensure proper alignment during quenching.. (b) The ingot is placed between the two copper plates. (c) The induction coil is turned on and the alloy is heated up to the two-phase temperature range. (d) Once sufficiently processed, the top copper mold piece is lowered and the coil is turned off. (e) The molten alloy has been pressed into the mold and quenched sufficiently to freeze in the desired microstructure. (f) A semi-solidly processed cylindrical rod is removed from the copper mold.....	67

Figure 3.5. Second iteration of parallel plate copper mold assembly inside of large vacuum chamber. Inset shows close-up of induction coil and copper plates with 25 g sample being heated. This set-up is capable of melting 150g samples.....	68
Figure 4.1.1. Variation in equilibrium liquidus temperature and alpha parameter with Fe-Mo substitution in $\text{Fe}_{67-x}\text{C}_{10}\text{B}_9\text{Mo}_{7+x}\text{Cr}_4\text{W}_3$	75
Figure 4.1.2. XRD patterns for as-quenched $\text{Fe}_{67-x}\text{C}_{10}\text{B}_9\text{Mo}_{7+x}\text{Cr}_4\text{W}_3$ ($x = 1-7$) alloys. Only the composition for $x=1$ yielded crystalline peaks in XRD.....	78
Figure 4.1.3. DSC curves for as-cast $\text{Fe}_{67-x}\text{C}_{10}\text{B}_9\text{Mo}_{7+x}\text{Cr}_4\text{W}_3$ ($x = 2-7$ at%) amorphous alloys.	80
Figure 4.1.4. DTA curve for amorphous $\text{Fe}_{62}\text{C}_{10}\text{B}_9\text{Mo}_{12}\text{Cr}_4\text{W}_3$ plate indicating all significant thermodynamic events.	81
Figure 4.1.5. XRD spectra demonstrating resistance to crystallization in the supercooled liquid region in $\text{Fe}_{67-x}\text{C}_{10}\text{B}_9\text{Mo}_{7+x}\text{Cr}_4\text{W}_3$ ($x = 2, 5, 7$). T_g was 808K, 820K, and 844K for compositions corresponding to $x = 2, 5$, and 7 , respectively.	84
Figure 4.1.6. XRD spectra for 120 min anneals at $\text{sub-}T_{x1}$, at T_{x1} , at T_{x2} , and at T_{x3} offsets for compositions $\text{Fe}_{60}\text{C}_{10}\text{B}_9\text{Mo}_{14}\text{Cr}_4\text{W}_3$ ($x = 7$), $\text{Fe}_{62}\text{C}_{10}\text{B}_9\text{Mo}_{12}\text{Cr}_4\text{W}_3$ ($x = 5$) and $\text{Fe}_{65}\text{C}_{10}\text{B}_9\text{Mo}_9\text{Cr}_4\text{W}_3$ ($x = 2$).....	87
Figure 4.1.7. Crystallization curves for $\text{Fe}_{62}\text{C}_{10}\text{B}_9\text{Mo}_{12}\text{Cr}_4\text{W}_3$ acquired via TG/DTA ...	91
Figure 4.1.8. Kissinger plot of DTA data for $\text{Fe}_{62}\text{C}_{10}\text{B}_9\text{Mo}_{12}\text{Cr}_4\text{W}_3$	92
Figure 4.2.1. Stress-strain curve of $\text{Fe}_{57}\text{C}_9\text{B}_{11}\text{Mo}_{12}\text{Cr}_8\text{W}_3$ rod with 3mm diameter tested in compression under strain rate of 10^{-3} s^{-1}	101

Figure 4.2.2. TG/DTA scan of amorphous $\text{Fe}_{57}\text{C}_9\text{B}_{11}\text{Mo}_{12}\text{Cr}_8\text{W}_3$, indicating glass transition temperature (T_g), 3-phase crystallization (T_{x1} , T_{x2} , T_{x3}), melting temperature (T_m), and liquidus temperature (T_l).....	101
Figure 4.2.3. XRD spectra of heat treated $\text{Fe}_{57}\text{C}_9\text{B}_{11}\text{Mo}_{12}\text{Cr}_8\text{W}_3$ at 5K below T_{x1} , and T_{x1} , T_{x2} , and T_{x3} offset (2 h anneals). Identified crystalline phases are indicated by symbols above Bragg peaks.	103
Figure 4.2.4. XRD spectra of $\text{Fe}_{57}\text{C}_9\text{B}_{11}\text{Mo}_{12}\text{Cr}_8\text{W}_3$ after 5 min anneals at successive step 10K intervals above T_g (814K). The 874K anneal is 7K above T_{x1} (867K).	107
Figure 4.2.5. DSC scans of $\text{Fe}_{57}\text{C}_9\text{B}_{11}\text{Mo}_{12}\text{Cr}_8\text{W}_3$ annealed for 5 minutes at 10K intervals throughout supercooled liquid region (T_g+10 to T_g+50) and 7K above T_{x1} (T_g+60).	108
Figure 4.2.6. Different microstructures achieved with 4 cooling rate conditions in 3 mm geometry paired with respective XRD spectra. The phases are labeled and indicated by arrows in the SEM images. (a) Rapid Quench condition - RQ, (b) Intermediate 1 condition – I1, (c) Intermediate 2 condition – I2, (d) Slow Cool condition – SC.....	112
Figure 4.2.7. SEM image of hardness indentations in 3 mm thick plate geometry samples of (a) the nanocrystalline matrix of the RQ condition, (b) the I1 condition, (c) a plate in the I2 condition, (d) the crystalline matrix of the I2 condition, (e) a eutectic crystal in the SC condition and (f) a plate in the SC condition.	115

Figure 4.2.8. XRD spectra of alloys cast with 4 cooling rate conditions in the 1 mm thick plate geometry.....	117
Figure 4.2.9. DSC scans of alloys cast with 4 cooling rate conditions in the 1 mm thick plate geometry. The crystallization enthalpies are listed with each curve. The plate cast in the SC condition has no crystallization enthalpy since it was fully crystallized.	118
Figure 4.2.10. (a) Back scatter electron image of α -Fe stabilized, $\text{Fe}_{60}\text{B}_9\text{C}_{10}\text{Cr}_6\text{Mo}_8\text{W}_2\text{Ti}_5$ microstructure, (b) corresponding compressive stress-strain curve showing ~ 1% plastic strain and σ_{max} of ~3GPa.....	121
Figure 5.1.1. Continuous heating DSC curves obtained at different heating rates.....	127
Figure 5.1.2. XRD spectra of $\text{Ti}_{48}\text{Ni}_{32}\text{Cu}_8\text{Si}_8\text{Sn}_4$ in the as-cast, fully amorphous state, and after annealing at each of the crystallization temperatures (T_{x1} , T_{x2}).	129
Figure 5.1.3. Bright field TEM image of annealed $\text{Ti}_{48}\text{Ni}_{32}\text{Cu}_8\text{Si}_8\text{Sn}_4$ indicating a fully crystallized state.....	130
Figure 5.1.4. Inverse heating rate ($1/\beta$) as a function of T_g , normalized by T_g^* (the onset of the glass transition at 1 K/min). The VFT parameters for the best fit to the DSC data according to Equation (5.1-4) are $\ln(B) = 7.69$ K/s, $D^* = 1.33$, and $T_g^0 = 684$ K.	133
Figure 5.1.5. Kissinger plots obtained from the shift of the transformation peak temperatures according to Equation (5.1-5). The inset shows the experimentally determined rate constant (k_{cr}) according to Equation (5.1-6).	134

Figure 5.1.6. Isothermal anneals showing the peak shift with time as the anneal temperature is increased.....	136
Figure 5.1.7. Isothermal transformation curves for the primary crystallization at each of the annealing temperatures.	139
Figure 5.1.8. JMA plots for the isothermal crystallization of $\text{Ti}_{48}\text{Ni}_{32}\text{Cu}_8\text{Si}_8\text{Sn}_4$	140
Figure 5.2.1. Schematic illustration of effect of alloying elements on phase diagrams of titanium alloys [149].	145
Figure 5.2.2. Ti-Ni-Cu liquidus profile with Si and Sn content held constant at 8 and 4 atomic %, respectively. White lines encompass broad glass forming compositional region. “X” denotes best glass forming composition. Temperatures in legend are equilibrium liquidus temperatures calculated using THERMOCALC [150].....	147
Figure 5.2.3. DSC traces of (a) the monolithic glass $\text{Ti}_{48}\text{Ni}_{32}\text{Cu}_8\text{Si}_8\text{Sn}_4$, and (b) the splat-quenched, metallic glass matrix composite, $(\text{Ti}_{58}\text{Ni}_{28}\text{Cu}_8\text{Si}_4\text{Sn}_2)_{94}\text{Mo}_6$	149
Figure 5.2.4. Backscattered electron image of semi-solidly processed $(\text{Ti}_{58}\text{Ni}_{28}\text{Cu}_8\text{Si}_4\text{Sn}_2)_{94}\text{Mo}_6$	151
Figure 5.2.5. XRD spectra showing various crystalline phases in $(\text{Ti}_{58}\text{Ni}_{28}\text{Cu}_8\text{Si}_4\text{Sn}_2)_{94}\text{Mo}_6$ BMG-derived composite.	152
Figure 5.2.6. True stress-True strain curves for $(\text{Ti}_{58}\text{Ni}_{28}\text{Cu}_8\text{Si}_4\text{Sn}_2)_{100-x}\text{Mo}_x$ at $x = 4, 6$, and 8 at. %. Inset shows strain hardening exponent dependence on molybdenum content.....	154
Figure 5.2.7. Features of the compressive deformation in $(\text{Ti}_{58}\text{Ni}_{28}\text{Cu}_8\text{Si}_4\text{Sn}_2)_{94}\text{Mo}_6$. White arrows indicate profuse slip within the dendrites, while black arrows	

indicate shear bands nucleating at the dendrite-nanoeutectic matrix interface, and propagating across the multiphase microstructure.	156
Figure 5.2.8. Ductile fracture of $(\text{Ti}_{58}\text{Ni}_{28}\text{Cu}_8\text{Si}_4\text{Sn}_2)_{94}\text{Mo}_6$ exhibiting copious intra- dendritic slip in nearly every β -Ti dendrite.	158
Figure 5.3.1. Liquidus profiles illustrating glass formation in the (Ti-Ni-Si)-Mo alloy system. Mo = 0 at.% in the ternary profile in (a), and Mo = 2 at.% in (b). The white hashed region encompasses the glass forming composition space in each profile.	167
Figure 5.3.2. Typical microstructures achieved during semisolid processing of $\text{Ti}_{51.4}\text{Ni}_{42.4}\text{Si}_{3.9}\text{Mo}_{2.3}$ at (a) 85% power for 10 seconds followed by simultaneously turning off power to the induction coil and quenching the sample with the top copper plate. The alloy resulting from this first semi- solid processing condition will be referred to as SSP1 (b) 75% power for 15 second followed by simultaneously turning off power to the induction coil and quenching the sample with the top copper plate. The alloy resulting from this second semi-solid processing condition will be referred to as SSP2, and (c) 70% for 15 seconds followed by 10 additional seconds of heating after lowering the top copper block to promote crystallization of the matrix. The alloy from this condition will be referred to as SSP3.	168
Figure 5.3.3. DSC curves of the BMG matrix composite $\text{Ti}_{51.4}\text{Ni}_{42.4}\text{Si}_{3.9}\text{Mo}_{2.3}$ and its fully amorphous matrix. T_g and T_x for both alloys are indicated with arrows. .	170
Figure 5.3.4. XRD spectra of (a) the fully amorphous monolithic glass, (b) an ideally semi-solidly processed BMG matrix composite $(\text{Ti}_{51.4}\text{Ni}_{42.4}\text{Si}_{3.9}\text{Mo}_{2.3})$ with a	

b.c.c. β -Ti phase embedded in the amorphous matrix (SSP2), (c) the isolated b.c.c. β -Ti phase, and (d) a BMG-derived composite (with the same composition as 5.3.4b) that has been semi-solidly processed for too long, resulting in a destabilization of the glass into a crystalline matrix (SSP3).171

Figure 5.3.5 Semi-solidly processed $\text{Ti}_{54.7}\text{Ni}_{39.1}\text{Si}_{4.4}\text{Mo}_{1.8}$ BMG-derived composite with nanocrystalline matrix. The inset shows additional peaks in the XRD spectrum indicating crystallization in the matrix..... 174

Figure 5.3.6. Uniaxial compressive stress-strain curves for the amorphous matrix composites, SSP1 and SSP2, and the crystalline matrix BMG-derived composite, SSP3. 176

Figure 5.3.7. Shear band evolution on outer surface of $\text{Ti}_{51.4}\text{Ni}_{42.4}\text{Si}_{3.9}\text{Mo}_{2.3}$ (SSP2) samples during stepwise compressive loading. The stress-strain curve in (a) is labeled with numerals I-V corresponding to the images in (b)-(h), where (b) is 5% total strain, (c) is 10% total strain, (d) is 15% total strain, (e) is 20% total strain, (f) is a hi magnification image of the 20% strain condition showing shear band deflection and crack arrest at the glass-crystal interface, and (g) is 28% total strain. The sample failed at 28% total strain. The image in (h) is a high magnification view of the outer surface of the sample taken near the fracture surface. The interaction of primary and secondary shear bands is apparent from the shear steps near intersection points. Large white arrows indicate primary shear bands, small black arrows indicate secondary shear bands, and small white arrows indicate slip bands..... 180

Figure 5.3.8. Backscatter electron image of deformation modes in SSP2, including dendrite penetrating shear band arrest, trans-dendritic shear bands, intra-dendritic slip, inter-dendritic microcracks, intra-dendritic crack arrest, and tortuous path crack morphology.	184
Figure 5.3.9. (a) Overview of SSP2 4 pt. bend sample fracture surface. I and II mark the two morphologically distinct fracture mechanisms. A high magnification image of region I depicts dendrite fracture in (b), and a high magnification image of region II depicts glass fracture in (c).	185
Figure 5.3.10. Tensile stress-strain curves for $\text{Ti}_{51.4}\text{Ni}_{42.4}\text{Si}_{3.9}\text{Mo}_{2.3}$ processed according to three different processing conditions to yield alloys SSP1, SSP2, and SSP3. Only alloys featuring an amorphous matrix exhibited tensile ductility (SSP1 and SSP2). Greater tensile ductility has been observed in SSP2 because the larger β -Ti microstructure is better able to arrest shear band propagation compared with the finer scale β -Ti in SSP1.	188

List of Tables

Table 2.3.1. Various glass forming compositions with associated glass transition and liquidus data. The reduced glass transition T_{rg} ($=T_g/T_m$) shows good coincidence with maximum achievable thickness, D_{max} [36]	22
Table 4.1.1. Listing of some iron-based bulk metallic glasses from literature. D_{max} is the maximum thickness at which a fully amorphous structure can be achieved.	73
Table 4.1.2. Glass transition, crystallization, liquidus temperatures and reduced glass transition ratio for $Fe_{67-x}C_{10}B_9Mo_{7+x}Cr_4W_3$ determined via DSC and DTA.	78
Table 4.1.3. Peak temperature for each alloy in substitutional system with calculated activation energy for crystallization.	92
Table 4.1.4. Average Vickers hardness data for $Fe_{67-x}C_{10}B_9Mo_{7+x}Cr_4W_3$ ($x=2,5,7$) within the supercooled liquid region and after the nucleation of each crystalline phase.	96
Table 4.2.1. Crystallization enthalpy, volume fraction, and average Vickers hardness values at each of the supercooled liquid anneal conditions.....	108
Table 5.1.1. Dependence of glass transition (T_g), crystallization (T_x) and peak (T_{p1} , T_{p2}) temperatures, as well as supercooled liquid region (ΔT_x), on heating rate (β).	128
Table 5.1.2. Kinetic parameters of $Ti_{48}Ni_{32}Cu_8Si_8Sn_4$ during isothermal annealing.....	139
Table 5.2.1. Mechanical Properties of $(Ti_{58}Ni_{28}Cu_8Si_4Sn_2)_{100-x}Mo_x$	153
Table 5.3.1. Glass transition (T_g), crystallization (T_x), and liquidus (T_l) temperatures of select glass forming alloys from the (Ti-Ni-Si)-Mo alloy system.....	167

Table 5.3.2. A summary of all relevant mechanical and material properties in the semi-solidly processed BMG composites SSP1, SSP2, and SSP3, each with nominal composition $\text{Ti}_{51.4}\text{Ni}_{42.4}\text{Si}_{3.9}\text{Mo}_{2.3}$. Data for the monolithic glass, $\text{Ti}_{52}\text{Ni}_{35}\text{Si}_{11}\text{Mo}_2$, as well as equi-atomic Nitinol, and Ti 6/4 are included for comparison.	175
---------------------------------------------------------------------------------------------------------------------------------------------------------------------------------------------------------------------------------------------------------------------------------------------------------------------------------------------------------------------------------------------------------------------	-----

Acknowledgements

I would first like to thank my parents, Ez and Shadia, and my brother, Kareem, for raising me, supporting me throughout my academic career, and instilling in me, since childhood, the thirst for knowledge. Thank you to Dr. Vecchio for giving me the opportunity to work in his lab. Thanks to the entire Vecchio Lab group; Christian Deck, Raghav Adharapurapu, Erik McKee, Robb Kulin, Zhang Xing, and Fengchun Jiang. Special thanks to Justin Cheney for working on the BMG project with me, and serving as my mentor when I arrived at UCSD. Thank you to Karla for her support and understanding, as well as all of my friends for helping me to keep things in perspective.

Chapter 4, section 1 in part, is a reprint of the material as it appears in Materials Science and Engineering A Volume 490, Issues 1-2, August 2008, Pages 221-228 and the Journal of Non-Crystalline Solids Volume 354, Issues 40-41, October 2008, Pages 4550-4555, written by Hesham E. Khalifa, Justin L. Cheney and Kenneth S. Vecchio. The dissertation author was the primary investigator and author of both of these papers.

Chapter 4, section 2 in part, is a reprint of the material as it appears in Advanced Engineering Materials Volume 10, 2008, Page 1056, written by Hesham E. Khalifa and Kenneth S. Vecchio. The dissertation author was the primary investigator and author of this paper.

Chapter 5, section 1 in part, is a reprint of the material accepted for publication in Journal of Non-Crystalline Solids, on August 31, 2009, written by Hesham E. Khalifa, Justin L. Cheney and Kenneth S. Vecchio. The dissertation author was the primary investigator and author of this paper.

Chapter 5, section 2 in part, is a reprint of the material as it appears in Advanced Engineering Materials Volume 11, 2009, Page 885, written by Hesham E. Khalifa and Kenneth S. Vecchio. The dissertation author was the primary investigator and author of this paper.

Vita

- 2004 Bachelor of Science, Cornell University
- 2006 Master of Science, University of California, San Diego
- 2009 Doctor of Philosophy, University of California, San Diego

Publications and Patents

Hesham E. Khalifa, Justin L Cheney, Kenneth S Vecchio. **Effect of Mo-Fe Substitution on Glass Forming Ability, Thermal Stability, and Hardness of Fe-C-B-Mo-Cr-W Bulk Amorphous Alloys.** *Materials Science and Engineering A*. **490**, 2008, p.221.

Hesham E. Khalifa, Justin L Cheney, Kenneth S Vecchio. **Effect of Mo-Fe Substitution on Glass Forming Ability and Thermal Stability of Fe-C-B-Mo-Cr-W Bulk Amorphous Alloys.** *Journal of Non-Crystalline Solids*. **354**, 2008, p.4550.

Hesham E. Khalifa, Kenneth S. Vecchio. **Devitrification and Cooling Rate Effects on Microstructure and Mechanical Properties of Fe₅₇C₉B₁₁Mo₁₂Cr₈W₃ Bulk Metallic Glass.** *Advanced Engineering Materials*. **10**, 2008, p. 1056.

Hesham E. Khalifa, Kenneth S. Vecchio. **High Strength (Ti₅₈Ni₂₈Cu₈Si₄Sn₂)_{100-x}Mo_x Nanoeutectic Matrix- β -Ti dendrite, BMG-derived Composites with Enhanced Ductility and Corrosion Resistance.** *Advanced Engineering Materials*. **11**, 2009, p.885.

Hesham E. Khalifa, Kenneth S. Vecchio. **Thermal Stability and Crystallization Phenomena of Low-cost Ti-based Bulk Metallic Glass.** Accepted to *Journal of Non-Crystalline Solids* August, 2009.

Hesham E. Khalifa, Kenneth S. Vecchio. **Development of Tough Ti-based Bulk Metallic Glass Matrix Composites without the Use of Beryllium.** Manuscript in Preparation.

Justin L. Cheney, Hesham E Khalifa, Kenneth S. Vecchio. **Modeling the Amorphous Forming Ability of Ti-based Alloys with Wide Supercooled Liquid Regions and High Hardness.** *Materials Science and Engineering A*. **506**, 2009, p.94.

Douglas C. Hofmann, Henry Kozachakov, Hesham E. Khalifa, Joseph P. Schramm, Marios D. Demetriou, Kenneth S. Vecchio, William L. Johnson. **Semi-solid Induction Forging of Metallic Glass Matrix Composites.** *Journal of Materials Science.* **61**, 2009 p.11.

U.S. provisional patent: “Amorphous Alloy Materials.” Kenneth S. Vecchio, Justin L. Cheney, Hesham E. Khalifa. **DOCKET NO. 15670-159P01 / SD2008-110**

Professional Societies

The Materials Research Society (MRS) - 2002

The Mineral, Metals, and Materials Society (TMS) - 2004

Abstract of the Dissertation

Bulk Metallic Glasses and their Composites: Composition Optimization, Thermal Stability, and Microstructural Tunability

by

Hesham Ezzat Khalifa

Doctor of Philosophy in Materials Science and Engineering
University of California, San Diego, 2009

Professor Kenneth S. Vecchio, Chair

A design protocol utilizing common elements for bulk metallic glass formation has been employed to develop novel, low cost Fe-, and Ti- based bulk metallic glasses. A critical obstacle that was successfully overcome in this work is the omission of beryllium in these alloys. Beryllium is of vital importance in many bulk metallic glass forming systems, but it is expensive and poses considerable health risks.

Bulk metallic glasses in these novel Fe-, and Ti-based systems exhibit extremely high mechanical strength and excellent thermal stability. Devitrification and cooling rate experiments were used to identify crystalline phase formation and assess activation energy for crystallization, as well as to explore and develop ductile BMG composites.

To better control microstructure in these BMG composites, a novel processing technique, called semi-solid forging was developed, wherein the alloy melt is heated to above the melt temperature of the glass, but below the melt temperature of the ductile

crystalline phase. Such an approach permits the maintenance of a glassy, or nanocrystalline matrix phase, while simultaneously coarsening and homogenizing the ductile, secondary phase. This processing approach leads to enhanced ductility in the alloys, which, to this point, has not been observed using conventional casting methods. The combination of novel, low-cost, alloy compositions with semi-solid forging has been successfully utilized to develop new high strength structural materials with enhanced ductility and toughness.

Microstructural and mechanical properties of these novel, toughened, BMG composites are presented. A comprehensive analysis of the relationship between deformation mechanisms and microstructure reveals that enhanced ductility is predicated on matching fundamental mechanical and microstructural length scales in a Ti-Ni-Si-Mo BMG composite. Under optimized microstructural conditions, a maximum compressive strength exceeding 2400 MPa with ~ 30% total strain to failure was achieved. Furthermore, a 400% increase in fracture toughness over the monolithic glass, and tensile ductility of 3.5% were observed.

The design of conventional, crystalline, high-performance structural materials is governed by optimizing combinations of mechanical properties such as strength, ductility, toughness, and elasticity. In general though, high strength comes at the expense of ductility. The development of ductile BMG composites represents the dawn of a new era in structural materials that couples ultra high strength with considerable ductility and enhanced fracture toughness.

Chapter 1: Motivation and Objectives

Amorphous materials have long been of interest to the scientific community. Amorphous polymers and various inorganic and organic glasses have been the subject of research for nearly a century. The development of bulk metallic glasses (BMG) with dimensions on the order of centimeters, however, is rather new, and has only gained momentum in the past 15 years.

Conventionally, amorphous materials have very little structural symmetry and can be made amorphous even at cooling rates below 0.1 K/s. Upon cooling, there is a rapid increase in viscosity coupled with extremely small intramolecular rearrangement such that atomic mobility is retarded, and the formation of a crystalline phase is correspondingly difficult. Metallic glass, on the other hand, is highly metastable and extremely difficult to form in most alloy systems, which tend towards their equilibrium, crystalline state. There is no singular, universal rule for predicting glass forming ability for a given metallic system. The discovery of the first metallic glass by Duwez at Caltech in 1960 actually came about unexpectedly in a study of binary solubility in a 25 at% Si-Au alloy [1]. Amorphous flakes were reported with a thickness of 10 μ m. Metallic glass production has since evolved from melt spinning of binary eutectic alloys into thin ribbons, to casting centimeter diameter bulk amorphous alloys. The prospect of using metallic glass for structural applications did not come about until the 1990's when the development of *bulk* metallic glass was reported by Inoue at Tohoku University in Japan [2], and Johnson at Caltech in the US [3]. BMGs differ from their metallic glass forerunners in that they often are multicomponent alloys, sometimes requiring more than

7 distinct atomic constituents of varying atomic radii and distinct chemical features to enhance glass forming ability.

The unique physical and mechanical properties exhibited by metallic glasses are a reflection of their amorphous structure. Metallic glasses exhibit extremely high strength, in excess of 4 GPa, high hardness [4], large elastic limit, excellent wear and corrosion resistance, and net-shape formability [5]. The lack of defects such as dislocations, as in crystalline materials, leads to vastly different mechanisms for deformation. In crystalline materials, macroscopic plastic deformation is the result of movement and interaction of numerous dislocations having defined slip systems in addition to other mechanisms like twinning. Furthermore, dislocations interact with other dislocations, grain boundaries, and second-phase particles in polycrystalline materials, giving rise to work hardening. Despite the immensely high strength of BMGs, their use as structural materials has been limited due to the fact that fully amorphous alloys invariably suffer brittle failure. Ductility in BMGs is limited at room temperature and at low strain rate by strain localization resulting from shear band formation; all of the deformation is confined within a few active shear bands. Ductility enhancement is predicated on delocalizing strain by increasing shear band density. This work will explore pathways towards achieving enhanced ductility in BMG derived materials.

To date, BMGs and BMG composites have largely depended on very expensive alloying elements that prohibit their use as structural materials. Vitreloy glasses are the most stable BMGs, however, zirconium is the solvent atom, and as much as 35 atomic % beryllium is required for optimized glass formation [3, 6, 7]. Both of these elements are expensive, and beryllium presents considerable health risks. Alternatively, other good

glass forming systems require elements like lanthanum, promethium, palladium, yttrium, erbium, gadolinium, and other rare earth metals [8-13]. While these elements are critical for enhancing the glass forming ability (GFA) in many bulk metallic glass systems, the associated cost and health issues have hindered the development of BMGs for commercial use.

The discovery of new glass forming compositions has been the result of both significant trial and error, and improved understanding of vitrification behavior in metals. Numerous theoretical models have been proposed to explain vitrification using phenomena thought critical to glass formation. However, no single model has been unanimously accepted. This dissertation explores the potential of two novel, low-cost glass forming systems; one Fe-based and one Ti-based, which were developed via a combinatorial modeling approach pulling from multiple theoretical models, and then experimentally optimized via comprehensive thermal analyses. This work also details how the discovery of stable, low cost amorphous alloys can be used to develop ductile BMG composites.

Chapter 4, Section 1 details the design and production of novel Fe-based metallic glass compositions. Many studies involving “amorphous steel” research rely on the use of rare earth elements as solute atoms to stabilize the glass forming melt. This study explores a BMG formation utilizing elements common to the current steel industry. The mechanisms for glass formation in a Fe-C-B-Mo-Cr-W alloy system can be evaluated by systematically varying solvent-solute ratios in the alloy system, $\text{Fe}_{67-x}\text{C}_{10}\text{B}_9\text{Mo}_{7+x}\text{Cr}_4\text{W}_3$ ($x = 1-7$ at. %), and correlating these compositional changes with the thermal stability of the alloy. Extensive X-ray diffractometry and thermal analyses can be used to

characterize a glass forming alloy's resistance to crystallization, as well as identify what phases form upon devitrification during heat treatments. A better understanding of glass stability and devitrification facilitates the design of new metallic glasses, and highlights the ability to precisely tune mechanical properties through controlled crystallization from the glassy state.

Chapter 4, Section 2 probes deeper into the ability to control microstructure and mechanical properties of Fe-based BMGs and BMG-derived composites through thermal analysis and alternative alloy processing techniques applied to $\text{Fe}_{57}\text{C}_9\text{B}_{11}\text{Mo}_{12}\text{Cr}_8\text{W}_3$; a compositionally different amorphous steel featuring improved thermal stability. Thermal analysis can be used to identify the phase evolution of BMGs upon heating. The glass transition is an intrinsic feature of amorphous materials around which stark structural changes occur. Metallic glasses become inherently less stable as the processing temperature approaches the glass transition, ultimately resulting in crystallization of the glass. Stronger glass formers are better able to resist crystallization at elevated temperatures. It is imperative to perform thermal experiments above and below the glass transition to understand how well a glass resists crystallization, and what happens once crystallization does occur. Above the glass transition, devitrification occurs, wherein the glass devolves into one or multiple crystalline phases. The identification of these phases, the processing conditions under which they can be nucleated, and their effect on the properties of the alloy provide a means to tailor the mechanical properties of these alloys.

Heat treatments from the glassy state yield slow reaction kinetics that permit precise tuning of crystal size and volume fraction, however, the kinetics are so slow that crystal size is limited to the nanocrystalline regime even after extended exposure to

elevated temperatures. As part of this dissertation, a novel processing technique has been developed that permits the coarsening of the crystalline microstructure by way of power modulated induction melting. The new processing technique is called semi-solid forging. This processing technique significantly expands the tunability of glass forming alloys developed in this work. The same alloy composition is prepared via both methods to gain a better fundamental understanding of how crystallization induced by heating from the glassy state differs from crystallization resulting from slow cooling from the molten state. The collective understanding gained from these experiments allows for controlled growth of preferred crystalline phases in order to optimize mechanical properties like hardness, strength, and toughness.

Chapter 5, Section 1 presents a detailed investigation of a novel titanium based bulk metallic glass forming system. Conventional titanium alloys are known to have high specific strength, low density, and excellent chemical stability. These features make titanium alloys excellent candidates for advanced aerospace, structural and biomedical applications. The inherently superior strength and corrosion resistance of BMGs over their crystalline counterparts provide ample motivation for developing a Ti-based BMG to compete, if not surpass, current titanium alternatives. A novel Ti-based amorphous alloy is developed using a combinatorial modeling approach to promote enhanced glass forming ability without the use of expensive alloying elements. This Ti-Ni-Cu-Si-Sn alloy system features a large supercooled liquid region indicative of a very stable glass former. The large SCLR permits ample incubation time for crystallization such that more intricate isothermal and non-isothermal heat treatments can be performed to elucidate how crystalline phases form from the destabilized glassy state, as well as how quickly

these phase grow. Less stable glasses cannot be subjected to the extreme time and temperature necessary to conduct these experiments without crystallizing immediately. In fact, this Ti-Ni-Cu-Si-Sn glass forming system is the first non-beryllium containing Ti-based glass stable enough for these experiments. Furthermore, developing glasses with extremely slow crystallization kinetics is critical for identifying viable BMG candidates for ductile BMG matrix composite design.

Chapter 5, Section 2 explores the conditions necessary to utilize stable glass forming compositions in commercially viable combinations of strength and ductility. Despite their immense strength, monolithic BMG will fail with zero plastic strain under an applied load. Brittle failure is the critical obstacle preventing BMGs from becoming a viable alternative in aerospace, structural, and biomedical applications. In this section, a new design methodology targeted at incorporating a second phase in a glassy matrix is introduced. The effect of compositional variation on glass stability is explored. However, unlike Chapter 4, the objective in compositional variation is not optimizing glass stability, but rather, in maintaining glass stability, while simultaneously promoting the nucleation of a ductile, crystalline, secondary phase embedded within the glassy matrix. The constraints on compositional variation and processing conditions as they pertain to microstructure and mechanical properties are discussed. The mechanical properties of a Ti-Ni-Cu-Si-Sn-Mo nanoeutectic matrix, β -Ti stabilized composite are reported.

Chapter 5, Section 3 is an extension of the discussion on amorphous matrix composites to larger sample geometries. A simplified glass forming system is designed with the intention of minimizing heterogeneous nucleation at the glass-crystal interface in

a BMG composite. A reformed semi-solid forging protocol is proposed to better maintain amorphous structure in the matrix, while simultaneously coarsening and homogenizing the b.c.c. phase. The Ti-Ni-Si-Mo alloy introduced in this study features a 2-phase microstructure consisting of a glassy matrix and a crystalline b.c.c. phase. The observation of ductility in BMG composites hinges on the ability to delocalize the strain by increasing the shear band density. Shear band density is increased by creating a microstructural landscape in which there are features to obstruct shear band propagation. Each time a shear band is arrested by an obstacle, a new one must form, and the shear band density increases. A series of different semi-solid processing conditions are employed to demonstrate the ability to control the size of the b.c.c. phase and the stability of the glassy phase. Mechanical testing is performed on alloys made according to each condition and the results are correlated with the microstructure. The deformation mechanisms are explored through stepwise mechanical testing such that the evolution of shear bands can be observed as the deformation increases. A correlation between microstructure and the degree of ductility and toughness enhancement is reported. The composites developed in this work feature higher specific strength, greater corrosion resistance, and comparable fracture toughness to conventional titanium alloys.

Chapter 2: Background

2.1 Metallic Glass and Glass Formation

In general, a glass can be described as an amorphous solid, or a vitrified liquid lacking any long range order. It is formed by quenching a liquid at a certain, critical cooling rate such that a viscosity of 10^{13} poise is achieved. This commonly quoted threshold viscosity sufficiently slows the kinetics of solidification so that no significant atomic reconfiguration is possible on cooling to the solid state [14]. Metallic glasses are a sub-class of glasses consisting primarily of metallic bonding, and containing metal and metalloid elements. Metallic glasses exhibit many characteristic properties associated with crystalline metals in terms of electrical, optical and magnetic behavior [15]. Many metallic glasses have fairly good electrical and thermal conductivity. Certain Fe-based metallic glasses have exhibited good soft magnetic properties [16]. Undoubtedly though, the most fascinating aspect of metallic glass is their immense strength. Unlike traditional high strength crystalline alloys, as-cast BMGs do not require any thermomechanical treatment to enhance their mechanical strength.

In cooling a liquid from above its melting temperature, three fundamental solidification possibilities exist. (1) The melt cools sufficiently slowly so that crystallization occurs and a crystalline solid results, (2) the undercooled melt is configurationally frozen in place, resulting in a fully amorphous solid (metallic glass), and (3) some intermediate state comes about where an amorphous state coexists with some interdispersed crystalline inclusions. This last possibility is of particular interest

because it permits the harnessing of the metallic glass strength, while at the same time offering the potential for ductility due to the presence of the crystalline phase.

2.2 Factors effecting metallic glass formation

A glass is a metastable phase in which the evolution towards equilibrium is retarded by a kinetic barrier [6]. This barrier is characterized by a sharp change in atomic mobility over a relatively small range in temperature. This temperature interval is called the glass transition. The presence of this kinetic barrier in a glass forming composition primarily depends on the nature of the atomic or molecular units comprising the liquid. For instance, the covalent or complex bonding typical in polymer and oxide melts tend not to form nuclei on account of the prolonged relaxation behavior and very high viscosity typical of strong liquids such as these. In strong liquids, crystallization cannot occur on a laboratory time scale. Metallic glasses, with very few exceptions, fall into the fragile class of liquids. The nucleation units are only a few times the size of individual atomic constituents, thus facilitating atomic diffusion, and ultimately, crystallization. This tendency is reinforced by the fact that even the best metallic glass formers exhibit significantly lower viscosity at normalized undercooled temperatures with respect to its glass transition temperature. In polymer and oxide melts, however, the opposite case is true [17].

The critical cooling rate of a metallic glass determines the maximum thickness which it can be fabricated to, while maintaining a fully amorphous structure. Recall that the first metallic glass was a binary Si-Au alloy. This metallic glass was formed by rapid

quenching using the “gun” technique [18], and resulted in a cooling rate of 10^7 K/s and a critical thickness of only $10\mu\text{m}$ [1]. Current bulk metallic glasses have reported critical cooling rates as low as 0.1K/s and a maximum thickness of 70mm for $\text{Pd}_{40}\text{Cu}_{30}\text{Ni}_{10}\text{P}_{20}$ [19].

There have been several explanations put forth to describe potential requirements for glass formation. From these assertions, several modeling techniques for predicting glass forming compositions have been developed. The most empirical and widely accepted requirements for metallic glass formation were first established by Inoue in 1995. It was determined that bulk metallic glass formers typically: (1) are multi-component systems consisting of at least three unique atomic constituents, (2) contain atomic constituents exhibiting a significant difference in atomic size ratios; above about 12% among the three main constituents, and (3) have a negative mixing enthalpy between the three main constituent atoms [20]. These fundamental guidelines for metallic glass formation are described in detail by several comprehensive studies of metallic glass formation that combine the thermodynamics, kinetics, and topological effects associated with vitrification [21-24].

Fundamentally, predictive models need to establish compositions that favor the formation of densely packed clusters that lack long range order and are tightly bound such that crystal nucleation and growth is inhibited. To achieve the tightest packing atomic clusters; the building blocks of metallic glasses, it is necessary to have a large ratio of atomic radii between atomic constituents. Such topological considerations are best accounted for in Miracle’s packing model [23, 24]. A kinetic treatment of glass formation is described well by Cowley’s chemical short range order calculations, which

help to predict alloy interactions that result in extremely slow atomic rearrangements upon cooling [22]. A third and final critical approach to glass forming compositions deals with the thermodynamics of glass formation. In the infancy of metallic glass research, Cohen and Turnbull identified the correlation between deep eutectics and glass forming compositions [25, 26]. Currently, the most comprehensive model for describing the coincidence between the compositional location of deep eutectics and glass forming alloys is Cheney's liquidus model [21, 27, 28]. The following sections will describe these three models in detail.

2.2.1 Miracle Packing Model

Miracle's primary assertion is that local order in glass forming systems is composed of a single solute atom surrounded by solvent atoms [23]. From this building block, atomic clusters are formed. The efficiency with which these atomic clusters are packed plays a critical role in the dense random packing of the bulk sample, and thus its glass forming ability. A system of coordination numbers was developed to better classify which solute atoms pack most efficiently with particular solvent constituents [23, 24]. The coordination number, N^T , for the solute-solvent type cluster is described by Equation (2.2-1). N^T describes the ratio of the solute radius to the solvent radius, where a higher ratio allows for a larger coordination number and therefore, a higher packing fraction.

$$N^T = \begin{cases} \frac{4\pi}{6 \arccos \left\{ \sin(\pi/3) \left[1 - 1/(R+1)^2 \right]^{1/2} \right\} - \pi} & \text{for } 0.225 \leq R < 0.414 \\ \frac{4\pi}{8 \arccos \left\{ \sin(\pi/4) \left[1 - 1/(R+1)^2 \right]^{1/2} \right\} - 2\pi} & \text{for } 0.414 \leq R < 0.902 \\ \frac{4\pi}{10 \arccos \left\{ \sin(\pi/5) \left[1 - 1/(R+1)^2 \right]^{1/2} \right\} - 3\pi} & \text{for } 0.902 \leq R \end{cases} \quad (2.2-1)$$

The packing arrangement is dictated by Equation (2.2-1), and is at a maximum when the boundary solvent atoms are touching both the central solute atom and neighboring solvent atoms. According to Miracle's model [23], this condition is optimized when the coordination number is equal to an integer value. Ideal glass forming compositions can then be determined using Equation (2.2-2) once the coordination number for various different solute atoms with one solvent species has been determined.

$$S_{\Omega} = N^T / [1 + (12/N^T)] \quad (2.2-2)$$

S_{Ω} is the number of solvent atoms per solute atom. The global density of the amorphous structure is at a maximum if there are four topologically distinct atomic species. In other words, with Miracle's model, an optimized amorphous alloy design will have three solute atoms with different, integer value, coordination numbers for a particular solvent species. Even the metallic glass compositions with the highest global densities do not achieve packing fractions as high as those of the crystalline state. The dense clusters that form in the amorphous structure represent the maximum packing fraction at the local order of several atomic spacings. The high density of these atomic clusters is energetically favorable at lower temperatures, promoting the formation of

more clusters and minimizing the driving force towards crystallization by retarding the kinetics of crystallization. Furthermore, a strong chemical short range order exists between atoms within a dense cluster, and the thermodynamics and kinetics of atomic interaction within these clusters work in concert to slow all aspects of crystallization down such that the disordered, metastable, amorphous state is frozen in place.

The natural tendency for alloys is towards their equilibrium crystalline state. Crystallization involves nucleation first and then growth. Nucleation comes about as compositional and thermal fluctuations yield an energetically favorable situation for embryos to emerge from the liquid state. If this embryo reaches a sufficiently large size, where the free energy decrease due to reduction in volume outweighs the interfacial enthalpy generated at the solid-liquid interface, the crystal will become stable and grow. In the case of bulk metallic glass forming compositions, many different sized atoms are present, and the embryo must accommodate atoms of mismatched size into its lattice. The result of squeezing atoms, either too large or too small, into a crystalline lattice is the generation of elastic strain; another critical component to metallic glass formation. Elastic strain, ε_i , increases the energy required to form a crystal, and is shown in Equation (2.2-3). It was determined that glass formation is optimized with respect to elastic strain when ε_i is at least 0.54%, a value linked to the density difference between the amorphous and crystalline states, which ranges from 0.3-0.54% [29]. It should be noted however that this model does not take into account the chemical interaction between neighboring atoms in the melt. This model assumes the melt is a randomly dispersed liquid, which in the case of a glass forming melt with extensive short range order, is clearly not the case.

$$\varepsilon_i = \frac{\sum_{j=1}^1 C_j \gamma_j \xi [X_j^{sub.} (R_j^3 - 1) + X_j^{int.} (R_j^3 - \eta^3)]}{1 + \sum_{j=1}^n C_j X_j^{sub.} (R_j^3 - 1)} \quad (2.2-3)$$

In Equation (2.2-3) for the elastic strain, C is the solute composition in atomic percent, $\gamma = (1 - 4\mu_i/2K_i)(1 + 4\mu_i/3K_j)$ where μ_j and K are the shear and bulk modulus respectively, ξ is the coefficient of compaction in close-packed lattice ($\xi=0.74$ for f.c.c), and $X_j^{sub.}$ and $X_j^{int.}$, described by Equation (2.2-4) and (2.2-5) are the fractions of solutes occupying the substitutional sites and interstitial sites in the lattice, respectively. In Equations (2.2-4) and (2.2-5), $\alpha = av(1-\eta^6)/kT$, $\beta = \exp[2v(1-\eta^3)/kT]$, $a = 2\mu_i C_6/3$, $C_6 = 3K_j/(3K_j + 4\mu_i)$, η is the volume of an undeformed interstitial site in the matrix, $\eta=0.414$ for an octahedral site in a close packed structure, v is the atomic volume, and i and j denote the solvent atom and solute atom, respectively.

$$X_j^{sub.} = \left[1 + \frac{\exp(\alpha / R^3)}{\beta} \right]^{-1} \quad (2.2-4)$$

$$X_j^{int.} = \left[1 + \frac{\beta}{\exp(\alpha / R^3)} \right]^{-1} \quad (2.2-5)$$

2.2.2 Chemical Short Range Order (CSRO) Model

The governing equations of the chemical short range order model are given in Equations (2.2-6)-(2.2-8). In Equation (2.2-6), η is the chemical short range order between two species in a given melt, where i, j , and k are indices for the different atomic

species in a ternary liquid. The atomic composition of element i is x_i , m , n and p are intermediate variables, z is the coordination number (from Miracle), T is the temperature, R is the ideal gas constant, and λ , μ , and ν are the functions of the binary enthalpies ε_{ij} , ε_{jk} , and ε_{ik} . These equations require a numerical solution [30].

$$\eta_{ij} = 1 - \frac{m}{x_i x_j}; \eta_{jk} = 1 - \frac{n}{x_j x_k}; \eta_{ki} = 1 - \frac{p}{x_k x_i} \quad (2.2-6)$$

$$\frac{m^2}{(x_i - m - p)(x_j - n - m)} = \exp\left(-\frac{2\lambda}{zRT}\right); \frac{n^2}{(x_j - n - m)(x_k - p - n)} = \exp\left(-\frac{2\mu}{zRT}\right); \frac{p^2}{(x_i - m - p)(x_k - p - n)} = \exp\left(-\frac{2\nu}{zRT}\right) \quad (2.2-7)$$

$$\lambda = z \left(\frac{\varepsilon_{ij} + \varepsilon_{ji}}{2} \right); \mu = z \left(\frac{\varepsilon_{jk} + \varepsilon_{kj}}{2} \right); \nu = z \left(\frac{\varepsilon_{ik} + \varepsilon_{ki}}{2} \right) \quad (2.2-8)$$

As it has been previously discussed, the classical energy barrier for nucleation can be increased in multicomponent liquids, where strong heteroatomic bonding, corresponding to large negative mixing enthalpies, exists. The above equations simply combine the net effect of the binary mixing enthalpies of the three unique atomic species in a ternary melt to give a broader picture of the chemical interaction between atomic constituents in a ternary melt. This same approach can be extended to higher order melts [22].

2.2.3 Liquidus Model

This model is an extension of the well established relationship between metallic glass formation and compositions featuring deep eutectics, set forth by Cohen and Turnbull [25, 26]. Further work along these lines has focused on developing theoretical

methodologies for glass prediction utilizing binary phase diagrams to produce binary metallic glasses or for extrapolating binary information in order to construct a ternary system [31]. More recent efforts have established the correlation between the compositional location of deep eutectics and good glass forming ability. Using liquidus profiles to locate deep eutectics is a reliable approach to novel metallic glass design [32]. The current model developed by Cheney and Vecchio [21], however, can be extended not just to ternary metallic glass forming systems, but also the higher order compositions commonly necessary for bulk glass formation. The weighted liquidus temperature of each component of an alloy is normalized by the liquidus temperature of the whole alloy to give a ratio that is a strong indicator of the glass forming ability of a particular alloy. The ratio is a parameter termed α . This parameter quantifies the relative depth of a eutectic in an alloy system. If an alloy has a deep eutectic at a particular composition, it will have a correspondingly larger α parameter, and likely be a strong glass former [21]. A deep eutectic will result in solidification at much lower temperatures, which in turn yields much higher melt viscosities. The high viscosity hinders atomic mobility and inhibits crystallization. A reduced liquidus temperature is indicative of a stable liquid phase and so this approach inherently takes into account the thermodynamics which have already been established as useful to glass prediction.

Liquidus profiles can be generated for any multi-component alloy using ThermoCalc TCC software, which uses a comprehensive thermodynamic database to calculate free energies for alloys with up to twenty elements. The profiles generated using this software attempt to describe the highly metastable process of metallic glass formation using equilibrium liquidus profiles. Nonetheless, it has been shown that the

liquidus modeling approach appropriately identifies good glass formers from a number of different metallic glass forming systems [21].

Davies [33] stated that glass forming tendencies exist in the case of abnormally deep eutectics, corresponding to an actual liquidus temperature far below that calculated assuming an ideal solution or weighted temperature. The α parameter, described in Equation (2.2-9), is a measure of the depth of a eutectic as related to its liquidus temperature. The atomic fraction of the i th element is x_i , the liquidus temperature of the i th element is T_i , and n is the number of elements in the alloy. T_l is the actual liquidus temperature of the alloy, and as prescribed by Davies, this value will be far lower than the weighted liquidus in a good glass forming system. Therefore, α will be large for a stronger glass former. Cheney and Vecchio [21] showed that a good glass former typically has an α parameter in excess of 1.5, while marginal glass formers have an α parameter closer to 1.0.

$$\alpha = \frac{\sum_{i=1}^n x_i \cdot T_i}{T_l} \quad (2.2-9)$$

The three methods presented for metallic glass prediction together represent a comprehensive picture used to design amorphous alloys, but numerous other approaches exist that are viable in their own right. In order to achieve an amorphous structure, the thermodynamic, kinetic and topological aspects of solidification, central to each of the respective modeling approaches described above, must be accounted for. The design methodology employed in this work utilized the three aforementioned models in a combinatorial protocol to identify and assess glass forming systems.

2.3 Characterization of Metallic Glass

To date no one unified method exists for quantifying how strong of a glass former a particular composition is. One can argue that the greater the maximum achievable amorphous thickness, the better a glass former is, but often times the other thermodynamic data commonly associated with good glass formation do not reinforce why exactly a particular composition can be made to a given thickness. This section will describe several of the most common methods used to characterize bulk metallic glass formation.

The glass transition (T_g) is an inherent feature of glassy structure. Although commonly identified as such in the literature, the glass transition is not a singular temperature, but rather, a temperature interval over which kinetics drastically change; it is a function of the thermal history of the glass, and in particular, a function of the heating rate [34]. Irrespective of the heating rate, the glass transition is a small endothermic event typically characterized via differential scanning calorimetry. The magnitude of this event is usually only a small fraction of the magnitude of the exothermic peaks associated with re-crystallization of amorphous alloys above T_g . In general there is an increase in the onset glass transition temperature as the heating rate is increased, as shown in Figure 2.3.1, for the very strong glass former $\text{Pd}_{43}\text{Ni}_{10}\text{Cu}_{27}\text{P}_{20}$. On account of this, the convention is to characterize the glass transition via differential scanning calorimetry at a heating rate of $20^\circ\text{C}/\text{min}$, and although it is a temperature interval, a particular glass transition temperature is reported, but it is merely the onset of the glass transition interval.

Another important feature of metallic glasses used to quantify the stability of the glass is the supercooled liquid region (SCLR). It is defined as the range in temperature between the onset of T_g and the onset of the initial crystallization, T_x , and is commonly referred to as ΔT_x . A large ΔT_x provides a larger incubation time for crystallization, and thus promotes the amorphous state. Figure 2.3.2 shows DSC profiles for several Fe-based metallic glasses with T_g and T_x clearly indicated. Good glass forming compositions typically have ΔT_x in excess of 50K, with some exceptional Zr-based alloys having reported ΔT_x in excess of 100K.

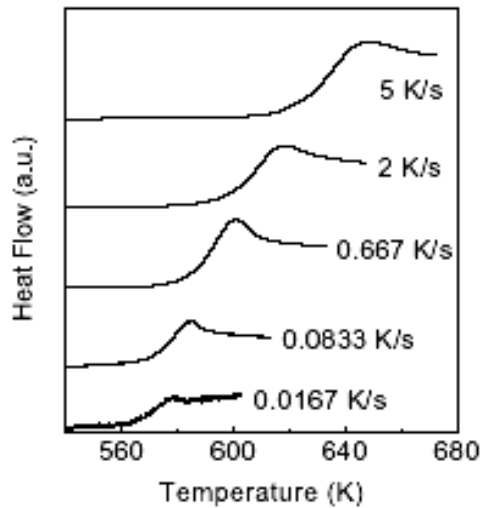


Figure 2.3.1. Differential Scanning Calorimetry for $\text{Pd}_{43}\text{Ni}_{10}\text{Cu}_{27}\text{P}_{20}$ indicating a dependence of T_g onset on heating rate. Endotherms are upwards [34].

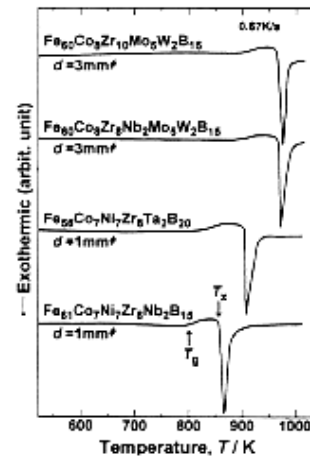


Figure 2.3.2. DSC curves for cast amorphous $\text{Fe}_{61}\text{Co}_7\text{Ni}_7\text{Zr}_8\text{Nb}_2\text{B}_{15}$, $\text{Fe}_{56}\text{Co}_7\text{Ni}_7\text{Zr}_8\text{Ta}_2\text{B}_{20}$, $\text{Fe}_{60}\text{Co}_8\text{Zr}_8\text{Nb}_2\text{Mo}_5\text{W}_2\text{B}_{15}$, and $\text{Fe}_{60}\text{Co}_8\text{Zr}_{10}\text{Mo}_5\text{W}_2\text{B}_{15}$ cylinders with diameters of 1 and 3 mm. T_g and T_x are clearly labeled.

Even after the establishment of the supercooled liquid region as a primary means to quantify glass forming ability, other parameters to quantify GFA arose. The glass transition and SCLR no doubt are good indicators of strong glass forming ability, but

using these parameters independently leads to some discrepancies. For instance $\text{Fe}_{56}\text{Co}_7\text{Ni}_7\text{Zr}_8\text{Nb}_2\text{B}_{20}$ has a ΔT_x of 86 K and can be made to a maximum thickness, D_{max} of 2mm, while $\text{Fe}_{60}\text{Co}_8\text{Zr}_{10}\text{Mo}_5\text{W}_2\text{B}_{15}$ has a ΔT_x of 64 K, yet can be made to a maximum thickness of 6 mm [20]. Similarly when we compare different bulk glass forming systems, $\text{Cu}_{45.5}\text{Zr}_{45}\text{Al}_7\text{Gd}_2\text{Ag}_{0.5}$ has $D_{max} = 11\text{mm}$ and $\Delta T_x = 108\text{ K}$ [35], while $\text{Zr}_{65}\text{Al}_{17.5}\text{Ni}_{10}\text{Cu}_{17.5}$ has $D_{max} = 16\text{mm}$, yet a ΔT_x of only 79K [36]. For comparison, the weak glass former $\text{Mg}_{80}\text{Ni}_{10}\text{Nd}_{10}$ can only be made to a thickness of 600 μm and has a ΔT_x of just 16 K. Although a strong glass former almost always coincides with a large SCLR or ΔT_x , it cannot adequately distinguish which glass former is better because of the unexplained variation in SCLR values across good glass forming compositions.

Another parameter used to quantify glass forming ability utilizes a good glass former's close proximity to deep eutectics by normalizing the glass transition temperature, T_g , with the melt temperature T_m . The resulting ratio tends to be higher for good glass formers because a deep eutectic corresponds to a smaller temperature interval between T_g and T_m . This is called the reduced glass transition, T_{rg} , and was adapted from Turnbull's treatment of amorphous solids such as silicate and organic glasses. Table 2.3.1 shows a number of glass forming compositions with their respective reduced glass transitions and D_{max} values. Note that good glass formers tend to have a T_{rg} in excess of 0.6 [26]. The combination of two separate parameters known to influence GFA greatly enhances the accuracy of the T_{rg} over the SCLR, although there are still some discrepancies. Note that several compositions in Table 2.3.1 have T_{rg} larger than that of other compositions, which have been made in larger thicknesses.

The critical cooling rate in metallic glasses is defined as the slowest cooling rate necessary to maintain a fully amorphous structure. Silicate glasses have critical cooling rate R_c as low as 0.001K/s [5]. Designing alloy compositions to lower critical cooling rates is central to achieving large amorphous thicknesses. The relationship between critical cooling rate and maximum achievable amorphous thickness is absolute; a lower critical cooling rate always corresponds to a larger maximum achievable amorphous thickness. Figure 2.3.3 indicates the relative cooling rates of thin foil amorphous alloys, bulk metallic glasses and silicate glasses. Figure 2.3.4 shows the range in critical cooling rate for various metallic glass forming systems. Note that in both Figures 2.3.3 and 2.3.4, there is a very strong correlation between both the critical cooling rate, R_c , and the critical thickness, D_{max} with thermodynamic parameters, T_{rg} and SCLR.

Table 2.3.1. Various glass forming compositions with associated glass transition and liquidus data. The reduced glass transition T_{rg} ($=T_g/T_m$) shows good coincidence with maximum achievable thickness, D_{max} [36].

Composition	T_g (K)	T_m (K)	T_l (K)	T_{rg}	D_{max} (mm)
Mg ₈₀ Ni ₁₀ Nd ₁₀	454.2	725.8	878.0	0.62579	0.6
Mg ₇₅ Ni ₁₅ Nd ₁₀	450.0	717.0	789.8	0.62762	2.8
Mg ₇₀ Ni ₁₅ Nd ₁₅	467.1	742.5	844.3	0.62909	1.5
Mg ₆₅ Ni ₂₀ Nd ₁₅	459.3	743.0	804.9	0.61817	3.5
Mg ₇₇ Ni ₁₈ Nd ₅	429.4	723.4	886.9	0.59359	0.1
Mg ₆₅ Cu ₂₅ Y ₁₀	424.5	727.9	770.9	0.58318	4
Zr ₆₅ Al _{7.5} Cu _{17.5} Ni ₁₀	656.5	1108.6	1167.6	0.59219	16
Zr ₅₇ Ti ₅ Al ₁₀ Cu ₂₀ Ni ₈	676.7	1095.3	1145.2	0.61782	20
Ti ₃₄ Zr ₁₁ Cu ₄₇ Ni ₈	698.4	1119.0	1169.2	0.62413	4
La ₅₅ Al ₂₅ Ni ₂₀	490.8	711.6	941.3	0.68971	3
La ₅₅ Al ₂₅ Ni ₁₅ Cu ₅	473.6	659.7	899.6	0.7179	10
La ₅₅ Al ₂₅ Ni ₁₀ Cu ₁₀	467.4	662.1	835.0	0.70594	5
La ₅₅ Al ₂₅ Cu ₂₀	455.9	672.1	896.1	0.67832	3
La ₅₅ Al ₂₅ Ni ₅ Cu ₁₀ Co ₅	465.2	660.9	822.5	0.70389	9
Pd ₄₀ Cu ₃₀ Ni ₁₀ P ₂₀	576.9	741.5	836.0	0.77802	72
Pd _{81.5} Cu ₂ Si _{16.5}	633.0	1008.8	1097.3	0.62748	3
Pd _{79.5} Cu ₄ Si _{16.5}	635.0	1019.3	1086.0	0.62298	0.75
Pd _{77.5} Cu ₆ Si _{16.5}	637.0	1019.4	1058.1	0.62488	1.5
Pd ₇₇ Cu ₆ Si ₁₇	642.4	1019.7	1128.4	0.62999	2
Pd _{73.5} Cu ₁₀ Si _{16.5}	645.0	1019.3	1135.9	0.63279	2
Pd _{71.5} Cu ₁₂ Si _{16.5}	652.0	1019.6	1153.6	0.63947	2
Pd _{64.5} Cu ₁₉ Si _{16.5}	640.0	1167.1	1234.3	0.54837	0.1
Pr ₆₀ Fe ₃₀ Al ₁₀	575.0	873.4	950.1	0.65835	3
Y ₆₀ Fe ₃₀ Al ₁₀	572.0	1075.9	1225.4	0.53165	0.7
Pd ₄₀ Ni ₄₀ P ₂₀	580.0	855.0	991.0	0.67836	25
Nd ₆₀ Al ₁₅ Ni ₁₀ Cu ₁₀ Fe ₅	430.0	709.0	779.0	0.60649	4
Nd ₆₁ Al ₁₁ Ni ₈ Co ₅ Cu ₁₅	445.0	729.0	744.0	0.61043	6
Zr _{41.2} Ti _{13.8} Cu _{12.5} Ni ₁₀ Be _{22.5}	638.0	937.0	993.0	0.6809	50

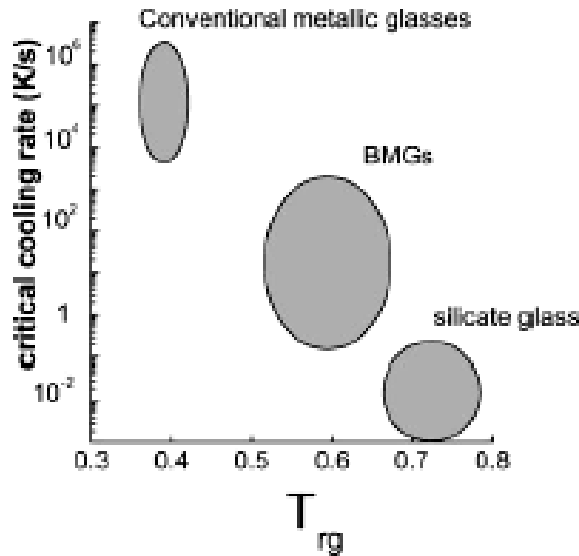


Figure 2.3.3. A comparison of critical cooling rate and reduced glass transition for conventional metallic glass, BMG, and silicate glass [5].

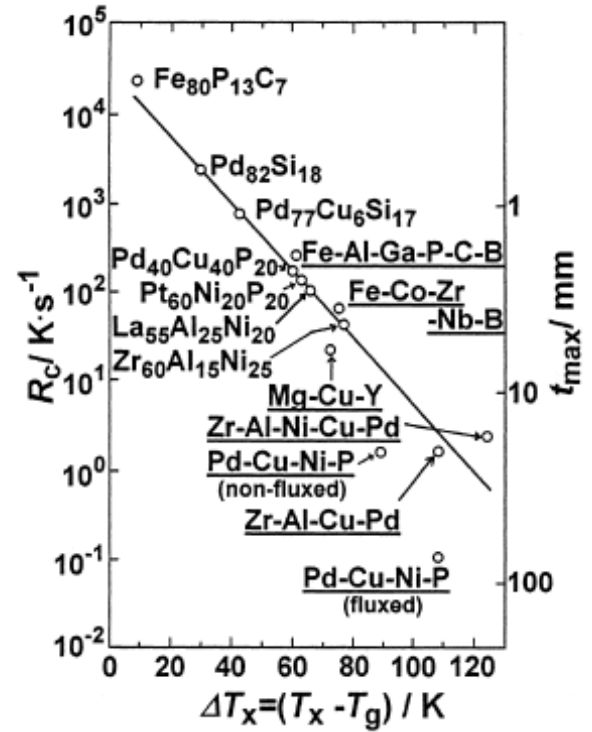


Figure 2.3.4. Relationship between R_c , t_{max} , and SCLR for various bulk amorphous alloys [20].

Free volume in metallic glasses and glass forming melts plays an imperative role in diffusion, viscosity, structural relaxation and many mechanical properties[37]. Free volume is defined as excess space between atoms necessary for atomic diffusion to occur. Cohen and Turnbull [25] provided the first description on the role of free volume effects in glass formation. Argon [38] is credited with the more accurate distributed free volume model thought to be more descriptive of metallic glass formation. In Argon's model, atoms are thought to move by small, sub-atomic steps as opposed to atomic distance jumps originally proposed by Turnbull [26]. Rapidly cooled glasses tend to have higher free volumes and are less stable. Upon annealing, the glass experiences structural relaxation and some of the free volume is annihilated. Bulk metallic glass formers tend

to lock in more free volume on solidification than do conventional metallic glasses such that the specific volume change upon solidification is smaller for better glass formers.

The crystallization process in BMGs is governed by the reduction in free energy as dictated by the free volume loss on moving from liquid to the crystalline state.

Equations (2.3-1) and (2.3-2) show the volume free energy change, ΔG_V , where r is the radius of the crystal, L_v is the latent heat of fusion, ΔT is the degree of undercooling, and T_M is the melting temperature. There is a competition between the volume free energy decrease and the surface free energy generated at the solid-liquid interface as the crystal grows. As shown in Equation (2.3-3), the surface free energy at the interface, ΔG_S , is dependent on the interfacial energy at the solid-liquid interface, γ_{SL} , and r . The total free energy change then becomes the sum of the two energy terms, $\Delta G_{\text{crystal}} = \Delta G_S + \Delta G_V$.

Figure 2.3.5 is a schematic illustrating the competition between surface free energy and volume free energy with respect to temperature. The surface free energy dominates for small crystal radii since the surface area is greater relative to the volume. As the crystal size grows, the volume free energy begins to dominate. The maximum in the total free energy curve, r^* , is the critical radius necessary for nuclei to stabilize.

$$\Delta G_V = \Delta g_v \times \frac{4}{3} \pi r^3 \quad (2.3-1)$$

$$\Delta g_v = \frac{L_v \Delta T}{T_M} \quad (2.3-2)$$

$$\Delta G_S = \gamma_{SL} \times 4 \pi r^2 \quad (2.3-3)$$

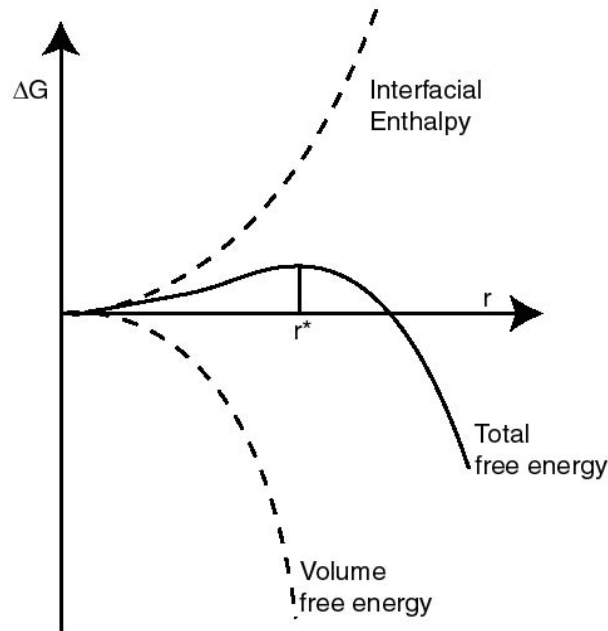


Figure 2.3.5. Free energy curve governing crystallization

Figure 2.3.5 gives a very clear illustration of the thermodynamic requirements for vitrification. Namely, it is important to increase the surface free energy term, while simultaneously minimizing the volume free energy term. Volume free energy is minimized by designing alloys with dense atomic clusters so that the liquid and glass state are similar to one another. In effect, glass forming melts are more organized than the liquid phase of a conventional alloy melt, but upon solidification of the glass forming melt, no significant atomic rearrangements occur, thus minimizing the volume free energy change. Metallic glass alloys have packing densities only slightly less than that of crystalline alloys. Increasing the surface free energy can be achieved by designing alloys with liquid structures that are vastly different from the initial crystalline phase structures.

This requires a significant energy contribution to generate new surfaces. Imposing these two thermodynamic constraints permits more stable metallic glasses to form by inhibiting crystallization, even at larger undercoolings.

In order to form a monolithic metallic glass, crystallization must be completely bypassed or severely limited. The nucleation rate, I_s is given in Equation (2.3-4) where k_s is a kinetic factor for surface nucleation, $\eta(T)$ is the temperature dependent viscosity, ΔG^* is the free energy of nucleation, T is the temperature, and $f(\theta)$ is a shape factor. In bulk metallic glass formation, it is therefore critical to minimize the nucleation rate through alloy design and material processing. Experimental determination of many of the parameters in Equation (2.3-4) is difficult for metallic glasses, making it nearly impossible to calculate nucleation rate using this method. From the expression though, it is clear that increasing the viscosity and decreasing the shape factor are useful steps to reducing the nucleation rate.

$$I_s = \frac{k_s}{\eta(T)} \exp\left(-\frac{\Delta G^*}{kT} f(\theta)\right) \quad (2.3-4)$$

The shape factor is a term related to the heterogeneous nucleation of a crystal. Heterogeneous nucleation occurs in the presence of a second surface or particulate. Thermodynamically, heterogeneous nucleation is easier than homogeneous nucleation, which occurs independently within an alloy melt. The interaction of an alloy melt with a crucible or mold wall is a common site for heterogeneous nucleation. Another critical factor in limiting nucleation during vitrification is the melting environment. The presence of oxygen during melting can lead to oxide formation in the melt. The surface of the oxide particles in the melt are sites for heterogeneous nucleation. Crystalline

phases with similar structure to that of the oxide may grow from the melt on top of these particles because the interfacial energy is much lower there. The reduction of the interfacial energy is dependent on the wetting angle of the alloy-oxide interface, but it will always result in smaller critical radius for stable nuclei, a lower degree of undercooling before crystallization, and a faster required cooling rate for vitrification. Special precautions must be taken during BMG processing to avoid such nucleation from occurring.

Accompanying the various thermodynamic aspects of solidification, the kinetics also play a critical role in avoiding nucleation. The viscosity is the most important and telling kinetic factor affecting nucleation. The degree to which atomic rearrangements are restricted governs whether or not the liquid structure can be frozen in place to make a glass.

When crystallization is kinetically constrained, a liquid can be undercooled with an accompanying rapid increase in viscosity or relaxation time. As the relaxation time of an undercooled liquid becomes comparable to the experimental time scale, the supercooled liquid begins to deviate from equilibrium and eventually forms a glass. The correlation between good metallic glass forming ability and the composition's proximity to a deep eutectic reinforces the correlation between high melt viscosity and high GFA. High temperature viscosity governs the crystallization kinetics close to the melting temperature, and thus, is of fundamental importance to the critical cooling rate for vitrification [39]. Cooling from above the liquidus temperature down to T_g yields a viscosity increase spanning 11 orders of magnitude from 10^1 - 10^{12} Pa's in some good glass forming, Zr-based alloys [40]. Conventionally it is assumed that the viscosity is 10^{12} Pa's

at T_g . Beyond glass formation, viscosity of metallic glass forming melts also plays a critical role in shaping and formability, as well as composite infiltration. Viscosity data near the melt temperature is difficult to obtain because of reactions between container walls and the glass forming melt yielding erroneous viscosity data. Levitation experiments [41] and other customized experiments [39, 42] have been designed to minimize invalid viscosity data.

The Cohen-Grest model [43] suggests a correlation between viscosity and free volume. In Equation (2.3-5), η is viscosity, v_f is the free volume per atom and bv_m is the critical free volume necessary for flow to occur.

$$\eta = \eta_o \exp(bv_m/v_f) \quad (2.3-5)$$

The free volume present in a liquid is indicative of the packing density, and therefore the atomic mobility. A densely packed liquid tends to have higher viscosity and smaller change in volume upon cooling. The volume change of good glass formers is notably smaller than that for pure metals during cooling [44-46].

C.A. Angell [47] developed the concept of fragility to quantify GFA based on the temperature dependence of viscosity or relaxation time. Metallic glass forming melts follow the Vogel-Fulcher-Tamman (VFT) relationship shown in Equation (2.3-6), where η_0 is the viscosity, A is a fitting parameter and T is the VFT temperature. The VFT relationship can also be expressed in terms of heating rate according to calorimetric experiments. Probing fragility via thermal analysis is an effective alternative to viscosity analysis, and is employed in Section 5.1.

$$\eta_o = \eta_o^* \exp\left(\frac{A}{T_0 - T}\right) \quad (2.3-6)$$

In metallic glass forming systems, the dependence of glass transition onset temperature on heating rate has an Arrhenius type fit. Fragility is a measurement of an alloys deviation from Arrhenius behavior. In Angell's treatment of glass stability, there are two primary classifications; strong and fragile liquids, characterized by Equation (2.3-7).

$$m = [d \log \eta / d(T_g/T)]|_{T=T_g} \quad (2.3-7)$$

In Equation (2.3-7), m is the fragility index, and is extracted from the Angell plot shown in Figure 2.3.6. The viscosity of strong liquids tends to have a smaller dependence on temperature compared to fragile liquids. Typically strong liquids are better glass formers [48]. It is generally accepted that a fragility index below twenty corresponds to a strong liquid, while a fragility index in excess of 100 corresponds to a fragile liquid.

The entropic changes associated with glass formation offer a better theoretical description of fragility. Figure 2.3.7 is a schematic representation of the entropy changes as a function of temperature for a glass forming liquid when cooled from an elevated temperature down to room temperature. In the diagram, the entropy of the glass forming liquid decreases with temperature. At the Kauzmann temperature [5], T_K , the equilibrium entropy of the liquid will be equal to that of the crystal. Below T_K , the entropy of the liquid will become smaller than that of the crystal. In effect, the Kauzmann temperature is the thermodynamic boundary of the glass transition, and the liquid ceases to exist before its entropy becomes smaller than that of the crystal [48]. The entropy change depends on both the entropy of fusion, ΔS_f , and the temperature interval between the melting temperature, T_m , and T_K , over which the entropy is lost. From these relations, a

thermodynamic description of fragility can be expressed by $\Delta S_f / (T_m - T_K)$. Similar to the fragility index, m , smaller values correspond to a strong liquid than for a fragile one.

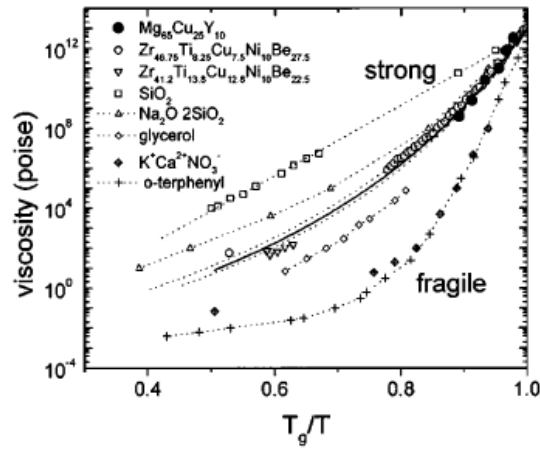


Figure 2.3.6. A comparison of viscosity of various glass forming liquids. Metallic Glass forming liquids fall intermediate between strong and fragile [5].

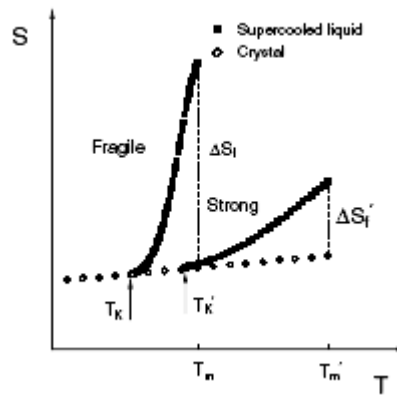


Figure 2.3.7. Schematic diagram for the entropy changes on cooling a liquid from T_m to T_K for fragile and strong liquids [48].

The free volume and viscosity of glass forming melts are intrinsic to the atomic rearrangements experienced by a glass around the glass transition region. This atomic rearrangement is called structural relaxation and plays an important role in defining glass stability and characterizing deformation in metallic glasses. The investigation of structural relaxation in early metallic glasses was not possible on account of the poor thermal stability and their tendency to crystallize when heated to temperatures near the glass transition. The development of BMG with much stronger resistance to crystallization provided the time frame necessary to conduct relaxation experiments [49]. The isothermal relaxation of metallic glasses is manifested by the annihilation of free volume towards an equilibrium value [50]. The free volume theory insists that the equilibrium free volume exists in both the supercooled and equilibrium liquids. The excess free volume present in the as-quenched glass state will tend towards a special thermodynamic state, called the fully relaxed state during isothermal annealing. When an as-quenched glass is isothermally annealed at a given temperature below T_g , the viscosity increases with time towards an equilibrium value according to the annihilation of quenched in excess free volume. Structural relaxation is often modeled using the Tool-Narayanaswamy (T-N) relationship, shown in Equation (2.3-8) fitted with the William-Watts relaxation function, shown in Equation (2.3-9) to account for the distribution in relaxation times typical in metallic glasses.

$$\tau = A \exp \left(\frac{x\Delta H}{RT} + \frac{(1-x)\Delta H}{RT_f} \right) \quad (2.3-8)$$

In the T-N relationship, ΔH is the activation energy for the relaxation times, A is the characteristic relaxation time, T is the temperature, T_f is the fictive temperature, and x is a

weighting constant between 0 and 1. The fictive temperature describes the influence of thermal history on the structural relaxation of the glass. Since the fictive temperature is directly related to the excess enthalpy and the free volume of the system, T_f in essence represents the degree of departure of the system from the equilibrium state. An x value of 1 corresponds to relaxation solely dependent on temperature, while a value of 0 indicates a dependence solely on fictive temperature; in reality an intermediate situation is the case.

$$\phi(\tau) = \exp \left[- \left(\frac{t}{\tau} \right)^\beta \right] \quad (2.3-9)$$

The William-Watts relaxation function is contained within the characteristic relaxation time, A , of the T-N model. In the relaxation function, β , where $0 < \beta \leq 1$, expresses the breadth of the distribution of the relaxation times and is sometimes called the Kohlrausch exponent [51]. A single relaxation time is denoted by $\beta=1$, and as the distribution becomes broader, the value of β is reduced and the enthalpy recovery spans a broader temperature range.

The features of metallic glasses that distinguish them from other glasses are low activation energy for relaxation, and broad transition temperature range; both a reflection of the instability of metallic glasses. The wide transition range can be attributed to the broad distribution in relaxation times and also to the complex compositional heterogeneity typical in bulk metallic glass forming systems. The T-N model has been applied with good success to several metallic glass forming systems. The validity of the model is verified by the accuracy with which it predicts peaks in specific heat curves according to the experimentally fitted relaxation distribution in the model [49].

An alloy melt's resistance to crystallization upon solidification is an excellent indicator of the degree to which its equilibrium state has been destabilized. The slow kinetics of metallic glass forming melts lead to strong resistance against crystallization. The activation energy for crystallization is used to quantify the resistance of an alloy melt to crystallization. The activation energy for crystallization is determined by the Kissinger method, shown in Equation (2.3-10),

$$\ln(\phi / T_p^2) = -\frac{Q}{RT_p} + \text{constant} \quad (2.3-10)$$

where ϕ is the heating rate, T_p is the peak temperature (the temperature at which the heat flow during crystallization reaches a maximum during differential thermal analysis), R is the universal gas constant, and Q is the activation energy for crystallization. The temperature at which the maximum heat flow is observed varies with heating rate.

Through analysis of several DSC curves generated at different heating rates, the kinetic constants, such as the activation energy can be determined [52]. Figure 2.3.8 shows how the activation energy, Q , is determined from the data for a $\text{Pd}_{76}\text{Y}_9\text{Si}_{15}$ alloy using the Kissinger method [53]. Q is taken from the slope of the Arrhenius plot generated from the Kissinger model. Note that for this alloy, two separate activation energies are given for the amorphous alloy in ribbon form (thickness $\sim 70 \mu\text{m}$) and rod form (diameter $\sim 3 \text{ mm}$). This difference indicates a dependence of the activation energy on alloy cooling rate. A thinner amorphous alloy sample will have greater resistance to crystallization than a thicker one of the same composition. This effect is less pronounced for a stronger, more stable glass former, which tends to have greater resistance to crystallization at larger sample thicknesses.

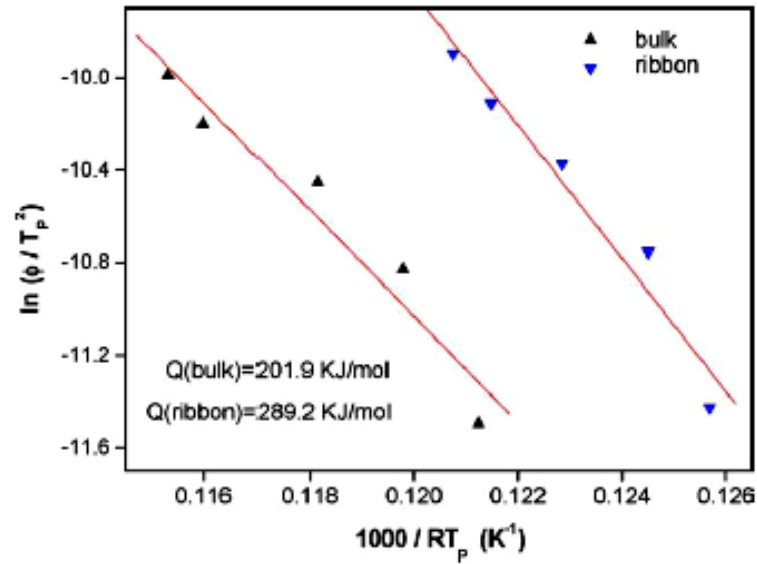


Figure 2.3.8. Kissinger plot of DTA data for $\text{Fe}_{61}\text{Co}_5\text{Zr}_8\text{Y}_2\text{Cr}_2\text{Mo}_7\text{B}_{15}$ rod and ribbon amorphous alloys [53].

2.4 Properties of BMG

Beyond fundamental research, BMGs offer excellent physical and chemical properties, which make them appealing as a viable future replacement in a number of different applications. This section will describe in detail some properties of bulk metallic glass.

2.4.1 Mechanical Properties

Plastic deformation in metallic glasses is associated with inhomogeneous flow in highly localized shear bands at low temperatures ($T < 0.7T_m$), and homogenous flow at elevated temperatures ($T > 0.7T_m$). At low temperatures, all bulk metallic glasses show nearly zero ductility in tension, where loading of a sample fails due to the propagation of a crack evolving from a single shear band [54]. In contrast, constrained loading such as compression can result in global plastic deformation in some metallic glasses, up to 3%

plastic strain [55]. The degree of plastic deformation before failure varies greatly from composition to composition among metallic glasses. Zr-, Pt-, and Pd-based BMGs have all shown plasticity in compression and fracture toughness as high as $70 \text{ MPa}\cdot\text{m}^{1/2}$ [20]. The fracture surface associated with such failure shows characteristic vein patterns with evidence of high local plasticity arising from instabilities in the shear band, which contains lower viscosity. In contrast, Mg- and Fe-based BMGs are both locally and globally brittle, showing significantly different fracture surfaces and fracture toughness less than $5 \text{ MPa}\cdot\text{m}^{1/2}$ [20].

Figure 2.4.1 summarizes the relationship between Young's Modulus (E) and tensile fracture strength ($\sigma_{t,f}$) or Vickers Hardness (H_v) for typical BMGs. The values are compared with some common crystalline alloys. The tensile fracture strength and Vickers hardness have a roughly linear relationship with E , expressed by $\sigma_{t,f} = 0.002E$ and $H_v = 0.06E/9.8$, respectively. Note that a linear trend exists for the crystalline alloys, but the slope is much steeper for the metallic glasses, indicating significantly larger elastic limits. High elastic limits are a common feature of all metallic glasses and are attributed to the formation of an ideally homogenized solid solution over the whole composition range of the glass forming system [5]. It can be summarized from Figure 2.4.1 that BMGs have much higher tensile strengths and much lower moduli than crystalline alloys of relatively similar compositions. The difference in these values between BMG and crystalline alloys is as large as 60%. The significant difference in mechanical properties is a reflection of the differences in deformation and fracture mechanisms between BMG and crystalline materials. Plastic deformation at low temperatures in metallic glasses is associated with inhomogeneous flow in areas of high

strain localization called shear bands [56]. Fully amorphous Fe- and Co-based BMG have the highest fracture strengths among all BMG with reported fracture strengths of up to 4250 MPa and H_v as high as 1200 [57].

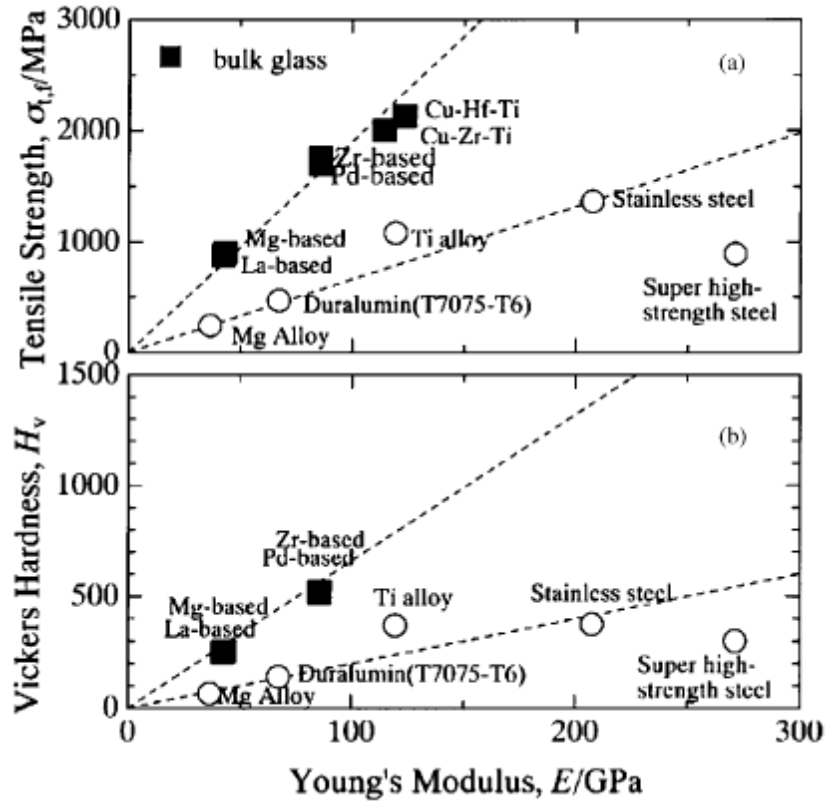


Figure 2.4.1. The relations between mechanical properties of typical BMGs: (a) tensile fracture strength ($\sigma_{t,f}$) with Young's modulus (E); (b) Vickers hardness (H_v) with Young's modulus (E) [20].

Bulk metallic glasses lack the long range order present in crystalline solids. As such, dislocations do not exist in metallic glasses, so slip is not a mode of deformation. Rather, at low temperatures, metallic glasses deform via highly localized shear bands. Shear bands yield brittle behavior in both tension and compression. All of the deformation experienced by the bulk sample is contained within these shear bands which propagate at a 45° angle to the loading axis [58]. Despite the typically brittle behavior of

metallic glasses, they tend to have extremely high yield stress and mechanical hardness. BMGs typically have lower elastic modulus, on the order of half that of crystalline materials of similar compositions. The lower modulus observed in metallic glass is a result of the more loosely bound atomic structure of the disordered glass, while the increased yield strength is a product of the very large elastic strain observed in BMGs.

Small regions of free volume between and within atomic clusters are the defects responsible for plastic flow in metallic glasses. These regions of free volume are distributed randomly throughout the bulk of the material. Regions of free volume are not to be confused with vacancies used to describe deformation in ionic solids. Rather, free volume regions in metallic glasses are of subatomic size and move in subatomic steps, unlike the atomic-sized jumps in network solids [56]. The free volume defects function though, in a way similar to a vacancy. Namely, they provide space for atomic rearrangement, but it is a collective movement of multiple free volume sites in subatomic steps that permits atoms to occupy new sites. The rearrangement of atoms facilitated by free volume can result in shear band initiation sites within regions of plastic flow [38]. Upon loading, the strain rate in shear bands accelerates ahead of the surrounding material, where the strain rate decelerates until a new stable equilibrium state of shear flow is achieved. The result of this offset in strain rates is the development of flow dilatation at the leading edge of the shear band. When a metallic glass is under stress, an atom may be forced into a region of free volume that is smaller than the atom itself. The result is the formation of excess free volume, since the site previously occupied by the atom is larger than that free volume region which it just moved into. Unlike defects in crystalline solids, which can only be annihilated at a free surface or grain boundary, free

volume may be annihilated within the bulk of a material by a collective diffusion of several atoms around the free volume site. A bulk metallic glass undergoing deformation is constantly experiencing both free volume creation and annihilation in localized regions of plastic flow, called shear transformation zones (STZ). At low stresses, free volume generation and annihilation are in equilibrium, but at high stresses, the annihilation of free volume lags and an excess of free volume results [38]. A single shear band can evolve to initiate a crack and eventual failure of the material due to this free volume instability. The global plasticity of a metallic glass is entirely contained within a few shear bands. In a theoretical study, the failure stress of a material was found to coincide very well with the localization stress required to initiate and propagate a shear band in an STZ [58].

The localization of shearing in BMG can sometimes lead to such intense energy released, that local melting is observed (even at low strain rates $\sim 10^{-3} \text{s}^{-1}$), resulting in a cup and cone fracture surface, which can be seen in Figure 2.4.2(a). The fracture surface shown in Figure 2.4.2(b) demonstrates a vein pattern characteristic of failure in bulk metallic glasses. Although the bulk material exhibits brittle failure, a vein like fracture surface is observed because failure occurs along a single shear band within which extensive plastic flow occurs [59]. The low temperature tensile behavior of metallic glasses is described as elastic-perfectly plastic because the shear banding mechanism does not provide any work hardening. It is possible though for metallic glasses to demonstrate some ductility in specific cases related to the number and distribution of shear bands within the bulk.

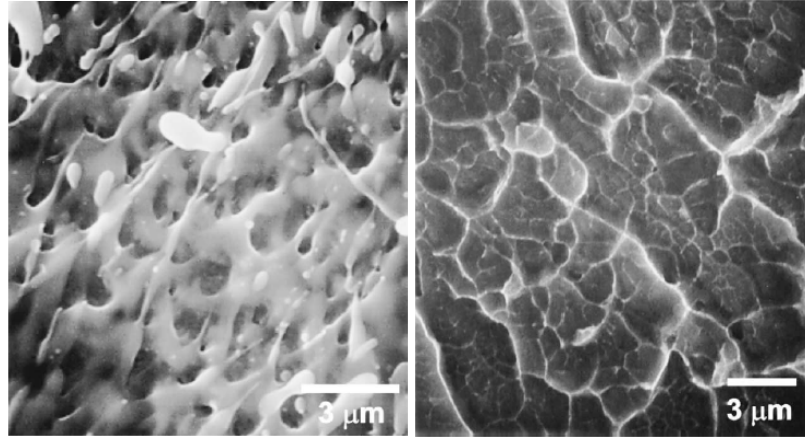


Figure 2.4.2. (a) Cup and cone failure surface of Zr-based BMG tested in tension indicating localized melting under high strain rate condition. (b) Vein pattern fracture surface in fracture toughness experiment of Zr-based BMG. The vein pattern suggests a decrease in glass viscosity resulting in highly localized flow process on the crack plane [5].

Melt spun ribbons of metallic glass exhibit bending ductility due to some interesting geometrical effects. Typically, melt spun metallic glass ribbons are on the order of $\sim 100\mu\text{m}$ thick. The small sample thickness confines the shear bands such that shear band spacings are small. Shear bands tend to nucleate near the outer surface of a material in a state of bending; in areas of tension or compression. Shear bands arrest within the bulk where no stresses are present [60]. The very high ratio of surface to bulk in a melt spun ribbon leads to a high shear band density [61]. Beyond a metallic glass thickness of about $500\mu\text{m}$, the shear band density is not high enough to maintain this ductile behavior. The critical shear band spacing for ductility to occur varies significantly with composition. For bulk metallic glasses, there are generally few shear bands with large spacing, resulting in brittle failure, since all of the plastic flow is confined within a very small volume fraction of the bulk material; high strain rates are an exception. Some bulk metallic glasses have exhibited limited plasticity at strain rates

exceeding 10^{-1} s^{-1} . Under such conditions, the stress relaxation rate resulting from shear band propagation cannot accommodate the strain rate in the bulk of the material. To compensate for the deficiency in stress relaxation, multiple shear bands nucleate and propagate. The higher fraction of shear bands permits more plastic flow, and, in the case of the Zr-based Vitreloy 1, plastic strains exceeding 5% have been observed [62]. Some results from this study are shown in Figure 2.4.3.

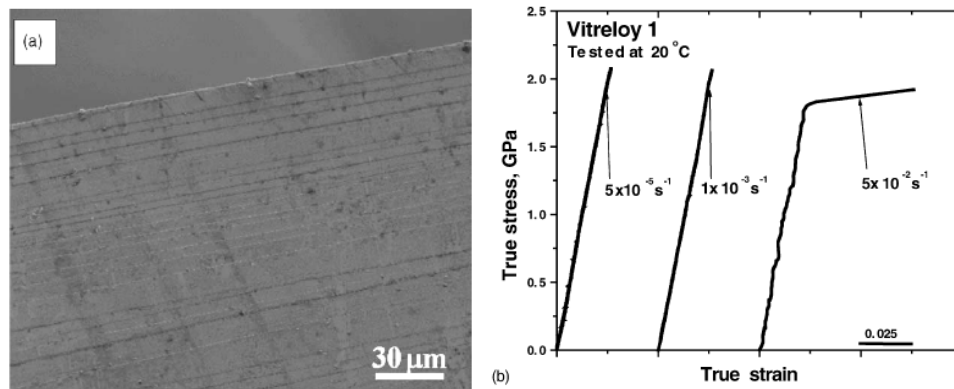


Figure 2.4.3. (a) Multiple shear bands in Zr-based Vitreloy 1 tested at a strain rate of 5×10^{-2} . (b) True stress-True strain curve indicating the development of plasticity above a critical strain rate in Vitreloy 1 [62].

Indentation tests are an easy to perform method for studying flow mechanisms in BMG. The sharp indenters create tremendous stress fields at the contact surface with the metallic glass, leading to shear band activation. Unlike other constrained deformation tests like uniaxial compression, microhardness indentation does not lead to catastrophic failure, thus permitting detailed studies of deformation processes beyond the elastic domain [63].

Mechanical hardness in BMG

For the same reasons that BMGs exhibit exceptional mechanical strength, namely high elastic limit and the lack of long range order, they also exhibit high mechanical hardness. Pd- and Zr-based alloys have reported hardnesses in excess of 500 H_v [64], while Fe-based metallic glass alloys have reported hardnesses in excess of 1000 H_v [4]. A dependence on indenter load has been observed in metallic glass hardness. Low indenter loads tend to give slightly higher hardness values. This has been attributed to the higher resistance to shear band nucleation at lower loads. Material pile-up is observed around the edges of the indentation in the form of semi-circular shear bands as shown in Figure 2.4.4. The size of the pile-up, or the distance from the edge of the indent to the outermost shear band, increases with increasing load. Furthermore, the size of the pile-up and the density of the shear bands are compositionally dependent. Zr-based BMGs have smaller pile-up zones than Pd-based alloys, indicating stronger resistance to deformation [64].

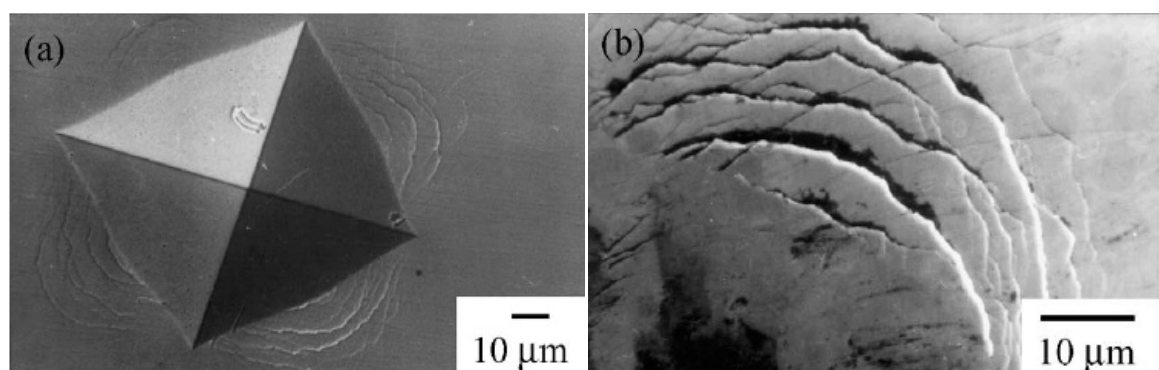


Figure 2.4.4. (a) Representative optical micrograph of semi-circular shear bands around a pyramidal Vickers indentation in a bulk metallic glass. (b) Zoomed in image of semi-circular shear bands from same sample highlighting the step-like nature of the shear bands.

Formability of BMG

At elevated temperatures, in excess of $0.7T_g$, homogeneous flow is observed in metallic glasses. Homogenous flow allows for superplastic flow to occur in metallic glass forming compositions, which is an important feature in the formability of metallic glasses. Superplastic flow allows for complex sample geometries to be made in a manner similar to conventional plastics. The nature of the superplastic flow permits the formation of very complex, precise shapes necessary for MEMS device fabrication [65]. Superplastic forming (SPF) typically takes place in the supercooled liquid region (between T_g and T_x), where pressure molding is used to form the sample to particular geometries. Recall also that the plasticity of fully solidified BMG improves significantly at small dimensions. A BMG MEMS part is shown in Figure 2.4.5.

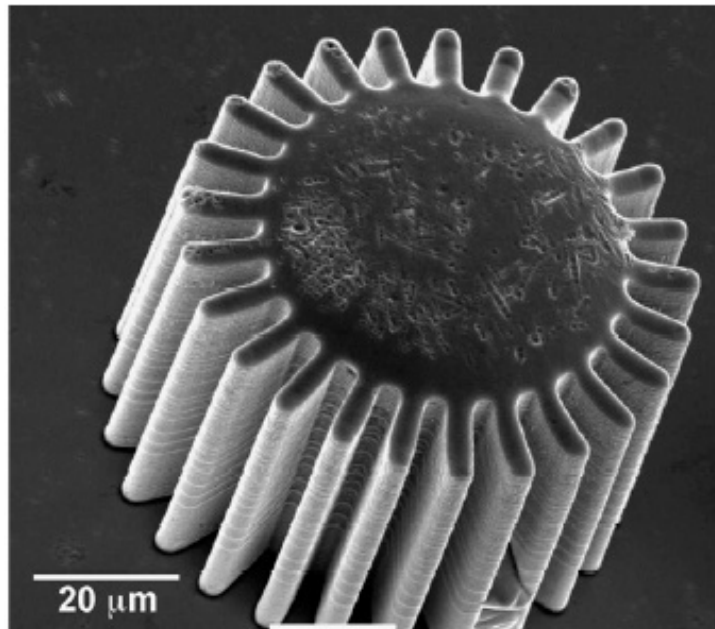


Figure 2.4.5. Complex micro gear fabricated by superplastic forming of BMG[65].

Kinetic processes occur faster at elevated temperatures. Inhomogeneous deformation is still observed in metallic glasses at elevated temperatures that remain below T_g , however free volume is eliminated faster on account of faster diffusive processes at high T . In contrast to the low-temperature, high-stress regime, at these elevated temperatures the elimination of free volume is in equilibrium with free volume creation up into the plastic regime. The transition temperature from inhomogeneous deformation to homogeneous deformation is strongly dependent on the strain rate, indicating that this type of deformation is associated with diffusion/relaxation processes [66]. By way of homogenous deformation at temperatures between T_g and T_x , metallic glasses can undergo tensile elongations in excess of 10,000% [67]. At strain rates below 10^{-3} s^{-1} , and at temperatures within the SCLR, BMGs behave as a Newtonian liquid. As the strain rate is increased, the glass behaves like a non-Newtonian liquid, likely because the material reverts back to a state of semi-inhomogeneous deformation, where the free volume being destroyed via diffusive processes cannot keep up with free volume creation. The transition to homogenous deformation is accompanied by significant softening in the range of $0.7T_g - 0.8T_g$, resulting in lower yield stress and more plastic flow [67].

Fatigue in BMG

Fatigue in metallic glasses is characterized by limited plastic deformation. Crack-growth thresholds are on the lower end of most structural metallic alloys, typically in the vicinity of $1.1\text{-}1.3 \text{ MPa}\cdot\text{m}^{1/2}$ [68-70]. The endurance limit in most metallic glasses is only about 10% of the ultimate tensile stress. Above this limit, fatigue cracks will propagate. In some Zr-based metallic glasses, endurance limits as high as 40% of the ultimate tensile

stress have been observed [71, 72]. For comparison, structural crystalline alloys typically have endurance limits in the range of 50% of their ultimate tensile strength. Due to their inherent nature towards surface cracking and brittle failure, extreme care is necessary in preparing BMG samples with pristine surfaces for fatigue testing, often with RMS surface roughness in the range of 0.1-0.5 μm . The mechanism for fatigue crack growth is shear band formation. Cracks initiate within shear bands, but the lack of homogeneous plastic deformation at low temperatures prevents crack blunting from occurring as is the case in crystalline alloys. Due to the lack of crack blunting, fatigue lifetime in metallic glasses is governed not by crack initiation time, but by crack growth time. In a study of fatigue lifetime in Zr-based metallic glasses, cracks initiate following the Mohr-Coulomb flow criterion [73, 74], resulting in a 49° angle with the loading axis under tension. The crack will grow until a critical length is reached, where the crack will abruptly change direction to an orientation perpendicular to the loading axis, and fast fracture occurs [75].

Mechanical behavior in BMG composites

It has been widely established that ductility enhancement in BMGs depends on the suppression of localized strain softening caused by shear bands [76]. The introduction of crystalline phases into a glassy matrix can provide dislocation-related work hardening that functions to suppress the strain softening of a single shear band, and, in fact, promote the generation of multiple shear bands within an amorphous matrix. The higher volume fraction of shear banding delocalizes the strain softening, resulting in enhanced global plasticity, although reduced strength is observed in some BMG matrix composites [77]. Devitrification of fully amorphous precursors is one method for

creating amorphous matrix composites, however, the slow kinetics inherent to glass forming compositions limit this method to nanometer sized crystalline phases and minimal plasticity enhancement. Slightly altering the composition away from ideal glass forming stoichiometry, adding in second phase particulates or fibers, as well as sample casting under varied cooling rates are all viable pathways to achieve crystalline microstructures with a distribution of sizes, while still, in some cases, maintaining an amorphous matrix. These latter techniques have proven effective in enhancing the plasticity of BMG derived materials. These methods will be described, using some examples from literature, in this section.

Initial efforts towards ductility enhancement in BMG composites were centered around the very good Zr-Ti-Cu-Ni-Be glass formers commonly called Vitreloy [59, 78]. The strong resistance to crystallization permitted the addition of stainless steel fibers [78], or refractory carbide particulates [59] to the alloy, while still maintaining an amorphous matrix. These early studies also established BMG as an excellent matrix candidate because the controllability of the reactive wetting process with secondary particles is very good and the thermal stresses upon solidification are minimal.

Choi-Yim [59] investigated the effect of SiC, WC, W and Ta addition to Zr-Nb-Al-Ni-Cu BMG. The mechanical properties of several BMG matrix composites are shown in Figure 2.4.6. Various volume fractions of each refractory material were simply added into the glass forming melt prior to casting. The distribution of the various microstructures achieved is shown in Figure 2.4.7. The very slow kinetics in the glass led to very little reactivity between the particulates and the surrounding matrix. In fact, the

supercooled liquid region of the amorphous phase was unaffected by the presence of crystalline phases in the matrix.

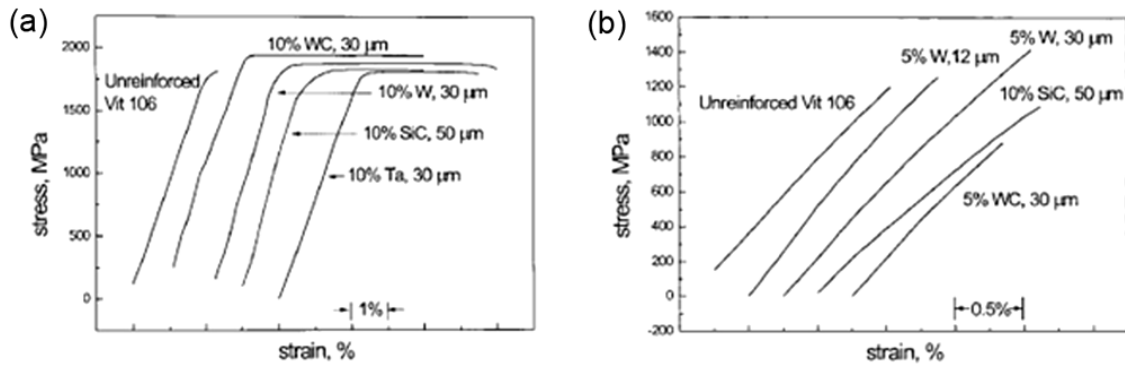


Figure 2.4.6. (a) Quasi-static compression stress-strain curves of Vit 106 and composites reinforced with WC, SiC, W, and Ta. (b) Quasi-static tensile stress-strain curves of Vit 106 and composites reinforced with WC, SiC, W, and Ta [59].

As shown in Figure 2.4.6(a), the presence of second phase particles in these BMG matrix composites leads to an improvement in compressive ductility compared to the fully amorphous glass. However, Figure 2.4.6(b) illustrates that no such enhancement in ductility was observed in tension. The enhancement in ductility is attributed to the arresting and deflection of shear bands induced by the presence of the WC, SiC, W, and Ta particles. As deformation continues, new shear bands inevitably form, but as the process repeats itself, the volume fraction of shear bands increases and the global plasticity is enhanced.

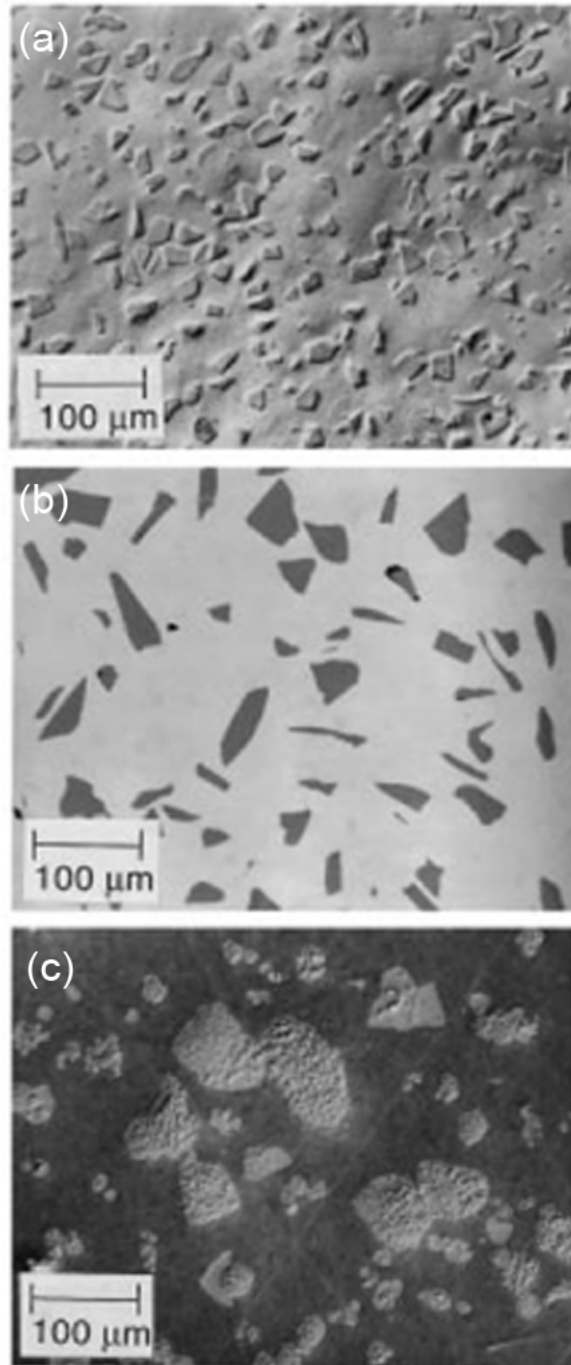


Figure 2.4.7. Optical micrographs of polished surfaces of (a) $\text{Zr}_{57}\text{Nb}_5\text{Al}_{10}\text{Cu}_{15.4}\text{Ni}_{12.6}$ alloy (Vit 106)/WC composites, (b) Vit 106/SiC composites, and (c) Vit 106/W composites, showing a uniform distribution of particles in the Vit 106 matrix [59].

More recently, alternative processing has led to new BMG-derived composites with hierarchical structures that have demonstrated superior ductility in both tension and compression. In order to become a viable structural alternative, a compromise between strength and ductility must be attained. It is often the case that coarse-grained alloys demonstrating good ductility have low yield strength, while amorphous alloys, exhibit very high strength, but extremely low plasticity. By controlling the cooling rate and subsequently annealing, both nucleation and growth can be adjusted to achieve a variety of different microstructural length scales in a BMG matrix composite. The result is an Fe-based BMG-derived composite alloy ($\text{Fe}_{42}\text{Co}_{7.3}\text{Ni}_{16}\text{Cr}_{11.8}\text{Cu}_{6.3}\text{C}_{14.8}\text{Y}_{1.8}$) with a structural hierarchy ranging from nanometers to millimeters [79].

Casting and subsequent annealing leads to a combination of lathy phase (~0.1 mm in length and 100-200 nm in width), as well as a homogeneously dispersed dendritic phase averaging 10 μm in length, and nanocrystalline particles ~3 nm in size, all embedded in an amorphous matrix. The hierarchical microstructure is illustrated in Figure 2.4.8.

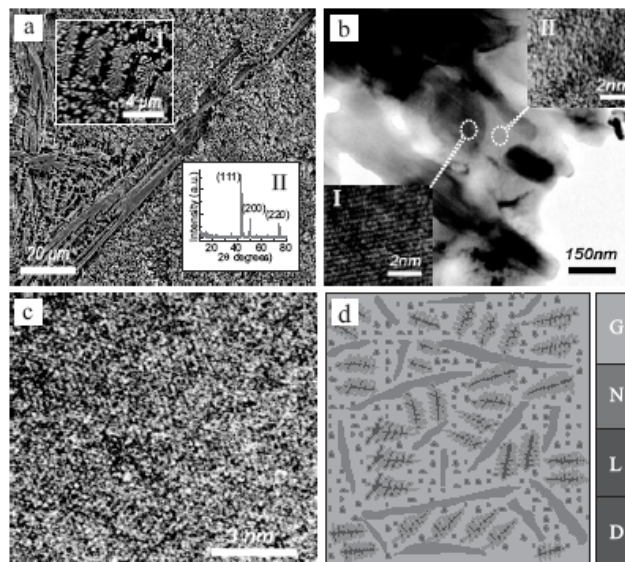


Figure 2.4.8. a) SEM image of lathy phase. (I: dendritic phase; II: XRD pattern of the alloy), b) Bright-field TEM image of alloy. (I: HRTEM image of the lathy phase, and II: HRTEM image of the amorphous matrix), c) HRTEM image of nanostructured grains embedded in the amorphous matrix, d) Schematic illustration of hierarchical microstructure for the Fe-based alloy [79].

Chemical analysis of the nucleating phases revealed that the nanocrystalline phase was rich in Cu and Y, the dendritic phase was Cu rich and Y scarce, and the lathy phase is both Cu and Y scarce, and primarily a face centered cubic Fe(Cr,C). Copious nucleation was achieved by slightly altering the ideal glass forming composition by adding an excess of Cu. The critical factor is that the largest feature in these alloys, the lath structure, acts as a stiff fiber, while the dendritic structure can itself deform because it is ductile, owing to its Fe and Cu rich composition. The fact that the dendritic features are ductile plays a crucial role in the mechanical behavior.

The data from mechanical tests is shown in Figure 2.4.9. This alloy exhibited a compressive yield strength of 1.70 GPa and fractures after 13.1% engineering strain at 3.79 GPa. It is the first demonstration of extensive plastic deformation and work

hardening observed in an Fe-based BMG-derived material. The work hardening observed is significant because it prevents inhomogeneous flow and catastrophic failure typical in monolithic BMGs.

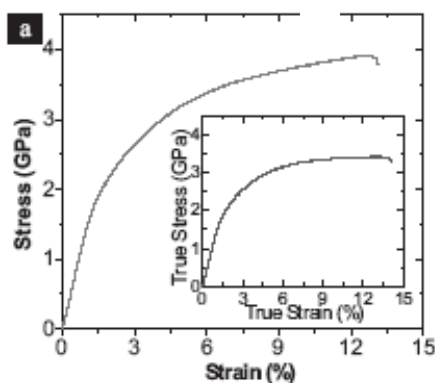


Figure 2.4.9. Compressive stress-strain curve for $\text{Fe}_{42}\text{Co}_{7.3}\text{Ni}_{16}\text{Cr}_{11.8}\text{Cu}_{6.3}\text{C}_{14.8}\text{Y}_{1.8}$ at ambient temperature with inset of true stress-true strain [79].

The fracture surfaces for alloys from this study are shown in Figure 2.4.10. Transgranular fracture characteristics resulting from rupture of the lath features (Figure 2.4.10(bI) indicate that energy is distributed across the matrix [80]. The presence of the nanoparticle phase within the glassy matrix results in the dimple structure typical of ductile failure observed in Figure 2.4.10(bII). Some vein patterns were also observed in Figure 2.4.10(bIV) indicating typical, localized softening type failure, of the glassy phase. Figure 2.4.10(c) is a bright field TEM image showing the interaction between crystalline grains and microcracks. A large intergranular crack (marked by large white arrow) is rechanneled to propagate along the boundary (marked by black arrows), and a smaller crack (marked by small white arrow) is blocked by nanoparticles (the inset is a HRTEM image of the grains and matrix in the fractured sample). The extensive microcracking, and frequent redirection of these cracks is due to the hierarchical

microstructural features in the alloy. Lastly, Figure 2.4.10(d) shows stacking faults within a crystalline grain. These stacking faults were not observed in the as-cast sample, which indicates that deformation is mainly accommodated in the crystalline portion of this unique, hierarchically designed alloy.

The glassy matrix of $\text{Fe}_{42}\text{Co}_{7.3}\text{Ni}_{16}\text{Cr}_{11.8}\text{Cu}_{6.3}\text{C}_{14.8}\text{Y}_{1.8}$ only accounts for about 5 volume percent of the BMG composite. Accordingly, an elastic limit much lower than typical BMG was observed. However, the elastic limit of 1.3% is still significantly higher than conventional crystalline materials (~0.2-0.6%). On account of the low volume fraction of amorphous material in this alloy, shear banding is no longer the primary mechanism for deformation. Instead, intergranular microcracks are diverted or blocked by the nanocrystalline phases, and, on account of the extensive microstructural development, it becomes very difficult for these microcracks to coalesce into one crack resulting in final failure.

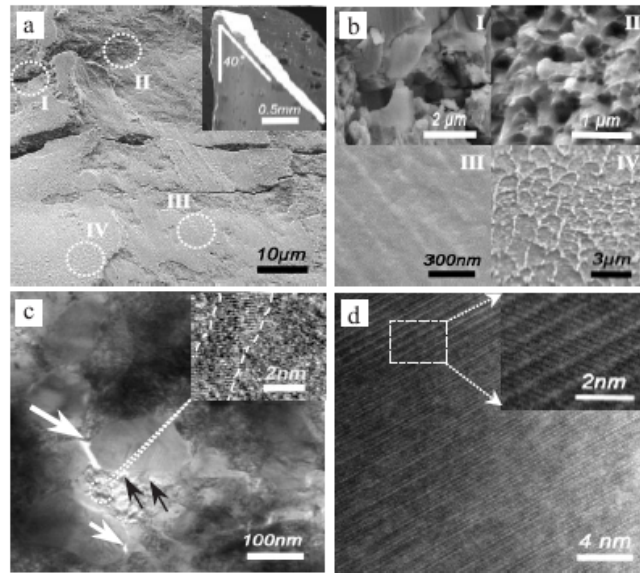


Figure 2.4.10. Fracture behavior and deformation mechanisms of the failed alloy: (a) SEM image of the fractured surface; b) SEM images showing magnified regions marked by I, II, III and IV in a); c), Bright field TEM image of the deformed sample; d) HRTEM image exhibiting numerous stacking faults in the deformed sample [79].

A third approach to achieving ductile BMG composites is a combination of the two methods discussed above; specialized processing was employed using the very stable Zr-based glasses. However, the composition was adjusted away from the ideal glass forming composition to induce copious crystallization. The composition was adjusted to guarantee the nucleation of ductile dendritic phases on the same length scale as the predominant deformation mechanism [81]. Namely, the feature size was tuned to ideally obstruct shear band propagation in the glass, since, unlike the study on microstructurally hierarchical Fe-based BMG composites, these Zr-based alloys are nearly 50% amorphous.

By matching fundamental mechanical and microstructural mechanisms, tensile ductility in excess of 10% was achieved in a series of Zr-Ti-Nb-Cu-Be BMG composites while still maintaining the extremely high strength of the monolithic BMG ($\sigma_y = 1.2-1.5$ GPa), and also achieving very high fracture toughness ($K_{IC} = 170$ MPa \sqrt{m}) [81]. This study is the first demonstration of tensile ductility in a BMG composite. The fundamental concept used to design these ductile BMG composites entails tailoring inhomogeneities in the material properties of the composite such that microstructural stabilization mechanisms become possible. The approach employed is similar to that used in the toughening of hard plastics by the inclusion of rubber particles [82].

Figure 2.4.11(a) shows the uniform distribution of b.c.c. Zr-Ti-Nb dendrites within an amorphous matrix. The dendrites are elastically soft compared to the matrix. This first critical feature of the crystalline phases in BMG composites enables global plasticity by localizing yielding and deformation within the elastically soft dendrites. Contrary to the case of hard second phase inclusions, where the sole purpose of the crystalline phase is to arrest and deflect shear bands, ductile phase BMG composites are designed to both arrest shear band propagation and also transfer load and localize deformation within regions that can plastically deform.

The achievement of a uniform distribution of ductile phases throughout the amorphous matrix is the second critical feature in designing ductile BMG composites. In order to uniformly interrupt shear band propagation, the microstructural length scale must be in tune with the mechanical deformation length scale throughout the sample. In general, standard mold casting cooling rate effects result in a dependence of microstructure size with distance from the copper mold wall. To avert this, samples were

only heated to within the semi-solid, two-phase region, between the liquidus and solidus temperatures, such that a uniform distribution of β -Ti dendrites was quenched into the sample. Figure 2.4.11(a) shows the microstructure of the composite, while Figure 2.4.11(b) shows a HRTEM image of the crystal/glass interface with associated SADPs.

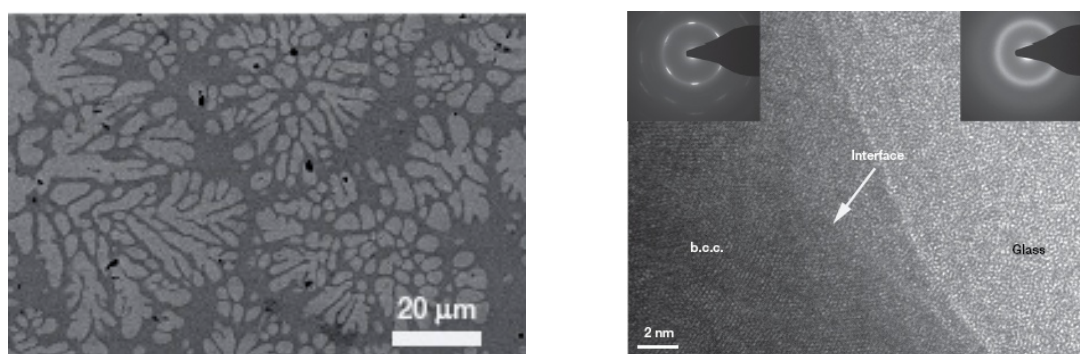


Figure 2.4.11. (a) SEM micrograph of microstructure achieved in Zr-Ti-Nb-Cu-Be BMG composite. (b) HRTEM micrograph of glass/crystal interface, SADP insets indicate b.c.c. structure in crystalline phase and amorphous structure in glassy matrix [81].

The observed tensile ductility in these alloys is associated with patterns of locally parallel shear bands that form in domains defined by the dendrite size and spacing within the amorphous matrix. The microstructure constrains primary shear bands resulting in the formation of secondary shear bands within the primary shear band. Figure 2.4.12(a) shows stress-strain curves for the fully amorphous alloy, Vitreloy 1 ($\text{Zr}_{41.2}\text{Ti}_{13.8}\text{Ni}_{10}\text{Cu}_{12.5}\text{Be}_{22.5}$), and 3 composites derived from Vitreloy1, $\text{Zr}_{36.6}\text{Ti}_{31.4}\text{Nb}_7\text{Cu}_{5.9}\text{Be}_{19.1}$, $\text{Zr}_{38.3}\text{Ti}_{32.9}\text{Nb}_{7.3}\text{Cu}_{6.2}\text{Be}_{15.3}$, and $\text{Zr}_{39.6}\text{Ti}_{33.9}\text{Nb}_{7.6}\text{Cu}_{6.4}\text{Be}_{12.5}$ (DH1, DH2, and DH3). Ni was found to decrease fracture toughness and also promote brittle intermetallic formation. The replacement of Ni with Nb promoted the formation of ductile Zr-Ti-Nb dendrites. All of the BMG composites exhibit significant tensile ductility. The degree of ductility is a direct function of the volume fraction of dendrites

in the composite. The volume fraction of ductile dendrites increases with decreasing beryllium content. Figure 2.4.12(b) demonstrates the scaling similarities between the microstructure and shear band size.

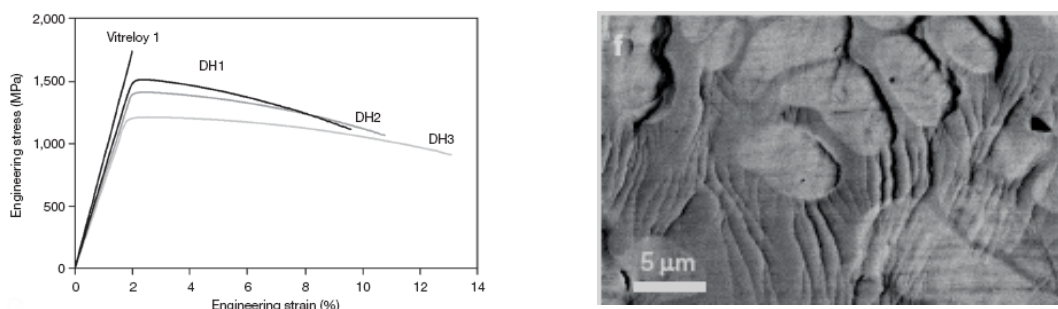


Figure 2.4.12. (a) Engineering stress-strain curves for Vitreloy1 and 3 different Vitreloy1-derived BMG composites. (b) High magnification SEM image of microstructure-shear band interaction [81].

The introduction of microstructural features either by addition of second phase particles, or control over the cooling rate of the alloy, results in enhanced ductility. In general, ductility enhancement in BMG matrix composites is achieved by redirecting or arresting shear bands in the glassy matrix. Subsequent deformation after shear band deflection results in the nucleation of new shear bands. The associated increase in regions of high plastic flow increases the global plasticity of the whole alloy. Alternatively, hierarchical microstructural tuning of the BMG composite can result in very low volume fractions of amorphous material such that no shear bands form in the matrix, and all plastic deformation is carried through a complex network of crystalline phases that deflect microcracks. Lastly, ductile phase BMG composites have been created that match fundamental mechanical and microstructural length scales. In ductile phase BMG composites, plasticity is achieved through the formation of multiple shear bands in the glassy matrix, in addition to ductile crystalline phases accounting for some

of the deformation. No matter what the pathway, the fundamental approach of using crystalline phases to obstruct typical deformation mechanisms in BMGs results in ductility enhancement that ultimately make the tremendous strength of BMG-derived materials a much more viable option as a structural material.

2.4.2 Corrosion resistance in BMG

Due to the lack of long range structural and compositional variations in metallic glasses, the corrosion resistance is inherently very high. The homogeneous structure of metallic glasses does not allow for galvanic cells to be produced within the material itself, thus limiting localized or preferential corrosion. Furthermore, all metallic glasses have inherently high reactivity because they are highly metastable materials. This increased reactivity allows for the rapid production of a passivation layer. As with many other features of metallic glass, corrosion resistance is strongly dependent on composition of the glass and its environment.

Corrosion resistance in BMGs is generally evaluated by weight loss and electrochemical measurements. This method of evaluation is common in many corrosion analyses. In general, the sample to be analyzed is subjected to a corrosive environment in the form of an electrolytic solution such as HCl, or NaCl under an applied voltage for a set duration. After removal from this solution, its corrosion resistance is quantified based on the mass loss due to the electrolyte. The change in the surface finish is also used to assess corrosion resistance. The composition and thickness of surface films such as a passivation layer are often investigated using energy dispersive X-ray spectroscopy (EDS).

The best Fe-based BMG alloys exhibit a corrosion rate 10^{-2} - 10^{-3} mm year⁻¹. Certain alloying elements like Nb and Cr have been shown to enhance corrosion resistance in Fe-based BMG alloys, however, it often comes at the expense of glass forming ability [83]. In the glass forming system, Fe-C-B-Mo-Cr, corrosion resistance and glass forming ability are simultaneously enhanced by the substitution of boron for iron [84]. Figure 2.4.13 shows some corrosion rate data for the alloy Fe_{50-x}Cr₁₆Mo₁₆C₁₈B_x. All of the alloys in this system demonstrate very strong resistance to corrosion in aggressive HCl solutions (1M, 6M, and 12 M). It is obvious from the data that the rate of corrosion decreases with increasing boron content, irrespective of the electrolyte concentration.

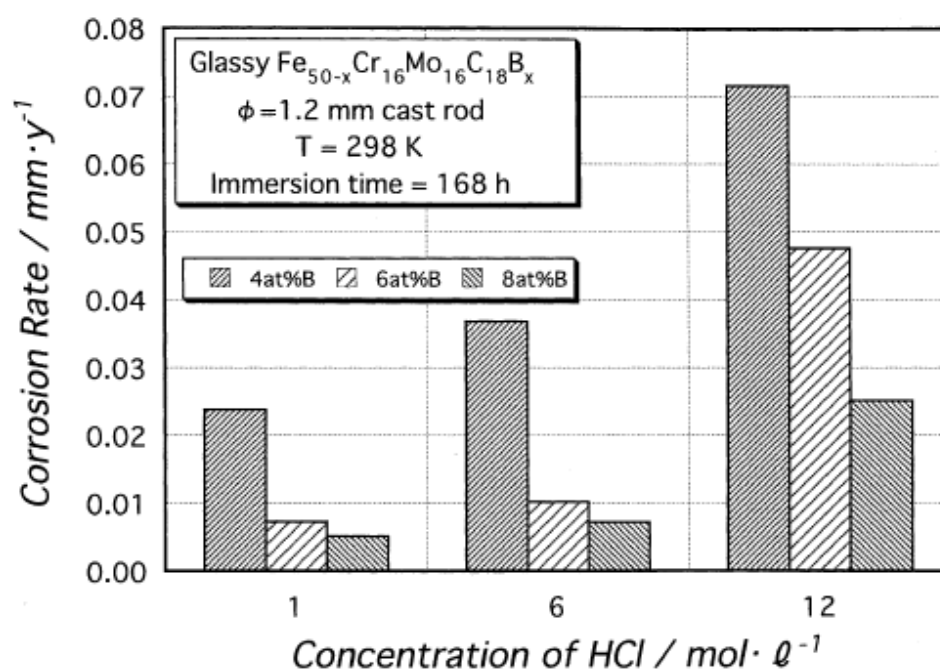


Figure 2.4.13. Corrosion rates of amorphous Fe_{50-x}Cr₁₆Mo₁₆C₁₈B_x rods 1.2 mm in diameter in HCl solutions open to air for 168 h at 298K [83].

Figure 2.4.14 shows SEM images of the outer surface of $\text{Fe}_{50-x}\text{Cr}_{16}\text{Mo}_{16}\text{C}_{18}\text{B}_x$ ($x=4,6,8$ at %). These data reinforce the positive role of high boron content in Fe-based BMGs. Figure 2.4.14(a) shows that pitting corrosion has occurred in the alloy with $x=4$ after 168h exposure to 12M HCl. The two high boron content alloys in Figure 2.4.14(b,c) show no pitting. In Figure 2.4.14(b) ($x=6$), a roughened surface indicates some general corrosion has occurred, but no pitting is observed. In Figure 2.4.14(c) ($x=8$) the surface appears very smooth, indicating very strong resistance to corrosion.

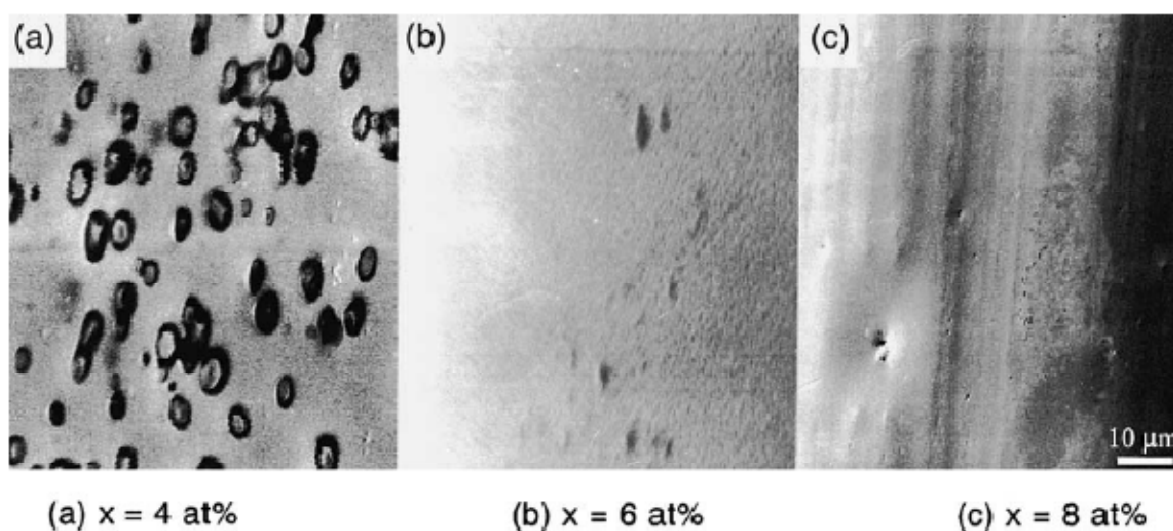


Figure 2.4.14. SEM micrographs of the surfaces of glassy $\text{Fe}_{50-x}\text{Cr}_{16}\text{Mo}_{16}\text{C}_{18}\text{B}_x$ 1.2 mm rods in 12 M HCl for 168 h at 298 K [83].

Another important aspect of corrosion resistance in BMGs is the formation of a passivation layer on the outer surface due to the inherent metastability of all BMGs. The presence of boron in $\text{Fe}_{50-x}\text{Cr}_{16}\text{Mo}_{16}\text{C}_{18}\text{B}_x$ promotes the diffusion of Cr to the outer surface, further enhancing corrosion resistance. The concentration of boron in the bulk alloy is directly related to the concentration of Cr, which diffuses to the surface. The first line of defense for a BMG alloy against corrosion is the passivation layer, and although it

is the presence of Cr in the passivation layer that actually improves corrosion resistance, the amount of boron plays a critical role in the kinetics of diffusion processes in the alloy, since it alters the dense random packing in the glassy state.

2.4.3 Magnetic features of BMGs

The unique structure of bulk metallic glass also gives rise to some intriguing magnetic phenomena. As is the case with their crystalline counterparts, the only metallic glasses exhibiting ferromagnetic properties are those containing Fe, Co, and Ni. To this point, Ni-based BMGs exhibiting magnetic properties have yet to be encountered. Fe- and Co-based BMG have exhibited excellent soft magnetic properties. Ferromagnetic BMG systems such as Fe-(Al, Ga)-(P, C, B, Si, Ge); Fe-TM (TM = IV–VIII group transition metal)-B; Fe(Co)-(Al, Ga)-(P, C, Si, B); Fe-(Co, Ni)-M-B (M = Zr, Hf, Nb, Ta, Mo, W); Fe-Co-Ln-B; Fe-(Nb, Cr, Mo, Ni)-(P, C, B); Co-Fe-(Zr, Hf, Nb)-B are soft magnetic BMGs.

In a study done by Makino [85], a comparison of a melt spun, Fe-based metallic glass ribbon with the same composition cast as a BMG rod with 1.5mm diameter revealed vastly different magnetic properties, with BMGs showing many advantages. The bulk glassy alloys had high electrical resistivity ranging from 200-500 $\mu\Omega\text{-cm}$, which can be attributed to the fact that no long range order exists to provide a pathway for electrons to travel. This high resistivity leads to low losses by eddy currents when subjected to an AC field, making BMGs very appealing for transformer cores. These BMGs also exhibited lower coercive field, $H_c \sim 0.2\text{-}4\text{ A/m}$, and higher initial and maximum permeability than the same composition processed as a ribbon. These

differences are attributed to the geometric differences between the samples; the constraints of the thin ribbon require greater field strength in order to get the same change in magnetization. The differences between the two geometries are represented in the I-H curves in Figure 2.4.15. Another appealing feature of the BMGs is high frequency permeability. This is an important soft magnetic property, which allows rapid switching from zero to high magnetization states, since the material can respond quickly to small changes in magnetic field, H . Good high frequency permeability is the collective result of two other features of magnetic BMGs working in conjunction with one another; the low coercive force coupled with the minimal current losses made possible by the high resistivity define the permeability characteristics of these alloys. The impressive soft magnetic properties of Fe- and Co-based BMG are attributed primarily to the well arrayed domain wall structure aligned in the circumferential orientation of a cast rod.

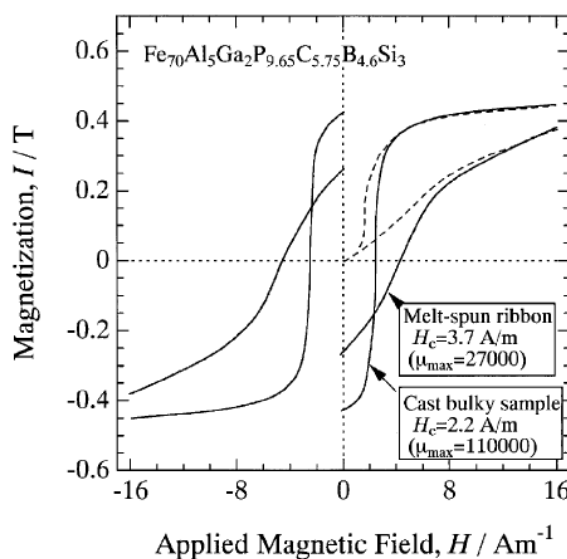


Figure 2.4.15 Comparison of I-H hysteresis loops for ring shaped Fe-based BMG with stacked melt spun ribbons making the same shape.

Heat treatment may also be used to tune magnetic properties in BMGs. Depending on the annealing time and temperature, an alloy may exhibit paramagnetic, soft magnetic or hard magnetic properties [16]. In an investigation of the alloy $\text{Fe}_{61}\text{Co}_7\text{Zr}_{9.5}\text{Mo}_5\text{W}_2\text{B}_{15.5}$, the relationship between annealed microstructure and magnetic properties was described in terms of domain wall pinning and magnetic exchange interaction.

The XRD spectra for $\text{Fe}_{61}\text{Co}_7\text{Zr}_{9.5}\text{Mo}_5\text{W}_2\text{B}_{15.5}$ indicate a multi-phased crystallization and can be seen in Figure 2.4.16. At the highest anneal condition, peaks corresponding to several different crystalline phases were observed. This type of multi-phased crystallization provides a vast canvas of opportunities to tailor magnetic properties based on heat treatments and microstructure. Each phase can be grown by isothermally annealing at the appropriate temperature.

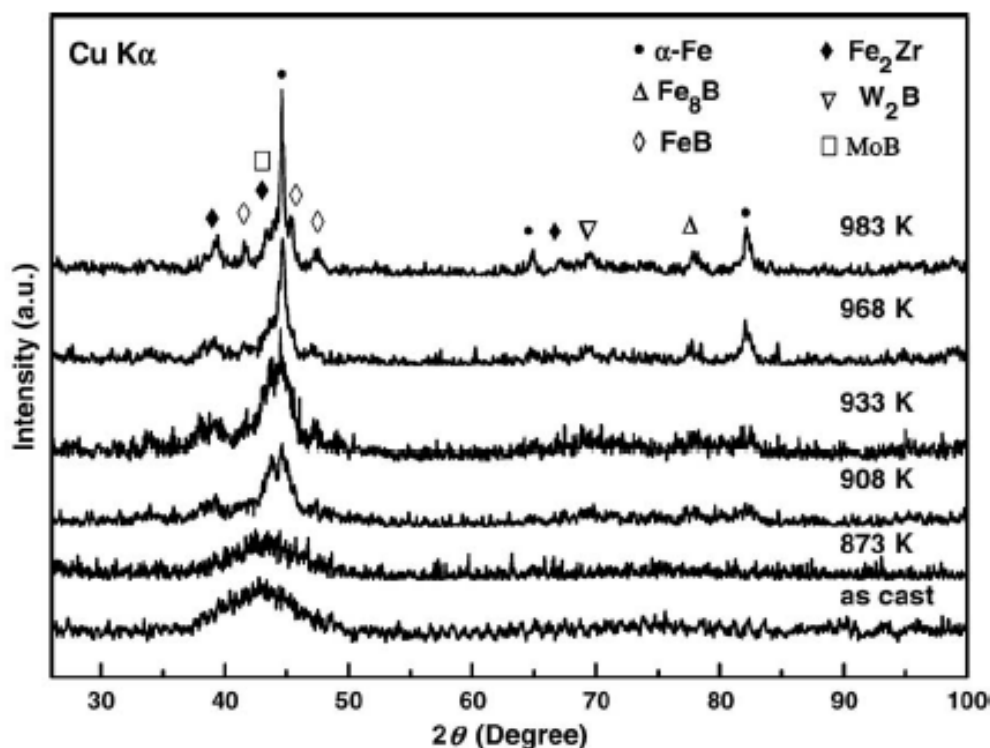


Figure 2.4.16 XRD spectra for $\text{Fe}_{61}\text{Co}_7\text{Zr}_{9.5}\text{Mo}_5\text{W}_2\text{B}_{15.5}$ annealed for 2h at 873, 908, 933, 968, and 983K.

The evolution of saturation magnetization and coercivity of

$\text{Fe}_{61}\text{Co}_7\text{Zr}_{9.5}\text{Mo}_5\text{W}_2\text{B}_{15.5}$ as a function of annealing temperature is shown in Figure 2.4.17.

The inset on the curve shows the hysteresis loops of the as-cast and annealed samples.

M_s is nearly unchanged below T_g . For the anneals above T_g however, M_s increases rapidly to a maximum of 99.8 emu/g at 983K. The effect of annealing on H_c , however is slightly more complex. The as-cast alloy had a coercivity of 127.0 Oe, but the minimum of 7.3 Oe occurred at 823 K and then increased sharply to 196.9 Oe as the temperature was increased further. This suggests a pronounced dependence of the magnetic properties on the microstructure, which can be easily controlled by heat treatment starting from the amorphous state. The decrease in H_c observed at 823 K has been attributed to

structural relaxation of the amorphous phase. When annealing takes place above the glass transition however, nanocrystalline phases form within the amorphous matrix and there is large increase in surface energy associated with this development. The continuous increase in interfaces and interfacial energy hinders the movement of domain walls, leading to the rapid increase in H_c above T_g .

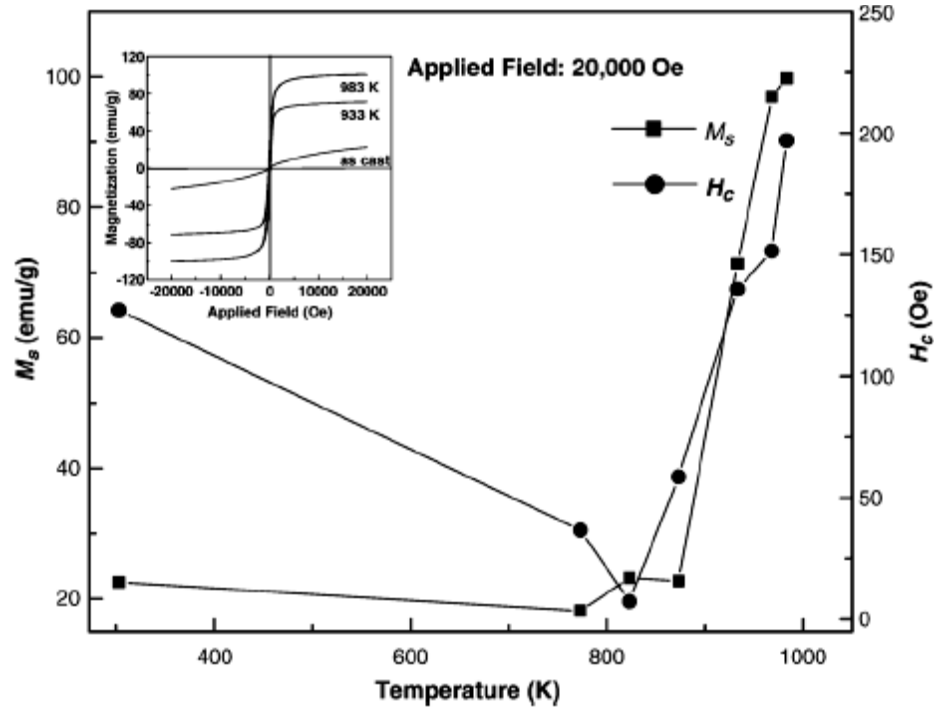


Figure 2.4.17 Dependence of M_s and H_c with annealing temperature. Inset shows hysteresis loops for as-cast and annealed samples [16] .

Chapter 3: Experimental Methods

3.1 Alloy Melting and Processing Methods

The alloys produced for this study were first arc-melted into ingots from pure elements, each with 99.9% purity or higher, in a zirconium-gettered, argon atmosphere. The ingots were melted several times to ensure homogeneity and weighed both prior to and after melting to verify no significant metalloid mass loss had occurred. The ingots were then either: (1) arc-melted and splat quenched into thin foils with a copper block (Figure 3.1), (2) induction melted and cast into 3, 4, or 5 mm diameter rods in a water cooled, copper mold (Figure 3.2), or (3) induction melted and cast into 1, 2, and 3 mm thick plates (Figure 3.3). The plates were cast in an induction coil, quartz tube furnace, in which two separate, water-cooled, copper mold pieces passing through the induction coil were pressed together to quench the sample; one containing a copper quenching block, the other containing the mold piece (Figure 3.3). This parallel plate copper mold casting set-up is the first iteration of a versatile new tool for tuning microstructure via power modulated induction heating.

Significant attention has been given to this new processing technique, termed semi-solid processing, in which alloys are heated to a temperature between the melt temperature of the glass and the melt temperature of a secondary crystalline phase. In this fashion, the glass forming behavior can be maintained, while the more stable, and thus higher-melting, crystalline nuclei remain present within the glassy matrix. By holding the melt in this two-phase region, the crystallites can coarsen to improve the

properties of the BMG matrix composite. Such processing requires extremely stable glass forming compositions, and to date, has only been successfully employed in the processing of expensive Zr-Ti-Be-based alloys. Furthermore, this type of processing does not currently allow net-shape casting of application specific parts. Instead, large ingots of BMG composites are created and later machined into parts, which is costly, and time consuming.

The power modulated, parallel plate copper mold casting technique presented in this work permits an alternative means to generating amorphous matrix composites in less stable glass forming compositions. Modified glass forming compositions designed to promote ductile phase nucleation can be heated up beyond the liquidus temperature of the glass, and then quenched into a mold. The resultant alloy has a glassy matrix, with embedded crystallites of the primary phase, which it has been designed to contain. The duration and temperature at which the alloy melt is held will dictate the size of the ductile crystalline phase. Furthermore, bulk metallic glass matrix composites (BMGMCs) can be heated just above the glass transition temperature and then formed into net shape parts. A schematic of the parallel plate design used for semi-solid processing is shown in Figure 3.4, while an image of the chamber and coil are shown in Figure 3.5(a) and (b).

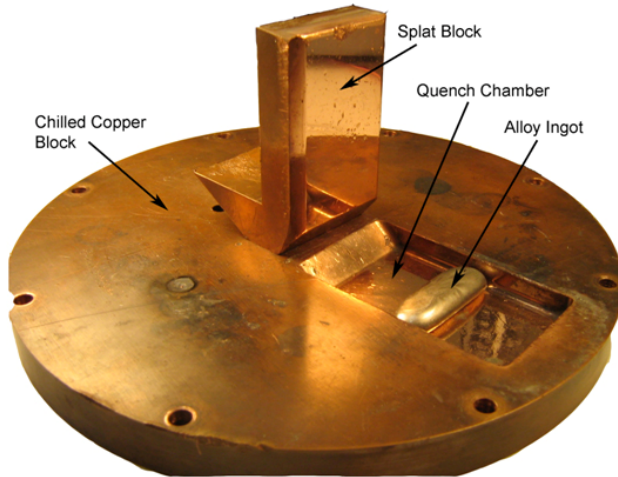


Figure 3.1. Assembly for splat-quenching alloys.



Figure 3.2. Copper mold featuring several different rod diameters.

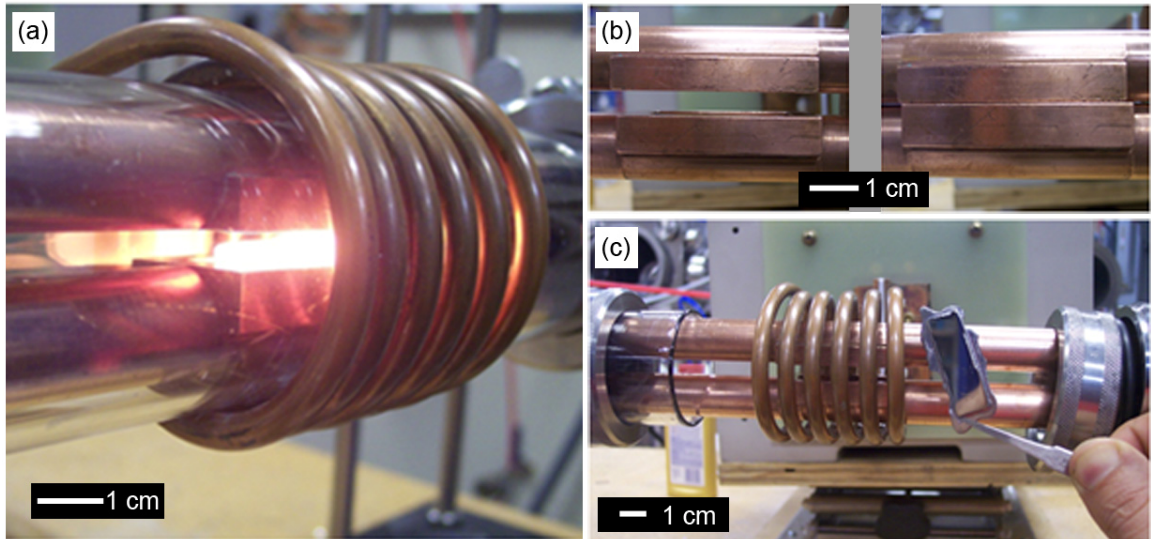


Figure 3.3. (a) Parallel pipe copper mold assembly heating 10 g sample of Ti-based BMG composite, (b) parallel plates in opened and closed positions, (c) a Ti-based BMG-derived composite cast using the parallel plate copper mold assembly. This set-up is capable of melting 15 g samples.

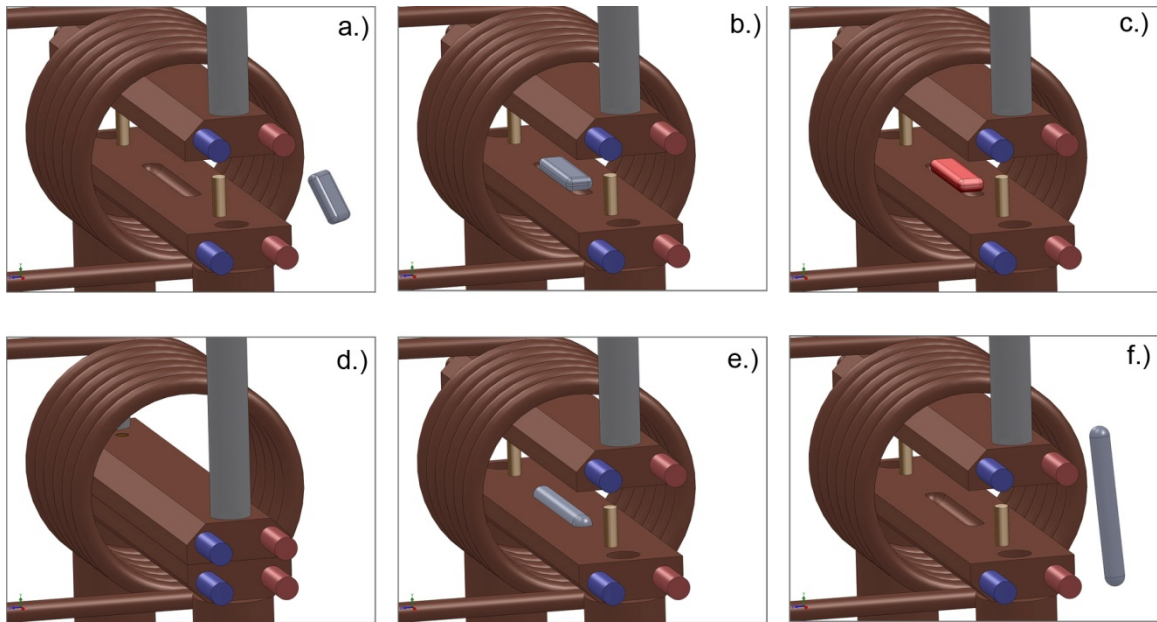


Figure 3.4. Schematic of semi-solid processing with parallel plate copper mold and induction coil. Blue and red represent ingoing and outgoing cooling water, respectively. (a) an ingot is prepared by arc-melting for the two part cylindrical mold piece. Each copper plate has a semi-cylinder mold machined into it. The brass posts in the bottom plate ensure proper alignment during quenching.. (b) The ingot is placed between the two copper plates. (c) The induction coil is turned on and the alloy is heated up to the two-phase temperature range. (d) Once sufficiently processed, the top copper mold piece is lowered and the coil is turned off. (e) The molten alloy has been pressed into the mold and quenched sufficiently to freeze in the desired microstructure. (f) A semi-solidly processed cylindrical rod is removed from the copper mold.

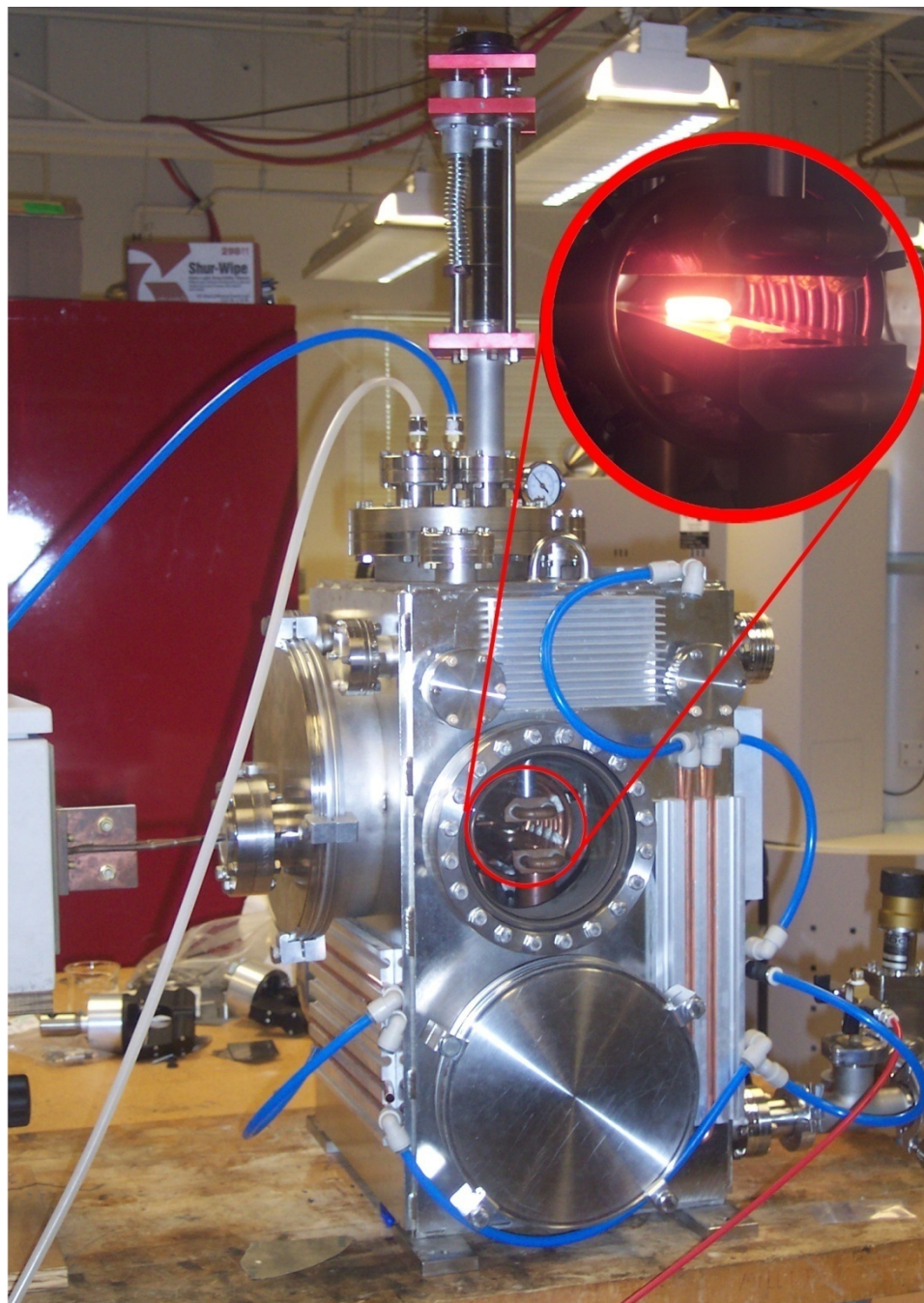


Figure 3.5. Second iteration of parallel plate copper mold assembly inside of large vacuum chamber. Inset shows close-up of induction coil and copper plates with 25 g sample being heated. This set-up is capable of melting 150g samples.

3.2 X-Ray Diffractometry

The amorphous structure of the alloys was verified using an X-ray diffractometer (XRD) with monochromatic Cu K α radiation. XRD-based identification of the crystalline phases required extended dwell times during acquisition for improved peak intensities; phase identification and crystallite size approximations were assisted by MDI Jade software. Samples were cut to roughly 10 mm x 7 mm size for all phase identification and peak comparisons in the XRD.

3.3 Thermal Analysis

Thermal analysis was carried out using a differential scanning calorimeter (DSC) at a heating rate of 20 K/min to determine both the glass transition temperature, T_g , and crystallization temperatures, T_x . DSC was also used for the isothermal and continuous heating experiments with heating rates ranging from 1-200 K/min, as well as for crystal volume fraction experiments. 50 mg samples were used for all crystal volume fraction experiments to ensure properly indicative peak measurements. A thermo-gravimetric differential thermal analyzer (TG/DTA) was used for melting and liquidus temperature determination. Heating rate experiments used to determine the activation energy for crystallization were also performed with the TG/DTA.

3.4 Corrosion Testing

Corrosion tests were carried out in sea-water, as well as 1M and 3M HCl solutions for at least 120 hours. Corrosion rates were calculated based on mass-loss of a parallel-piped sample of exactly known dimensions and density.

3.5 Mechanical Testing

Micro-hardness tests were performed under a load of 1960mN and 15s time interval. A minimum of 10 hardness tests were performed on each sample, otherwise a sufficient number of tests were performed to achieve a standard deviation of less than 2%.

Compression samples were made from as-cast, fully amorphous 3 mm diameter rods, as well as semi-solidly processed plates of BMG composite. Compression samples were prepared in a roughly 2:1 height to diameter ratio, and tested using a servohydraulic load frame under an applied strain rate of 10^{-1} s^{-1} .- 10^{-4} s^{-1} . Elastic modulus and poisson's ratio were determined via wavespeed measurements. Four point bending was carried out at an extension rate of 0.5 mm/min. Samples were prepared according to the ASTM standard 1421. Tension samples were cut from semi-solidly processed plates via electron discharge machining (EDM) with a rectangular gauge cross section of 3mm by 3mm and a gauge length of 20mm at a strain rate of 10^{-3} s^{-1} .

3.6 Microstructural and Chemical Characterization

Microstructural characterization was done using a scanning electron microscope (SEM) operated at 20kV. Chemical characterization was carried out with an energy dispersive X-ray spectrometer (EDS). A scanning transmission electron microscope (STEM) operated at 200 kV was employed for crystallite size and morphology identification.

Chapter 4: Iron-based Bulk Metallic Glasses and BMG-derived Composites

4.1 Effect of Mo-Fe Substitution on Glass Forming Ability and Thermal Stability of Fe-C-B-Mo-Cr-W Bulk Amorphous Alloys

4.1.1 Abstract

Amorphous $\text{Fe}_{67-x}\text{C}_{10}\text{B}_9\text{Mo}_{7+x}\text{Cr}_4\text{W}_3$ ($x = 1-7$ at. %) plates with 640 μm thickness were prepared by copper mold casting. The thermal properties and microstructural development during heat treatments were investigated. The glass forming ability (GFA) and activation energy for crystallization have a distinct dependence on molybdenum content which has been attributed to the optimization of elastic strain imposed by the large atomic radius of molybdenum atoms. $\text{Fe}_{62}\text{C}_{10}\text{B}_9\text{Mo}_{12}\text{Cr}_4\text{W}_3$ was the best glass former in this study, demonstrating a super-cooled liquid region, $\Delta T_x = 51\text{K}$, and an activation energy for crystallization, $Q = 453$ kJ/mol. Heat treatments were performed to demonstrate resistance to crystallization under typical processing conditions. Alloys in this system exhibited a 3 phase evolution during crystallization. A second set of heat treatments was performed to identify each of these phases. Hardness data was collected at each of the heat treatment conditions, and a BMG-derived composite containing a molybdenum-rich phase exhibited Vickers Hardness in excess of 2000. The fully amorphous alloys had an average hardness approaching 1500.

4.1.2 Introduction

Investigation of crystallization behavior in metallic glass has been the focus of much attention due to its implications towards the stability of amorphous alloys and the

processing of nanostructured and amorphous materials for industrial applications.

Metallic glasses have been extensively studied due to their potential for a variety of technological applications. Specifically, iron-based metallic glasses are of importance due to their relatively low cost compared to most other bulk metallic glasses, and their unique properties as compared to conventional materials. Iron-based amorphous alloys have evolved from binary Fe-B glasses [86], which could be made into thin foils, to multi-component amorphous steels with dimensions of up to 12 mm [87-93]. Iron-based glasses have been successfully produced with compressive fracture strengths of over 4 GPa [57], among the strongest of metallic glasses. Furthermore, metallic glasses have demonstrated significant improvements in magnetic and mechanical properties when nano-scale particles are introduced into the amorphous matrix by means of heat treatment [94].

Designing cost effective amorphous alloys, or nanostructured amorphous composites, requires a sufficient understanding of crystallization kinetics of metallic glasses, to properly define processing parameters that will yield the desired properties and microstructure. This chapter discusses the implications towards application-specific processing of iron-based bulk metallic glasses through the analysis of the thermal stability of a series of Mo-Fe substituted amorphous steels. Intrinsic to the BMG field is the relationship between alloy thermal stability, most notably, the width of the supercooled liquid region, and the critical size, D_{max} (the maximum achievable thickness of a sample along its smallest dimension). The tradeoffs between cost and critical size are also important in moving bulk metallic glasses towards widespread application. In order to compete commercially with conventional materials, bulk amorphous alloys need to be

made of relatively inexpensive components, while maintaining a sufficiently large critical size for a given application. Producing metallic glasses closer in composition to conventional engineering materials, such as common steels, is a viable method toward achieving this goal.

Table 4.1.1. Listing of some iron-based bulk metallic glasses from literature. D_{\max} is the maximum thickness at which a fully amorphous structure can be achieved.

Alloy Composition	D_{\max} (mm)
$[(\text{Fe}_{0.5}\text{Co}_{0.5})_{0.75}\text{B}_{0.2}\text{Si}_{0.5}]_{96}\text{Nb}_4$	5
$\text{Fe}_{58}\text{Co}_6\text{Ni}_4\text{Zr}_{10}\text{Mo}_5\text{W}_2\text{B}_{15}$	3
$\text{Fe}_{65.5}\text{Cr}_4\text{Mo}_4\text{Ga}_4\text{P}_{12}\text{C}_5\text{B}_{5.5}$	4
$(\text{Fe}_{44.3}\text{Cr}_5\text{Co}_5\text{Mo}_{12.8}\text{Mn}_{11.2}\text{C}_{15.8}\text{B}_{5.9})_{98.5}\text{Y}_{1.5}$	12
$\text{Fe}_{61}\text{Y}_2\text{Zr}_8\text{Co}_5\text{Cr}_2\text{Mo}_7\text{B}_{15}$	5
$\text{Fe}_{50}\text{Mn}_{10}\text{Mo}_{14}\text{Cr}_4\text{C}_{16}\text{B}_6$	4
$\text{Fe}_{48}\text{Cr}_{15}\text{Mo}_{14}\text{Er}_2\text{C}_{15}\text{B}_6$	12

In this study, a series of Mo-Fe substituted amorphous steels were created of the form $\text{Fe}_{67-x}\text{C}_{10}\text{B}_9\text{Mo}_{7+x}\text{Cr}_4\text{W}_3$ ($x=1-7$). Of note is the absence of rare earth metals and other expensive elements from this study, here only utilizing elements common to the conventional steel industry. The majority of amorphous steels reported in literature to date rely on alloying elements such as Y, Ga, and the Lanthanides to enhance glass forming ability [53, 90, 95]. Whether expensive alloying elements are present or not, amorphous steels are among the more complex metallic glasses, typically consisting of 5 or more elements, with a significant atomic fraction coming from metalloid additions. A listing of the most successful current iron-based bulk metallic glasses (BMG) is given in Table 4.1.1.

The primary goal of this study is to investigate the changes in thermal stability of amorphous steels through a stepwise compositional substitution of molybdenum for iron. The intention is to explore the composition space and identify alloys that show good glass forming ability, strong resistance to crystallization in the supercooled liquid region and high hardness, while limiting the necessary amount of expensive alloying elements known to enhance these properties. This study introduces a set of amorphous steels containing ≥ 60 atomic % iron, with all other alloying elements currently utilized in the steel industry. This composition space is not currently represented in the literature, and is an attempt at improving the cost effectiveness of amorphous steels. In this section the thermal behavior of Fe-Mo-Cr-W-C-B amorphous alloy plates, prepared by copper mold casting, are assessed by means of X-ray diffractometry and thermal analysis. Amorphous alloys were annealed for various times at temperatures within and above the supercooled liquid region to investigate aspects regarding crystallization kinetics and identification of crystalline phase formation. For further comparison, the activation energy for crystallization was calculated for these alloys and compared with other iron-based amorphous alloys. Hardness tests reveal that alloys in this glass forming system are superior to other glass forming systems, and the nucleation of crystalline phases offered more versatility in tuning the mechanical properties in extremely hard BMG derived composites.

4.1.3 Results and Discussion

Design Principles

In this study, the first principle of alloy design was the maximization of the α parameter. The α parameter alone, however, was not sufficient to predict good glass forming ability because it is a purely thermodynamic parameter [21]. Other factors like kinetics and local topology also play a critical role [23, 24, 96, 97]. In light of this, additional constituents were added by taking into account factors such as atomic size mismatch and elastic strain. A comparison of the equilibrium liquidus temperature and alpha parameter is shown in Figure 4.1.1.

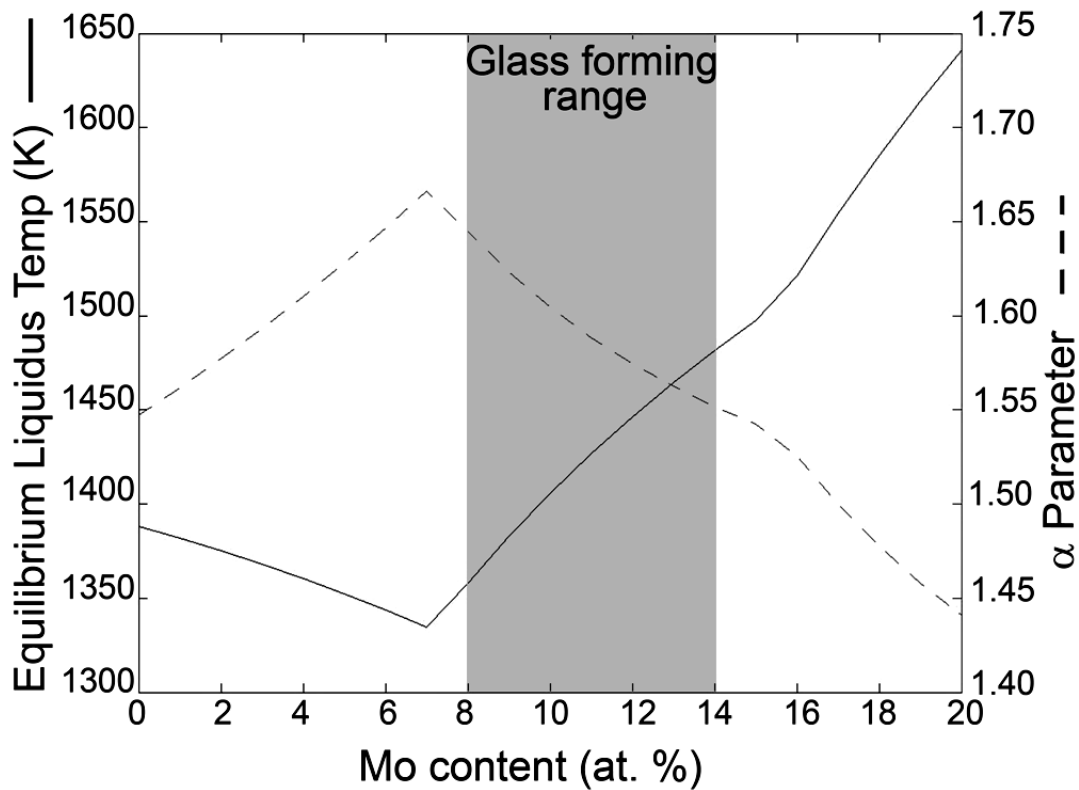


Figure 4.1.1. Variation in equilibrium liquidus temperature and alpha parameter with Fe-Mo substitution in $\text{Fe}_{67-x}\text{C}_{10}\text{B}_9\text{Mo}_{7+x}\text{Cr}_4\text{W}_3$.

It is well known that boron is a required constituent in iron-based BMGs because of its contributions to dense random packing [53, 57, 86, 96, 98]. Although both carbon and boron possess eutectic compositions in iron-based alloys, the presence of boron in particular is critical to the development of atomic clusters in the liquid state. Evteev *et al.* [86] determined via computer simulations that Fe-B melts have a distinctly different topology compared with its crystalline state, whereas Fe-C melts form identical local topologies in the liquid and crystalline states. The presence of boron therefore creates a greater hindrance to crystal formation, since a significant change in topology is required for crystallization to occur. Inoue's empirical rules for metallic glass formation state that a good metallic glass forming alloy must also have at least three distinct atomic constituents to generate atomic radius mismatch [2]. Miracle has shown that atomic radius mismatch can generate elastic strains, which hinder crystallization [23, 24, 29]. To generate atomic radius mismatch, the large atomic radius of molybdenum was utilized in the glass forming system $\text{Fe}_{67-x}\text{C}_{10}\text{B}_9\text{Mo}_{7+x}\text{Cr}_4\text{W}_3$ ($x = 1-7$ at. %) of this study to optimize dense random packing and improve glass-forming ability by generating elastic strain. The concentration of molybdenum was directly related to the GFA of the alloys in this study. Using this understanding of iron-based metallic glass formation coupled with the utility of the α parameter, a range of amorphous compositions have been identified and can be tuned for specific applications. This alloy system exhibits large supercooled liquid regions across a broad compositional range.

Glass Characterization

Figure 4.1.2 shows XRD spectra for the $\text{Fe}_{67-x}\text{C}_{10}\text{B}_9\text{Mo}_{7+x}\text{Cr}_4\text{W}_3$ ($x = 1-7$) system. Alloys corresponding to $x = 2-7$ in this study yielded a single, broad peak, indicating a fully amorphous structure with no distinct crystalline peaks present. For $x = 1$, crystalline peaks corresponding to the phase $\text{Fe}_{23}(\text{C,B})_6$ are superimposed on a broad peak, indicating the presence of the crystalline phase embedded in an amorphous matrix. The DSC curves in Figure 4.1.3 indicate a clearly resolved glass transition for each of the 6 fullyamorphous alloys ($x = 2-7$). The glass transition temperature, T_g , and crystallization temperature, T_x , both decrease as the molybdenum content is decreased. The thermal data from the DSC scans are summarized in Table 4.1.2. The supercooled liquid region achieves a maximum of 51K in the composition $\text{Fe}_{62}\text{C}_{10}\text{B}_9\text{Mo}_{12}\text{Cr}_4\text{W}_3$. Furthermore, each of the alloys in this study exhibit ΔT_x regions in excess of 40K. The width of the supercooled liquid region is thought to provide longer incubation time for nucleation and growth of crystalline phases, and thus is indicative of an alloy with better glass forming ability [99].

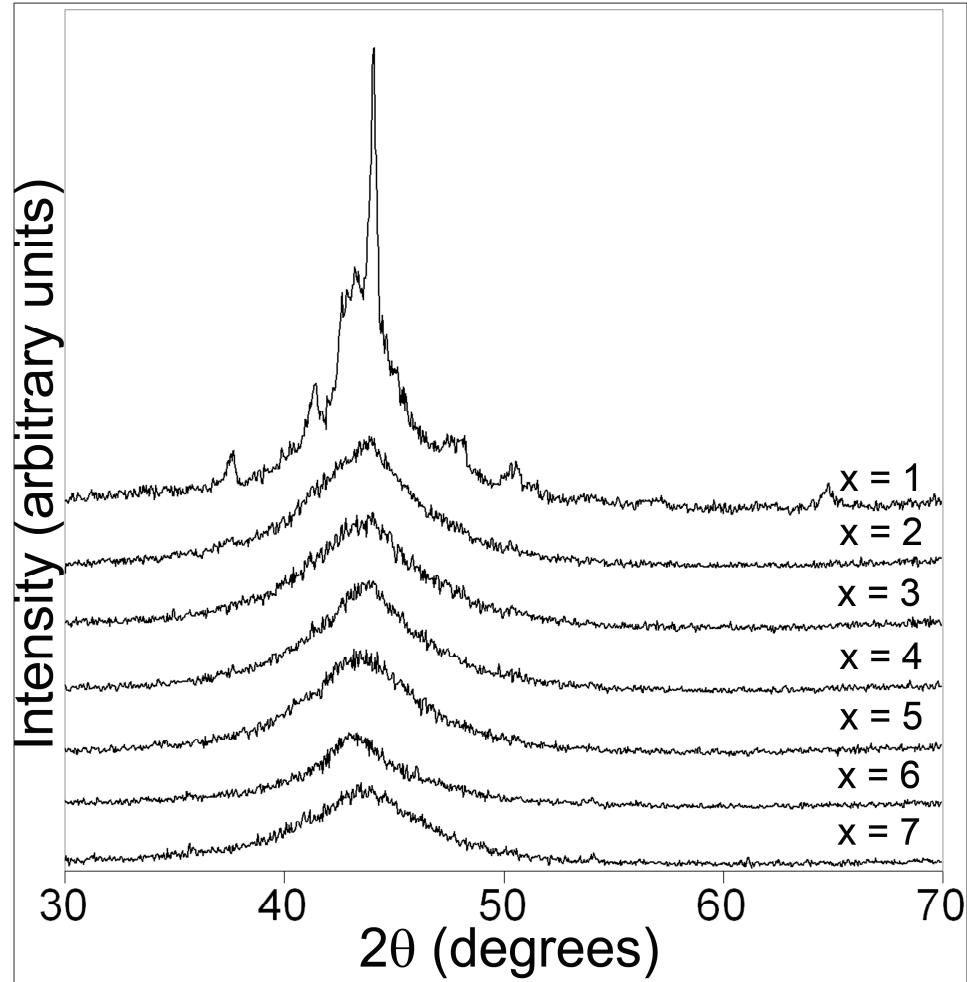


Figure 4.1.2. XRD patterns for as-quenched $\text{Fe}_{67-x}\text{C}_{10}\text{B}_9\text{Mo}_{7+x}\text{Cr}_4\text{W}_3$ ($x = 1-7$) alloys. Only the composition for $x=1$ yielded crystalline peaks in XRD.

Table 4.1.2. Glass transition, crystallization, liquidus temperatures and reduced glass transition ratio for $\text{Fe}_{67-x}\text{C}_{10}\text{B}_9\text{Mo}_{7+x}\text{Cr}_4\text{W}_3$ determined via DSC and DTA.

Composition	T_g (K)	T_x (K)	ΔT_x (K)	T_l (K)	T_{rg}
$\text{Fe}_{60}\text{C}_{10}\text{B}_9\text{Mo}_{14}\text{Cr}_4\text{W}_3$	844	884	40	1385	0.609
$\text{Fe}_{61}\text{C}_{10}\text{B}_9\text{Mo}_{13}\text{Cr}_4\text{W}_3$	832	875	43	1382	0.602
$\text{Fe}_{62}\text{C}_{10}\text{B}_9\text{Mo}_{12}\text{Cr}_4\text{W}_3$	820	871	51	1379	0.595
$\text{Fe}_{63}\text{C}_{10}\text{B}_9\text{Mo}_{11}\text{Cr}_4\text{W}_3$	818	862	44	1375	0.595
$\text{Fe}_{64}\text{C}_{10}\text{B}_9\text{Mo}_{10}\text{Cr}_4\text{W}_3$	812	853	41	1372	0.592
$\text{Fe}_{65}\text{C}_{10}\text{B}_9\text{Mo}_9\text{Cr}_4\text{W}_3$	808	848	40	1371	0.589
$\text{Fe}_{66}\text{C}_{10}\text{B}_9\text{Mo}_8\text{Cr}_4\text{W}_3$	-	839	-	1366	-

The DTA scan for $\text{Fe}_{62}\text{C}_{10}\text{B}_9\text{Mo}_{12}\text{Cr}_4\text{W}_3$ in Figure 4.1.4 shows 3 distinct exothermic peaks at 871, 915, and 980K, respectively, corresponding to the nucleation of three separate crystalline phases upon reheating. Table 4.1.2 shows that the liquidus temperature decreases as the molybdenum content decreases. According to analyses by Marcus and Turnbull [31], and also in accordance with our previously described alpha parameter [21], glass forming ability is enhanced by depressing the liquidus temperature.

The optimum composition in this study however, occurred in the middle of the substitutional system, where the supercooled liquid region was greatest, yet had a liquidus temperature intermediate amongst the 6 amorphous alloys studied. It is thus concluded that the ideal composition is determined by the ratio of molybdenum to iron in the system necessary to create sufficient elastic strain for optimized dense random packing. The relative success of this glass forming system is attributed to the base composition's proximity to a deep eutectic, but the optimization of the alloy at 12 at.% molybdenum comes about through consideration of the elastic strain requirements for dense random packing.

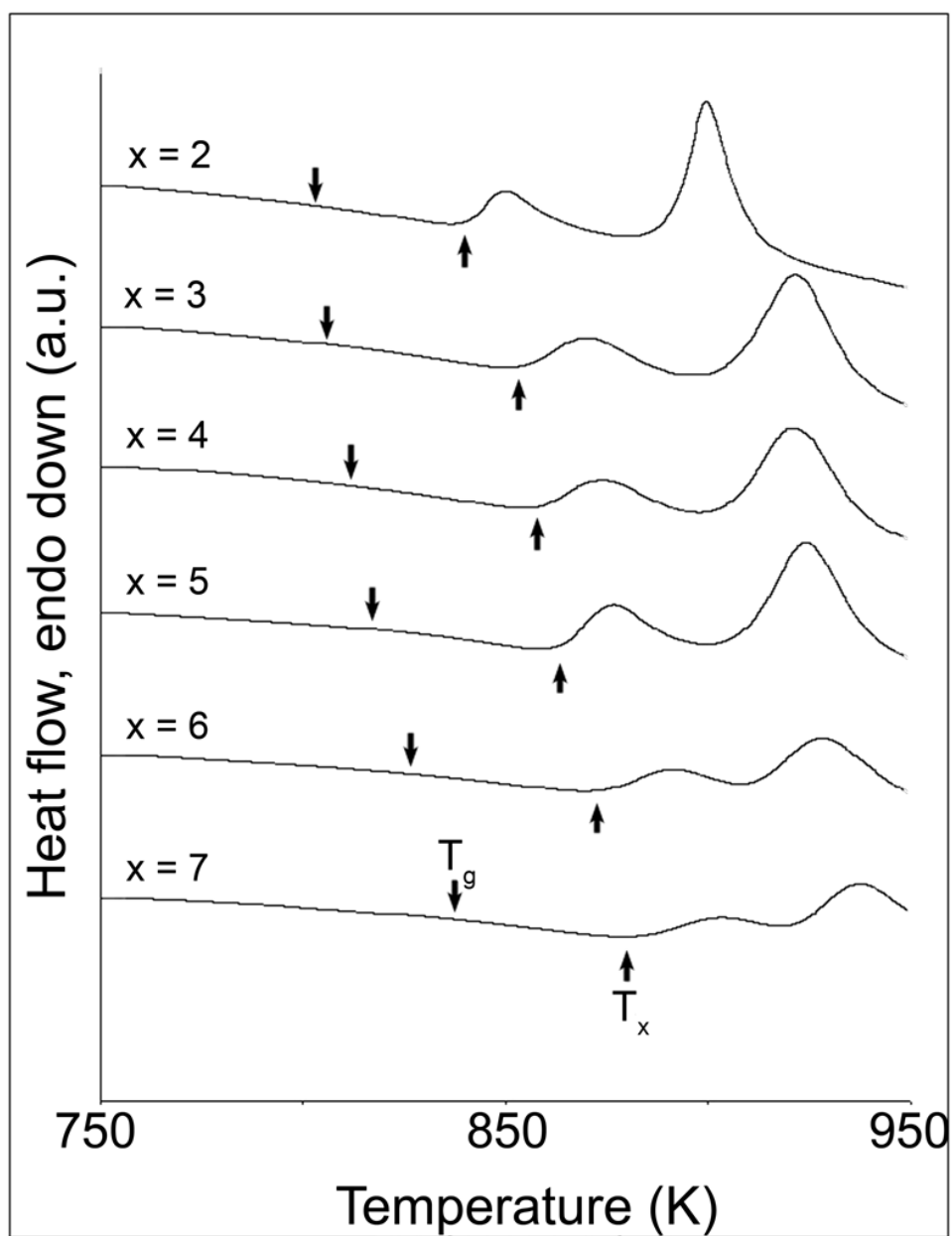


Figure 4.1.3. DSC curves for as-cast $\text{Fe}_{67-x}\text{C}_{10}\text{B}_9\text{Mo}_{7+x}\text{Cr}_4\text{W}_3$ ($x = 2-7$ at%) amorphous alloys.

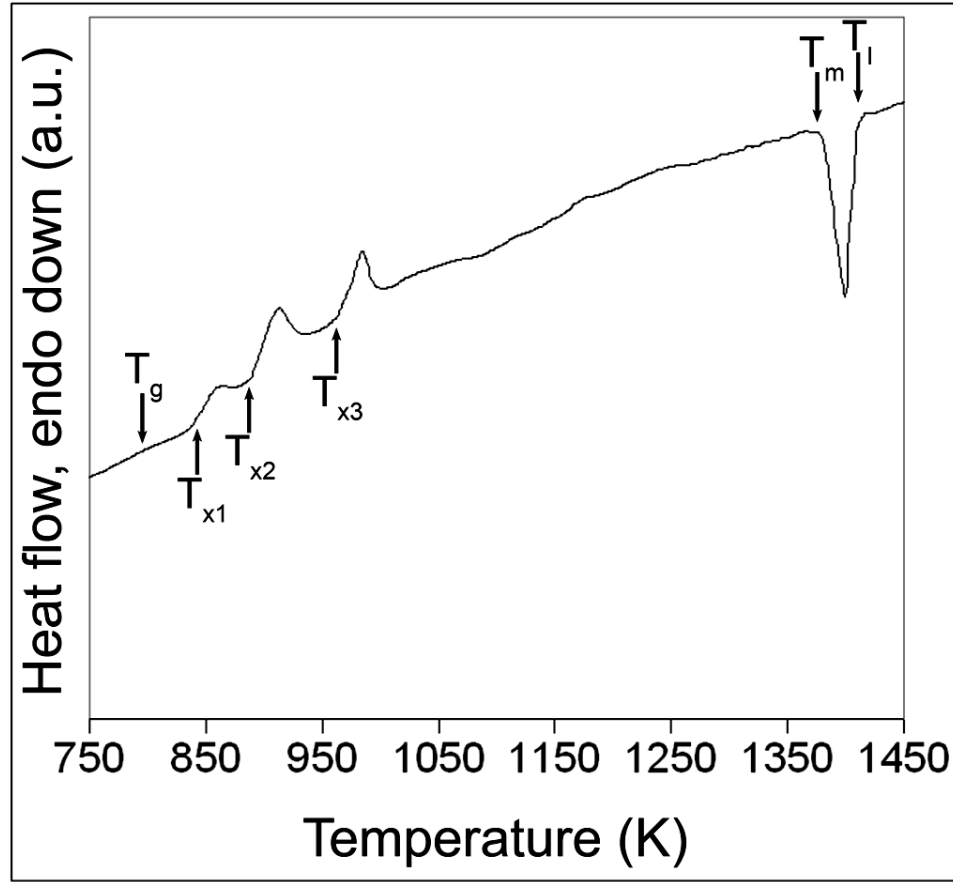


Figure 4.1.4. DTA curve for amorphous $\text{Fe}_{62}\text{C}_{10}\text{B}_9\text{Mo}_{12}\text{Cr}_4\text{W}_3$ plate indicating all significant thermodynamic events.

Increasing the molybdenum concentration only marginally increased the liquidus temperature. $\text{Fe}_{66}\text{C}_{10}\text{B}_9\text{Mo}_8\text{Cr}_4\text{W}_3$ had a liquidus temperature of 1371K, while $\text{Fe}_{60}\text{C}_{10}\text{B}_9\text{Mo}_{14}\text{Cr}_4\text{W}_3$ had a liquidus temperature of 1385K. The alloy with the largest supercooled liquid region in this study, $\text{Fe}_{62}\text{C}_{10}\text{B}_9\text{Mo}_{12}\text{Cr}_4\text{W}_3$, had a liquidus temperature of 1379K. From the liquidus and glass transition data, the reduced glass transition was calculated to be 0.595 for $\text{Fe}_{62}\text{C}_{10}\text{B}_9\text{Mo}_{12}\text{Cr}_4\text{W}_3$. This reduced glass transition is comparable to other documented iron-based BMGs [4], and this study verifies the versatility and robustness of alloys throughout this compositional system. As the

molybdenum content is increased within the system, there is a corresponding increase in liquidus temperature. Since T_g increases more rapidly than T_l as molybdenum content is increased, a corresponding increase in T_{rg} is observed, which can be seen in Table 4.1.2. The trend in T_{rg} does not coincide with improving glass forming ability as expected. The GFA optimization must therefore be governed by other factors in addition to the thermodynamics of solidification. Kinetic constraints clearly play a role in the suppression of crystal formation. This study underscores the importance of elastic strain optimization through molybdenum substitution for iron. The large atomic radius of molybdenum atoms serves as a barrier to atomic motion, facilitating the maintenance of only short to medium range order in the alloy melt. If however, the molybdenum is present in too high a concentration, there are not sufficient numbers of sites to accommodate all molybdenum atoms, and glassy behavior gets destabilized in favor of crystalline phases above 14 at.% molybdenum. If the molybdenum content is less than the optimum value, a destabilization of the glassy state occurs at increasingly lower temperatures as the molybdenum content is decreased. The destabilization of the glassy state is reflected by the decrease in the supercooled liquid region with decreasing molybdenum content. Below 9 at.% molybdenum, glassy behavior cannot be achieved in this system. Despite having slightly smaller supercooled liquid regions, the alloys in this study with less molybdenum are appealing because they have lower T_g making them processable at lower temperatures, as well as significantly lower cost.

Heat Treatments

Alloy resistance to crystallization and crystalline phase evolution were investigated via various heat treatments. The resistance to crystallization within the supercooled liquid region was investigated by heating each alloy up to T_g+20K , T_g+30K , T_g+40K , and T_g+50K , and then holding for 10 minutes at each condition. Shaping and forming of BMGs for specific applications is done in this temperature range. The anneal time for these experiments represents more than ample time for shaping processes employed in BMGs such as thermoplastic forming (TPF) [100], aerodynamic levitation [101], and conventional mold casting. Each of the alloys demonstrated a strong retention of amorphous behavior up to T_x ; XRD spectra demonstrating this behavior are shown in Figure 4.1.5. The best glass former ($Fe_{62}C_{10}B_9Mo_{12}Cr_4W_3$) is shown along with the amorphous compositions on either extreme of the compositional spectrum ($Fe_{60}C_{10}B_9Mo_{14}Cr_4W_3$ and $Fe_{65}C_{10}B_9Mo_9Cr_4W_3$). Those alloys with ΔT_x regions less than 50K experienced some loss of amorphous behavior at the T_g+50 anneal condition. The crystalline peaks beginning to form coincide with the composition dependent initial crystalline phase, which will be discussed with the next set of heat treatments. $Fe_{62}C_{10}B_9Mo_{12}Cr_4W_3$ had a ΔT of 51K and retained its fully amorphous structure through the T_g+50 anneal treatment of 10 minutes.

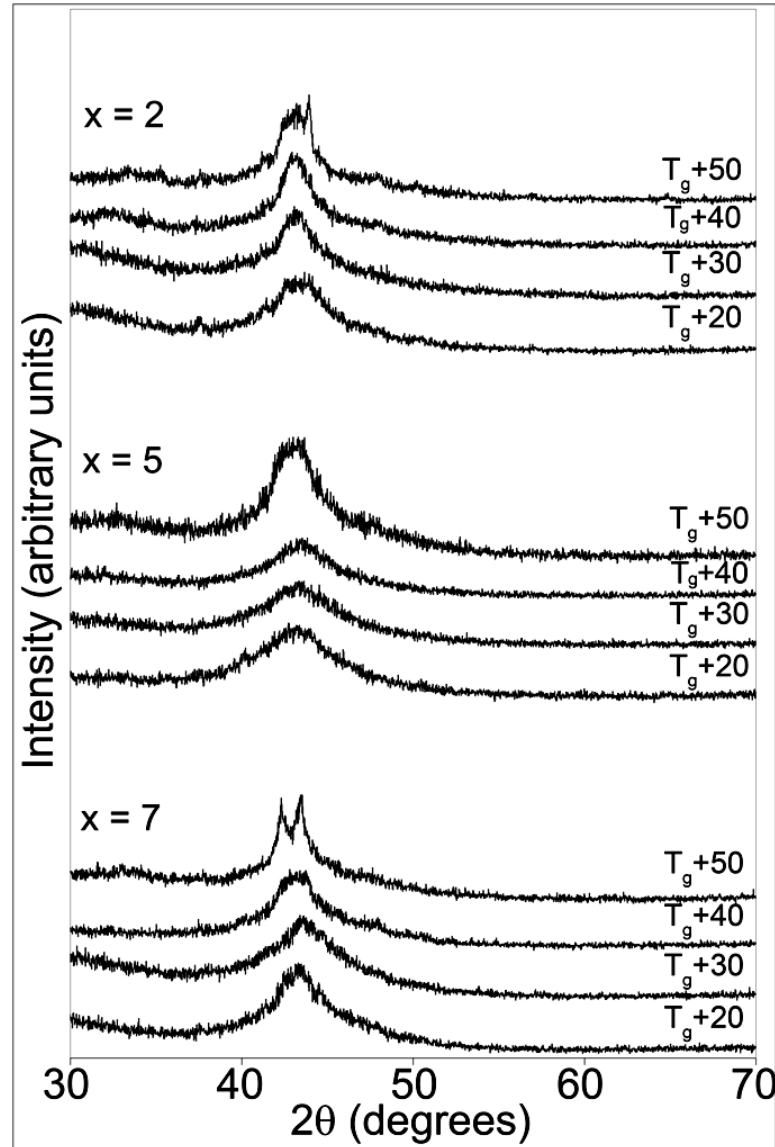


Figure 4.1.5. XRD spectra demonstrating resistance to crystallization in the supercooled liquid region in $\text{Fe}_{67-x}\text{C}_{10}\text{B}_9\text{Mo}_{7+x}\text{Cr}_4\text{W}_3$ ($x = 2, 5, 7$). T_g was 808K, 820K, and 844K for compositions corresponding to $x = 2, 5$, and 7 , respectively.

It is worthwhile to note that the formability of a BMG is greatly enhanced when forming occurs at the upper extreme of the supercooled liquid region [100]. Above T_g there is a steady increase in atomic mobility and associated decrease in viscosity, making

the alloy softer [102]. For this reason, alloys demonstrating good resistance to crystallization, even near T_x , are ideal for industrial applications.

The second set of heat treatments was performed to identify the crystalline phases that evolve from the amorphous state upon heating. Separate DSC anneals were performed to grow each crystalline phase that forms upon heating. All alloys from the $\text{Fe}_{67-x}\text{C}_{10}\text{B}_9\text{Mo}_{7+x}\text{Cr}_4\text{W}_3$ ($x = 1-7$) system exhibit three distinct exothermic peaks in DSC corresponding to three separate crystalline phases. The DTA curve for $\text{Fe}_{62}\text{C}_{10}\text{B}_9\text{Mo}_{12}\text{Cr}_4\text{W}_3$ in Figure 4.1.4 shows the 3 characteristic exothermic peaks for these alloys (peak onsets labeled T_{x1} , T_{x2} , and T_{x3}). To identify these phases, 2 hour anneals were performed at 5K below T_{x1} , and at the offset temperatures of each crystalline phase. Offset temperatures were used rather than onset temperatures to ensure more complete crystallization of each phase. The samples were then analyzed by X-ray diffractometry, and the peaks identified.

The phase evolution for $\text{Fe}_{60}\text{C}_{10}\text{B}_9\text{Mo}_{14}\text{Cr}_4\text{W}_3$, $\text{Fe}_{62}\text{C}_{10}\text{B}_9\text{Mo}_{12}\text{Cr}_4\text{W}_3$, and $\text{Fe}_{65}\text{C}_{10}\text{B}_9\text{Mo}_9\text{Cr}_4\text{W}_3$ has been identified via XRD shown in Figure 4.1.6. Even after 2 hour heat treatments just before the onset of the first crystallization, each of these alloys demonstrates completely amorphous behavior, indicating excellent thermal stability across the compositional spectrum of this study. The initial crystalline phase (T_{x1}) identified for all alloys in this study was $\text{Fe}_{23}(\text{C},\text{B})_6$. Although the evolution of the topology of Fe-B and Fe-C are vastly different from one another on cooling from the liquid state [86], upon reheating, it was observed that both carbides and borides nucleate concurrently. The characteristic Bragg peaks of Fe_{23}B_6 and Fe_{23}C_6 are very close together. The crystalline peaks from the initial phase of this study are not exclusively

from the boride or carbide, but rather lie in between, indicating that the ternary phase iron borocarbide, $\text{Fe}_{23}(\text{C},\text{B})_6$, exists. Most iron-based BMGs in the literature contain only boron and feature an initial crystalline phase of Fe_{23}B_6 [53, 57, 84, 87, 88, 103]. Iron-based BMG containing carbon as the only metalloid has not been realized. Instead all iron-based BMG in the literature containing carbon also contain boron [89, 91, 93]. Boron, therefore, is required to facilitate amorphization in these Fe-based BMGs. Carbon provides additional small atoms to promote atom size mismatch while also minimizing material costs. Good glass forming ability can be retained with carbon present so long as a critical amount of boron is kept in the alloy (9 at.% in this study). The second crystallization corresponds to the phase $\text{Fe}_4\text{W}_2(\text{B},\text{C})$, while the third crystallization corresponds to $(\text{Mo},\text{W})_{23}\text{Fe}_{21}\text{Mo}_2(\text{B},\text{C})$.

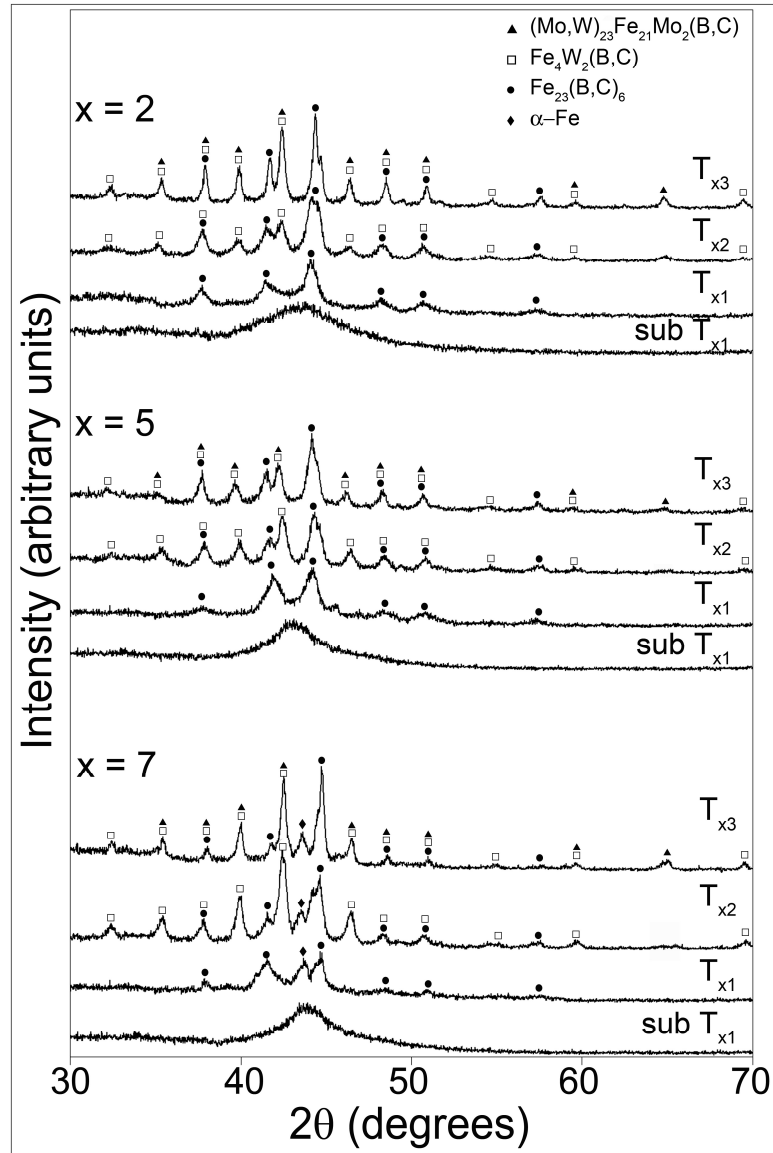


Figure 4.1.6. XRD spectra for 120 min anneals at $\text{sub-}T_{x1}$, at T_{x1} , at T_{x2} , and at T_{x3} offsets for compositions $\text{Fe}_{60}\text{C}_{10}\text{B}_9\text{Mo}_{14}\text{Cr}_4\text{W}_3$ ($x = 7$), $\text{Fe}_{62}\text{C}_{10}\text{B}_9\text{Mo}_{12}\text{Cr}_4\text{W}_3$ ($x = 5$) and $\text{Fe}_{65}\text{C}_{10}\text{B}_9\text{Mo}_9\text{Cr}_4\text{W}_3$ ($x = 2$).

Although the same three crystalline phases nucleate out of each composition, there is one distinct difference in the phase evolution that arises from the compositional variation in $\text{Fe}_{67-x}\text{C}_{10}\text{B}_9\text{Mo}_{7+x}\text{Cr}_4\text{W}_3$. There is a transition from a two-phase primary crystallization at high molybdenum content, to a single-phase primary crystallization at

lower molybdenum concentration. A comparison of the XRD spectra for T_{x1} anneals, seen in Figure 4.1.6, shows a peak corresponding to α -Fe(Mo) observed in the molybdenum-rich $\text{Fe}_{60}\text{C}_{10}\text{B}_9\text{Mo}_{14}\text{Cr}_4\text{W}_3$, in addition to $\text{Fe}_{23}(\text{C,B})_6$. No such α -Fe(Mo) peak is observed in the spectra for $\text{Fe}_{62}\text{C}_{10}\text{B}_9\text{Mo}_{12}\text{Cr}_4\text{W}_3$ or $\text{Fe}_{65}\text{C}_{10}\text{B}_9\text{Mo}_9\text{Cr}_4\text{W}_3$. A similar two-phase primary crystallization was observed in a study of $\text{Fe}_{71.2-x}\text{C}_{7.0}\text{Si}_{3.3}\text{B}_{5.5}\text{P}_{8.7}\text{Cr}_{2.3}\text{Al}_{2.0}\text{Mo}_x$ ($x = 0\text{-}6.5$ at.%) [104].

An analysis of the peak widths from the X-ray analysis also revealed a distinct difference in crystallite size after 2 hour anneals, which reinforces the compositional dependence of GFA and the resistance to crystallization. Peak broadening was approximated using a Pearson-VII distribution applied to XRD spectra for T_{x3} anneals, and crystallite size was estimated using the Williamson Hall method with MDI's Jade software. The crystallite size measurements were also in good agreement with those values determined via Scherrer's method [105]. The most significant peak-broadening was observed in $\text{Fe}_{62}\text{C}_{10}\text{B}_9\text{Mo}_{12}\text{Cr}_4\text{W}_3$, which had an average crystallite size of $35 \text{ nm} \pm 3 \text{ nm}$. $\text{Fe}_{60}\text{C}_{10}\text{B}_9\text{Mo}_{14}\text{Cr}_4\text{W}_3$ and $\text{Fe}_{65}\text{C}_{10}\text{B}_9\text{Mo}_9\text{Cr}_4\text{W}_3$ exhibited less peak-broadening, resulting in calculated crystallite sizes of $60 \text{ nm} \pm 5 \text{ nm}$ and $55 \text{ nm} \pm 2 \text{ nm}$, respectively. These differences are related to the optimization of elastic strain as dictated by the molybdenum content in each alloy. An optimum molybdenum content kinetically hinders the tendency for Fe-B and Fe-C ordering, thus suppressing $\text{Fe}_{23}(\text{C,B})_6$ for longer times. When the molybdenum content is greater than the optimum value of 12 at.%, a slightly different phase evolution is observed. Molybdenum in effect supersaturates the disordered structure and upon reheating, the excess molybdenum comes out leading to a primary crystallization featuring a mixture of α -Fe(Mo), and $\text{Fe}_{23}(\text{C,B})_6$. The phase

evolution for $\text{Fe}_{65}\text{C}_{10}\text{B}_9\text{Mo}_9\text{Cr}_4\text{W}_3$ is identical to that of $\text{Fe}_{62}\text{C}_{10}\text{B}_9\text{Mo}_{12}\text{Cr}_4\text{W}_3$, however a notably larger crystallite size was observed. The low atomic mobility of molybdenum minimizes crystallite size in the optimum composition, and as the molybdenum content is decreased, atomic mobility increases, permitting crystallites to grow larger in size upon annealing. The stepwise adjustment of molybdenum content leads to a stepwise change in elastic strain and thus a variation in constraint on crystallite size. This type of complexity in crystalline phase evolution offers versatility in microstructure type and size that can be utilized in a multitude of applications.

Activation Energy for Crystallization

The kinetics of the amorphous to crystalline transition were studied via differential thermal analysis. The Kissinger method [52] utilizes DTA with varying heating rates to calculate the activation energy for crystallization in a glass. The Kissinger Equation describes the shift of the peak temperature, T_p with the change in heating rate, ϕ , where Q is the activation energy:

$$\ln(\phi / T_p^2) = -\frac{Q}{RT_p} + \text{constant} \quad (4.1-2)$$

The peak temperatures are found at the maximum of the heat flow exotherm of the first crystallization at each heating rate shown in Figure 4.1.7. Using the peak temperatures and the Kissinger relationship, an Arrhenius plot can be used to calculate the activation energy for crystallization, Q , as shown in Figure 4.1.8. The activation energy for crystallization in this system compares favorably to that of other high iron content BMGs, and numerous other documented BMG systems. In most cases, activation energies are

calculated using melt spun ribbons with thicknesses less than 100 μm . Chen [53] reported higher activation energies for melt spun ribbons than in bulk rods, with $Q_{\text{ribbon}} = 289.2$ kJ/mol for a 70 μm thick ribbon, and $Q_{\text{rod}} = 201.9$ kJ/mol for a 3mm diameter rod of $\text{Fe}_{61}\text{Co}_5\text{Zr}_8\text{Y}_2\text{Cr}_2\text{Mo}_7\text{B}_{15}$. Shapaan [106, 107] reported $Q_{\text{ribbon}} = 405$ kJ/mol and $Q_{\text{ribbon}} = 471$ kJ/mol for 35 μm thick ribbons of $(\text{Fe}_{67}\text{Co}_{33})_{62}\text{Nb}_8\text{B}_{30}$ and $\text{Fe}_{62}\text{Nb}_6\text{Zr}_2\text{B}_{30}$, respectively. A study of the effect of small iron additions on the crystallization of Vitreloy showed that a 30 μm thick ribbon of $\text{Zr}_{55}\text{Cu}_{30}\text{Al}_{10}\text{Ni}_3\text{Fe}_2$ had $Q_{\text{ribbon}} = 231.7$ kJ/mol [108]. A maximum activation energy of $Q_{\text{plate}} = 453$ kJ/mol was calculated for $\text{Fe}_{62}\text{C}_{10}\text{B}_9\text{Mo}_{12}\text{Cr}_4\text{W}_3$ in this study. The values presented in this study were generated based on 0.64 mm thick plates made via copper mold casting. Although there is no direct method to correlate activation energies for different alloy geometries, Chen clearly showed that there is a dependence of the activation energy on the alloy's cooling rate. The fact that the alloys in the current study have such high activation energies in the plate geometry is indicative of an alloy system with tremendous resistance to crystallization. These alloys compare even more favorably due to the significantly lower materials costs. A listing of the peak temperatures and activation energy for each alloy in the current study is shown in Table 4.1.3.

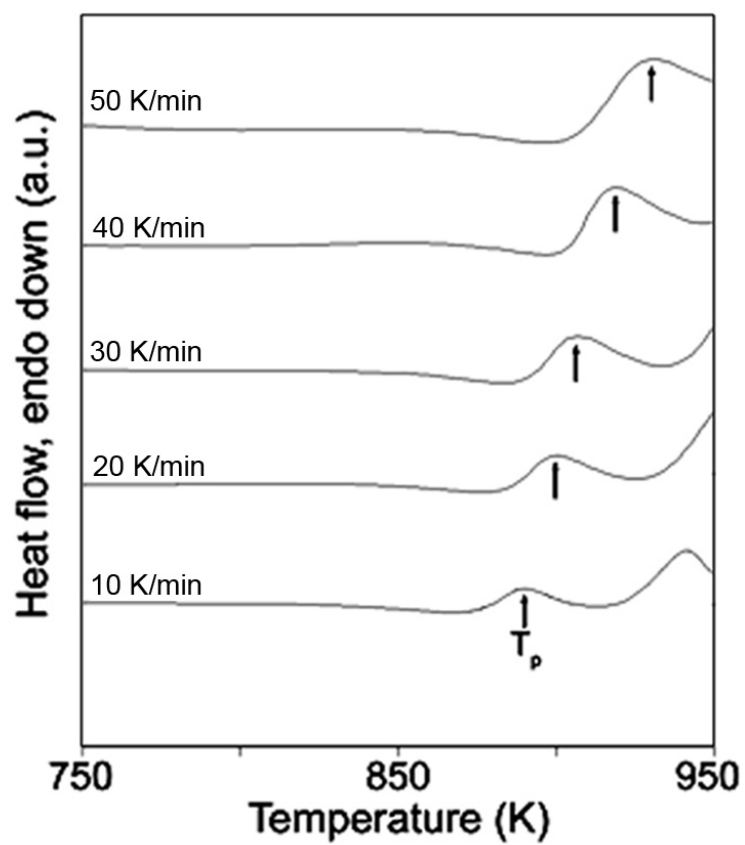


Figure 4.1.7. Crystallization curves for $\text{Fe}_{62}\text{C}_{10}\text{B}_9\text{Mo}_{12}\text{Cr}_4\text{W}_3$ acquired via TG/DTA.

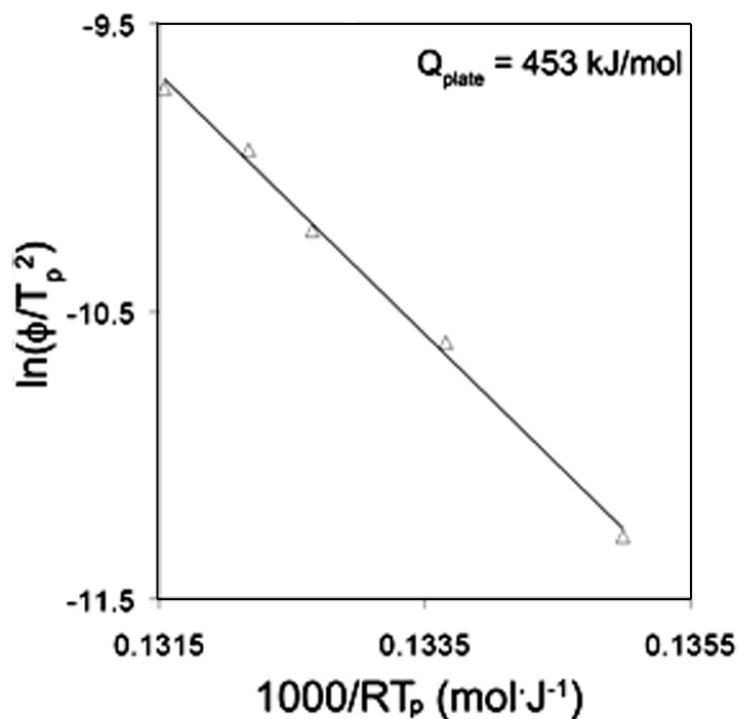


Figure 4.1.8. Kissinger plot of DTA data for $\text{Fe}_{62}\text{C}_{10}\text{B}_9\text{Mo}_{12}\text{Cr}_4\text{W}_3$.

Table 4.1.3. Peak temperature for each alloy in substitutional system with calculated activation energy for crystallization.

Peak Temperature (T_p) in K at various heating rates						
	10K/min	20K/min	30K/min	40K/min	50K/min	Q(kJ/mol)
$\text{Fe}_{60}\text{C}_{10}\text{B}_9\text{Mo}_{14}\text{Cr}_4\text{W}_3$	903.1	914.8	922.4	931.4	938.4	305
$\text{Fe}_{61}\text{C}_{10}\text{B}_9\text{Mo}_{13}\text{Cr}_4\text{W}_3$	898.9	912.7	920.5	925.9	932.8	324
$\text{Fe}_{62}\text{C}_{10}\text{B}_9\text{Mo}_{12}\text{Cr}_4\text{W}_3$	891.0	899.9	906.7	910.0	914.4	453
$\text{Fe}_{63}\text{C}_{10}\text{B}_9\text{Mo}_{11}\text{Cr}_4\text{W}_3$	884.1	891.6	899.9	904.6	909.3	402
$\text{Fe}_{64}\text{C}_{10}\text{B}_9\text{Mo}_{10}\text{Cr}_4\text{W}_3$	879.6	887.8	895.2	901.3	905.6	388
$\text{Fe}_{65}\text{C}_{10}\text{B}_9\text{Mo}_9\text{Cr}_4\text{W}_3$	869.3	879.7	888.2	892.4	896.5	364

The activation energy shows a unique trend that parallels the changes in the supercooled liquid region. As described earlier, modeling predicted a minimization in molybdenum content for the best GFA. Experiments revealed however, that there is an ideal molybdenum content that optimizes elastic strain in the amorphous structure resulting in a peak in the GFA at 12 at.% molybdenum. This peak also coincides with a maximum in activation energy significantly higher than the amorphous compositions surrounding it. Above this critical molybdenum content, GFA decreases, and there is a corresponding decrease in activation energy. A comparison of the alloys at the extremes of this substitutional system reveals that the low molybdenum content alloys investigated ($x = 1-4$) have a significantly better resistance to crystallization than the alloys at the high end ($x = 6,7$) of the molybdenum substitutional spectrum.

Hardness Testing

Thermal aging below the glass transition temperature has been shown to alter mechanical properties, such as plasticity and mechanical hardness, via structural relaxation [109]. As an extension of this concept, hardness testing was performed on samples annealed within the supercooled liquid region, where a strong retention of amorphous behavior was observed in this glass forming system. Hardness tests were performed on various samples in accordance with the heat treatments from this study (alloys corresponding to $x = 2, 5$, and 7 from $\text{Fe}_{67-x}\text{C}_{10}\text{B}_9\text{Mo}_{7+x}\text{Cr}_4\text{W}_3$ ($x = 1-7$ at. %)). Namely, hardness data was gathered for samples annealed for ten minutes at 10K intervals throughout the supercooled liquid region, and at each of the crystallization

temperatures T_{x1} , T_{x2} , and T_{x3} . Additionally hardness data was gathered on samples annealed for 2 hours at T_{x1} , T_{x2} , and T_{x3} ; Table 4.1.4 summarizes the hardness results.

There is a slight increase in hardness as the temperature is increased within the supercooled liquid region in each alloy. Recall from Figure 4.1.5, it was shown that alloys corresponding to $x = 2, 5$, and 7 retain fully amorphous structure throughout the supercooled liquid region. Thus, the increase in hardness in the supercooled liquid region is likely on account of densification due to structural relaxation and free volume annihilation. Alloys on the outer extremes of the substitutional spectrum tended to crystallize at $T_g + 50K$. This crystallization manifests itself as a larger jump in hardness at $T_g + 50$, observed in alloys ($x = 2$) and ($x = 7$) than was observed in ($x = 5$), where the alloy remained fully amorphous after the same heat treatment, because the initial crystalline phase, $Fe_{23}(C,B)_6$, proved to be harder than the fully amorphous alloy.

The nucleation of the initial crystalline phase, $Fe_{23}(C,B)_6$, results in a marked increase in hardness over the fully amorphous alloy. The data for the three different alloys indicate that while the nucleation of $Fe_{23}(C,B)_6$ does increase the hardness, there is an additional dependence on the molybdenum content of the alloy as well. The second crystallization, corresponding to the nucleation of Fe_4W_2C imparts tremendous structural reinforcement to the surrounding matrix. $Fe_{62}C_{10}B_9Mo_{12}Cr_4W_3$ had an average hardness of 1932 after the T_{x2} heat treatment. The high tungsten content in this phase likely accounts for its high hardness. For each of the alloys in this study, T_{x3} corresponded to the nucleation of the phase $(Mo,W)_{23}Fe_{21}Mo_2(B,C)$. This phase further enhanced the hardness of the alloys in this system, resulting in hardness exceeding 2000 Vickers for alloys containing more than 12 at.% molybdenum. The crystal size of these precipitated

phases was not large enough to resolve via optical microscopy or scanning electron microscopy, and therefore hardness testing was not performed on individual phases. The data clearly indicates that the nucleation of each phase results in a marked change in the hardness of each alloy, and there is a clear dependence of hardness on the molybdenum content of the alloy. The high fraction of molybdenum present in the phase corresponding to T_{x3} results in the exhaustion of available molybdenum in the matrix at successively lower volume fractions of $(\text{Mo,W})_{23}\text{Fe}_{21}\text{Mo}_2(\text{B,C})$, as molybdenum content is decreased. The effect of this is the successively lower hardness observed in $\text{Fe}_{60}\text{C}_{10}\text{B}_9\text{Mo}_{14}\text{Cr}_4\text{W}_3$, $\text{Fe}_{62}\text{C}_{10}\text{B}_9\text{Mo}_{12}\text{Cr}_4\text{W}_3$, and $\text{Fe}_{65}\text{C}_{10}\text{B}_9\text{Mo}_9\text{Cr}_4\text{W}_3$. Since less molybdenum is available for phase formation, a larger volume fraction of the molybdenum depleted matrix, with presumably lower hardness, is present. It can therefore be inferred that $(\text{Mo,W})_{23}\text{Fe}_{21}\text{Mo}_2(\text{B,C})$ is in fact even harder than the 2000 Vickers hardness values would indicate, since this must also incorporate the molybdenum-depleted matrix.

Table 4.1.4. Average Vickers hardness data for Fe_{67-x}C₁₀B₉Mo_{7+x}Cr₄W₃ (x=2,5,7) within the supercooled liquid region and after the nucleation of each crystalline phase.

Fe_{67-x}C₁₀B₉Mo_{7+x}Cr₄W₃			
H_v L=1960mN			
	x=2	x=5	x=7
T_g+20 K	1452	1466	1576
T_g+30 K	1474	1493	1607
T_g+40 K	1489	1524	1671
T_g+50 K	1503	1545	1711
subT_{x1}_10m	1521	1533	1703
T_{x1}_10m	1597	1667	1774
T_{x1}_120m	1574	1654	1753
T_{x2}_10m	1659	1932	1862
T_{x2}_120m	1627	1864	1846
T_{x3}_10m	1890	2009	2104
T_{x3}_120m	1858	1911	1953

4.1.4 Conclusion

Amorphous alloys from the system Fe_{67-x}C₁₀B₉Mo_{7+x}Cr₄W₃ (x = 1-7 at. %) demonstrate supercooled liquid regions as high as 51K, and activation energies for crystallization as high as 453 kJ/mol. Through a series of heat treatments, it was determined that each amorphous alloy in this system has excellent resistance to crystallization even at the upper threshold of the supercooled liquid region. Furthermore, there is an optimum molybdenum content for glass formation in this system, governed by the elastic strain that large molybdenum atoms impart on the alloy melt. Departure from this optimum value alters the phase evolution and obstructs the kinetic pathway to amorphous structure. Heat treatments also revealed that there is a 3 stage phase evolution, offering a versatile template for the formation of nanostructured materials. The nucleation of secondary phases via devitrification results in tremendously hard

BMG-derived nanocrystalline reinforced composite materials, with H_v in excess of 2000. The results obtained in this investigation compare favorably to other iron-based BMG, and reinforce the potential for low cost amorphous alloys for industrial applications.

Chapter 4, section 1 in part, is a reprint of the material as it appears in “Materials Science and Engineering A,” Volume 490, Issues 1-2, August 2008, Pages 221-228 and “Journal of Non-Crystalline Solids,” Volume 354, Issues 40-41, October 2008, Pages 4550-4555, written by Hesham E. Khalifa, Justin L. Cheney and Kenneth S. Vecchio. The dissertation author was the primary investigator and author of both of these papers.

4.2 Devitrification and cooling rate effects on microstructure and mechanical properties in $\text{Fe}_{57}\text{C}_9\text{B}_{11}\text{Mo}_{12}\text{Cr}_8\text{W}_3$ metallic glass

4.2.1 Abstract

The bulk metallic glass (BMG), $\text{Fe}_{57}\text{C}_9\text{B}_{11}\text{Mo}_{12}\text{Cr}_8\text{W}_3$, has been studied in terms of its devitrification behavior and kinetics, as well as its crystallization during slow cooling processes. The thermal properties and microstructural development during devitrification heat treatments or controlled melt cooling were investigated by a combination of differential scanning calorimetry, differential thermal analysis, X-ray diffractometry, scanning electron microscopy and microhardness. This Fe-based BMG exhibited the same 3-phase evolution during crystallization, whether via devitrification of the amorphous solid or through crystallization from slow cooled melts. The crystallization leads to markedly increased hardness, as well as marginal fracture toughness enhancement, compared to the amorphous condition. It was found that due to the slow crystallization kinetics, the volume fraction, phase size, phase morphology, and the type of phase could be controlled and optimized to yield useful combinations of hardness and toughness in BMG matrix composites.

4.2.2 Introduction

The *in situ* formation of crystalline phases in bulk metallic glasses is of importance for two primary reasons: (1) an understanding of how, when and which crystalline phases form is paramount in achieving BMG composites exhibiting enhanced

mechanical and magnetic properties [110, 111], and (2) knowledge of the crystalline phases competing with the amorphous structure facilitates the design of better metallic glass forming compositions.

There are several different pathways to achieving *in situ* BMG composites. One pathway is the annealing of as-cast, fully amorphous BMG samples, which leads to devitrification and resultant nanocrystalline phases embedded in an amorphous matrix [112]. A second pathway is through variation in the cooling rate so as to achieve a spectrum of different states ranging from fully amorphous, to nanocrystalline-amorphous matrix composites, to fully nanocrystalline alloys, and finally complex crystalline microstructures, which may be a combination of several different crystalline phases. This latter pathway has been investigated extensively by Löser in Zr-based [113] and Zhang in La-based [114] glass forming systems, but no such study has been performed on low cost Fe-based glass forming systems to date. Other pathways towards the formation of crystalline phases in metallic glass forming systems include compositional variation and processing conditions [115], however, these latter two options will not be included in this investigation. Recent studies have shown that both the type and size of nucleating phases play a critical role in enhancing plasticity in BMG derived composites [79]. It has been shown that when microstructural feature sizes are on the same order as the shear band spacing in an amorphous matrix composite, plasticity is more likely to be enhanced. Furthermore, these crystalline features must be more ductile than the matrix surrounding it [77].

In this study we investigate the microstructural evolution in $\text{Fe}_{57}\text{C}_9\text{B}_{11}\text{Mo}_{12}\text{Cr}_8\text{W}_3$ along both a devitrification pathway and a cooling rate controlled pathway. Of note is the

high iron content and absence of expensive alloying elements in this composition. All of the alloying elements utilized in this study are common to the conventional steel industry. Controlled devitrification is used to identify the phases associated with the crystallization cascade of this alloy. The various phases and microstructures associated with each of the cooling rate conditions are identified. The effect of the microstructure on mechanical properties is discussed.

4.2.3 Results and Discussion

The $\text{Fe}_{57}\text{C}_9\text{B}_{11}\text{Mo}_{12}\text{Cr}_8\text{W}_3$ alloy was successfully cast into amorphous rods 3 mm in diameter, which were used for mechanical testing. This alloy demonstrates a very high compressive strength of 4.2 GPa, and elastic strain of 3.5%, but exhibits no notable plasticity (Figure 4.2.1). Figure 4.2.2 shows a clearly resolved glass transition (T_g) in $\text{Fe}_{57}\text{C}_9\text{B}_{11}\text{Mo}_{12}\text{Cr}_8\text{W}_3$ at 814K and primary onset crystallization at 867K (T_{x1}). The thermal analysis shows a large super-cooled liquid region ($T_{x1}-T_g$) of 53K. Figure 4.2.2 also indicates that crystallization in $\text{Fe}_{57}\text{C}_9\text{B}_{11}\text{Mo}_{12}\text{Cr}_8\text{W}_3$ follows a 3-stage evolution. Based on this result, a series of heat treatments were used to nucleate and grow phases coinciding with the onset crystallization temperatures, T_{x1} , T_{x2} , and T_{x3} . To identify these phases, 2 hour anneals were performed at 5K below T_{x1} , and at the offset temperatures of each crystalline phase. Offset temperatures were used rather than onset temperatures to ensure complete crystallization of each phase. The offset temperatures for $\text{Fe}_{57}\text{C}_9\text{B}_{11}\text{Mo}_{12}\text{Cr}_8\text{W}_3$ were 903K, 972K, and 1041K for the first, second and third crystallization events, respectively. The samples were then analyzed by X-ray diffractometry, and the diffraction peaks were identified.

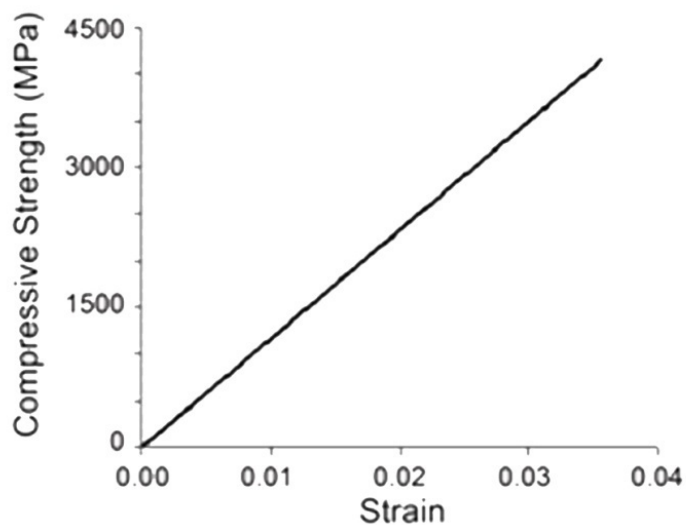


Figure 4.2.1. Stress-strain curve of $\text{Fe}_{57}\text{C}_9\text{B}_{11}\text{Mo}_{12}\text{Cr}_8\text{W}_3$ rod with 3mm diameter tested in compression under strain rate of 10^{-3} s^{-1} .

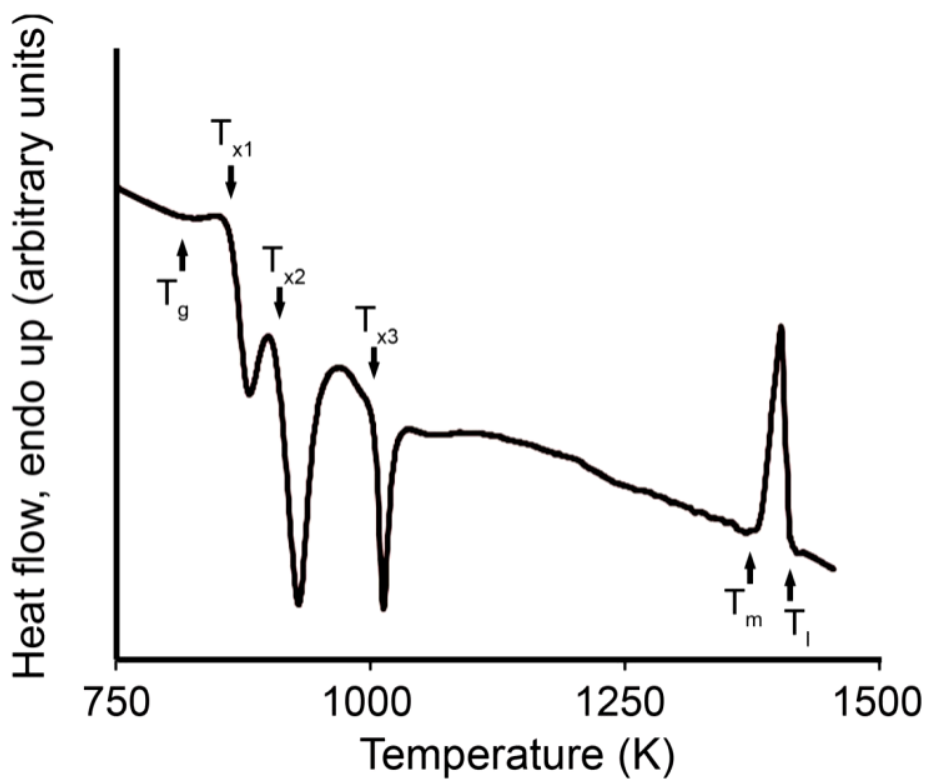


Figure 4.2.2. TG/DTA scan of amorphous $\text{Fe}_{57}\text{C}_9\text{B}_{11}\text{Mo}_{12}\text{Cr}_8\text{W}_3$, indicating glass transition temperature (T_g), 3-phase crystallization (T_{x1} , T_{x2} , T_{x3}), melting temperature (T_m), and liquidus temperature (T_l).

The phase evolution for $\text{Fe}_{57}\text{C}_9\text{B}_{11}\text{Mo}_{12}\text{Cr}_8\text{W}_3$, as determined by XRD is shown in Figure 4.2.3. The sub T_{x1} anneal indicates a full retention of amorphous behavior, suggesting very good thermal stability, and slow crystallization kinetics in this alloy. Slow crystallization kinetics are useful for creating amorphous matrix composites and fully nanocrystalline BMG-derived composites, since the long incubation time for the nucleating phases provides a window to tune mechanical behavior by precisely controlling crystal volume fraction and microstructural development. Furthermore, thermal aging at temperatures near the glass transition region results in structural relaxation [109]. The associated destruction of free volume results in densification of the material and an improvement in hardness compared to the as-cast, fully amorphous material. Hardness tests on $\text{Fe}_{57}\text{C}_9\text{B}_{11}\text{Mo}_{12}\text{Cr}_8\text{W}_3$ revealed an average Vickers hardness of 1455 for the alloy annealed for 2 hours at 862K (sub T_{x1}), compared to an average hardness of 1360 for the as-quenched, fully amorphous alloy. Furthermore, there was a correlation between mechanical hardness and heat treatments below the onset crystallization temperature. A more complete investigation of hardness in the super-cooled liquid region will be discussed in the next section.

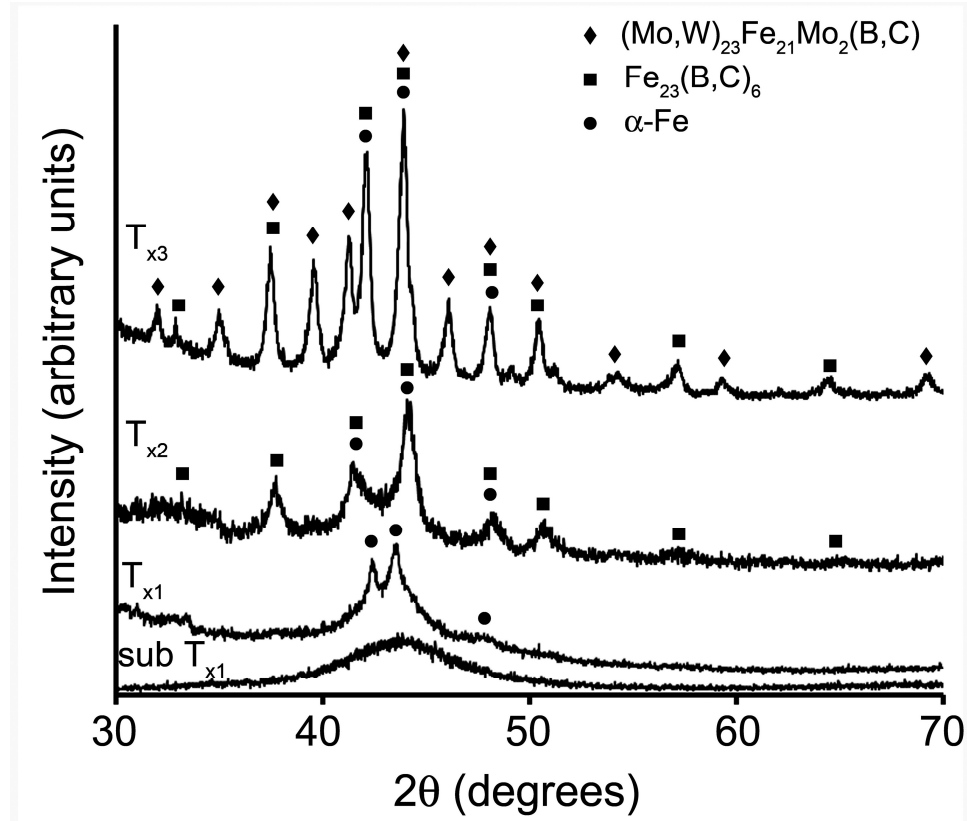


Figure 4.2.3. XRD spectra of heat treated $\text{Fe}_{57}\text{C}_9\text{B}_{11}\text{Mo}_{12}\text{Cr}_8\text{W}_3$ at 5K below T_{x1} , and T_{x1} , T_{x2} , and T_{x3} offset (2 h anneals). Identified crystalline phases are indicated by symbols above Bragg peaks.

The T_{x1} anneal resulted in the nucleation of body centered cubic $\alpha\text{-Fe}$. This primary phase nucleation of $\alpha\text{-Fe}$ has been observed in several Fe-based BMG [94, 112, 116]. An average Vickers hardness of 1484 coincided with the nucleation of $\alpha\text{-Fe}$. The T_{x2} anneal in this study corresponded to the nucleation of $\text{Fe}_{23}(\text{B,C})_6$. The average Vickers hardness observed in the devitrified alloy containing $\text{Fe}_{23}(\text{B,C})_6$ was 1634. The nucleation of Fe_xB_y type phases has been observed in several other Fe-based BMG [4, 28, 94, 96, 103, 116]. The presence of carbon and boron together in $\text{Fe}_{57}\text{C}_9\text{B}_{11}\text{Mo}_{12}\text{Cr}_8\text{W}_3$ is uncommon amongst Fe-based glasses and leads to the nucleation of combined borocarbide phases of the form $\text{Fe}_x(\text{B,C})_y$.

The T_{x3} anneal resulted in the identification of the complex iron-molybdenum-tungsten borocarbide, $(\text{Mo,W})_{23}\text{Fe}_{21}\text{Mo}_2(\text{B,C})$ as the final phase in the crystallization of $\text{Fe}_{57}\text{C}_9\text{B}_{11}\text{Mo}_{12}\text{Cr}_8\text{W}_3$. The final phase in the crystallization cascade of $\text{Fe}_{57}\text{C}_9\text{B}_{11}\text{Mo}_{12}\text{Cr}_8\text{W}_3$ led to a further enhancement of the mechanical hardness up to an average of 1753 Vickers.

Peak width measurements made on the XRD spectra of the samples annealed for 2 hours at T_{x1} , T_{x2} , and T_{x3} indicate average crystal sizes ranging from 40-80 nm for all nucleating phases. The XRD spectra indicate that the crystalline phases formed via devitrification did not get completely converted to a new phase upon subsequent phase nucleation. All of the nucleating phases could still be identified in the XRD spectrum after the T_{x3} anneal. The crystallization cascade was instead a stepwise decomposition of the metastable amorphous precursor first into $\alpha\text{-Fe}$, then to a combination of $\alpha\text{-Fe}$ and $\text{Fe}_{23}(\text{B,C})_6$, and finally, on account of excess molybdenum and tungsten due to $\alpha\text{-Fe}$ and $\text{Fe}_{23}(\text{B,C})_6$ formation, to the end state, consisting of stable $\alpha\text{-Fe}$, $\text{Fe}_{23}(\text{C,B})_6$, and $(\text{Mo,W})_{23}\text{Fe}_{21}\text{Mo}_2(\text{C,B})_{12}$. The fact that enhanced hardness was observed in spite of the persisting presence of $\alpha\text{-Fe}$ after T_{x2} and T_{x3} anneals indicates that the nucleating phases corresponding to these heat treatments are in fact even harder individually than the reported hardness values suggest.

The viability of single-phase nucleation in multi-stage BMG derived crystallization processes is dictated by the crystallization peak separation in thermal analysis. In order to nucleate out one phase, at say T_{x1} , the peak-to-peak difference between T_{x1} and T_{x2} , $\Delta T_{p(1,2)}$ must be at least 30 K [112]. For $\text{Fe}_{57}\text{C}_9\text{B}_{11}\text{Mo}_{12}\text{Cr}_8\text{W}_3$,

$\Delta T_{p(1,2)} = 932\text{K} - 884\text{K} = 48\text{K}$, and $\Delta T_{p(2,3)} = 1013 - 932 = 81\text{K}$. The XRD spectra used for phase identification verify that individual phases were indeed successfully nucleated for each of the crystallization events identified in the DTA scan (Figure 4.2.2). The 3-stage crystallization process in $\text{Fe}_{57}\text{C}_9\text{B}_{11}\text{Mo}_{12}\text{Cr}_8\text{W}_3$, and the associated enhancement in mechanical hardness with each nucleating phase, permits a versatility unique to this Fe-based glass forming system.

A second set of shorter heat treatments was performed on $\text{Fe}_{57}\text{C}_9\text{B}_{11}\text{Mo}_{12}\text{Cr}_8\text{W}_3$ to investigate how heat treatment within the super-cooled liquid region affects mechanical hardness. The volume fraction of crystals in an annealed amorphous alloy can be calculated through calorimetric measurements of crystallization enthalpies in the fully amorphous and partially crystallized material according to the equation,

$$V_f = \frac{\Delta H_A - \Delta H_X}{\Delta H_A} \quad (4.2-1)$$

where V_f is the volume fraction, ΔH_A is the crystallization enthalpy of the fully amorphous alloy, and ΔH_X is the crystallization enthalpy of the partially crystallized alloy.

It has been noted in previous studies that thermal aging results in structural relaxation and phase separation in the under-cooled liquid state [117]. In turn, the primary crystallization observed in metallic glasses is triggered by the diffusion controlled decomposition of the alloy. This time-dependent process is the result of local atomic rearrangements that slowly facilitate the formation of the primary crystalline phase. Accompanying local atomic rearrangement, there is a continuous change in the mechanical properties of the alloy. Similar to structural relaxation observed in sub- T_g

anneals of bulk metallic glasses, the local atomic rearrangements leading up to crystallization result in a densification of this alloy, and increased mechanical hardness [109].

Anneals were performed for 5 min at 10K intervals between T_g and T_x (824K, 834K, 844K, 854K, 864K) and at 7K above T_x (874K). In Figure 4.2.4, XRD spectra of the samples annealed within the super-cooled liquid region show that amorphous structure was maintained throughout the super-cooled liquid region. Heat treatments above T_x (867K) resulted in partial crystallization of the alloy. Although XRD analysis indicate that fully amorphous character was maintained, DSC analysis shows a decrease in crystallization enthalpy as the anneal temperature is increased throughout the super-cooled liquid region. This trend was attributed to local atomic rearrangements arising on account of the short exposure time to elevated temperature. These atomic rearrangements destabilized the amorphous state, such that less energy was required to achieve primary crystallization for alloys annealed at successively higher temperatures within the supercooled liquid region.

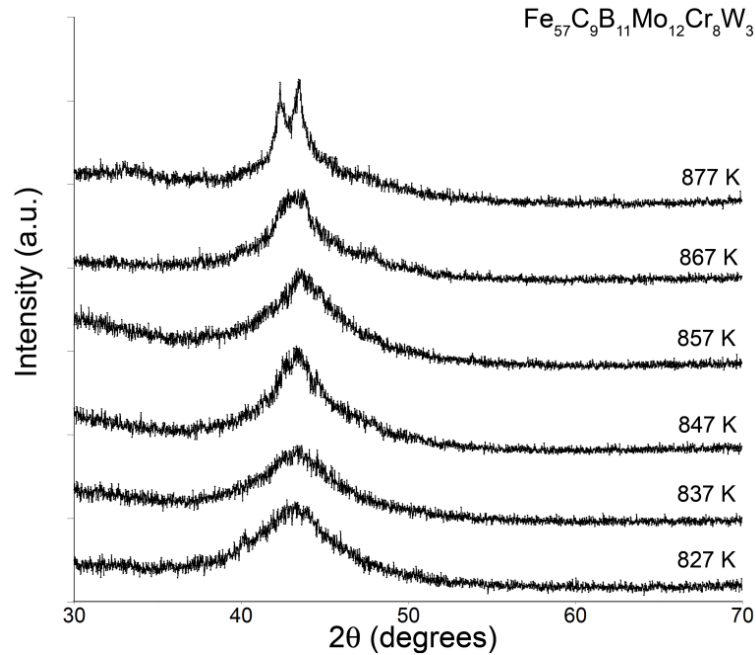


Figure 4.2.4. XRD spectra of $\text{Fe}_{57}\text{C}_9\text{B}_{11}\text{Mo}_{12}\text{Cr}_8\text{W}_3$ after 5 min anneals at successive step 10K intervals above T_g (814K). The 874K anneal is 7K above T_{x1} (867K).

Figure 4.2.5 shows the change in crystallization enthalpy peak magnitude measured with DSC, and Table 4.2.1 tabulates the crystal volume fraction (V_f) and mechanical hardness (H_v) results for the super-cooled liquid region heat treatments. V_f increases with annealing temperature throughout the supercooled liquid region. Even after annealing at T_g+60 , above the onset crystallization temperature, for 5 minutes, a glass transition can be resolved, indicating the retention of some amorphous character. It is possible that the super-cooled liquid region anneals actually result in very fine scale nanocrystallization beyond the resolution limit of the X-ray diffractometer, however, the larger jump in crystal volume fraction and hardness between T_g+50 and T_g+60 suggest a transition from local atomic rearrangement dependent hardness enhancement to crystallization dependent hardness enhancement once the anneal temperature exceeds the onset crystallization temperature.

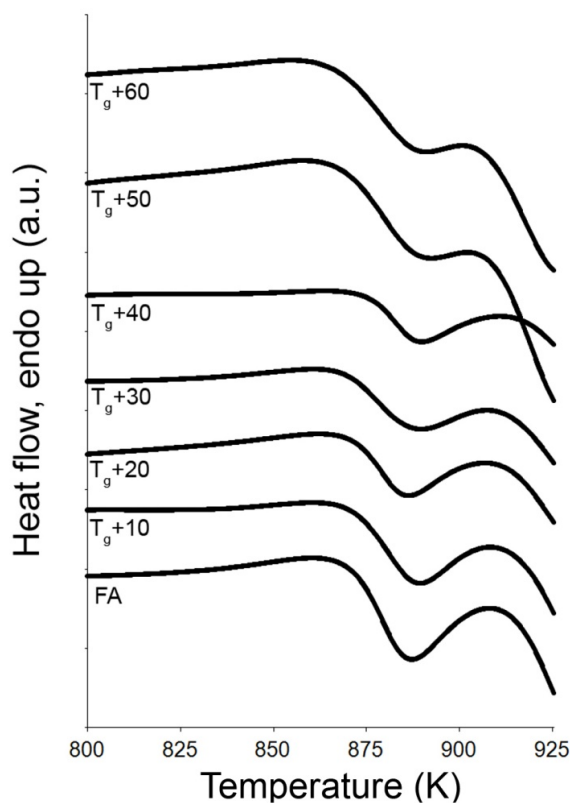


Figure 4.2.5. DSC scans of $\text{Fe}_{57}\text{C}_9\text{B}_{11}\text{Mo}_{12}\text{Cr}_8\text{W}_3$ annealed for 5 minutes at 10K intervals throughout supercooled liquid region (T_g+10 to T_g+50) and 7K above T_{x1} (T_g+60).

Table 4.2.1. Crystallization enthalpy, volume fraction, and average Vickers hardness values at each of the supercooled liquid anneal conditions.

L=200gf, t=15s		$\Delta H_{A,X}$ (J/g)	V_f	H_v
As-cast	ΔH_A	20.93	0.000	1360
T_g+10	ΔH_X	18.90	0.097	1388
T_g+20	ΔH_X	16.77	0.199	1418
T_g+30	ΔH_X	15.16	0.276	1425
T_g+40	ΔH_X	13.55	0.353	1435
T_g+50	ΔH_X	11.47	0.452	1442
T_g+60	ΔH_X	8.64	0.587	1477

Cooling rate controlled microstructural evolution.

In addition to devitrification, controlling the cooling rate during solidification of bulk metallic glass melts is a viable pathway to create BMG derived composite materials. $\text{Fe}_{57}\text{C}_9\text{B}_{11}\text{Mo}_{12}\text{Cr}_8\text{W}_3$ was cast at different cooling rates to achieve a broad spectrum of different microstructures, and the results were analyzed. The various microstructures were achieved by controlling the cooling rate via power modulation of an induction melting coil during the casting process. Samples were cast under four separate cooling conditions. The four different cooling conditions were used to make both 1 mm and 3 mm thick plates.

3 mm thick plate geometry

Backscatter electron images generated via scanning electron microscopy showing the 4 different states achieved in the 3 mm thick plate geometry are presented with corresponding XRD spectra in Figure 4.2.6. For each microstructural state, an ingot of $\text{Fe}_{57}\text{C}_9\text{B}_{11}\text{Mo}_{12}\text{Cr}_8\text{W}_3$ was first heated until fully molten for several seconds to ensure that all crystalline phases melted into the solution. To achieve the microstructure in Figure 4.2.6a, the sample was rapidly quenched as the induction coil was simultaneously turned off. This rapid quench condition will be denoted RQ for both 3mm and 1 mm geometries from this point on. For the condition in Figure 4.2.6b, the sample was quenched and the induction coil power was lowered from 100% to 75% and held for 15s before being turned off. This first intermediate condition will be denoted I1. The condition in Figure 4.2.6c was achieved in a similar fashion to I1 but the power was reduced to 50% and held for 30s. This second intermediate condition will be denoted I2. To achieve the final

condition, shown in Figure 4.2.6d, the sample was quenched in the copper mold and the induction coil power was continuously reduced from 100% down to 20% over a 60s interval. This final, slow cool condition, will be denoted SC.

In Figure 4.2.6a, the Bragg peaks indicate similar phase nucleation to the devitrification experiments. The phases were also verified via EDS and are labeled in the SEM image. The largest features observed in the RQ condition were the hard $(\text{Mo,W})_{23}\text{Fe}_{21}\text{Mo}_2(\text{B,C})$, typically $1\mu\text{m}$ in size, while the surrounding nanocrystalline matrix exhibited two compositionally distinct regions. Within $10\mu\text{m}$ of the $(\text{Mo,W})_{23}\text{Fe}_{21}\text{Mo}_2(\text{B,C})$, there is a region deficient of molybdenum and tungsten (darker in backscatter mode). Within this region, nanocrystalline $\alpha\text{-Fe}$ and $\text{Fe}_{23}(\text{B,C})_6$ have nucleated, while the lighter gray regions of the nanocrystalline matrix have a composition similar to that of the nominal glass forming composition. The I1 condition resulted in a denser, more uniform distribution of microstructural features (Figure 4.2.6b), but the crystalline phases are identical to those nucleating in the RQ condition, namely, $\alpha\text{-Fe}$, $\text{Fe}_{23}(\text{C,B})_6$ and $(\text{Mo,W})_{23}\text{Fe}_{21}\text{Mo}_2(\text{B,C})$, now with an average feature size around $3\mu\text{m}$. The I2 condition (Figure 4.2.6c) resulted in a coarsening of the microstructure, averaging $5\text{-}20\mu\text{m}$ in size, with finer featured intermetallic compounds similar in composition to the nominal amorphous alloy comprising the surrounding matrix. Concurrent with the coarsening of the larger features, a precipitation of sub-micrometer scale $(\text{Mo,W})_{23}\text{Fe}_{21}\text{Mo}_2(\text{B,C})$ was observed within the surrounding matrix. The SC condition (Figure 4.2.6d) resulted in a further coarsening of the microstructure, exhibiting a eutectic morphology of $\alpha\text{-Fe}$ and $\text{Fe}_{23}(\text{B,C})_6$ (dark regions in backscatter image) and

(Mo,W)₂₃Fe₂₁Mo₂(B,C) (white regions in backscatter image) combined with a large plate-like morphology of (Mo,W)₂₃Fe₂₁Mo₂(B,C) on average 30-50μm in size, and some finer structured intermetallic phases in the surrounding matrix. The eutectic structures are characterized by primary dendrite axes with lengths 30-70μm and radius about 2-4μm. The secondary dendritic arms of the eutectic structures had a spacing $\lambda \approx 5-10\mu\text{m}$ and exhibited slightly smaller radii. Some sub-micrometer eutectic (Mo,W)₂₃Fe₂₁Mo₂(B,C) features were also observed within the matrix. It is of note to point out that the resulting XRD spectrum was nearly identical to the fully devitrified Fe₅₇C₉B₁₁Mo₁₂Cr₈W₃. For a given glass forming composition, controlled devitrification of the fully amorphous alloy, or controlled cooling of the molten alloy results in identical crystalline phase formation. To state it another way, irrespective of whether the matrix is a solid amorphous structure or a random liquid structure, the same sequence of crystalline phases form.

Figure 4.2.7 shows SEM images of Vickers hardness indentations for each of the 4 cooling rate conditions, in the 3 mm thick plate geometry. The nanocrystalline matrix of samples cast in the RQ condition had an average hardness of 1453 (Figure 4.2.7a). Comparing this value with those attained in the devitrified Fe₅₇C₉B₁₁Mo₁₂Cr₈W₃, it can be concluded that the nanocrystalline matrix attained in the RQ condition is closer to the structurally relaxed amorphous alloys created by annealing in the high temperature end of the super-cooled liquid region than to the fully amorphous, as-cast alloy. The average hardness in the alloys annealed for 5 minutes at T_g+50K was 1442, while the as-cast, fully amorphous alloy had an average hardness of 1360.

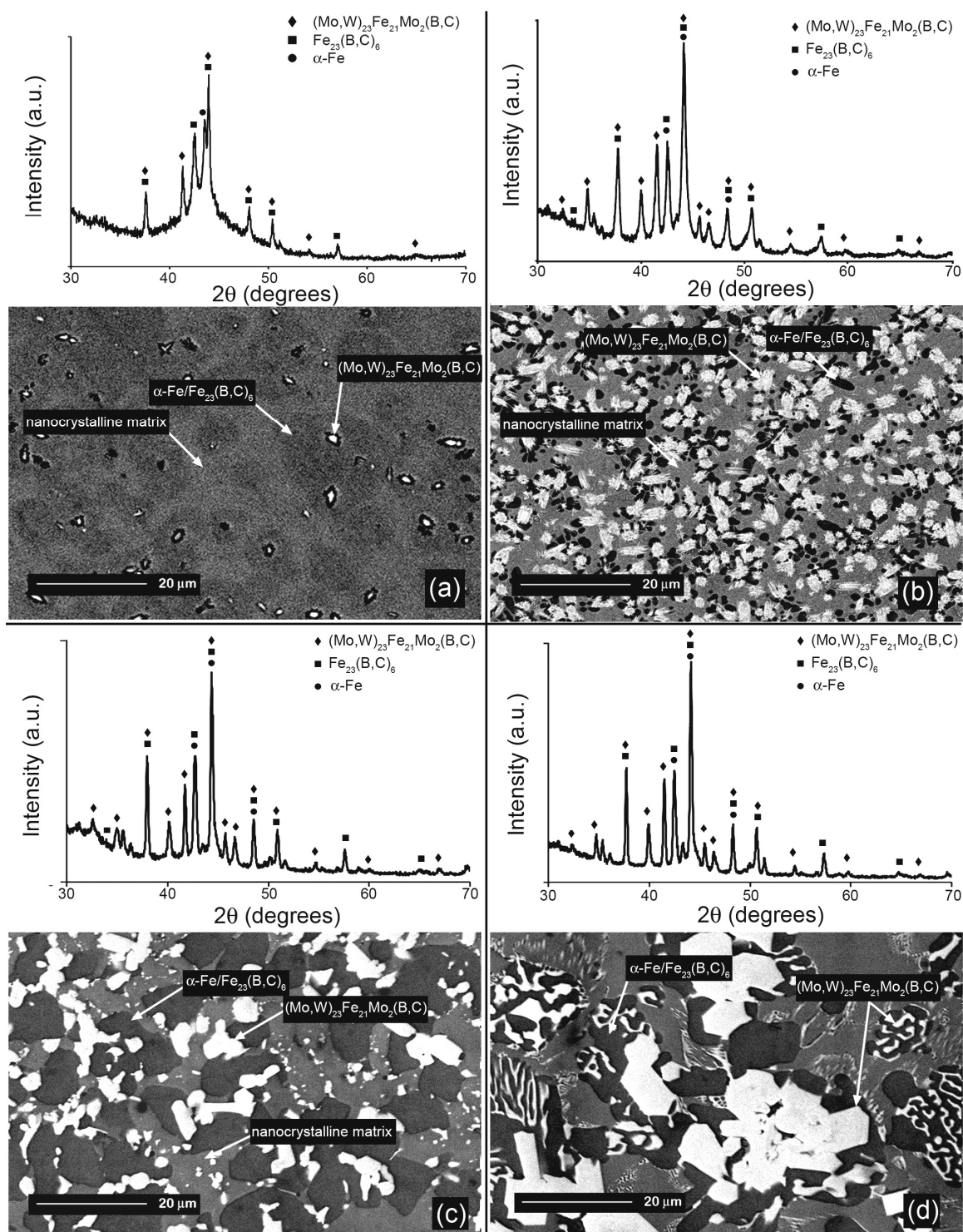


Figure 4.2.6. Different microstructures achieved with 4 cooling rate conditions in 3 mm geometry paired with respective XRD spectra. The phases are labeled and indicated by arrows in the SEM images. (a) Rapid Quench condition - RQ, (b) Intermediate 1 condition - I1, (c) Intermediate 2 condition - I2, (d) Slow Cool condition - SC.

The I1 condition demonstrated an average Vickers hardness of 1617 (Figure 4.2.7b). The microstructure was uniformly distributed throughout the sample and the feature size was significantly smaller than the indenter such that indentations were a good indicator of the bulk mechanical hardness of the alloy. The large $(\text{Mo,W})_{23}\text{Fe}_{21}\text{Mo}_2(\text{B,C})$ plate-like crystals arising in the I2 condition lead to two regions of markedly different mechanical hardness. EDS analysis indicated a migration of molybdenum and tungsten into these large plate-like structures, accompanied by a large deficiency of iron and chromium content within the plate-like structure compared to the surrounding matrix. The large concentrations of molybdenum and tungsten result in a significant increase in mechanical hardness within these plate-like structures, where an average Vickers hardness of 2431 was observed (Figure 4.2.7c). The surrounding molybdenum and tungsten deficient material had an average hardness of 1545 (Figure 4.2.7d). This molybdenum and tungsten deficient matrix contained different iron and chromium borocarbides such as $(\text{Fe,Cr})_{23}(\text{C,B})_6$, $\text{Fe}_3(\text{C,B})$, $\text{Fe}_2(\text{C,B})$, $\text{Fe}(\text{C,B})$, and $\text{Cr}_7(\text{C,B})_3$, as well as some other unidentified intermetallic phases.

The SC condition resulted in similar phase nucleation to the I2 condition, however the presence of large eutectic morphologies was observed in addition to the plate-like crystals. EDS results revealed that the eutectic phase had a composition identical to the $(\text{Mo,W})_{23}\text{Fe}_{21}\text{Mo}_2(\text{B,C})$ plate-like structures. The regions directly adjacent to the $(\text{Mo,W})_{23}\text{Fe}_{21}\text{Mo}_2(\text{B,C})$ part of the eutectic are completely depleted of molybdenum and tungsten. These regions are likely a combination of $\alpha\text{-Fe}$ and $\text{Fe}_{23}(\text{B,C})_6$. The coarse microstructure achieved in this casting condition again led to two distinct regions of mechanical hardness. The average hardness observed across eutectic

morphologies was 1087 (Figure 4.2.7e). The lower hardness observed at the eutectic structures is likely on account of the molybdenum and tungsten deficiency surrounding the structures themselves. The large local volume fraction of α -Fe near the $(\text{Mo,W})_{23}\text{Fe}_{21}\text{Mo}_2(\text{B,C})$ eutectics leads to the low hardness values. Hardness values acquired from tests within several large $(\text{Mo,W})_{23}\text{Fe}_{21}\text{Mo}_2(\text{B,C})$ structures averaged 2813 (Figure 4.2.7f). However, the formation of these large, tremendously hard $(\text{Mo,W})_{23}\text{Fe}_{21}\text{Mo}_2(\text{B,C})$ phases does not significantly enhance the overall hardness of the bulk alloy due to their low overall volume fraction. It is important to note that the cracking observed at the edges of the indentations, particularly in the hard $(\text{Mo,W})_{23}\text{Fe}_{21}\text{Mo}_2(\text{B,C})$ phase, implies a slightly lower hardness value than what has been reported, since indentations likely would have been larger, had cracking not occurred.

Fracture toughness was calculated using the crack lengths from microhardness indentation [118]. Fe-based metallic glasses are among the most brittle of all metallic glasses. The as-cast monolithic $\text{Fe}_{57}\text{C}_9\text{B}_{11}\text{Mo}_{12}\text{Cr}_8\text{W}_3$ glass had a fracture toughness of just $1.6 \text{ MPa}\cdot\text{m}^{1/2}$. The RQ condition represents initial destabilization of the glass. While the presence of α -Fe suggests an improved fracture toughness, the destabilization of the glass to a nanocrystalline state counteracts this effect resulting in a fracture toughness of $1.4 \text{ MPa}\cdot\text{m}^{1/2}$. As the microstructure coarsens, the fracture toughness improves marginally to 2.6 and $3.2 \text{ MPa}\cdot\text{m}^{1/2}$ for the I1 and I2 conditions respectively, yet the increased volume fraction of borocarbides in the SC condition results in fracture toughness of just $2.4 \text{ MPa}\cdot\text{m}^{1/2}$. The very high metalloid content in this glass forming composition limits the enhancement of fracture toughness because preferential nucleation

of the ductile α -Fe is obstructed by uncontrolled nucleation of various brittle carbides and borides.

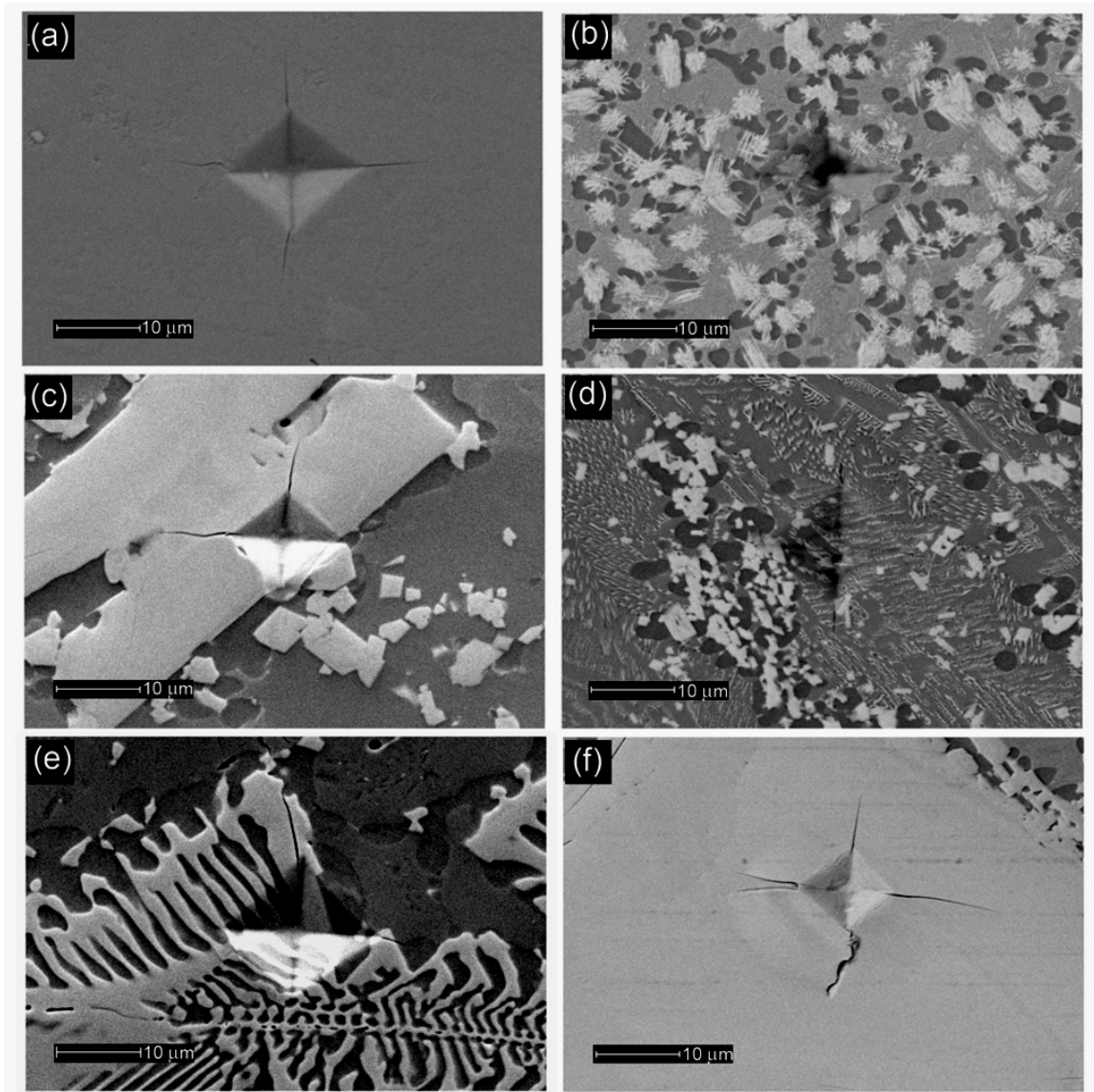


Figure 4.2.7. SEM image of hardness indentations in 3 mm thick plate geometry samples of (a) the nanocrystalline matrix of the RQ condition, (b) the I1 condition, (c) a plate in the I2 condition, (d) the crystalline matrix of the I2 condition, (e) a eutectic crystal in the SC condition and (f) a plate in the SC condition.

In the 3 mm thick plate geometry, cooling rate control provides a means to achieve several microstructurally distinct states. The RQ and I1 conditions result in small

features such that the hardness is uniform under the test conditions. The I2 and SC conditions result in extremely hard plate-like $(\text{Mo,W})_{23}\text{Fe}_{21}\text{Mo}_2(\text{B,C})$ structures, but the net diffusion of molybdenum and tungsten into these features decreases the hardness in the matrix surrounding them.

1 mm thick plate geometry

In the 1 mm geometry, the RQ condition yielded a fully amorphous structure, the two intermediate conditions yielded composite states consisting of nanocrystalline phases embedded in an amorphous matrix, and the slow cool condition was fully crystallized. The XRD spectra in Figure 4.2.8 indicate that the RQ condition was fully amorphous. α -Fe and $\text{Fe}_{23}(\text{B,C})_6$ are both present within an amorphous matrix for the intermediate cooling conditions, I1 and I2 in the 1 mm geometry. The additional peaks present in the spectrum for the fully crystallized SC condition indicate $(\text{Mo,W})_{23}\text{Fe}_{21}\text{Mo}_2(\text{B,C})$ nucleation.

Differential scanning calorimetry results for the 1 mm geometry are presented in Figure 4.2.9. The presence of a clearly resolved glass transition temperature and reduced crystallization enthalpies for intermediate cooling processes (I1 and I2) indicate the retention of some amorphous character accompanied by some crystallization, while the disappearance of the exothermic peak for the amorphous phase's crystallization indicates complete loss of amorphous behavior in the SC condition in the 1 mm geometry.

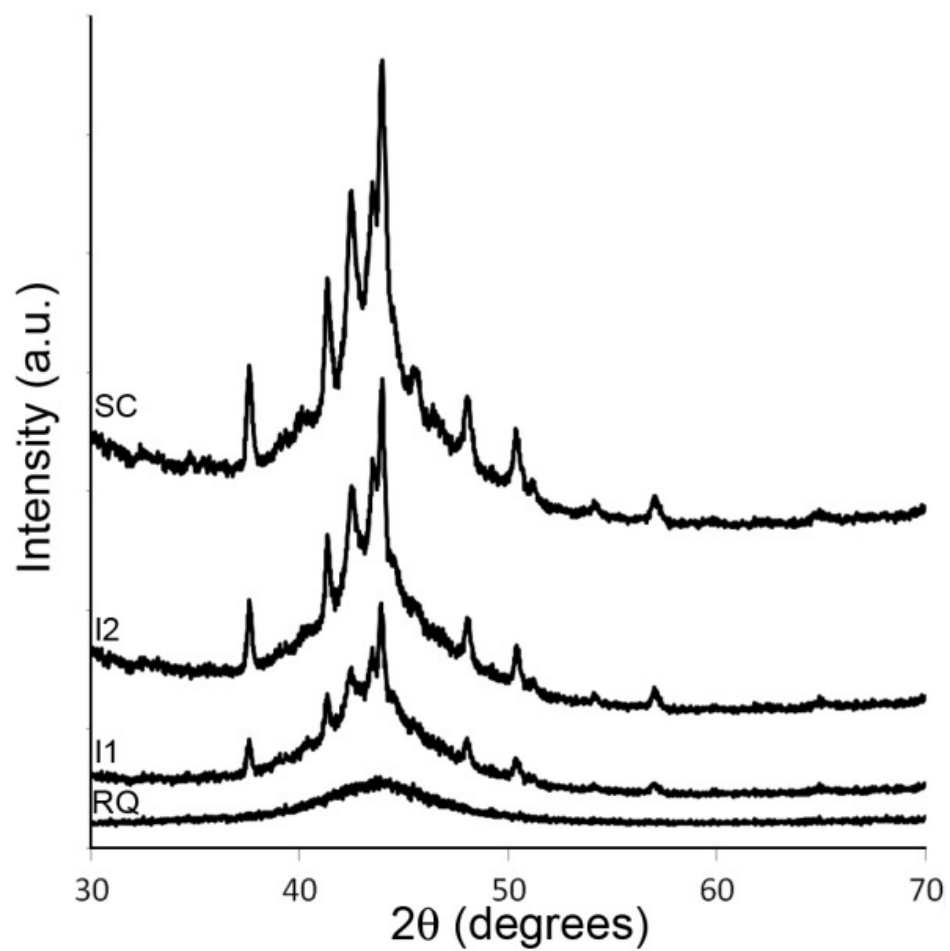


Figure 4.2.8. XRD spectra of alloys cast with 4 cooling rate conditions in the 1 mm thick plate geometry.

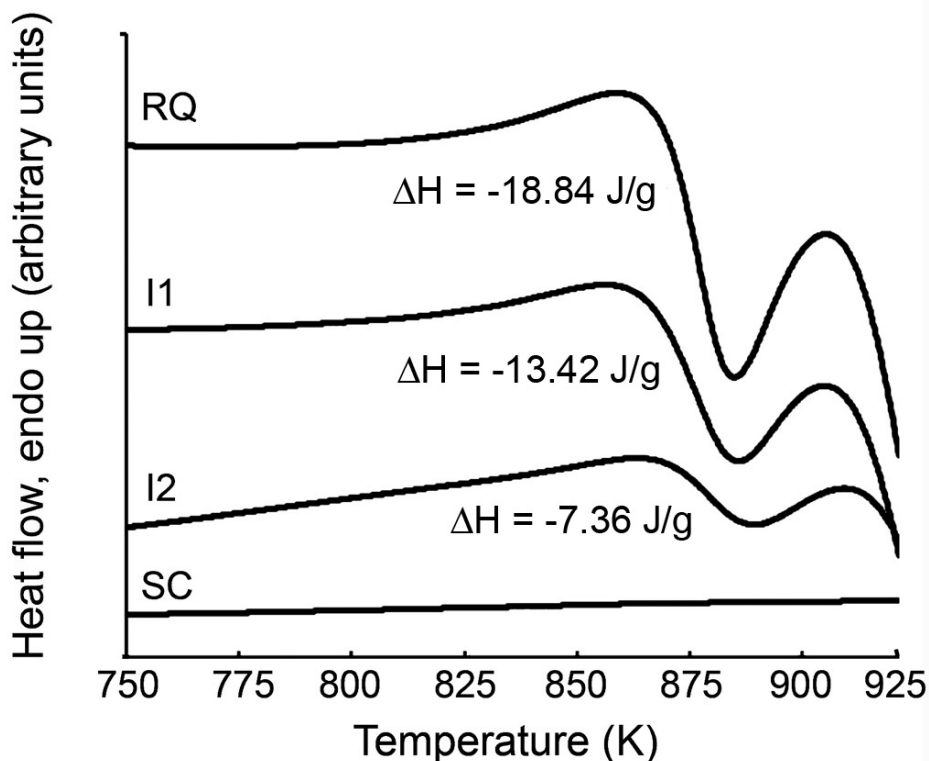


Figure 4.2.9. DSC scans of alloys cast with 4 cooling rate conditions in the 1 mm thick plate geometry. The crystallization enthalpies are listed with each curve. The plate cast in the SC condition has no crystallization enthalpy since it was fully crystallized.

Based on the change in the enthalpy of crystallization peak for each of the cooling rate conditions in the 1 mm geometry, a relationship between the cooling pathway and the crystal volume fraction was developed. Hardness data was also collected at each of the cooling conditions such that a relationship between the crystal volume fraction and the Vickers hardness could be established.

The crystal volume fraction, V_f , was calculated using Equation (4.2-1). It should be noted that the amorphous crystallization enthalpy, ΔH_A , was measured again for samples cast in the 1 mm geometry, rather than using the data collected for the fully amorphous alloy made by splat-quenching. A slightly lower crystallization enthalpy of 18.84 J/g was observed in the rapid quench, 1 mm thick plate, compared to the splat-

quenched alloy ($\Delta H = 20.93 \text{ J/g}$). This discrepancy coupled with the fact the splat-quenched alloy had an average Vickers hardness of 1360 compared to 1396 in the rapidly quenched, 1 mm thick plate, suggest that the local amorphous structure and the mechanical hardness of the amorphous state are dependent on the cooling rate in this alloy system. The I1 condition resulted in a crystallization enthalpy of 13.42 J/g, the I2 condition 7.36 J/g, and the SC condition was fully crystallized and thus had no crystallization enthalpy peak, resulting in a V_f of 0.29, 0.61, and 1.00, respectively.

The RQ casting condition had an average Vickers hardness of 1396, the I1, I2, and SC conditions yielded an average hardness of 1455, 1591, and 1745, respectively. The large jump in mechanical hardness between the I2 and SC condition coincides with the nucleation of $(\text{Mo,W})_{23}\text{Fe}_{21}\text{Mo}_2(\text{B,C})$, as well as the transition from partially amorphous to fully nanocrystalline structure. Within the subset of alloys cast to have a partially crystalline phase embedded in an amorphous matrix, a further dependence of hardness on crystal volume fraction was observed. The destabilization of the glass and associated elimination of free volume lead to enhanced hardness in these alloys. The densification coinciding with free volume elimination, though, adversely affects fracture toughness. Every condition in the 1 mm plate geometry resulted in fracture toughness values of less than $2 \text{ MPa}\cdot\text{m}^{1/2}$.

Outlook for ductile Fe-based BMG-derived composites

The approach utilized for composite design in this study did not yield significant improvement in alloy toughness. In compression, the coarsened microstructure of the

processed alloys did not lead to plasticity; the alloys fail after ~3-4% elastic strain with zero plasticity at fracture strengths of ~ 3GPa.

Among all glass forming compositions, Fe-based glasses contain the largest atomic fraction of light metalloids (e.g. C and B). On account of the large concentration of small metalloid atoms, the amorphous structure of Fe-based glasses contain very dense clusters of atoms, with the small metalloids occupying interstitial sites between large solvent Fe atoms and the various solutes. The high density of the clusters increases the driving force necessary for crystal formation, because all atomic constituents are bound tightly within these atomic clusters. These dense atomic clusters are also what give rise to the tremendous strength inherent to Fe-based glasses. However, the tightly bound clusters lead to extremely brittle behavior, even when compared to other BMGs. Fe-based BMGs typically have fracture toughness in the range of 1-3 MPa*m^{1/2}; among the lowest of all BMGs [119].

The path towards plasticity improvement in Fe-based alloys ultimately rests on stabilizing a ductile phase within an amorphous, or nanocrystalline matrix. The obvious candidate for the ductile phase is α -Fe, since it readily nucleates out from the alloy independent of processing pathway. The processing procedures employed in this study were not sufficient to stabilize enough α -Fe to enhance plasticity or toughness in these alloys. Promoting the nucleation of α -Fe by altering the composition is another viable option to achieve this goal. The α -stabilizer, titanium, was added to the alloy to promote plasticity. The addition of titanium results in only 1-2% plastic strain with fracture strength of ~3GPa, and improves fracture toughness to 5.5 MPa*m^{1/2}. Figure 4.2.10a shows the microstructure of the α -Fe stabilized alloy, Fe₆₀B₉C₁₀Cr₆Mo₈W₂Ti₅, while

4.2.10b shows the corresponding stress-strain curve. While the improvement in mechanical properties resulting from the addition of titanium are minimal, the strength and hardness of these alloys places them competitively among such materials as Co-sintered WC and other hard ceramics[120].

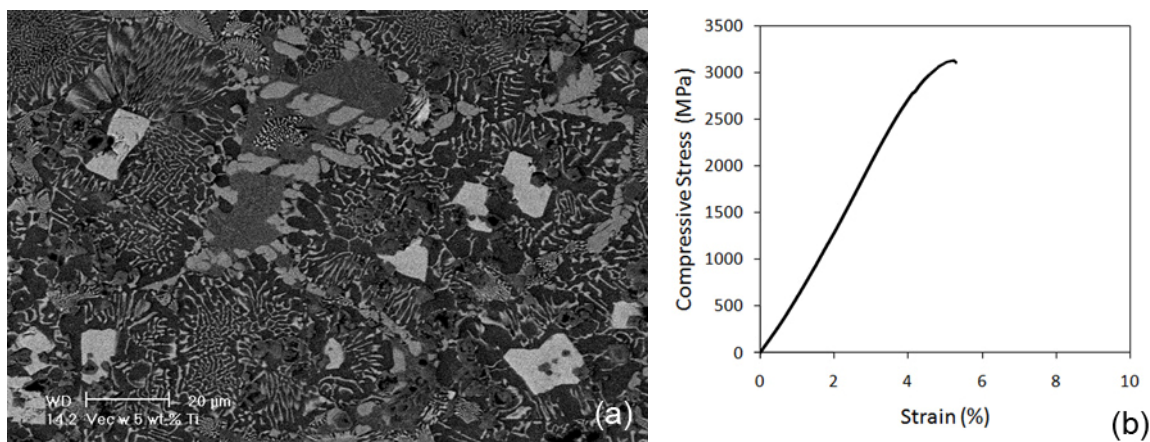


Figure 4.2.10. (a) Back scatter electron image of α -Fe stabilized, $\text{Fe}_{60}\text{B}_9\text{C}_{10}\text{Cr}_6\text{Mo}_8\text{W}_2\text{Ti}_5$ microstructure, (b) corresponding compressive stress-strain curve showing $\sim 1\%$ plastic strain and σ_{max} of $\sim 3\text{GPa}$.

The development of ductile BMG composites not only requires the successful nucleation of a ductile phase, but also some degree of ductility in the glass itself. If the glass is too brittle, the shear bands developing in the glass will evolve into cracks and circumnavigate the ductile crystalline phase rather than transferring the strain into the ductile phase as the propagating shear band interacts with the ductile phase.

Furthermore, the high metalloid content generally leads to carbide and boride formation in the destabilized glass. Carbides in particular, are tremendously stable phases that are very difficult to avoid in a multi-phase landscape. Carbides will quickly form via heterogeneous nucleation at the interface between the glass forming melt and the ductile

secondary phase. The brittle behavior exhibited by carbides and borides have hindered the development of nanocrystalline matrix composites with enhanced ductility.

The low cost of these Fe-based alloys is derived from the high metalloid content in them. The only way to minimize metalloid content is through the use of often expensive large atoms such as erbium and gadolinium [90-92]. The development of ductile Fe-based BMG-derived composites will require further investigations of new glass forming systems that are not as dependent on metalloids for glass formation.

4.2.4 Conclusion

The new bulk metallic glass, $\text{Fe}_{57}\text{C}_9\text{B}_{11}\text{Mo}_{12}\text{Cr}_8\text{W}_3$, was successfully cast into fully amorphous 3 mm rods and demonstrated a compressive strength of ~ 4.2 GPa. Calorimetric experiments revealed the crystalline phases nucleating out from the amorphous state with initial crystalline phase being α -Fe, the second crystallization resulted in the nucleation of $\text{Fe}_{23}(\text{B,C})_6$, and the third crystallization corresponded to $(\text{Mo,W})_{23}\text{Fe}_{21}\text{Mo}_2(\text{B,C})$. The nucleation of the two borocarbide species resulted in a marked enhancement in mechanical hardness. Heat treatment within the super-cooled liquid region resulted in a maintenance of amorphous structure, demonstrating excellent thermal stability, and an enhancement in mechanical hardness, which was attributed to local atomic rearrangements preceding crystallization of the alloy.

$\text{Fe}_{57}\text{C}_9\text{B}_{11}\text{Mo}_{12}\text{Cr}_8\text{W}_3$ was also cast into 1 mm and 3 mm thick plates under 4 different cooling conditions. In addition to fully amorphous, and nanocrystalline-amorphous matrix composite materials, fully crystalline alloys with complex crystalline microstructures and extremely high hardness were achieved. The phase nucleation

observed in the slow-cooled, fully crystalline alloy processed via cooling rate control was nearly identical to the fully devitrified alloy annealed above its highest crystallization temperature. The understanding of the crystallization behavior of $\text{Fe}_{57}\text{C}_9\text{B}_{11}\text{Mo}_{12}\text{Cr}_8\text{W}_3$ gained in this study has provided a comprehensive means to control the mechanical hardness in a variety of microstructurally distinct BMG-derived composites.

Chapter 4, section 2 in part, is a reprint of the material as it appears in “Advanced Engineering Materials,” Volume 10, 2008, Page 1056, written by Hesham E. Khalifa and Kenneth S. Vecchio. The dissertation author was the primary investigator and author of this paper.

Chapter 5: Titanium-based Bulk Metallic Glass Composites

5.1 Thermal Stability and Crystallization Phenomena of Low Cost Ti-based Bulk Metallic Glass

5.1.1 Abstract

The thermal stability, kinetics of crystallization, and glass forming ability of a $\text{Ti}_{48}\text{Ni}_{32}\text{Cu}_8\text{Si}_8\text{Sn}_4$ bulk amorphous alloy have been studied by differential scanning calorimetry using both isothermal and non-isothermal experiments. The activation energy, frequency factor, and rate constant for the crystallization cascade were determined via the Kissinger method. X-ray diffractometry and transmission electron microscopy studies revealed that crystallization starts with the primary precipitation of α -Ti(Ni,Cu), followed by the nucleation of Cu_3Ti from the amorphous precursor. The kinetics of nucleation of the primary crystalline phase was also investigated using the Johnson-Mehl-Avrami method and the Avrami exponent, n , was determined.

5.1.2 Introduction

Bulk metallic glasses (BMGs) have been the focus of extensive research over the past 20 years on account of their good glass forming ability (GFA), processing ability, and thermal stability with respect to crystallization, as well as unique properties for structural and functional applications. To date, several ternary and higher order, multicomponent BMGs have been designed and characterized [6, 67, 91, 121]. Among them, Zr-Ti-Cu-Ni-Be alloys are the most processable, and have been used in several commercial applications. The low cost (relative to other amorphous alloys) of Fe- and Ti-

based BMGs, makes them superlative candidates for more widespread commercial application beyond a few niche markets. Titanium glasses in particular present a unique opportunity for commercial application due to their high strength (~ 2 GPa), elastic strain limit ($\sim 2\%$), low elastic modulus (60-100 GPa), low specific density (~ 6 g/cm³) and good wear and corrosion resistance [122, 123].

Conventional titanium alloys have been widely used in the aerospace industry due to their availability, low density, and high specific strength. Additionally, titanium alloys are bioinert, making them safe options for the biomedical industry. The inherent lack of plasticity in monolithic BMGs, however, prohibits their use for bioimplantation. The poor plasticity renders these alloys prone to catastrophic failure due to shear localization in one, or very few shear bands, in load bearing applications. However, the basic tenets governing metallic glass formation promote slow kinetics that lend glass forming alloys well to controlled crystallization events, such that the strength, modulus, and plasticity may be tuned to fit specific applications. In fact, much of the recent work on bulk metallic glasses has been geared towards developing metallic glass matrix composites, in order to enhance plasticity, while still maintaining the high strength intrinsic to amorphous alloys. Zr-Ti-Cu-Ni-Be alloys have demonstrated plasticity of up to 5%. This plasticity has been attributed to the presence of an icosahedral quasicrystalline phase embedded within the glassy matrix [124]. More recently, Ti-based glass forming compositions have been adjusted to promote the nucleation of a ductile crystalline phase within an amorphous matrix [123]. This development has yielded plastic strains as high as 20% in a Ti-Nb-Sn-Cu-Ni BMG composite, and 10% in a Ti-Zr-Hf-Cu-Ni-Si BMG composite. A new Ti-based BMG exhibiting excellent thermal stability and designed to

exclude Be, RE, and other expensive alloying elements is introduced here. Several experiments probing the crystallization cascade have been performed in order to better understand which crystalline phases are favored upon devitrification.

The experimental techniques employed in this study help to characterize the crystallization process. Armed with the knowledge of how a good metallic glass former crystallizes, deviation from the optimal glass forming conditions, either by altering processing parameters or composition, can be used to promote the nucleation and growth of, for example, a ductile crystalline phase of particular morphology and size, that will work in concert with the amorphous matrix to create a ductile, high strength, BMG composite.

5.1.3 Results and Discussion

The glass forming ability (GFA) and thermal stability of fully amorphous $\text{Ti}_{48}\text{Ni}_{32}\text{Cu}_8\text{Si}_8\text{Sn}_4$ were examined by continuous heating experiments, shown in Figure 5.1.1. At heating rates ranging from 1-200 K/min, a distinct glass transition temperature (T_g), and a large supercooled liquid region ($\Delta T_x = T_x - T_g$) were resolved. Directly following the supercooled liquid region, this alloy exhibits two overlapping exothermic crystallization peaks, designated by their respective peak temperatures (T_{p1} and T_{p2}) in Figure 1. As the heating rate is increased, there is an associated increase in T_g , T_x , T_{p1} , and T_{p2} . The results of the DSC heating experiments are presented in Table 5.1.1. $\text{Ti}_{48}\text{Ni}_{32}\text{Cu}_8\text{Si}_8\text{Sn}_4$ demonstrates a maximum ΔT_x of 92 K at a heating rate of 20 K/min, indicating very high resistance of the undercooled liquid to crystallization, which functions to retard nucleation of the primary crystalline phase. The DTA resolved

liquidus temperature was 1319 K, resulting in a reduced glass transition temperature ($T_{rg} = T_g/T_l$) of 0.59, which is also indicative of good GFA. $Ti_{48}Ni_{32}Cu_8Si_8Sn_4$ was successfully cast into fully amorphous rods, 3 mm in diameter. This alloy demonstrated a compressive fracture strength of 1760 MPa, and elastic strain of 2.3% with no significant plasticity. These values are in good agreement with other reported monolithic Ti-based BMGs [121, 123].

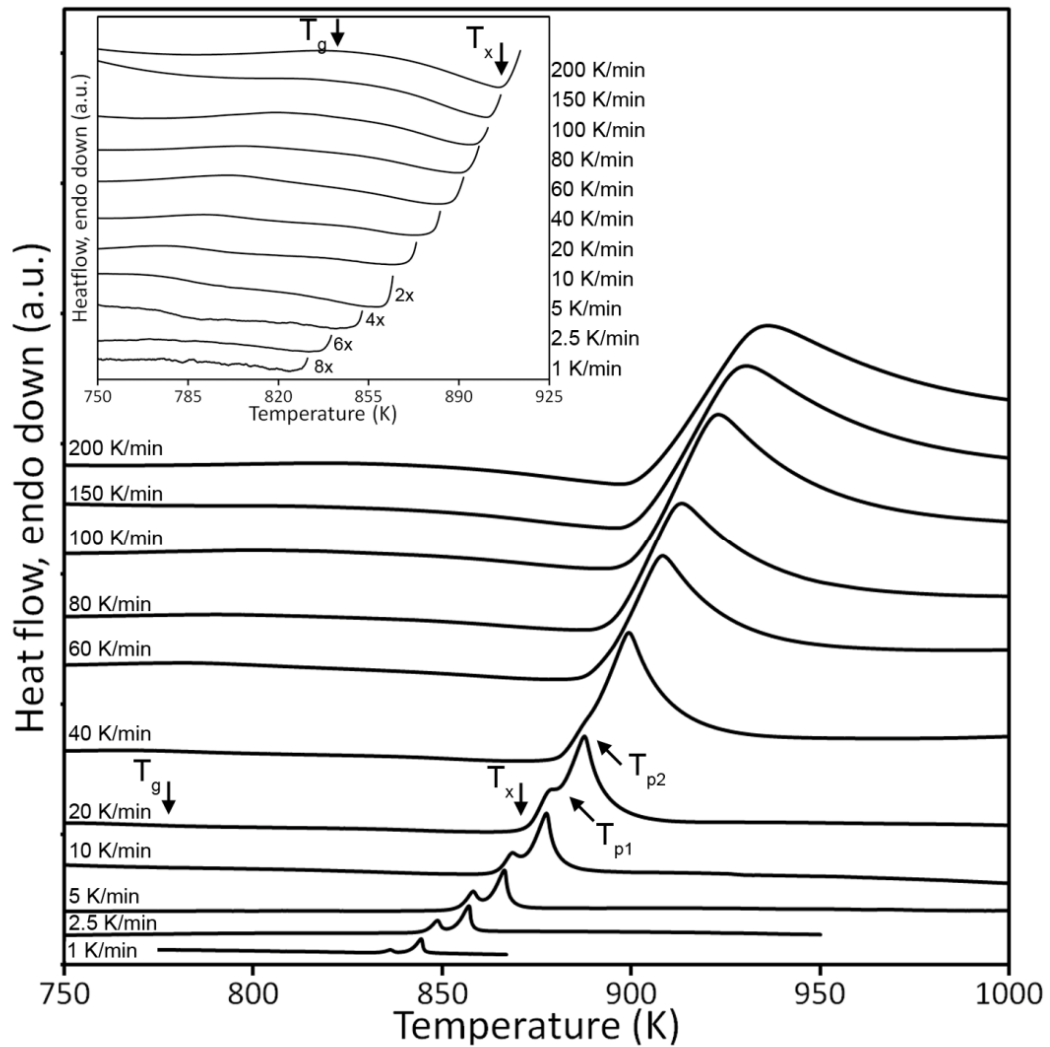


Figure 5.1.1. Continuous heating DSC curves obtained at different heating rates.

The evolution of the microstructure during the crystallization process can be followed on the XRD spectra presented in Figure 5.1.2. The XRD spectrum for as-cast alloy exhibits the typical broad hump indicative of a fully amorphous structure. Two hour heat treatment to nucleate the phase corresponding to the first exothermic peak yields an XRD spectrum that suggests significant retention of amorphous structure, however, small peaks superimposed on the broad hump are attributed to the primary crystallization (T_{x1}) of Ti(Ni,Cu). This result has been reported in previous studies of Ti-based metallic glasses [123]. The secondary crystallization (T_{x2}) yielded an XRD spectrum exhibiting sharper, higher intensity peaks, typical of a fully crystalline structure. The additional peaks in the T_{x2} XRD spectrum confirm that Cu_3Ti is the second crystalline phase to nucleate out from the fully amorphous $\text{Ti}_{48}\text{Ni}_{32}\text{Cu}_8\text{Si}_8\text{Sn}_4$ precursor. Calin [122] also observed the secondary nucleation of Cu_3Ti in the alloy $\text{Ti}_{50}\text{Cu}_{20}\text{Ni}_{24}\text{Sn}_3\text{Si}_2\text{B}_1$.

Table 5.1.1. Dependence of glass transition (T_g), crystallization (T_x) and peak (T_{p1} , T_{p2}) temperatures, as well as supercooled liquid region (ΔT_x), on heating rate (β).

β (K/min)	T_g (K)	T_x (K)	T_{p1} (K)	T_{p2} (K)	ΔT_x (K)
1	765.7	830.3	837.3	843.6	64.6
2.5	769.1	838.2	848.8	856	69.1
5	772.6	852.8	857.1	865.6	80.2
10	776.9	864.4	869.7	876.9	87.5
20	783.8	878.6	877	887	94.8
40	794.2	886.7	888.4	898.4	92.5
60	801.8	889.1	896.4	906.4	87.3
80	808.33	890.9	904.9	912.4	82.57
100	820.8	900.3	-	919.6	79.5
150	832.9	904.3	-	926.5	71.4
200	838.4	907.2	-	931.8	68.8

The bright field TEM image in Figure 3 was acquired from a sample annealed for two hours at 868 K (T_{x2}). The observation of Moiré fringes in the image confirms crystallinity. The crystallites are homogenously dispersed with an average size of approximately 20-30 nm. The average crystallite size is in good agreement with the value of 29 ± 2 nm obtained using Scherrer's method of XRD peak measurement on the T_{x2} annealed sample [125].

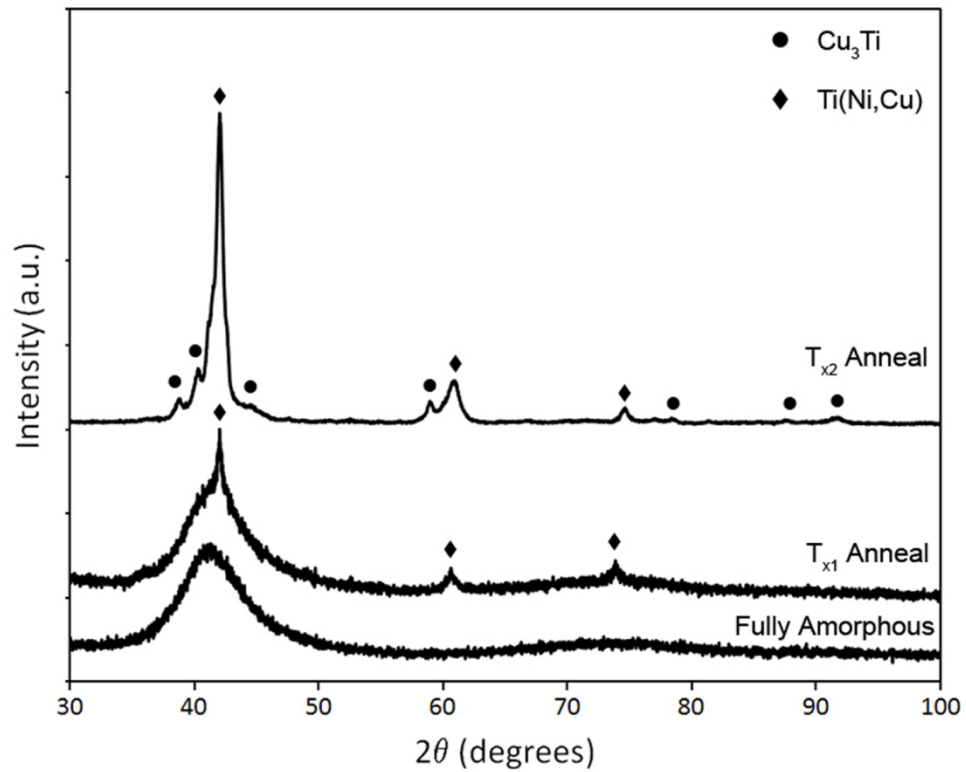


Figure 5.1.2. XRD spectra of $\text{Ti}_{48}\text{Ni}_{32}\text{Cu}_8\text{Si}_8\text{Sn}_4$ in the as-cast, fully amorphous state, and after annealing at each of the crystallization temperatures (T_{x1} , T_{x2}).

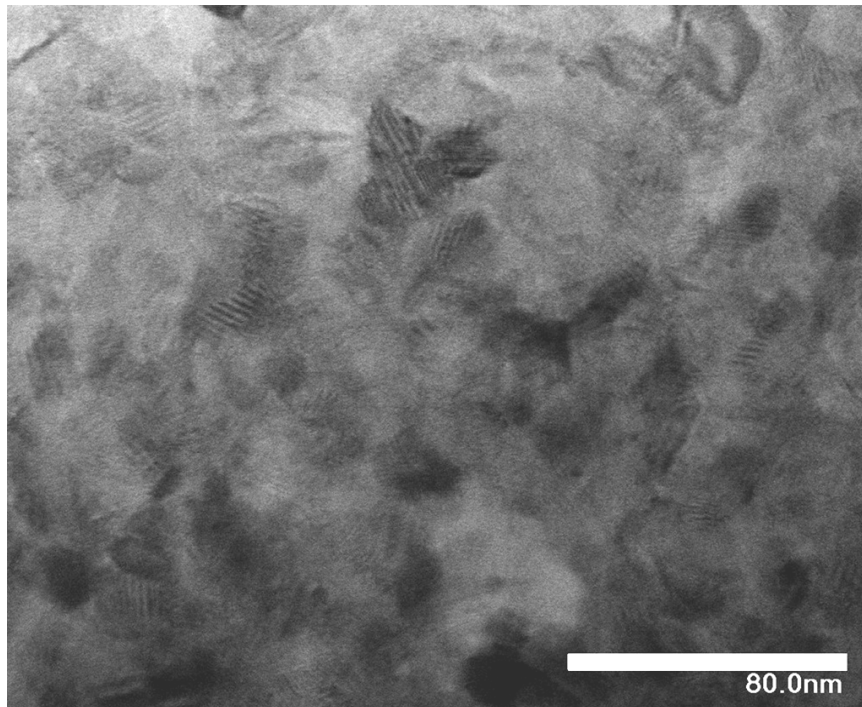


Figure 5.1.3. Bright field TEM image of annealed Ti₄₈Ni₃₂Cu₈Si₈Sn₄ indicating a fully crystallized state.

The amorphous to supercooled liquid transition phenomenon can be described using two different methods. In previous studies [126], calorimetric studies have shown a linear dependence of T_g on the heating rate, called the Lasocka relationship [127]:

where T_0 and U are constants. In general the onset crystallization, T_x , is shifted to higher temperatures to a greater degree than T_g or T_m as the calorimetric heating rate is increased. It has been shown [72] that the dependence of T_g as a function of β for stronger metallic glass formers is better described by a Vogel-Fulcher-Tamann (VFT)-type fit [128, 129] :

$$\beta = B \exp\left(\frac{A}{T_g^0 - T_g}\right) \quad (5.1 - 2)$$

where A is a constant, T_g^0 is the asymptotic value of T_g , generally approximated as the onset of the glass transition within the limit of infinitely slow cooling and heating rate, and B is a constant with the same dimension as heating rate. The fragility parameter, which quantifies GFA based on the temperature dependence of atomic rearrangements [47], can be expressed as:

$$D^* = A/T_g^0 \quad (5.1 - 3)$$

Applying Equation (5.1-3) to Equation (5.1-2) permits fitting of the experimental data according to:

$$\ln \beta(T_g) = \ln B - \frac{D^* T_g^0}{T_g - T_g^0} \quad (5.1 - 4)$$

where B, D^* , and T_g^0 are three simultaneously adjustable VFT parameters. The best fit VFT curve for the glass transition data is shown in Figure 5.1.4.

Activation energy for crystallization (E) and frequency factor (Z) corresponding to the glass transition and individual crystallization events are estimated using the Kissinger method [52]. The dependencies of the peak temperatures (T_g , T_{p1} , T_{p2}) on the heating rate can be given by:

$$\frac{\beta}{T_i^2} = \frac{Z_i R}{E_{a,i}} \exp\left(\frac{-E_{a,i}}{RT_i}\right) \quad (5.1 - 5)$$

where R is the universal gas constant, and the index i refers to either glass transition or crystallization (g , $p1$, or $p2$). The determination of the activation energies ($E_{a,i}$) for each event is enabled by plotting $\ln(\beta/T_i^2)$ vs. T_i^{-1} . A large activation energy for crystallization indicates that crystallization takes place slowly through a nucleation and

growth process [130]. The activation energies $E_{a,g}$, $E_{a,p1}$, $E_{a,p2}$ were determined to be 369, 405, and 396 kJ/mol, respectively. The frequency factor (Z), which measures the probability that an atom having energy E_a joins an existing nucleus, can be determined from the intercept of the Arrhenius curve. The values determined ($Z_{p1} = 1.02 \cdot 10^{24} \text{ min}^{-1}$, $Z_{p2} = 2.01 \cdot 10^{23} \text{ min}^{-1}$) are in agreement with several other good metallic glass formers [129, 131]. The temperature dependence of the rate constant, k_{cr} also follows an Arrhenius-type relationship:

$$k_{cr}(T) = Z \exp\left(\frac{-E_{a,i}}{RT}\right) \quad (5.1 - 6)$$

as seen on the monotonically increasing curves in the inset of Figure 5.1.5 for the peaks (T_{p1} and T_{p2}) of the exothermic transformations. Lower k_{cr} has been correlated with better glass forming ability and larger ΔT_x [132].

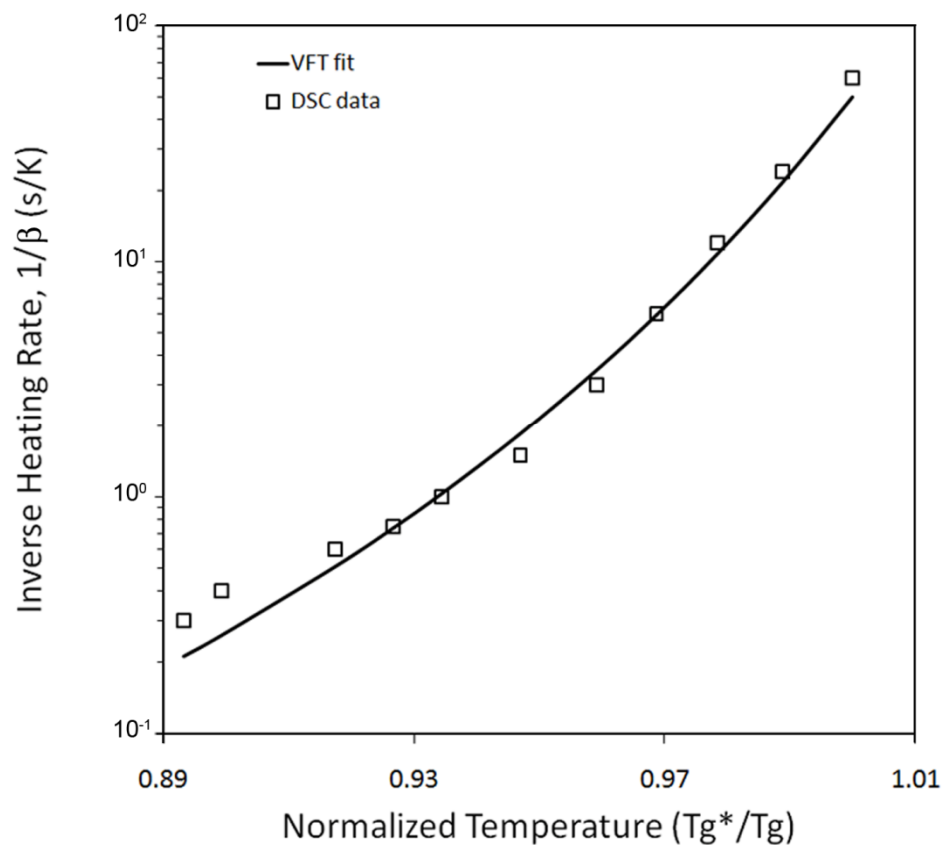


Figure 5.1.4. Inverse heating rate ($1/\beta$) as a function of T_g , normalized by T_g^* (the onset of the glass transition at 1 K/min). The VFT parameters for the best fit to the DSC data according to Equation (5.1-4) are $\ln(B) = 7.69$ K/s, $D^* = 1.33$, and $T_g^0 = 684$ K.

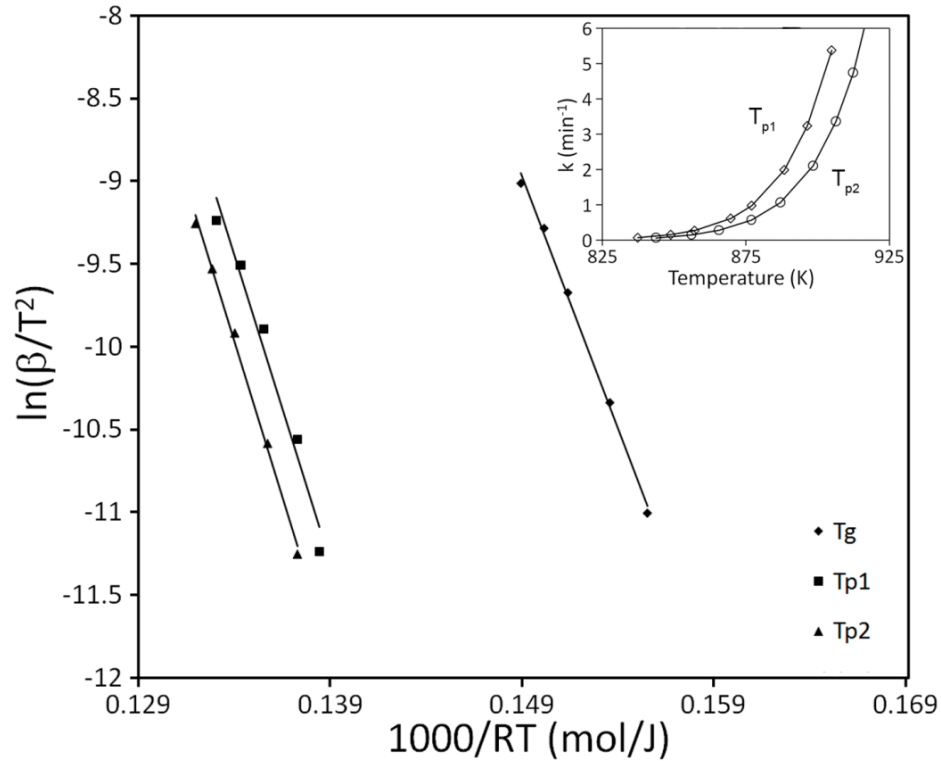


Figure 5.1.5. Kissinger plots obtained from the shift of the transformation peak temperatures according to Equation (5.1-5). The inset shows the experimentally determined rate constant (k_{cr}) according to Equation (5.1-6).

Isothermal annealing of the as-cast $Ti_{48}Ni_{32}Cu_8Si_8Sn_4$ alloy was carried out in order to study the crystallization mechanism in greater detail. The isothermal experiments were designed such that both crystallization events observed in the continuous heating experiments (Figure 5.1.1) occurred within the first hour of annealing. The lowest temperature in which this requirement was fulfilled was at $T_{ann} = 813$ K, roughly halfway between T_g and T_x . If a glass transition is not observed, amorphous structure may still be present, however, it may be obscured by crystallization. In such a case, unambiguous identification of microcrystalline structure is possible through observation of isothermal crystallization kinetics [133]. There is a fundamental difference between the nucleation and growth of crystals from an originally amorphous

state, versus the coarsening of a crystal structure from an originally microcrystalline state, and this difference would present itself, through differences between isothermal and non-isothermal treatment, in the energy required to activate a crystalline cluster.

The DSC curves for the one hour isothermal experiments are shown in Figure 5.1.6. Each isotherm has two distinct exothermic transformation peaks corresponding to nucleation of the two aforementioned crystalline phases determined in the continuous heating experiments (Figure 5.1.1), indicating that the crystallization process occurs via a nucleation and growth mechanism. As the anneal temperature is increased, the transformation peaks (t_{p1} and t_{p2}) occur after shorter and shorter incubation times, and the peaks become larger in magnitude. In much the same way that activation energy for crystallization was determined in the continuous heating experiments, the activation energy for isothermal crystallization $E_{a,i}^{iso}$ may be gleaned from a plot of $\ln(t_p)$ vs. T_{ann}^{-1} . The apparent isothermal activation energies were determined to be 422 and 409 kJ/mol for $E_{a,p1}^{iso}$ and $E_{a,p2}^{iso}$, respectively. The good agreement between the activation energy values obtained for continuous heating and isothermal annealing indicate that atoms participating in crystal nucleation during isothermal and non-isothermal treatments require nearly the same energy to trigger crystallization.

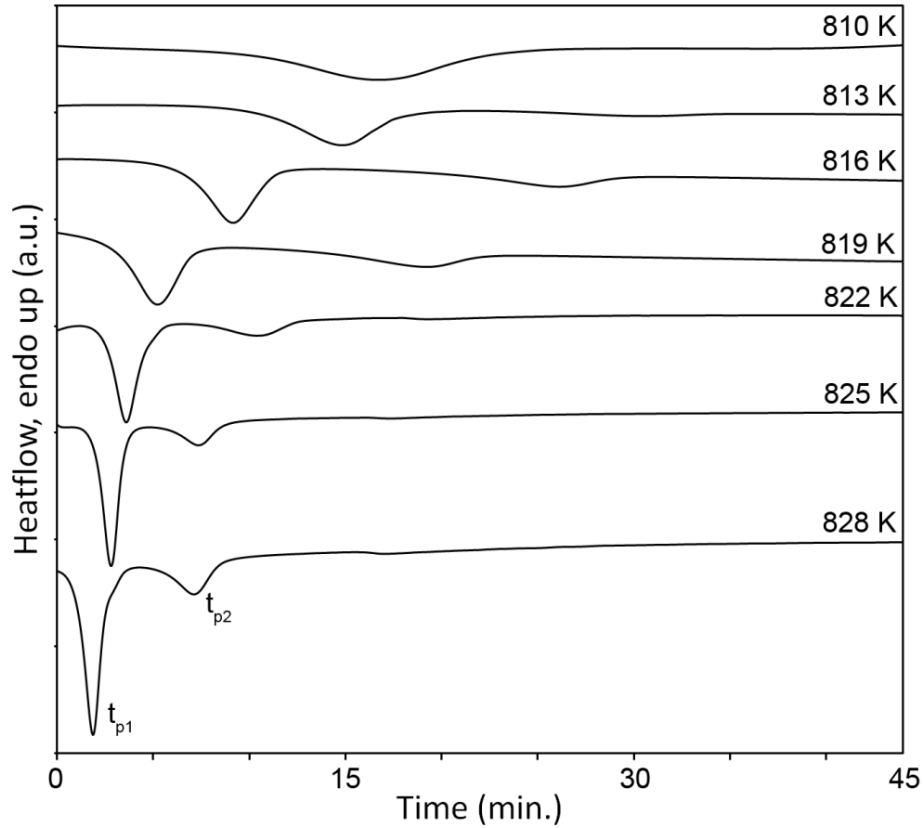


Figure 5.1.6. Isothermal anneals showing the peak shift with time as the anneal temperature is increased.

The crystallization kinetics can be studied in depth through mathematical manipulation of the isothermal annealing data (Figure 5.1.6). Isothermal experiments permit the calculation of the transformed volume fraction corresponding to a single reaction (crystallization) based on the change in crystallization enthalpy with time and anneal temperature. Figure 5.1.7 shows the sigmoidal isothermal transformation curves for Ti(Ni,Cu) crystallization at several different anneal temperatures between 810 K and 828 K obtained directly from isothermal measurements (Figure 5.1.6) according to the Equation:

$$x(t) = \frac{\int_0^t \dot{H}_l^{iso}(t') dt'}{\Delta H_l^{iso}} \quad (5.1 - 7)$$

where $x(t)$ is the transformed fraction, $\dot{H}_l^{iso}(t')$ is the measured incremental heat flow over time dt' , and ΔH_l^{iso} is the total isothermal crystallization enthalpy for primary nucleation of Ti(Ni,Cu). It should be noted that baseline subtraction and peak deconvolution were required to obtain viable results. Note also in Figure 5.1.7, that as the anneal temperature increases, the incubation time for crystallization becomes shorter, and, consequently, the transformation is completed in shorter times.

The isothermal crystallization kinetics of amorphous materials are described with classical nucleation theory by the Johnson-Mehl-Avrami (JMA) equation if one assumes constant nucleation frequency [134, 135]:

$$x(t) = 1 - \exp[(-K(t - t_0)^n)] \quad (5.1 - 8)$$

where $x(t)$ is the transformed volume fraction, t_0 is the incubation time for crystallization, n is the Avrami exponent, and K is the reaction constant. Equation 5.1-8 describes the fraction of the transformed material in an isothermal process. The reaction constant, K , is a function of annealing temperature according to the Arrhenius relationship:

$$K = K_0 \exp \left[-\frac{E_{a,i}^{iso}}{RT} \right] \quad (5.1 - 9)$$

where K_0 is a constant and $E_{a,i}^{iso}$ is the isothermal activation energy for crystallization.

The value of K and n can be obtained from:

$$\ln[\ln(1/(1 - x))] = n \ln K + n \ln(t - t_0) \quad (5.1 - 10)$$

and plotting $\ln[\ln(1/(1 - x))]$ versus $\ln(t - t_0)$ for different temperatures. The JMA plots are shown in Figure 5.1.8. The Avrami exponent n , and the reaction constant K can be extracted from the slope and intercept of the JMA plots, respectively. The results are

tabulated for the different annealing temperatures in Table 5.1.2. The Avrami exponent typically varies between 0.5 and 4 depending on the nature of the nucleation and growth mechanism [136]. The calculated Avrami exponent for this alloy ranges from 1.87-2.83, indicating that the crystallization mechanism changes as the anneal temperature is increased. For low annealing temperature ($T_{\text{ann}} = 810 \text{ K}$), $n \sim 2$, which implies constant nucleation rate with all crystallites growing from small dimensions. As the anneal temperature increases, n shifts upwards to a maximum of 2.83, implying an increase in nucleation rate with steady, diffusion-controlled growth of the initial crystalline phase from the amorphous matrix [135, 137]. The Avrami exponent is related to the mobility of atoms upon crystallization and is indicative not only of the nucleation and growth process, but also of the atomic cluster size governing glass behavior. Although this study is isolated to a single glass forming composition, it is likely that the development of atomic clusters resulting from short range atomic rearrangements preceding crystallization may increase in size due to elevated diffusion rates as anneal temperature is increased. This phenomenon, in concert with the more rapid growth of the Ti(Ni,Cu), leads to the increase in n as anneal temperature is increased.

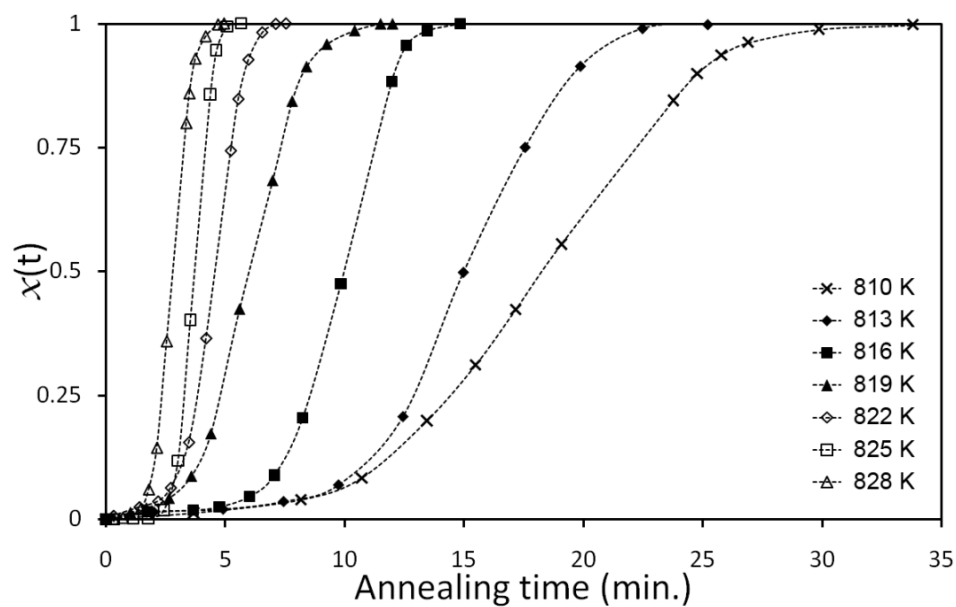


Figure 5.1.7. Isothermal transformation curves for the primary crystallization at each of the annealing temperatures.

Table 5.1.2. Kinetic parameters of $\text{Ti}_{48}\text{Ni}_{32}\text{Cu}_8\text{Si}_8\text{Sn}_4$ during isothermal annealing.

Isothermal Anneal Temperature							
	810 K	813 K	816 K	819 K	822 K	825 K	828 K
Incubation time, t_0 (min)	10.42	9.31	6.38	2.6	2.31	1.8	1.45
Avrami exponent, n	1.87	1.94	2.13	2.22	2.59	2.75	2.83
Reaction Constant, k	0.017	0.026	0.048	0.052	0.096	0.153	0.244

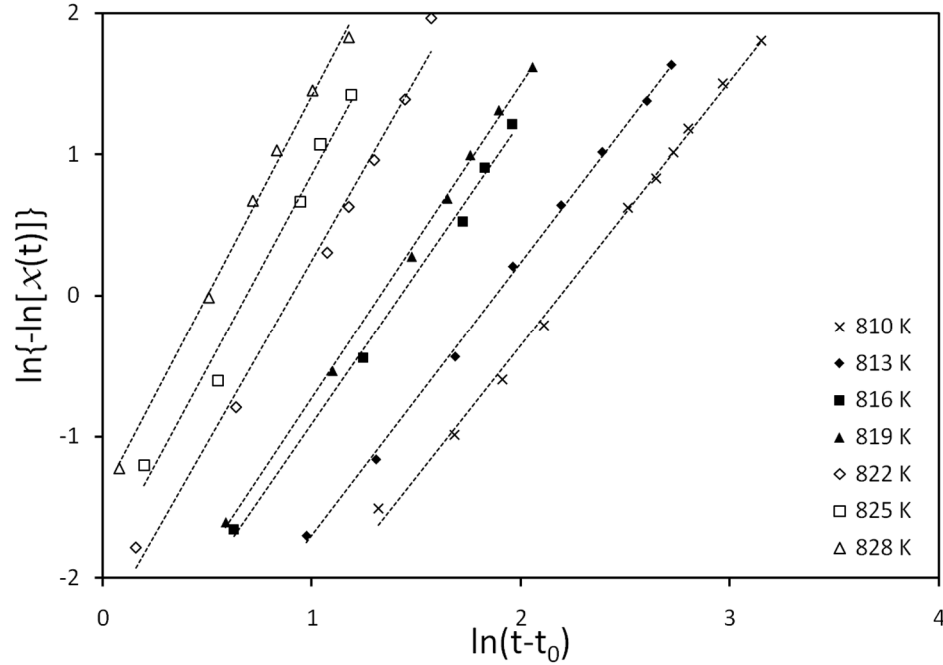


Figure 5.1.8. JMA plots for the isothermal crystallization of $\text{Ti}_{48}\text{Ni}_{32}\text{Cu}_8\text{Si}_8\text{Sn}_4$.

5.1.4 Conclusions

The $\text{Ti}_{48}\text{Ni}_{32}\text{Cu}_8\text{Si}_8\text{Sn}_4$ bulk metallic glass exhibits excellent glass forming parameters such as large supercooled liquid region, $\Delta T_x = 94.8$ K and high reduced glass transition and $T_{rg} = 0.59$, which have to this point not been observed in any non-Be, non-RE containing Ti-based metallic glasses. The liquid to glass transition exhibits VFT-type behavior, in accordance with other good glass forming alloys. The high activation energy for the initial crystalline phase suggests excellent thermal stability and resistance to crystallization. During the first exothermic transformation, the precipitation of nanocrystalline $\text{Ti}(\text{Ni,Cu})$ occurs, while at higher temperatures, Cu_3Ti nucleates out from the amorphous precursor. The kinetics of crystallization of $\text{Ti}(\text{Ni,Cu})$ were investigated by isothermal annealing experiments, wherein it was determined that nucleation and diffusion-controlled growth govern the kinetics of the primary crystalline phase.

Chapter 5, section 1 in part, is a reprint of the material accepted for publication in “Journal of Non-Crystalline Solids,” on August 31, 2009, written by Hesham E. Khalifa, Justin L. Cheney and Kenneth S. Vecchio. The dissertation author was the primary investigator and author of this paper.

5.2 High Strength $(\text{Ti}_{58}\text{Ni}_{28}\text{Cu}_8\text{Si}_4\text{Sn}_2)_{100-x}\text{Mo}_x$ nanoeutectic matrix- β -Ti dendrite BMG-derived composites with enhanced ductility and corrosion resistance

5.2.1 Abstract

BMG-derived, β -Ti stabilized, $(\text{Ti}_{58}\text{Ni}_{28}\text{Cu}_8\text{Si}_4\text{Sn}_2)_{100-x}\text{Mo}_x$ nanoeutectic matrix composites are prepared by semi-solid processing. The basis of alloy design is the very broad compositional range in which glass formation has been observed in the Ti-Ni-Cu-Si-Sn glass forming system. $(\text{Ti}_{58}\text{Ni}_{28}\text{Cu}_8\text{Si}_4\text{Sn}_2)_{94}\text{Mo}_6$ has a fracture strength in excess of 2300 MPa and 15% total strain to failure. The β -Ti stabilizing element in this study, molybdenum, is critical to maintaining a nanocrystalline matrix, because it dictates the temperature difference between constituent phases during processing. Increasing the molybdenum content also coincides with a strain hardening enhancement. A maximum strain hardening exponent, $n = 1.68$ is reported. Copious slip band formation within the β -Ti phase, and distributed across the nanoeutectic matrix, suggests that dislocation-slip is the primary deformation mechanism contributing to strain hardening in these alloys. Subsequent shear band activation ensues after the β -Ti phase hardens, resulting in enhanced composite plasticity.

5.2.2 Introduction

Nanostructured matrix-dendrite reinforced composites are emerging new materials critical to the development of advanced composites. An offshoot of research efforts toward developing BMG composites, these new materials, in fact, exceed

nanocrystalline materials, and BMG composites, in mechanical properties under certain conditions. Specifically, nanostructured matrix-dendrite reinforced composites exhibit higher strength than BMG composites, and more ductility than monolithic glasses and nanocrystalline materials[79, 138]. Much in the same way BMG composites derive their impressive properties, the high strength, but brittle nanostructured matrix is toughened by incorporating a ductile, micrometer-sized secondary or ternary phase [79, 138-141]. In order to stabilize these complex microstructures, a complete understanding of the alloy composition space, as well as precise control over solidification, are required. It is this latter requirement that connects nanostructured matrix-dendrite composites with BMG composites. Utilizing the tenets intrinsic to metallic glass formation permits the extremely slow reaction kinetics that are required for maintaining a nanocrystalline matrix while simultaneously controlling the size of a micrometer-scale, ductile dendritic phase. As would be the case in developing BMG composites, the logical first step in nanostructured matrix-dendrite reinforced composite design is the identification of a composition space with a broad glass forming region. Only the most stable glasses can maintain amorphous structure during in-situ ductile dendrite growth [81], however, a moderately stable glass is still required when the objective is to keep a nanostructured matrix, rather than a glass [79]. Only minimal destabilization of a metallic glass will result in nanocrystallization upon cooling, due to heterogeneous nucleation at the matrix-secondary phase interface. On the other hand, marginal glass formers are so unstable that the introduction of a secondary dendritic phase (and the associated composition change) will totally alter the solidification kinetics, therefore significantly altering the crystallization process, and bypassing the nanocrystalline regime. On account of the

fundamental similarities shared with BMG design and stability, these nanostructured matrix-dendrite reinforced composites are also called BMG-derived composites.

A common design methodology in BMG- derived composites is the in-situ incorporation of a b.c.c. (body centered cubic) phase. This strategy has been employed in Ti- [142], Zr- [81, 143], Cu- [144] , Fe- [79] and Mg- [145] based systems. Titanium alloys are superior by comparison, on account of their high corrosion resistance [146, 147], and low density, while still maintaining similar mechanical properties to the other aforementioned alloy systems. The presence of these b.c.c. dendrites has been credited with the enhanced ductility observed in BMG-derived composites [138, 139, 142]. The b.c.c phase serves to arrest, deflect and retard the rapid propagation of shear bands, in effect, delocalizing the strain instabilities commonly associated with brittle failure in metallic glasses [5, 148].

The b.c.c. phase utilized in BMG-derived composite design for Ti-, Zr- and Cu-based [81, 142, 144] systems has been a β -Ti based phase. β -Ti is the common choice because it is known to exhibit significant ductility and lower modulus compared with its parent glasses than α -Ti [149], and of course because titanium is a common component in these composites. β -Ti is metastable at room temperature, and therefore requires certain alloying elements to be added to the parent alloys in order to stabilize the β -Ti phase. Vanadium, niobium, and tantalum are known isomorphous β -Ti stabilizers [149], which have been used in the development of toughened Ti-, Zr-, and Cu-based BMG composites, respectively. Molybdenum is another strong, isomorphous β -Ti stabilizer [149], which to date has not been employed in the development of β -Ti stabilized, BMG-

derived composites. The eutectoid β -Ti stabilizer, iron, has also been used to develop nanoeutectic matrix composites in the Ti-Fe-Sn system [138]. A summary of common alloying elements use in titanium alloys is given in Figure 5.2.1.

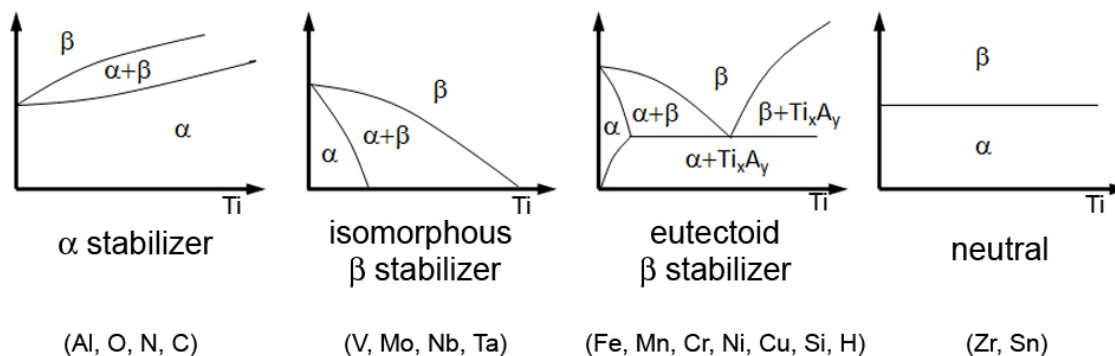


Figure 5.2.1. Schematic illustration of effect of alloying elements on phase diagrams of titanium alloys [149].

In this investigation, a Ti-Ni-Cu-Sn-Si glass forming system [150] is utilized in the development of a molybdenum-containing, β -Ti stabilized, nanoeutectic matrix-ductile dendrite reinforced, BMG-derived composite. This alloy is different from other Ti-based alloy systems in that it contains significantly more Ni than previously reported Ti-based BMG-derived composites, and also contains Si, both of which play a vital role in retarding crystallization kinetics. The glass from which this composite is based demonstrates a broad glass forming composition space and slow reaction kinetics, which, when coupled with the molybdenum containing, b.c.c. β -Ti phase, results in a very high strength, low modulus composite material with 15% total strain to failure.

5.2.3 Results and Discussion

Alloy Design

Composites were based off the Ti-Ni-Cu-Si-Sn glass forming system. A comprehensive discussion of the glass modeling and design, as well as a full report on all glass forming compositions in this system, is described by Cheney [150]. The liquidus profile shown in Figure 5.2.2 highlights the broad glass forming composition space of this alloy. A maximum SCLR (supercooled liquid region) in excess of 92 K has been reported for $\text{Ti}_{48}\text{Ni}_{32}\text{Cu}_8\text{Si}_8\text{Sn}_4$ [150]. The SCLR drops off as the composition departs from the best glass forming composition (denoted by an “X” in Figure 1), but the boundaries of the glass forming region highlighted in the liquidus profile still represent alloys with a minimum SCLR of 40K. Despite this vast glass forming composition space, the significant dependence of SCLR on composition is in sharp contrast to the very stable Zr-based glass formers, in which large SCLR exists independent of composition [5]. Nonetheless, the ability of this Ti-Ni-Cu-Si-Sn system to maintain amorphous structure despite significant compositional variation, provides a template from which amorphous and nanostructured advanced composites can be designed on account of the relative stability of the supercooled liquid.

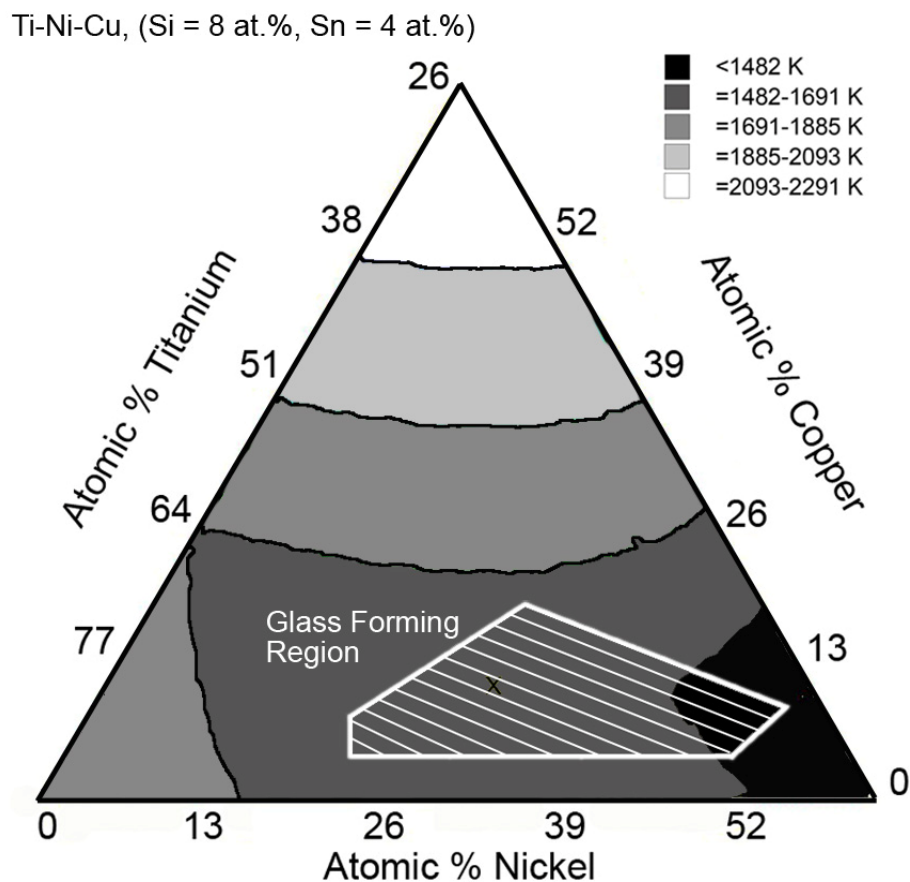


Figure 5.2.2. Ti-Ni-Cu liquidus profile with Si and Sn content held constant at 8 and 4 atomic %, respectively. White lines encompass broad glass forming compositional region. "X" denotes best glass forming composition. Temperatures in legend are equilibrium liquidus temperatures calculated using THERMOCALC [150].

With a prospective glass in place, the next step in BMG-derived composite design is stabilizing and growing the b.c.c. phase. Molybdenum is a strong β -Ti stabilizer, but has not been used in BMG-derived composites to date on account of its high melting temperature and relatively low solubility in titanium [151]. Careful pre-alloying steps were taken to ensure full dissolution of the molybdenum into the alloy. Additionally, the composition space was shifted toward higher titanium content in an effort to promote β -Ti formation while still maintaining appropriate glass forming stoichiometry with the

remaining elements. Compared to the monolithic glass, $\text{Ti}_{48}\text{Ni}_{32}\text{Cu}_8\text{Si}_8\text{Sn}_4$, significantly lower silicon was used in the composites due to its partitioning entirely into the matrix, and its propensity to form titanium silicides when present in higher concentrations. In general, all of the constituents in the alloy were adjusted with the goal of simplifying the crystallization of the alloy. Initial attempts resulted in more complex microstructural landscapes consisting of up to 5 different phases. The b.c.c. microstructure was coarsened via semi-solid processing [142]; a process wherein the volume fraction, morphology, and size of the dendrites may be controlled by heating into the semi-solid, two-phase region between the liquidus temperature of the metastable glass, and the solidus temperature of the b.c.c. phase, holding it isothermally for several seconds, and then quenching it to rapidly solidify the molten glass. The high melting temperature of the base glass necessitated the use of molybdenum to stabilize the b.c.c. phase, because it created the largest difference between the liquidus temperatures of the glass and b.c.c. phase. The preferential partitioning of the molybdenum almost entirely into the b.c.c. phase results in a significant increase in the β -Ti melting temperature up to 1428K; more than 100K higher than the monolithic glass, which has $T_l=1319\text{K}$. Although several other β -Ti stabilizing elements have been utilized to date, in various glass forming systems, little attention has been paid to what other roles that β -Ti stabilizing element plays. This is the first study where the β -Ti stabilizer was chosen out of necessity, for the purposed of improving semi-solid processability.

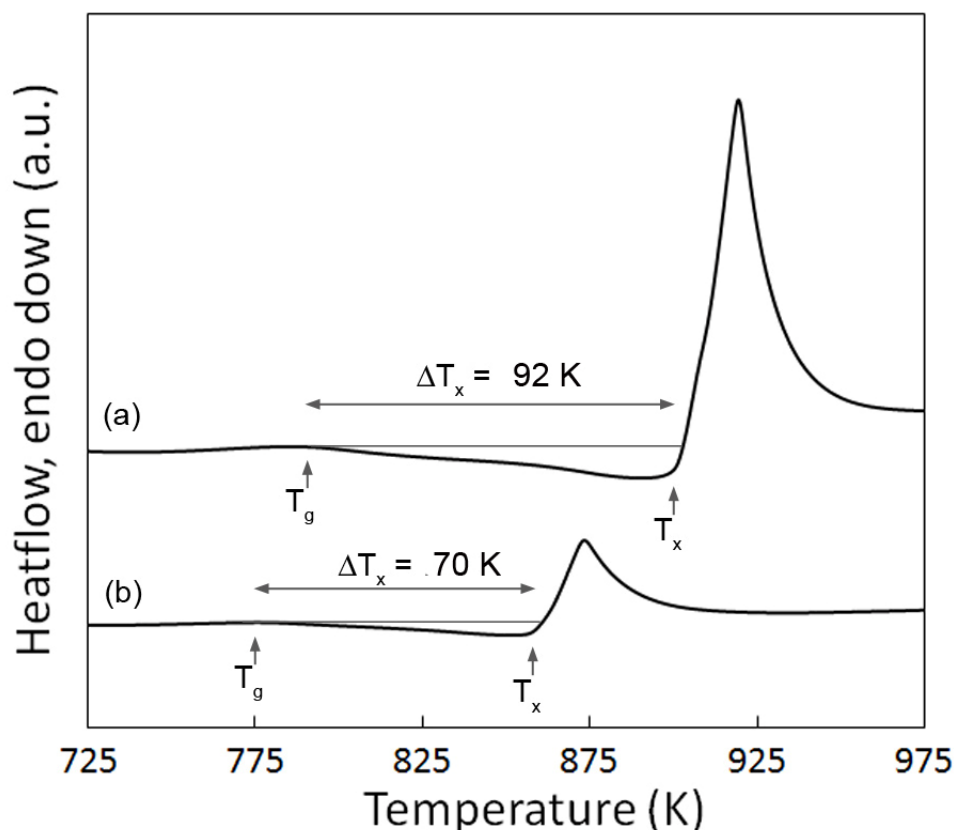


Figure 5.2.3. DSC traces of (a) the monolithic glass $\text{Ti}_{48}\text{Ni}_{32}\text{Cu}_8\text{Si}_8\text{Sn}_4$, and (b) the splat-quenched, metallic glass matrix composite, $(\text{Ti}_{58}\text{Ni}_{28}\text{Cu}_8\text{Si}_4\text{Sn}_2)_{94}\text{Mo}_6$.

Although this system forms glasses over a broad compositional spectrum, the glass simply isn't stable enough to maintain amorphous structure during the coarsening of the β -Ti phase in bulk form. The destabilized glass forming melt solidifies into a 2 phase nanoeutectic matrix. When cooled more rapidly, into a splat quenched foil, however, amorphous character was maintained, but with a much finer scale β -Ti phase. The DSC traces of the monolithic glass, $\text{Ti}_{48}\text{Ni}_{32}\text{Cu}_8\text{Si}_8\text{Sn}_4$, and a splat quenched foil of the composite, $(\text{Ti}_{58}\text{Ni}_{28}\text{Cu}_8\text{Si}_4\text{Sn}_2)_{94}\text{Mo}_6$, are shown in Figure 5.2.3. Notice that the composite exhibits a clearly defined glass transition at a lower temperature, as well as a smaller SCLR, indicating that a different glass composition from the parent glass from

which these alloys are based, has formed. The smaller magnitude of the crystallization peak for the splat-quenched composite is a result of the smaller volume fraction of glass present in the composite compared with the monolithic glass. The glass matrix in the splat-quenched composite was determined to have the composition $\text{Ti}_{52}\text{Ni}_{30}\text{Cu}_7\text{Si}_7\text{Sn}_3\text{Mo}_1$. The β -Ti microstructure in the splat-quenched foil was too small to be observed in SEM. Validation of its presence in the thin foil comes exclusively from the XRD spectrum presented in Figure 5.2.5.

The microstructure of the semi-solidly processed $(\text{Ti}_{58}\text{Ni}_{28}\text{Cu}_8\text{Si}_4\text{Sn}_2)_{94}\text{Mo}_6$ is shown in Figure 5.2.4. The 5-10 micrometer scale β -Ti phase occupies 66% of the alloy by volume. The molybdenum partitions almost entirely into the β -Ti phase, which had a composition of $\text{Ti}_{56}\text{Ni}_{20}\text{Cu}_9\text{Si}_3\text{Sn}_1\text{Mo}_{11}$. The light phase in the matrix is the eutectic $\text{Ti}_{55}\text{Ni}_{35.5}\text{Sn}_8\text{Mo}_{1.5}$, and represents 20% of the alloy by volume, while the remaining 14% of the alloy is the dark phase in the matrix, Ti_2Cu , with 1-2 at.% Si dissolved in it. It was determined, via XRD analysis (Figure 5.2.5), that the Ti-Ni-Sn-Mo phase is actually an α -Ti solid solution; α -Ti(Ni, Sn, Mo). As x is changed in $(\text{Ti}_{58}\text{Ni}_{28}\text{Cu}_8\text{Si}_4\text{Sn}_2)_{100-x}\text{Mo}_x$, the molybdenum content in the β -Ti phase varies only slightly. However, the volume fraction of β -Ti jumps from 57, to 66, to 74% when $x=4, 6$, and 8 at. %, respectively. It should be noted that the morphology of the constituent phases does not change significantly when molybdenum is varied between 4 and 8 at. %.

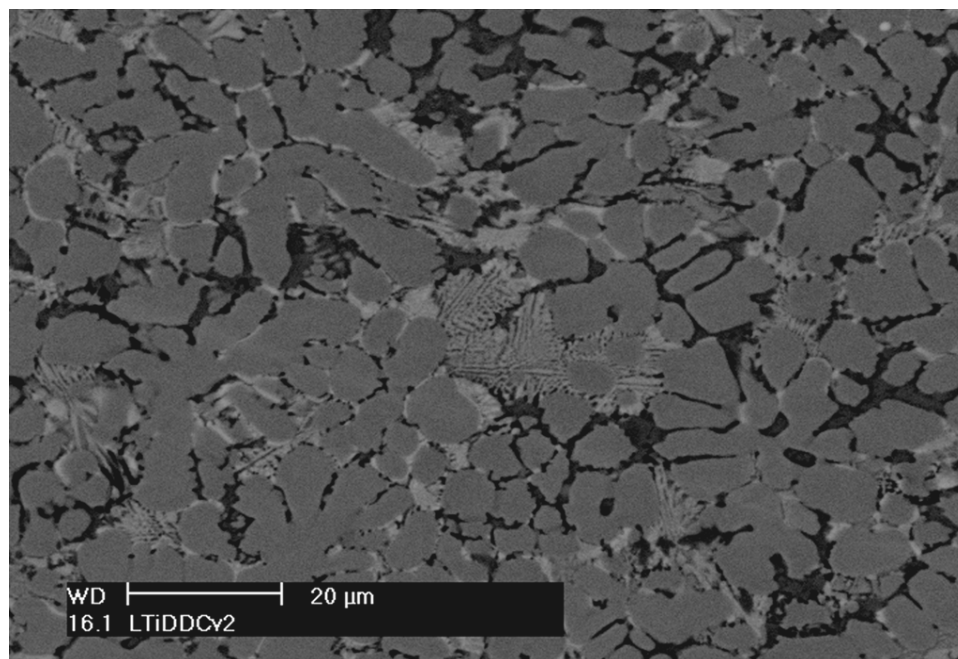


Figure 5.2.4. Backscattered electron image of semi-solidly processed $(\text{Ti}_{58}\text{Ni}_{28}\text{Cu}_8\text{Si}_4\text{Sn}_2)_{94}\text{Mo}_6$.

XRD spectra for the monolithic glass $\text{Ti}_{48}\text{Ni}_{32}\text{Cu}_8\text{Si}_8\text{Sn}_4$, as well as the BMG-derived composite, $(\text{Ti}_{58}\text{Ni}_{28}\text{Cu}_8\text{Si}_4\text{Sn}_2)_{94}\text{Mo}_6$ are presented in Figure 5.2.5. Three separate spectra for $(\text{Ti}_{58}\text{Ni}_{28}\text{Cu}_8\text{Si}_4\text{Sn}_2)_{94}\text{Mo}_6$ are shown, corresponding to three separate microstructural states, resulting from different cooling rates. The splat-quenched foil retains an amorphous matrix in the presence of β -Ti. The semi-solidly processed alloy shows 4 of the b.c.c. signature peaks within the scan range, indicative of more extensive β -Ti nucleation compared to the splat-quenched sample. However, very small peaks corresponding to the nanocrystalline phases can also be observed. In the spectrum for the slow cooled ingot, the same β -Ti signature can still be observed, however the α -Ti(Ni,Sn,Mo) and Ti_2Cu peaks are much more prominent, because the slower cooling results in coarser microstructure of the matrix phases. Analysis of the slow cooled ingot

was a necessary measure for phase identification. Similar results have been observed in other Ti-Ni-Cu-Sn systems [152, 153].

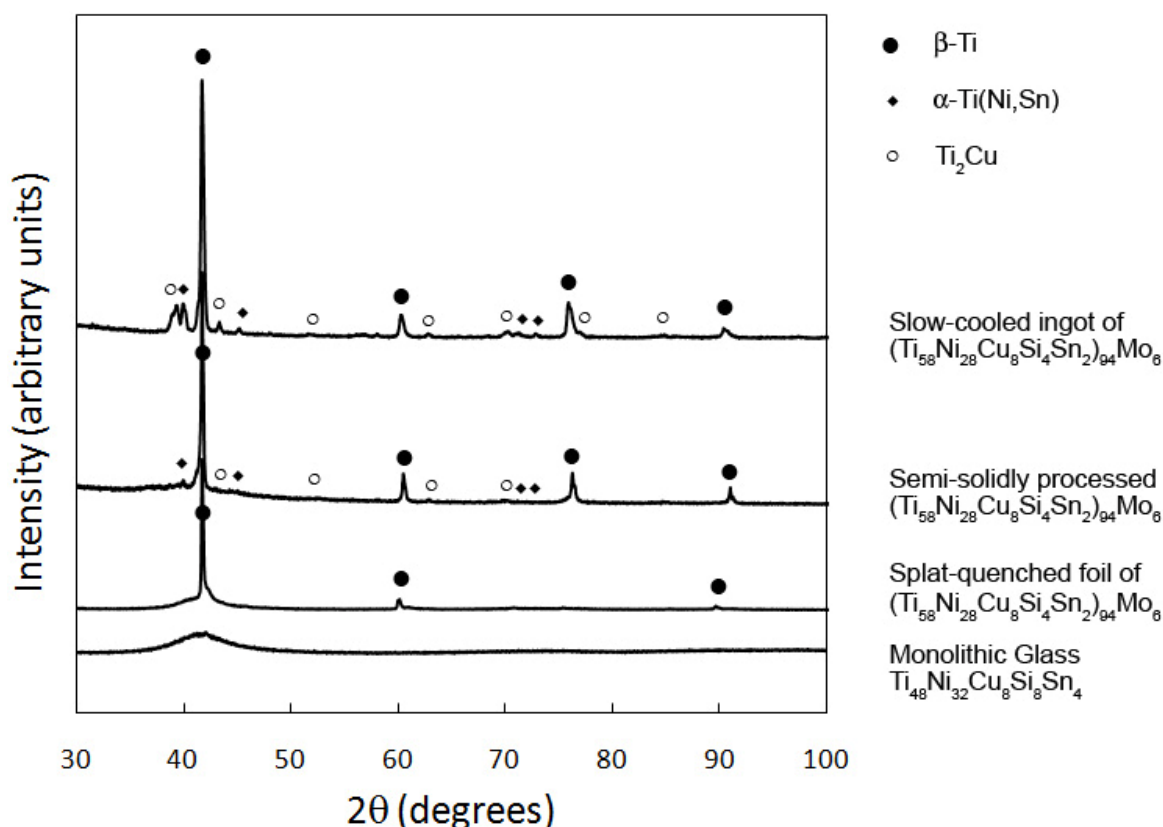


Figure 5.2.5. XRD spectra showing various crystalline phases in $(\text{Ti}_{58}\text{Ni}_{28}\text{Cu}_8\text{Si}_4\text{Sn}_2)_{94}\text{Mo}_6$ BMG-derived composite.

Mechanical Properties

The results of compression tests on $(\text{Ti}_{58}\text{Ni}_{28}\text{Cu}_8\text{Si}_4\text{Sn}_2)_{100-x}\text{Mo}_x$ where $x = 4, 6$, and 8 at. %, are shown in Figure 5.2.6. The molybdenum content plays a critical role in many facets of the mechanical behavior. The range in molybdenum controls the relative volume fraction of β -Ti phase, which subsequently dictates the elastic modulus of the material according to a simple rule of mixtures. As the amount of molybdenum in the alloy increases, so too does the volume fraction of the β -Ti phase, resulting in a decrease in the elastic modulus of the overall composite. The yield strength also decreases with

increasing molybdenum content, on account of the low strength of the β -Ti dendrites. However, the total strain to failure is maximized at the intermediate molybdenum content of 6 at. %, where a total strain of 14.84% was observed. After yielding, the flow stress continues to increase up until failure. Larger total strain to failure resulted in higher failure stress. Each of the three alloys presented in this study exhibit compressive fracture strength in excess of 2000 MPa. The mechanical properties are listed in Table 5.2.1.

Table 5.2.1. Mechanical Properties of $(\text{Ti}_{58}\text{Ni}_{28}\text{Cu}_8\text{Si}_4\text{Sn}_2)_{100-x}\text{Mo}_x$

Mechanical Properties of $(\text{Ti}_{58}\text{Ni}_{28}\text{Cu}_8\text{Si}_4\text{Sn}_2)_{100-x}\text{Mo}_x$						
x (at. %)	E (GPa)	σ_y (MPa)	σ_{\max} (MPa)	ϵ_y (%)	ϵ_{tot} (%)	ρ (g/cm³)
4	105.3	1306	2003	2.88	8.31	6.31
6	98.7	1134	2372	2.66	14.84	6.54
8	91.4	996	2231	2.52	11.95	6.70

In order to evaluate the strain hardening exponent (n) in these alloys, a plot of $\ln(\sigma_t)$ vs $\ln(\epsilon_t)$ is presented in the inset of Figure 5.2.6. A dependence of the work hardening exponent on molybdenum content is observed in this alloy system. Though all three alloys demonstrate significant work hardening behavior, more enhanced work hardening coincides with increased molybdenum content. The use of molybdenum in these alloys resulted in a maximum strain hardening exponent of $n = 1.68$ for the alloy $(\text{Ti}_{58}\text{Ni}_{28}\text{Cu}_8\text{Si}_4\text{Sn}_2)_{92}\text{Mo}_8$. Previous reports of the strain hardening exponent in b.c.c. reinforced nanostructured matrix composites quoted strain hardening values of only $n \sim 0.7$ in $\text{Zr}_{73.5}\text{Nb}_9\text{Cu}_7\text{Ni}_1\text{Al}_{9.5}$ [154]. A Ti-Fe-Sn nanoeutectic composite, reinforced with hexagonal Ti_3Sn has a reported strain hardening exponent of $n = 1.64$ [138]. The large

strain hardening exponent in $(\text{Ti}_{58}\text{Ni}_{28}\text{Cu}_8\text{Si}_4\text{Sn}_2)_{92}\text{Mo}_8$ is the highest reported to date in any BMG-derived composite.

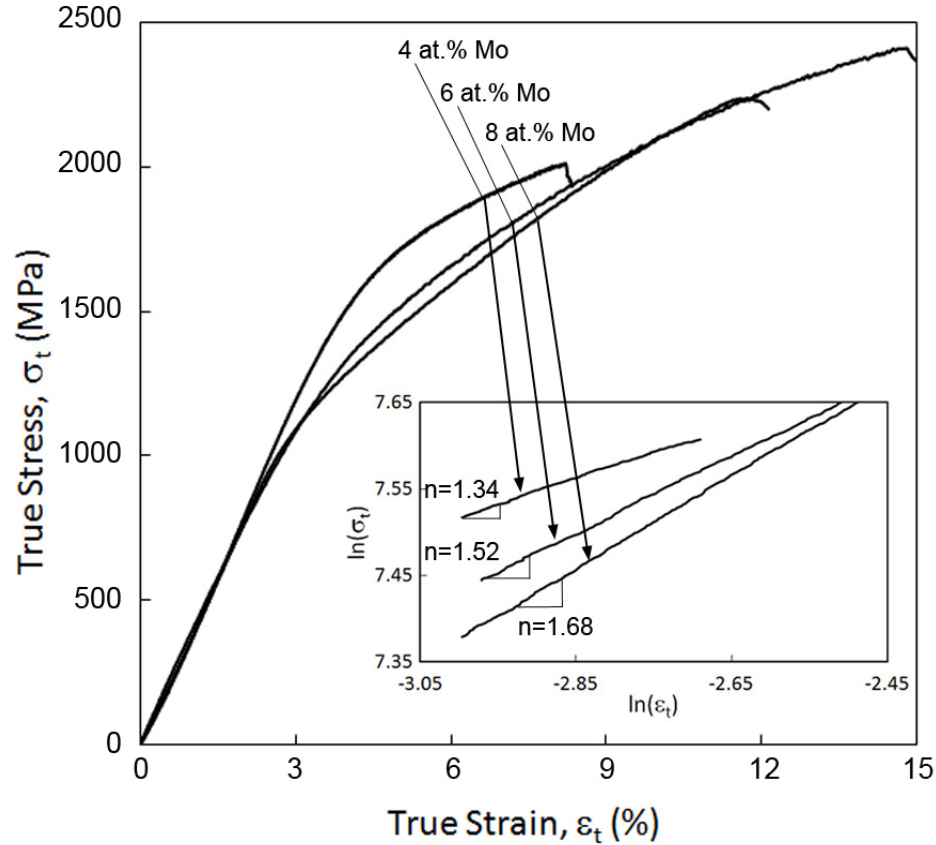


Figure 5.2.6. True stress-True strain curves for $(\text{Ti}_{58}\text{Ni}_{28}\text{Cu}_8\text{Si}_4\text{Sn}_2)_{100-x}\text{Mo}_x$ at $x = 4, 6$, and 8 at. %. Inset shows strain hardening exponent dependence on molybdenum content.

The β -Ti phase is primarily responsible for work hardening in these alloys.

Therefore, the molybdenum content also is directly related to the strain hardening of the overall alloy. This increase in the molybdenum content is responsible for the strain hardening enhancement as x is increased in $(\text{Ti}_{58}\text{Ni}_{28}\text{Cu}_8\text{Si}_4\text{Sn}_2)_{100-x}\text{Mo}_x$, simply because a greater overall fraction of the alloy can accommodate strain via slip band formation and the associated work hardening behavior observed in the β -Ti phase. If $x > 8$ at. % though, it exceeds its saturation limit in the b.c.c phase and alters the nanocrystalline matrix,

resulting in brittle failure with minimal plastic strain. Due to the low solubility of molybdenum in titanium, there is a threshold beyond which no further molybdenum can be accommodated within the β -Ti phase. This limit was determined to be about 12.5 at. %. Beyond this threshold, excess molybdenum results in the formation of a brittle boundary phase between the β -Ti phase and the nanocrystalline matrix, which ultimately inhibits plasticity.

Prior to compression testing, the surfaces of each sample were polished such that the deformation mechanisms could be investigated after testing. Figure 5.2.7 is indicative of the overall features of deformation in this alloy system, after sample failure. The white arrows point to very fine slip bands ($\sim 0.5 \mu\text{m}$ spacing). Copious slip traces are apparent across the sample surface in Figure 5.2.7. Figure 5.2.8 demonstrates the very ductile fracture surface observed in $(\text{Ti}_{58}\text{Ni}_{28}\text{Cu}_8\text{Si}_4\text{Sn}_2)_{94}\text{Mo}_6$, as well as regions of profuse slip occurring within the sample and at the fracture surface. Furthermore, these bands exhibit no preferred orientation in the sample, relative to the load axis. With few exceptions, these slip bands are restricted to within the β -Ti dendrites. In some instances in Figure 5.2.7 though, slip bands can be seen passing from one dendrite to another, across the nanoeutectic matrix. The copious formation of slip bands resulting from dislocation movement and multiplication within the low strength dendrites, as well as the dislocation-slip transfer across the multiphase landscape, are the predominant mechanisms for strain hardening in these alloys. Similar strain hardening behavior has been described in other Ti-based BMG-derived composites [153].

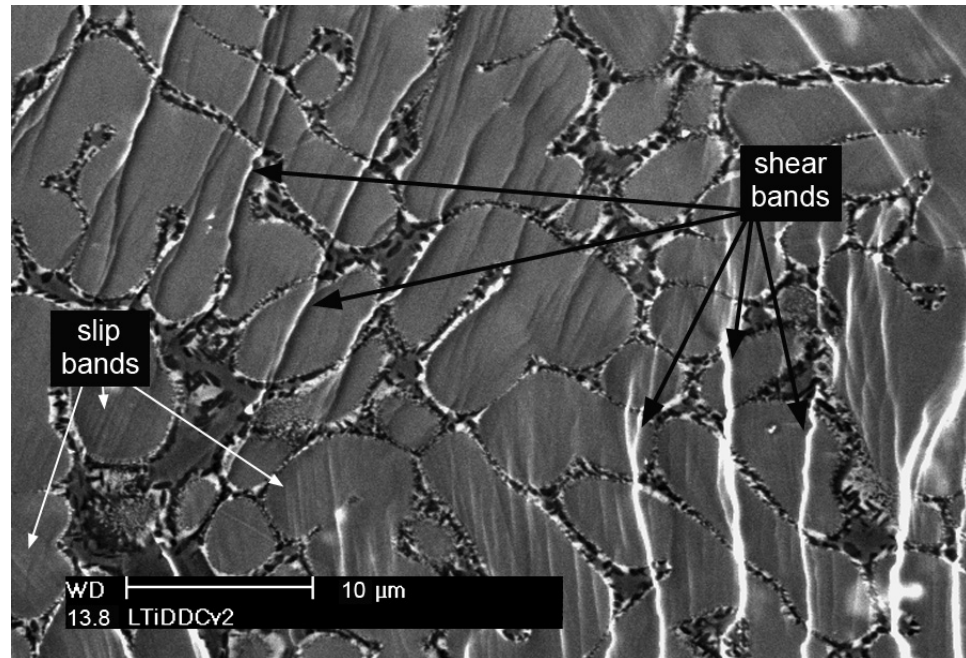


Figure 5.2.7. Features of the compressive deformation in $(\text{Ti}_{58}\text{Ni}_{28}\text{Cu}_8\text{Si}_4\text{Sn}_2)_{94}\text{Mo}_6$. White arrows indicate profuse slip within the dendrites, while black arrows indicate shear bands nucleating at the dendrite-nanoeutectic matrix interface, and propagating across the multiphase microstructure.

The black arrows in Figure 5.2.7 indicate shear bands on the deformed sample surface. In this particular figure, there are several sets of shear bands. Each domain of shear bands contains parallel shear bands with $\sim 5 \mu\text{m}$ spacing. However the different shear band domains are propagating along different trajectories. This phenomenon is likely due to the fact that new shear band nucleation is related to the degree of work hardening in nearby dendrites. The strengthening effect of profuse slip formation in the dendrites facilitates the nucleation of shear bands at the dendrite-matrix interface.

Notice that the contrast of the shear bands is markedly different than the slip bands. The differing contrast between shear and slip bands is related to the varying displacement caused by the two deformation features. The amount of shear off-set and the associated strain relief is more significant in shear bands than in slip bands. Shear

bands propagate through both the matrix and dendrites, however, interfacial deflection effects can be seen when a shear band passes from the matrix into a β -Ti dendrite. A TEM study of the stepped morphology generated by a passing shear band at the b.c.c. dendrite-nanoeutectic matrix interface in a $\text{Ti}_{66.1}\text{Cu}_8\text{Ni}_{4.8}\text{Sn}_{7.2}\text{Nb}_{13.9}$ alloy with similar matrix phases (α -Ti and Ti_2Cu) explains these interfacial deflection effects in detail [155]. The large off-set at the dendrite-matrix interface is the result of secondary shear bands arresting at the interface and primary shear bands penetrating into the dendrites. The complex interfacial strain accommodation associated with these two phenomena leads to enhanced ductility. The bright fringes surrounding some of the dendrites in Figure 5.2.7 are shear off-sets exhibiting displacement similar in magnitude to the shear bands. These interfacial shear off-sets provide microscopic evidence of the nanoscale shear-stepping mechanism contributing to enhanced ductility in nanoeutectic matrix, BMG-derived composites.

Given that two distinctly different mechanisms for strain accommodation are present in the sample, and that one resides entirely in the b.c.c. phase (dislocation-slip), while the other passes from dendrite to matrix with little preference (shear band formation), the overall strain distribution can be described as inhomogenous; deformation originates via dislocation movement and slip band formation within the β -Ti phase, and subsequently progresses to shear banding such that strain accommodation is distributed into the nanoeutectic matrix as well. Given that the strain hardening remains constant throughout the deformation, it is likely that even after shear band formation begins, dislocation multiplication and slip band formation within the dendrites continues.

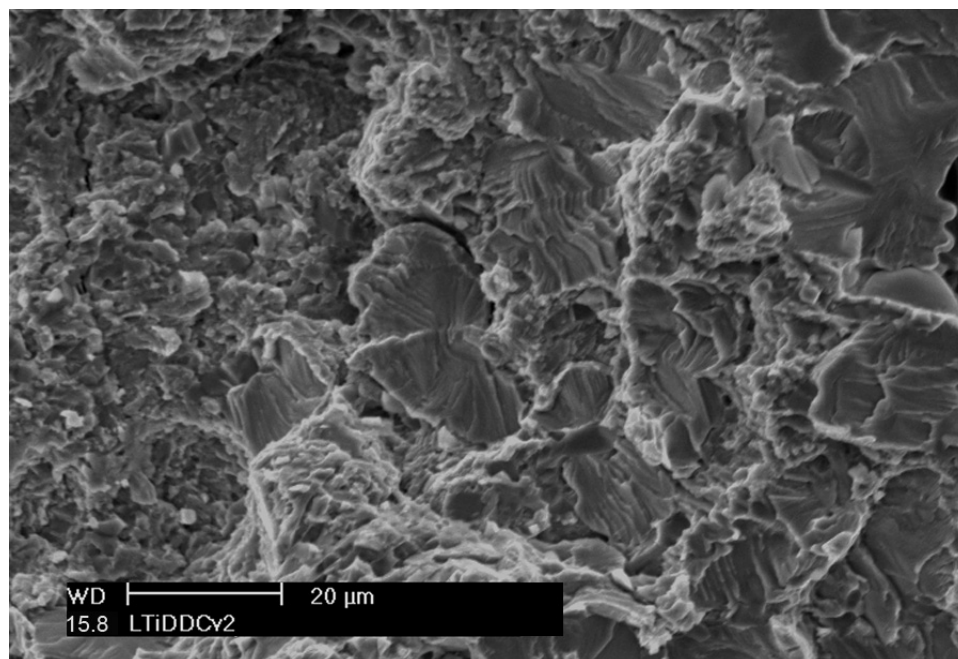


Figure 5.2.8. Ductile fracture of $(\text{Ti}_{58}\text{Ni}_{28}\text{Cu}_8\text{Si}_4\text{Sn}_2)_{94}\text{Mo}_6$ exhibiting copious intra-dendritic slip in nearly every β -Ti dendrite.

Corrosion Behavior

Conventional titanium alloys exhibit excellent resistance to general corrosion in most environments due to the formation of a TiO_2 passivation layer on its surface. A passivation layer forms in most oxidizing environments, for example in salt solutions like chlorides and sulfates, as well as in nitric acid, resulting in excellent corrosion resistance [156]. In reducing environments, such as hydrochloric acid, however, the corrosion resistance of titanium alloys is not good because HCl breaks down the oxide passivation layer and attacks the metallic titanium. The addition of nickel and molybdenum improve the corrosion resistance in reducing environments in β -titanium alloys [147], providing yet another incentive to use molybdenum as the β -Ti stabilizer in this alloy system. Corrosion tests were performed on $(\text{Ti}_{58}\text{Ni}_{28}\text{Cu}_8\text{Si}_4\text{Sn}_2)_{94}\text{Mo}_6$ in sea water, 1 M HCl , and

3 M HCl for a duration of 120 hours at room temperature. The corrosion rate was calculated according to the Equation,

$$R = \frac{8.76 \times 10^7 \times (m_o - m_f)}{s \rho t} \quad (5.2 - 1)$$

where m_o and m_f are the initial and final mass in grams, s is the total surface area in cm^2 , $\rho = 6542 \text{ kg/m}^3$ is the density (Table 1), and $t = 120 \text{ h}$ is the duration of the corrosion test.

(Ti₅₈Ni₂₈Cu₈Si₄Sn₂)₉₄Mo₆ demonstrates excellent corrosion resistance, in both oxidizing and reducing environments. The alloys maintain a lustrous finish after 120 hours in both sea water and 1 M HCl at room temperature. In sea water, the sample gained 0.3 mg due to the formation of a surface oxide film. The presence of oxygen on the sample surface was verified via EDS after completion of the corrosion test. As expected, passivation makes these alloys very stable in oxidizing environments. Furthermore, no detectable mass-loss was observed in 1 M HCl tests, suggesting exceptional corrosion resistance in weak reducing environments, as well. Increasing the concentration to 3 M HCl resulted in a 0.6 mg ($m_o = 1.6429 \text{ g}$, $m_f = 1.6423 \text{ g}$) mass-loss after 120 hours, giving a corrosion rate of only 20.4 $\mu\text{m/yr}$. Examination of the sample surface after corrosion testing revealed only general corrosion. No pitting, and only minimal surface damage resulted from exposure to the corrosive environment. Preferential corrosion could be observed within the matrix in the Ti₂Cu phase. The nickel in the α -Ti(Ni,Sn,Mo), and the molybdenum together with nickel in the β -Ti phase led to enhanced corrosion resistance in those two phases, respectively. Given the significantly more aggressive reducing environment provided by the 3 M HCl solution,

$(\text{Ti}_{58}\text{Ni}_{28}\text{Cu}_8\text{Si}_4\text{Sn}_2)_{94}\text{Mo}_6$ demonstrates remarkable corrosion resistance when compared with conventional titanium alloys [157], monolithic BMGs [158, 159], and other BMG-derived composites [79].

5.2.4 Conclusions

The incorporation of a low strength β -Ti phase into a high strength nanoeutectic matrix greatly enhances the compressive strain to failure of $(\text{Ti}_{58}\text{Ni}_{28}\text{Cu}_8\text{Si}_4\text{Sn}_2)_{100-x}\text{Mo}_x$ Ti-based BMG-derived composites, compared with the parent glass from which the alloys were based. A maximum compressive strength of 2372 MPa after 14.84% total strain was observed in $(\text{Ti}_{58}\text{Ni}_{28}\text{Cu}_8\text{Si}_4\text{Sn}_2)_{94}\text{Mo}_6$. The choice of molybdenum as the β -Ti stabilizing constituent was critical for raising the melting temperature of the β -Ti phase, thus widening the gap between the melt temperature of the BMG derived matrix, and the b.c.c. phase, and ultimately facilitating semi-solid processing. Furthermore, enhanced strain hardening was correlated to increasing the molybdenum content in the alloy. Dislocation-slip generated by deformation of the low strength b.c.c. β -Ti phase is the prevailing deformation mechanism contributing to the hardening of these high strength BMG-derived composites. Following slip band formation, the activation of a high density of shear bands also plays a significant role in ductility enhancement in this alloy system. The hardening of the b.c.c. dendrites with increasing load facilitates the nucleation of new shear bands. Lastly, the presence of high nickel levels, in addition to molybdenum in this alloy system, result in exceptional corrosion resistance in reducing environments.

Chapter 5, section 2 in part, is a reprint of the material as it appears in Advanced Engineering Materials Volume 11, 2009, Page 885, written by Hesham E. Khalifa and Kenneth S. Vecchio. The dissertation author was the primary investigator and author of this paper.

5.3 Development of tough Ti-based bulk metallic glass matrix composites without the use of beryllium

5.3.1 Abstract

An amorphous matrix composite reinforced with a ductile b.c.c., β -Ti phase is presented. The microstructure has been precisely tuned to match the mechanical length scales governing deformation. Microstructural control was facilitated by semi-solid forging; a novel process wherein an alloy's microstructure can be coarsened and homogenized. The featured alloy of this study, $\text{Ti}_{51.4}\text{Ni}_{42.4}\text{Si}_{3.9}\text{Mo}_{2.3}$, exhibits compressive fracture strength of 2.4 GPa and 30% compressive strain, tensile ductility of 3.5%, and enhanced fracture toughness of $39 \text{ MPa}\cdot\text{m}^{1/2}$. This is the first observation of tensile ductility in a non-beryllium containing Ti-based amorphous matrix composite, and the fracture toughness represents a nearly 400% increase over the parent glass. The enhancement of the mechanical properties is attributed to the confinement of shear band extension resulting from an optimally tuned microstructural length scale.

5.3.2 Introduction

The high strength of metallic glasses has garnered significant research interest for many years, yet has been tempered by the extreme brittle failure of monolithic glasses. More recently, investigations of BMG-derived composites have aimed at overcoming the brittle failure of these glasses through incorporation of secondary phases. The development of advanced materials has always boiled down to increasing ductility at the expense of strength, or vice versa. The use of β -Ti stabilizers as a low modulus, ductile reinforcement of the glassy matrix has yielded tough BMG composites. To date, these

two-phase ductile, BMG composites have only been reported in the extremely stable BMG systems Zr-Ti-Cu-Be-Nb [81], and Ti-Zr-Cu-Be-V [142]. In both cases, the use of large amounts of the expensive element, Zr, as well as the very expensive and potentially toxic element, Be, are necessary to retain amorphous structure in the alloy. These two elements are imperative for depressing the liquidus temperature, and retarding the kinetics of the alloy melt, thus enabling BMG formation. A BMG composite exhibiting tensile ductility has also been discovered in the La-Al-Cu-Ni system [160], however the predominant element in this system, La (~70 at. %), is also very expensive.

This work presents a new BMG composite with a fully amorphous matrix, in the low cost alloy system, Ti-Ni-Si-Mo, which has been reinforced with a Mo-stabilized β - Ti phase that imparts global plasticity, tensile ductility, and enhanced fracture toughness to the overall composite by constraining shear band propagation, such that deformation is delocalized.

In bending, plasticity is greatly enhanced when the characteristic dimension, R_P , of the crack tip's plastic zone exceeds $\sim D/2$ [161], where D is the sample thickness, and R_P is a material length scale related to fracture toughness according to:

$$R_P \approx (1/2\pi)(K_{IC}/\sigma_y)^2 \quad (5.3-1)$$

R_P is associated with the maximum spatial extension of shear bands originating at the crack tip; it is related to the maximum allowable shear off-set along the shear band.

K_{IC} is the fracture toughness for a mode one crack, and σ_y is the yield stress [162, 163].

R_P ranges from $\sim 1\mu\text{m}$ to $\sim 500\mu\text{m}$ on going from brittle to tough BMGs [119]. A Pt-based BMG with $R_P \sim 500\mu\text{m}$ exhibited significant plastic bending strain, yet tensile

ductility of less than 1% strain [65]. The reason for this unlikely result is due in part to the fact that there are compressive and tensile states during bending. Under compression, an operating shear band is subject to a normal stress that results in frictional and closing forces that both arrest shear band propagation and activate new shear bands in the glass. Tension, though, is an unconfined stress state in which the shear bands are subject to opening stresses that enhance strain softening. Frictional forces are absent in this case, and a propagating shear band lengthens until cavitation occurs within a slipping shear band, resulting in a crack [164].

In order to promote tensile ductility and enhanced fracture toughness, a means to limit shear band extension during unconfined loading is required. Microstructurally induced shear band stabilization mechanisms can be achieved by introducing inhomogeneities in elastic or plastic material properties at a microstructural length scale, S [81, 82]. In essence, a composite can be designed in which shear bands initiate in the amorphous matrix but get arrested by surrounding regions of low shear modulus, ductile material. Stabilization requires that $S \approx R_p$, where S refers to the spacing between adjacent ductile dendrites occupied by the amorphous matrix.

Cooling rate variations within arc-melted ingots and suction cast rods of previous BMG matrix composites resulted in a large variation in inter-dendrite spacings [77, 111]. Semi-solid processing was employed in this work to coarsen and homogenize the microstructure and precisely tune the microstructural length scale, S , to match the characteristic plastic zone criterion and fulfill the requirement for tensile ductility. The alloy is heated to between the alloy solidus and liquidus temperature. The glassy phase is designed around a deep eutectic and is a highly metastable phase ($T_1 \sim 1300\text{K}$), while the

β -Ti is more stable and melts at a much higher temperature ($T_1 \sim 1450\text{K}$), resulting in a large range in temperatures where the β -Ti may be coarsened, yet upon rapid cooling, the molten phase can still be vitrified.

The omission of expensive alloying elements while maintaining high strength and ductility in these alloys represents a monumental step forward in BMG composites, as the low density and significant cost savings of this new composition space presents endless opportunities for commercial structural, aerospace and biomedical applications.

5.3.3 Results and Discussion

To design a Ti-based BMG composite with enhanced ductility, several criteria must be met: (1) A glass forming system with a strong resistance to crystallization must be identified for the matrix, (2) a 2-phase microstructure consisting of the glassy phase and a low shear modulus dendrite must be created through careful compositional tuning, (3) the microstructure must be coarsened and homogenized by way of processing to match the length scale of deformation in the glass.

A low cost Ti-Ni-Cu-Si-Sn glass forming system with large GFA has been previously reported by Cheney, Khalifa, and Vecchio [150, 165]. Despite the very large SCLR of this glass, it could not maintain its amorphous structure in the presence of a b.c.c. β -Ti phase; Cu- and Sn-rich crystalline phases nucleated out from the destabilized matrix along the dendrite-matrix interface [166]. The starting point for the amorphous matrix composite in the current study was based on simplifying the Ti-Ni-Cu-Si-Sn glass forming system in order to prevent crystallization in the matrix. For this study, constituent elements which formed deep binary eutectics somewhere in the Ti-rich

composition space were chosen [150, 167] (with the exception of Mo which only accounts for 2 at% of the alloy). Each constituent has a large negative mixing enthalpy with Ti; $\Delta H_{mix}^{Ti-Ni} = -140 \text{ kJ/mol}$, $\Delta H_{mix}^{Ti-Si} = -211 \text{ kJ/mol}$, and $\Delta H_{mix}^{Ti-Mo} = -16 \text{ kJ/mol}$ [168]. Furthermore, solute elements were selected of various atomic sizes, to allow for an efficient topology to develop in the glassy structure. Selecting Ni, Si, and Mo, establishes three unique topological species, which may occupy unique sites in the metallic glass structure as described by Miracle's structural model [24]. The matrix glass in the current study omits Sn and Cu and, instead, utilizes Mo to enhance the GFA of the alloy by creating greater atomic radius mismatch among the constituent atoms, in accordance with Inoue's empirical rules for BMG formation [2]. A comparison of Ti-Ni-Si ternary liquidus profiles illustrating the effect of Mo on glass formation is presented in Figure 5.3.1. Although the addition of Mo raises the liquidus temperature significantly, it broadens the glass forming composition space, and pushes glass formation towards more Ti-rich compositions, which is useful for lowering alloy density. A summary of glass forming compositions is given in Table 5.3.1.

To design a two-phase composite structure, the (Ti + Ni) content was raised relative to Si, and additional Mo (a potent isomorphous β -Ti stabilizer [149]) was added to promote β -Ti formation in a Si-enriched glass-forming liquid at elevated temperatures. The optimized Mo-stabilized β -Ti phase was successfully incorporated into the glassy matrix through careful compositional adjustments to the overall alloy and precise semi-solid processing to tune the microstructure.

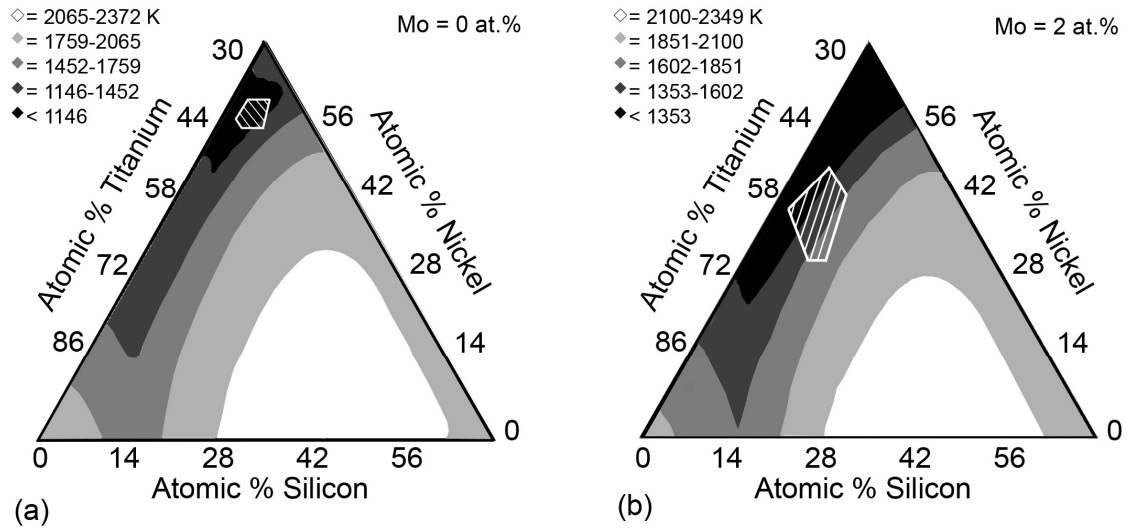


Figure 5.3.1. Liquidus profiles illustrating glass formation in the (Ti-Ni-Si)-Mo alloy system. Mo = 0 at. % in the ternary profile in (a), and Mo = 2 at. % in (b). The white hashed region encompasses the glass forming composition space in each profile.

To better convey the importance of microstructure scale, alloys of the composition $\text{Ti}_{51.4}\text{Ni}_{42.4}\text{Si}_{3.9}\text{Mo}_{2.3}$ were subjected to three distinct semi-solid processing conditions designed to yield markedly different microstructures. Different heating time and temperature was used to achieve the different microstructural states. SEM images of the 3 states; SSP1, SSP2, and SSP3, are presented in Figure 5.3.2a, b, and c, respectively. Analysis of these 3 microstructural states revealed that SSP1 and SSP2 maintain an amorphous matrix, while SSP3 contains a multi-phase crystallized matrix.

Table 5.3.1. Glass transition (T_g), crystallization (T_x), and liquidus (T_l) temperatures of select glass forming alloys from the (Ti-Ni-Si)-Mo alloy system.

Alloy Composition (at. %)	T_g (K)	T_x (K)	T_l (K)	ΔT (K)
$\text{Ti}_{39}\text{Ni}_{59}\text{Si}_2$	663	710	1137	47
$\text{Ti}_{42}\text{Ni}_{54}\text{Si}_4$	651	693	1156	42
$\text{Ti}_{49}\text{Ni}_{43}\text{Si}_6\text{Mo}_2$	741	798	1315	57
$\text{Ti}_{51}\text{Ni}_{38}\text{Si}_9\text{Mo}_2$	757	827	1328	70
$\text{Ti}_{52}\text{Ni}_{35}\text{Si}_{11}\text{Mo}_2$	777	862	1352	85
$\text{Ti}_{55}\text{Ni}_{31}\text{Si}_{12}\text{Mo}_2$	786	855	1394	69
$\text{Ti}_{58}\text{Ni}_{37}\text{Si}_3\text{Mo}_2$	761	811	1328	51

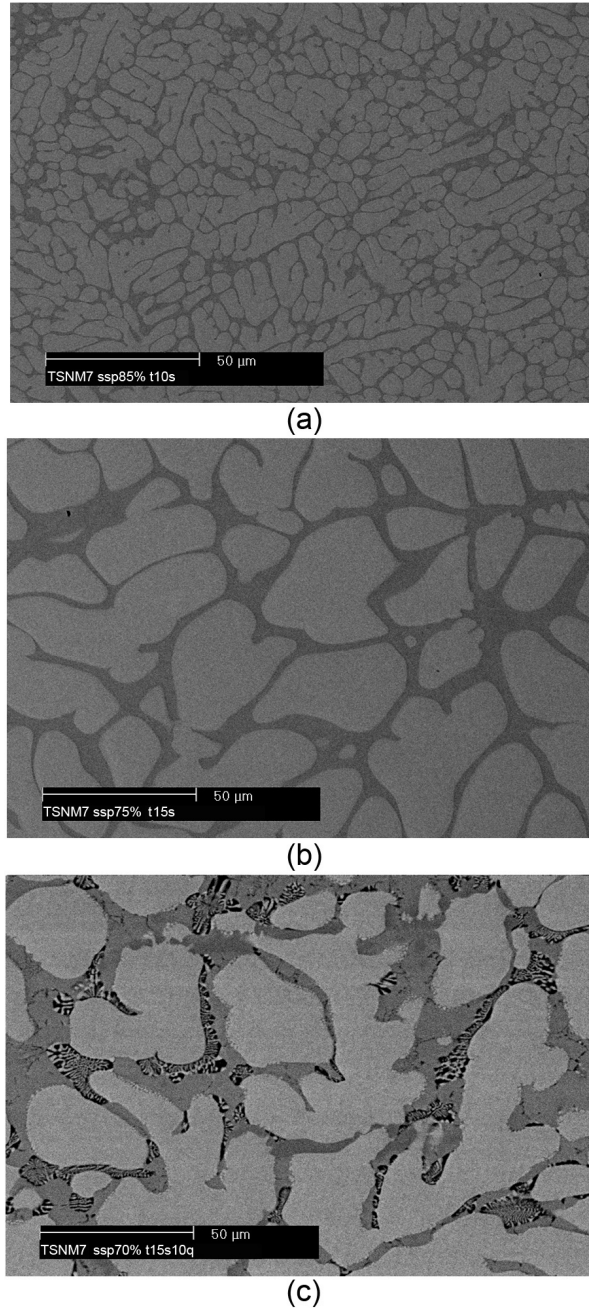


Figure 5.3.2. Typical microstructures achieved during semisolid processing of $\text{Ti}_{51.4}\text{Ni}_{42.4}\text{Si}_{3.9}\text{Mo}_{2.3}$ at (a) 85% power for 10 seconds followed by simultaneously turning off power to the induction coil and quenching the sample with the top copper plate. The alloy resulting from this first semi-solid processing condition will be referred to as SSP1 (b) 75% power for 15 second followed by simultaneously turning off power to the induction coil and quenching the sample with the top copper plate. The alloy resulting from this second semi-solid processing condition will be referred to as SSP2, and (c) 70% for 15 seconds followed by 10 additional seconds of heating after lowering the top copper block to promote crystallization of the matrix. The alloy from this condition will be referred to as SSP3.

The DSC curves in Figure 5.3.3 show a clearly resolved glass transition in the BMG composite, $\text{Ti}_{51.4}\text{Ni}_{42.4}\text{Si}_{3.9}\text{Mo}_{2.3}$. It should be noted that the SCLR is 69 K for the composite, compared to 85K for the monolithic glass from which this composite was initially based. This large disparity comes about due to the variation in glass composition arising during semi-solid processing. Smaller SCLR has been observed in moving from monolithic glasses to BMG composites, and the reduction has been attributed to the presence of heterogeneous nucleation sites at the glass/crystal interface. In most cases, however, the glass in the matrix has had the same T_g as the parent glass. The lower glass stability of this Ti-Ni-Si-Mo glass forming system, relative to the Ti-Zr-Be-based systems that have been successfully utilized in BMG composites, results in much more active diffusion across the glass/crystal interface during processing, as well as a greater dependence of SCLR on composition. The glass composition changes during semi-solid processing. While this highlights the broad compositional range across which glass formation is observed, small changes in the composition of the glass have shifted the T_g from 777K for the monolithic glass up to 786K for the composite. The most important aspect of Figure 5.3.3, though, is that there is a clearly resolved glass transition in the composite, meaning the matrix is, in fact, amorphous in the presence of a second phase.

The XRD spectra presented in Figure 5.3.4 confirm that the semi-solidly processed composite has an amorphous matrix. It is clear that the spectrum for the amorphous matrix composite (Figure 5.3.4b) is a superposition of the signature b.c.c. peaks of the β -Ti phase (Figure 5.3.4c) and the broad, featureless hump of the monolithic glass (Figure 5.3.4a). When crystallization does occur in the matrix, the broad hump

indicative of amorphous structure is not detectable, and numerous small peaks in addition to the b.c.c. signature peaks corroborate the loss of amorphous structure (Figure 5.3.4d).

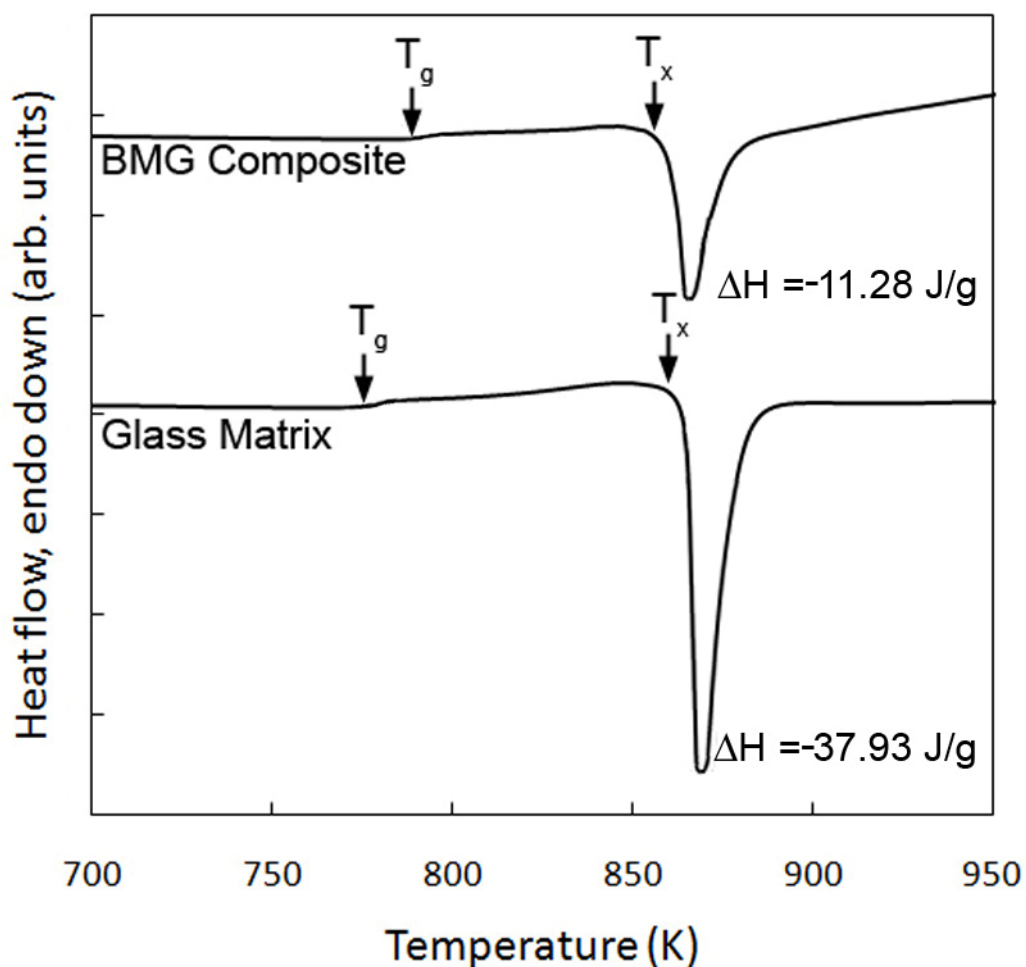


Figure 5.3.3. DSC curves of the BMG matrix composite $\text{Ti}_{51.4}\text{Ni}_{42.4}\text{Si}_{3.9}\text{Mo}_{2.3}$ and its fully amorphous matrix. T_g and T_x for both alloys are indicated with arrows.

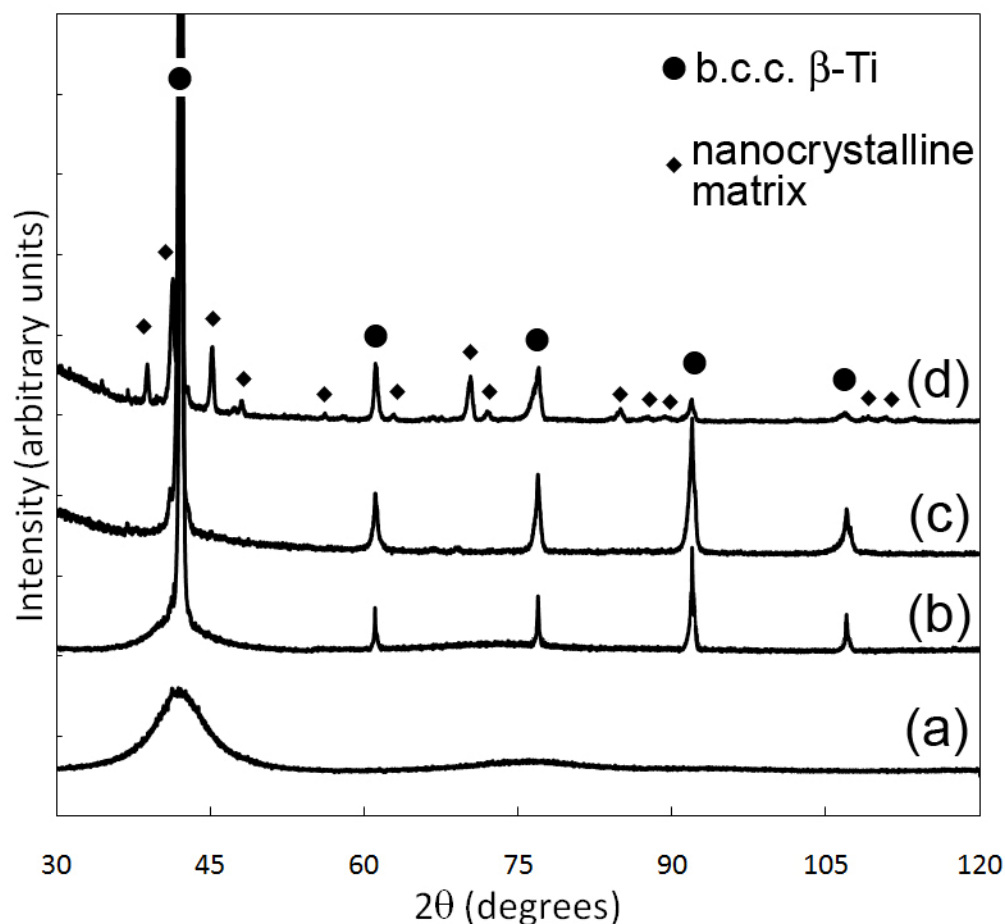


Figure 5.3.4. XRD spectra of (a) the fully amorphous monolithic glass, (b) an ideally semi-solidly processed BMG matrix composite ($\text{Ti}_{51.4}\text{Ni}_{42.4}\text{Si}_{3.9}\text{Mo}_{2.3}$) with a b.c.c. β -Ti phase embedded in the amorphous matrix (SSP2), (c) the isolated b.c.c. β -Ti phase, and (d) a BMG-derived composite (with the same composition as 5.3.4b) that has been semi-solidly processed for too long, resulting in a destabilization of the glass into a crystalline matrix (SSP3).

Further SEM and EDS analysis was used to characterize the discerning features of the bulk microstructure in each of the composites. The amorphous matrix composite, SSP1 is composed of approximately $26 \pm 2\%$ glass and $73 \pm 2\%$ β -Ti, while SSP2 is composed of approximately $28 \pm 3\%$ glass and $72 \pm 2\%$ β -Ti. These results were obtained by analyzing the contrast in SEM images. The results were also verified based on crystallization enthalpies from the DSC curves in Figure 5.3.3. The monolithic glass

had $\Delta H_{\text{cryst}} = -37.93 \text{ J/g}$, while the amorphous matrix composite had $\Delta H_{\text{cryst}} = -11.28 \text{ J/g}$. Recall that crystal volume fraction can be calculated using Equation 4.2-1. The ratio of the crystallization enthalpies in Figure 5.3.3 indicates approximately 70% of the composite is crystalline material. Dendrite compositions measured using EDS ranged over $\text{Ti}_{47-50}\text{Ni}_{41-44}\text{Si}_{1-3}\text{Mo}_{2-4}$, while the glass matrix ranged over $\text{Ti}_{51-57}\text{Ni}_{29-33}\text{Si}_{8-13}\text{Mo}_{1-2}$. In SSP1, dendrite size varied from $L \approx 10-40 \text{ }\mu\text{m}$, while inter-dendrite spacings varied from $S \approx 1-5 \text{ }\mu\text{m}$. In SSP2, dendrite size varied from $L \approx 20-80 \text{ }\mu\text{m}$, while inter-dendrite spacing ranged from $S \approx 5-25 \text{ }\mu\text{m}$. In SSP3, dendrite size varied from $L \approx 20-80 \text{ }\mu\text{m}$, while inter-dendrite spacing ranged from $S \approx 10-30 \text{ }\mu\text{m}$. However, the matrix has clearly crystallized during the extended processing time in this condition. Notice that the average dendrite size and spacing do not change significantly between SSP2 and SSP3. Dendrite coarsening is dictated by processing prior to quenching, however, maintenance of glassy structure in the matrix is only achieved when heating is stopped prior to lowering the quench block. The amorphous structure in the matrix is dependent on the rapid cooling supplied by the quench block in the absence of an inductive field. The rationale for selecting these specific processing conditions lies in matching the length scales, L and S , with R_p . R_p for the glass matrix can be estimated from its K_{IC} ($10 \text{ MPa}\cdot\text{m}^{1/2}$ for the monolithic glass $\text{Ti}_{52}\text{Ni}_{53}\text{Si}_{11}\text{Mo}_2$) to be $5 \text{ }\mu\text{m}$. Since the span of amorphous material between adjacent dendrites is on the same length scale as R_p , microstructurally-induced shear band stabilization will occur. Shear bands cannot extend beyond the critical length scale, R_p , without encountering a dendrite that will arrest or

deflect that shear band, thereby forcing new ones to nucleate, ultimately resulting in global ductility.

Different processing conditions performed on the same composition did not significantly affect the volume fraction of the respective phases, only the scale of the microstructure. Composition dictates the volume fraction, and more effectively impacts dendrite-dendrite spacing. Increasing the glass volume fraction requires an increase in Ti and Si, and a decrease in Ni and Mo. Given the significantly lower glass stability of Ti-Ni-Si-Mo compared with Ti-Zr-Be glasses, the glass destabilizes quickly as the composition is changed.

One alloy from the Ti-Ni-Si-Mo system designed to achieve higher glass fraction is presented in Figure 5.3.5. The alloy in Figure 5.3.5 has the composition $\text{Ti}_{54.7}\text{Ni}_{39.1}\text{Si}_{4.4}\text{Mo}_{1.8}$. It is obvious from the image that β -Ti has still been stabilized, however, the compositional change necessary to alter the amount of β -Ti that forms, leads to a compositional change in the matrix, and subsequent crystallization therein. In contrast to the Ti-Zr-Be-Cu-Nb/V BMG composites, these Ti-Ni-Si-Mo composites do not contain any elements with complete insolubility in either the glass or matrix; no one element can be adjusted to directly and precisely control the glass volume fraction like one can with Be in the Ti-Zr-Be-Cu-Nb/V composites [81, 142, 169]. This complicates the precise tuning of the volume fraction for a number of reasons. First, very small changes in composition can have a profound effect on the microstructure. Secondly, the instability of the glass necessitates adjusting the chemistry of multiple elements in the alloy. While it seems logical to decrease the Mo content in order to lower the volume fraction of β -Ti, it is also necessary to decrease Si and Ni content just to maintain an

appropriate morphology in the β -Ti phase. However, even these subtle changes can result in a loss of glassy structure in the matrix. Adjusting a single constituent without considering the others typically led to rapid crystallization of the matrix upon cooling, such that nanocrystalline structure was bypassed and a coarse multi-phase matrix resulted. In Figure 5.3.5, the matrix accounts for 39% of the alloy, while the β -Ti accounts for 61%. Once again, variation of the processing conditions only leads to a coarsening of the microstructure, but the matrix volume fraction was exclusively controlled by the composition of the alloy.

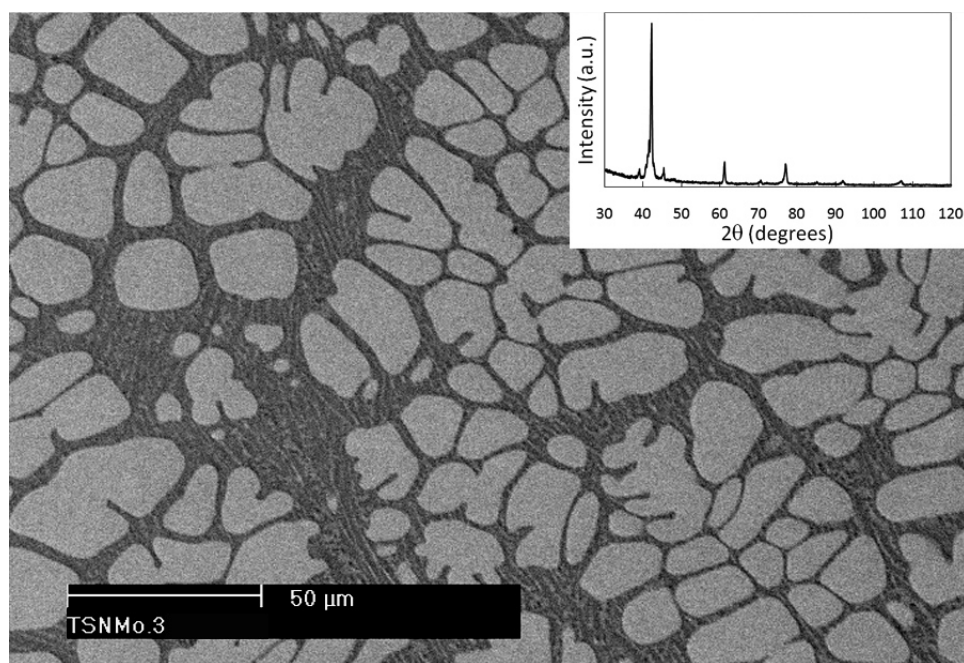


Figure 5.3.5 Semi-solidly processed $\text{Ti}_{54.7}\text{Ni}_{39.1}\text{Si}_{4.4}\text{Mo}_{1.8}$ BMG-derived composite with nanocrystalline matrix. The inset shows additional peaks in the XRD spectrum indicating crystallization in the matrix.

Compressive stress-strain curves for the alloys SSP1-SSP3 are shown in Figure 5.3.6. For SSP1 and SSP2, which contained an amorphous matrix, yield stress, $\sigma_y = 990 \pm 30$ MPa, is about the same. This suggests that yielding is not a function of

microstructural scale, but rather, volume fraction of the glassy matrix. The dependence of yield stress on matrix volume fraction has been noted before in amorphous matrix composites [81, 142], and nanocrystalline matrix composites [170], as well. SSP3 exhibits a lower yield stress, $\sigma_y = 870 \pm 25$ MPa, and significantly less elastic strain. The loss of amorphous structure in the matrix leads to the notable drop off in elastic strain, from 2.7 ± 0.2 % for amorphous matrix composites, to 1.8 ± 0.2 % for a composite with a crystalline matrix. The large elastic strains in amorphous matrix composites are attributed to large free volume, which is locked into the glass upon solidification from the liquid state [171]. Large free volume permits more recoverable atomic rearrangement to occur during deformation.

Table 5.3.2. A summary of all relevant mechanical and material properties in the semi-solidly processed BMG composites SSP1, SSP2, and SSP3, each with nominal composition $\text{Ti}_{51.4}\text{Ni}_{42.4}\text{Si}_{3.9}\text{Mo}_{2.3}$. Data for the monolithic glass, $\text{Ti}_{52}\text{Ni}_{35}\text{Si}_{11}\text{Mo}_2$, as well as equi-atomic Nitinol, and Ti 6/4 are included for comparison.

Alloy	ρ (g/cm ³)	E (GPa)	G (GPa)	ν	K _{IC} (MPa·m ^{1/2})	$\sigma_{y, \text{com}}$ (MPa)	$\epsilon_{y, \text{com}}$ (%)	$\sigma_{\text{max, com}}$ (MPa)	$\epsilon_{\text{tot, com}}$ (%)	$\sigma_{y, \text{ten}}$ (MPa)	$\epsilon_{y, \text{ten}}$ (%)	$\sigma_{\text{max, ten}}$ (MPa)	$\epsilon_{\text{tot, ten}}$ (%)
SSP1	5.9	90.9	33.4	0.362	33.1	995	2.7	2331	25.7	1241	1.2	1390	2.2
SSP2	5.9	92.8	34.1	0.358	38.7	990	2.8	2462	28.8	1382	1.4	1425	3.4
SSP3	6.0	106.7	39.5	0.352	24.3	870	1.8	2047	15.5	1156	1.0	1171	1.0
$\text{Ti}_{52}\text{Ni}_{35}\text{Si}_{11}\text{Mo}_2$	5.5	107.0	38.9	0.374	9.6	-	-	1848	3.1	-	-	-	-
NiTi [172]	6.5	~75	~25	~.3	39.2	470	1.3	2110	19.2	560	1.1	960	15.5
Ti 6/4 [149]	4.4	113.8	43.9	0.330	43.0	950	3.9	1750	21.1	1100	1.0	1170	10.0

The spatial confinement of the matrix phase by adjacent dendrites constrains shear band propagation in each of the BMG-derived composites. The result of this shear band confinement is a significant increase in compressive plasticity. In looking at the plastic deformation, the amorphous matrix composites behave similarly to one another, while the crystalline matrix composite exhibits significantly less total strain to failure.

SSP3 exhibited a total strain to failure, $\varepsilon_t = 15 \pm 2\%$ and maximum strength, $\sigma_{\max} = 2050 \pm 40$ MPa. The retention of amorphous structure in the matrix produced substantial plasticity enhancement; SSP1 failed at a maximum strength, $\sigma_{\max} = 2330 \pm 30$ MPa with total strain to failure, $\varepsilon_t = 26 \pm 2\%$, while SSP2 exhibited total strain to failure, $\varepsilon_t = 29 \pm 2\%$ and maximum strength, $\sigma_{\max} = 2460 \pm 60$ MPa. To date, no other BMG, or BMG-derived composite has demonstrated such extensive plastic strain coupled with high mechanical strength.

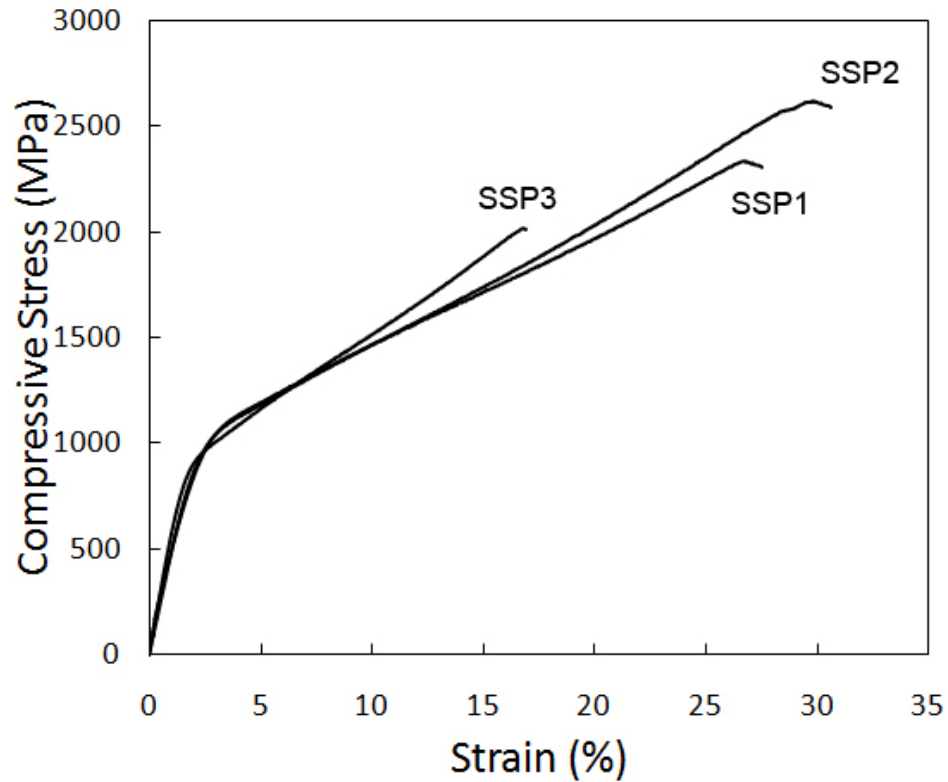


Figure 5.3.6. Uniaxial compressive stress-strain curves for the amorphous matrix composites, SSP1 and SSP2, and the crystalline matrix BMG-derived composite, SSP3.

To better explore the evolution of plastic deformation in these composites, a series of compression tests were performed on SSP2, and the deformation was analyzed

after varying degrees of plastic strain. The roman numerals on the stress-strain curve in Figure 5.3.7a denote the degree of plastic strain experienced by the specimens in each test; namely I is 5%, II is 10%, III is 15%, IV is 20%, and V is to failure, which in this case was 28% total strain.

Figure 5.3.7b shows the deformation in the alloy after 5% total strain (2.1% plastic strain). Shear bands have nucleated on a small fraction of the outer sample surface; the vast majority of the sample surface showed no signs of deformation. Shear bands form and propagate parallel to one another at roughly 45° to the load axis, which is typical of Ti-based BMGs [60]. Propagating shear bands pass through dendrites, deflecting slightly at the glass-dendrite interface. The shear bands nucleate at the glass-dendrite interface, while termination occurs within a dendrite. The termination of a shear band sometimes leads to the nucleation of a new shear band along the same trajectory. These shear bands had an average spacing of 60-80 μm . The yield stress of these composites is significantly lower than the monolithic glass, indicating that the dendrites are deforming when the overall composite yields. Both components of the composite alloy account for plasticity enhancement; the dendrites themselves are yielding, while their presence also delocalizes the strain in the glass matrix by forcing more shear bands to nucleate.

Figure 5.3.7c depicts the outer surface after 10% total strain. The shear band spacing has decreased to roughly 20-40 μm . Additionally the shear bands have extended further along the sample, and occupy more of the overall sample surface. The increased shear band density permits greater strain accommodation.

After 15% total strain, several interesting new features arise. Primary shear band spacing remains roughly 20 μm , but the formation of secondary shear bands, propagating along intersecting trajectories with the primary shear bands, have formed. Secondary shear bands are spaced roughly 5 μm apart. This added feature of the deformation accommodates significantly more strain, and serves to delocalize the deformation. The impetus for secondary shear band formation has been attributed to work hardening within the dendrites. The work hardening is the result of slip band formation and dislocation movement within the dendrite [122, 152, 153]. As the dendritic phase hardens, each dendrite imposes a greater obstacle to primary shear band propagation. In turn, this forces the nucleation of secondary shear bands, thereby increasing global plasticity.

After 20% total strain, primary and secondary shear bands cover nearly the entire outer surface in order to accommodate all of the deformation. The continued work hardening observed in the overall stress-strain curve is the result of extensive slip band formation within the dendrites. A good example of slip within a dendrite can be seen in Figure 5.3.7f. When a shear band encounters a hardened dendrite, its propagation is arrested or deflected. Notice that after 20% total strain, many of the shear bands appear wavy. This is the result of greater deflection of the shear bands at the glass-dendrite interface, induced by the work hardened b.c.c. phase. As a shear band is deflected, it loses energy, and enhances the likelihood of shear band arrest upon subsequent interaction with a dendrite. The only way for the alloy to accommodate more deformation, is by nucleating new shear bands. Arresting of shear bands within the dendrites at 20% strain leads to different behavior than what is observed at lower strain. Unlike shear band nucleation after 5% total strain, which occurred along the same

trajectory as the arrested shear bands, the nucleation of new shear bands in the presence of hardened dendrites occurs along a different trajectory. The result is domains of shear bands propagating along different directions. Hardened dendrites are better able to fully arrest shear band propagation, and prevent shear transfer back into the matrix along the direction of propagation. The prevention of shear transfer across the glass-crystal interface ultimately increases shear band density, and thus, plasticity. Lastly, the first signs of micro-cracking in the glassy matrix can be observed after 20% total strain. Inter-dendritic cracks were observed in several places on the sample surface. An example is shown in Figure 5.3.7f. Notice that the cracks are arrested as soon as they interact with a dendrite.

Fracture occurred after 28% total strain. It can be seen in Figure 5.3.7g, that the shear band density is even greater than at 20% strain. There is a large amount of impingement and interaction between intersecting primary and secondary shear bands. The larger contrast observed along primary shear bands is indicative of significant shear off-set occurring; material on opposing sides of the primary shear band slide away from one another. The high magnification image in Figure 5.3.7h shows primary shear band spacing of 5-10 μm and secondary shear band spacing of less than 1 μm .

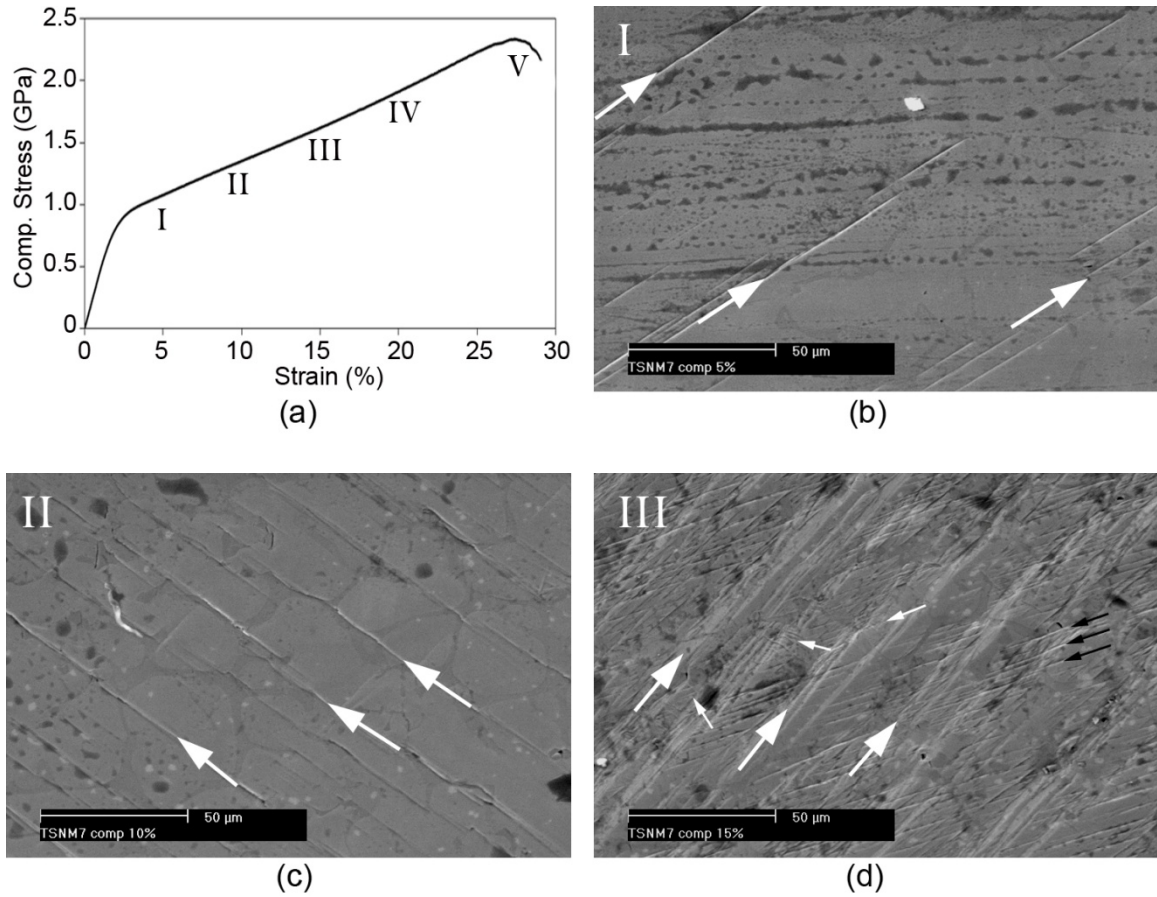


Figure 5.3.7. Shear band evolution on outer surface of $\text{Ti}_{51.4}\text{Ni}_{42.4}\text{Si}_{3.9}\text{Mo}_{2.3}$ (SSP2) samples during stepwise compressive loading. The stress-strain curve in (a) is labeled with numerals I-V corresponding to the images in (b)-(h), where (b) is 5% total strain, (c) is 10% total strain, (d) is 15% total strain, (e) is 20% total strain, (f) is a hi magnification image of the 20% strain condition showing shear band deflection and crack arrest at the glass-crystal interface, and (g) is 28% total strain. The sample failed at 28% total strain. The image in (h) is a high magnification view of the outer surface of the sample taken near the fracture surface. The interaction of primary and secondary shear bands is apparent from the shear steps near intersection points. Large white arrows indicate primary shear bands, small black arrows indicate secondary shear bands, and small white arrows indicate slip bands.

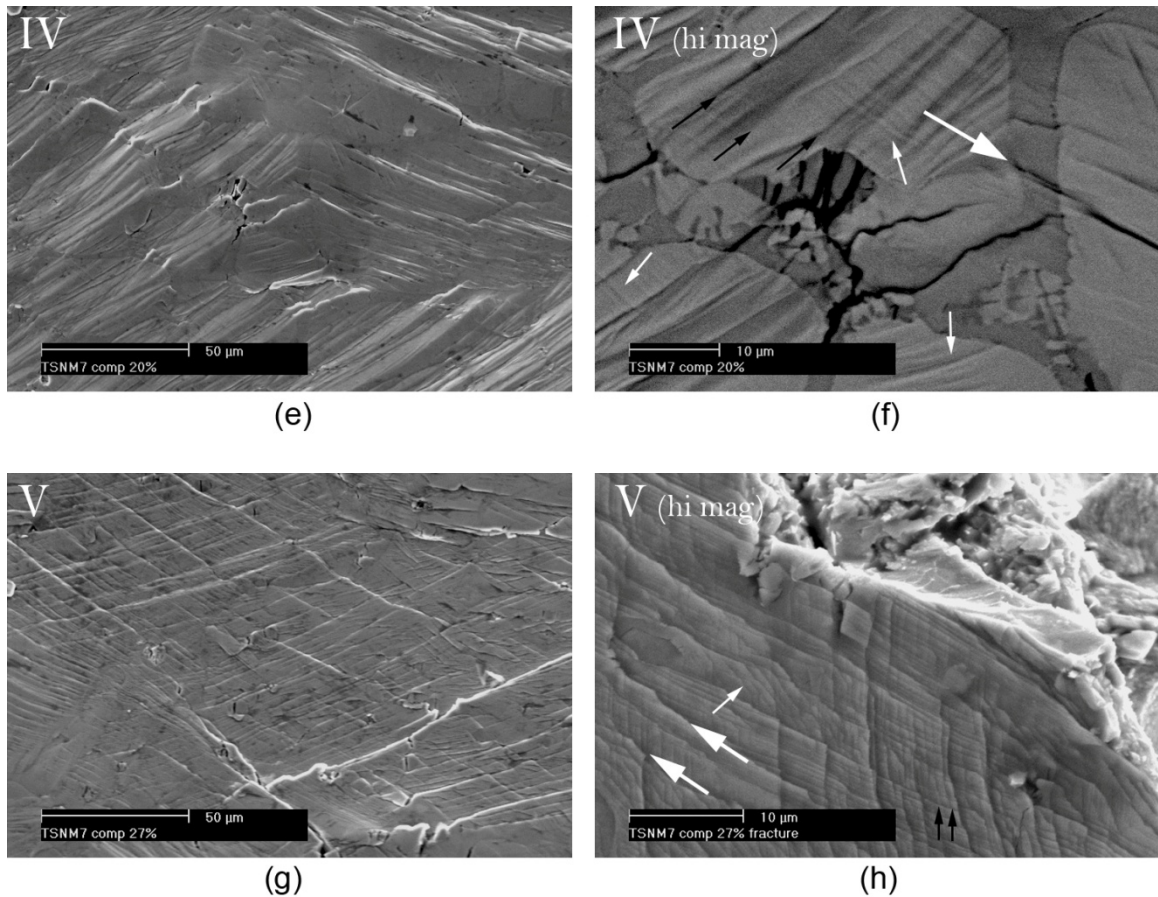


Figure 5.3.7 continued

Notice that primary shear bands propagate approximately parallel to the fracture surface. Note also the step-like pattern formed by shear off-sets at the intersection of primary and secondary shear bands. At these intersections, compound shear off-set resulting from the interacting shear bands results in discontinuities in the primary shear bands. The cumulative sum of primary and secondary shear band formation, shear band arrest and deflection, slip band formation, work hardening, and inhibition of shear and slip transfer, result in delocalization of the strain, and benchmark global plasticity in the BMG composites.

Plane strain fracture toughness measurements were performed on each of the 3 composites. K_{IC} measurements were obtained from 4 point bending tests performed on 3 mm thick plates in accordance with ASTM standards. The fracture toughness results, as well as a summary of all mechanical and material properties of the BMG composites are presented in Table 5.3.2. Compared to the monolithic glass, $Ti_{55}Ni_{31}Si_{12}Mo_2$, the amorphous matrix composites show a remarkable increase in fracture toughness of nearly 400%. SSP1 and SSP2 had $K_{IC} \approx 33.1 \pm 2.8 \text{ MPa}\cdot\text{m}^{1/2}$, and $K_{IC} \approx 38.7 \pm 1.7 \text{ MPa}\cdot\text{m}^{1/2}$, respectively. This enhanced fracture toughness is comparable to Ti-Zr-Cu-Be-V BMG composites containing 15 at% Be [142]. SSP3 had a fracture toughness of $K_{IC} \approx 24.3 \pm 3.2 \text{ MPa}\cdot\text{m}^{1/2}$.

While the mechanism responsible for this toughness enhancement again has to do with the optimization of microstructural and mechanical length scales, another important phenomenon is at play. Toughness enhancement and tensile ductility are achieved only when the shear modulus (G) of the dendrite is lower than G of the glass [81]. Shear bands have previously been likened to mixed mode cracks by Hofmann [142]. In this scenario, an operating shear band at the interface between dissimilar elastic materials will be attracted to and penetrate the inclusion if the Dundurs' parameter $\alpha = (G_{\text{dendrite}} - G_{\text{matrix}}) / (G_{\text{dendrite}} + G_{\text{matrix}}) < 0$ [173]. For a positive α , the shear band will be deflected away from the inclusion and any crack forming within the matrix will extend without constraint, en route to failure. A penetrating shear band will be arrested within the inclusion because deformation within the inclusion is stabilized by slip-induced work hardening, or the shear band will lose energy as it passes through a dendrite. Greater toughness was observed in SSP2 compared with SSP1 because the larger b.c.c. dendrites

more effectively arrest propagating shear bands, while the finer scale b.c.c. phase in SSP1 is more prone to shear band and crack transfer through the β -Ti phase; larger β -Ti microstructure provides better shear band arrest and crack blunting capabilities. Using Table 5.3.2, the shear modulus for the dendrite is determined by a simple rule of mixtures, such that $\alpha \approx -0.1$ for both SSP1 and SSP2. Due to the multi-phase nature of the matrix in SSP3, it is difficult to accurately calculate its Dundurs' parameter. Brittle silicides, and the formation of α -Ti in the matrix lead to crack propagation through the matrix, such that the deformation cannot be as efficiently accommodated by the low modulus dendrites (the b.c.c. phase in SSP3 had nearly the same composition as the b.c.c. phase in SSP1 and SSP2). For comparison, a toughened Zr-based BMG composite had $\alpha \approx -0.07$ [81, 169]. Figure 5.3.7f is a good example of both shear bands and microcracks arresting as they encounter a ductile dendrite; even those microcracks and shear bands that are deflected by dendrites get arrested as they encounter adjacent dendrites. When shear bands evolve into cracks in composites meeting the Dundurs' criterion, propagation of the cracks is arrested via a cascade of interactions. Figure 5.3.8 is a descriptive example of the various mechanisms at work. Several domains of shear bands are propagating along different trajectories, and each of the shear bands arrests within a dendrite. Copious slip can be seen within the majority of the dendrites. Numerous inter-dendritic cracks spanning only a single dendrite-dendrite spacing can be observed. A few of the microcracks have evolved and propagated, exhibiting a "tortuous path" crack morphology. This is a highly energetic form of crack propagation wherein the crack must navigate around inclusions. However, once the crack encounters a dendrite head-on, it penetrates into or through the dendrite, which absorbs the crack's

energy, and, upon subsequent interaction with an adjacent dendrite, the crack is arrested. This type of circuitous crack path has been seen in numerous metallic and biological composites exhibiting good fracture toughness [174, 175].

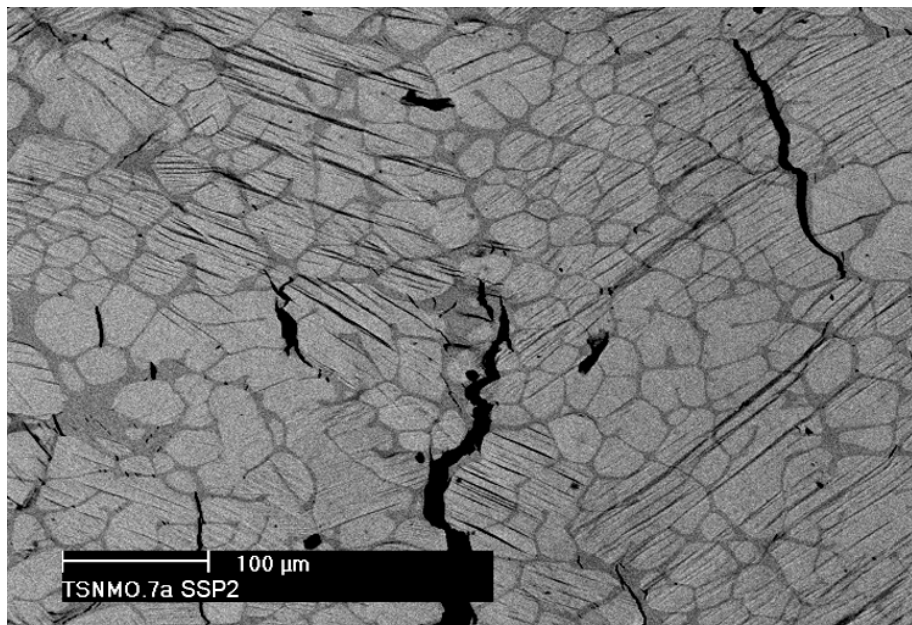


Figure 5.3.8. Backscatter electron image of deformation modes in SSP2, including dendrite penetrating shear band arrest, trans-dendritic shear bands, intra-dendritic slip, inter-dendritic microcracks, intra-dendritic crack arrest, and tortuous path crack morphology.

Figure 5.3.9 displays SEM micrographs of the fracture surface of SSP2 after compression testing. The rough overall fracture surface shown in Figure 5.3.9a is indicative of ductile failure. Two distinct fracture morphologies can be observed: dendritic fracture features (I), and glass fracture features (II). A magnified view of fracture in the dendritic phase is shown in Figure 5.3.9b. The plateau and ledge morphology is the result of slip-induced cleavage along certain crystallographic planes. These cleavage steps are commonly described as “river patterns,” wherein finer steps merge into larger ones. Similar fracture morphology has been observed in Ti-based, β -Ti reinforced, nanocrystalline matrix composites and bimodal Ti alloys [122, 170, 176], and

is a common fracture feature of b.c.c. phases [177]. Vein-like fracture features are enlarged in Figure 5.3.9c, and correspond to fracture of the metallic glass matrix. Vein-like patterns are a typical feature of glass fracture [5, 178-180].

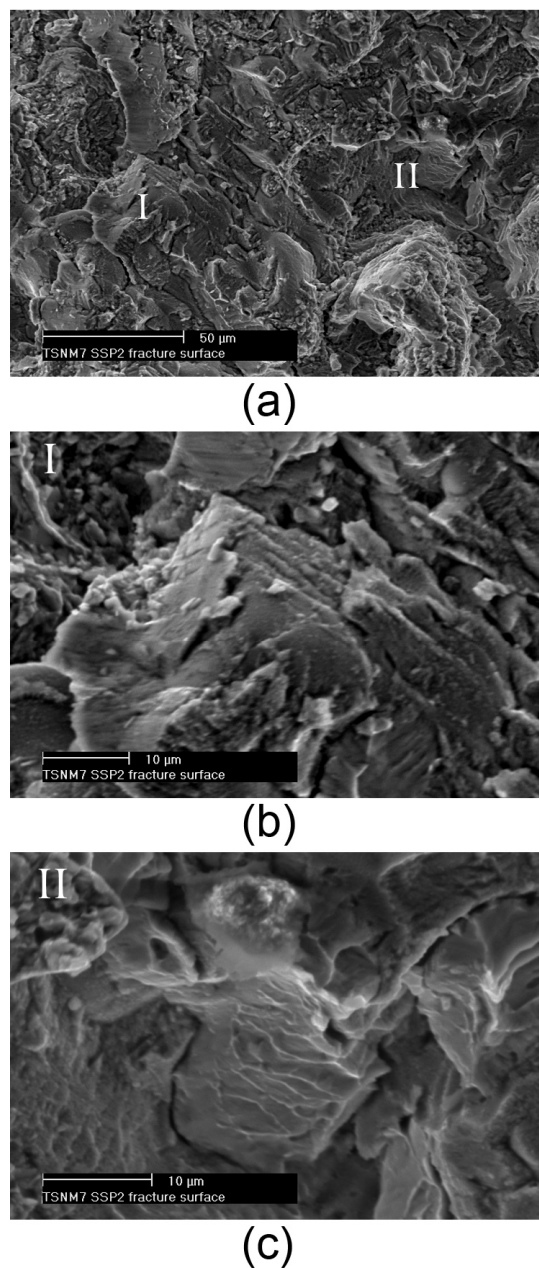


Figure 5.3.9. (a) Overview of SSP2 4 pt. bend sample fracture surface. I and II mark the two morphologically distinct fracture mechanisms. A high magnification image of region I depicts dendrite fracture in (b), and a high magnification image of region II depicts glass fracture in (c).

It is somewhat counter-intuitive that vein-like patterns arise in metallic glass fracture because it is a morphological feature of ductile failure. But failure in metallic glasses occurs within an operating shear band [38]. The material within the shear band behaves like a low viscosity liquid trapped between two solid plates, and exhibits traits of perfectly plastic behavior [38, 181]. Despite the fact that metallic glasses exhibit little or no plastic strain globally, the fracture surface exhibits vein-like patterns because failure occurs within a shear band where perfectly plastic behavior is observed. This argument also explains why increasing shear band density results in enhanced ductility.

To date enhanced plasticity has been observed in several Ti-based BMG-derived composites containing nanocrystalline matrices, however none of these alloys has demonstrated tensile ductility. Tensile ductility has been elusive because a means to precisely control the microstructure was not in place. The development of semi-solid processing in this work permits the control necessary to properly match microstructural and mechanical length scales such that tensile ductility has been achieved.

The tensile stress-strain curves for SSP1, SSP2 and SSP3 are presented in Figure 5.3.10. The marquee alloy of this study, SSP2, exhibits 3.5% tensile strain. This is the first report of tensile ductility in a non-Be containing Ti-based amorphous matrix composite of any kind. The alloy still exhibits typical bulk metallic glass traits like high yield stress ($\sigma_y = 1382$ MPa) and large elastic strain ($\epsilon_y = 1.4$ %). However the optimally coarsened microstructure prevents shear bands from rapidly extending, and evolving into cracks. The shear band extension is confined by the dimensions of the glassy matrix between adjacent β -Ti dendrites. As shear bands are arrested, new ones must form to accommodate the strain, resulting in a delocalization of the deformation and global

ductility. Shear band extension is much faster in unconfined loading conditions such as tension, so lower ductility is generally observed in tensile conditions versus compression. Shear band extension is also faster in more brittle glasses. Tensile ductility of 9.8% has been reported for $\text{Ti}_{62}\text{Zr}_{15}\text{V}_{10}\text{Cu}_4\text{B}_9$; an amorphous matrix composite with nearly identical microstructural features as the SSP2 alloy featured in this work [142]. The discrepancy in the tensile ductility has to do with the fracture toughness of the matrix glass. Although both alloys were designed to match fundamental microstructural and mechanical length scales (i.e. have $R_p \approx S$), the significantly higher fracture toughness of the Ti-Zr-Be-Cu matrix glass ($K_{IC} \approx 40 \text{ MPa}\cdot\text{m}^{1/2}$) results in a significantly larger critical shear band extension length, $R_p \approx 90 \text{ }\mu\text{m}$. By comparison, the matrix glass in this study, $\text{Ti}_{55}\text{Ni}_{31}\text{Si}_{12}\text{Mo}_2$ has $K_{IC} \approx 10 \text{ MPa}\cdot\text{m}^{1/2}$ and a corresponding critical shear band extension length of only $5 \text{ }\mu\text{m}$. While careful processing enabled the fabrication of alloys with dendrite-dendrite spacings on the same length scale as R_p , there was very little margin for error. Conversely, $\text{Ti}_{62}\text{Zr}_{15}\text{V}_{10}\text{Cu}_4\text{B}_9$ has similar dendrite spacings yet the critical shear band extension length is far greater than the average length a shear band actually extends in the alloy. Since shear bands are operating well below their critical extension limit in $\text{Ti}_{62}\text{Zr}_{15}\text{V}_{10}\text{Cu}_4\text{B}_9$, tensile ductility is more greatly enhanced. In the $\text{Ti}_{51.4}\text{Ni}_{42.4}\text{Si}_{3.9}\text{Mo}_{2.3}$ alloys of this study, the dendrite-dendrite spacing has been minimized, but the glass is so brittle that the critical shear band extension length is still almost identical to, if not exceeded by the dendrite-dendrite spacing, indicating that many shear bands can in fact reach the critical extension length after which they may evolve into a crack. Nonetheless, it is the first observation of tensile ductility in an alloy system capable of glass formation without the use of beryllium.

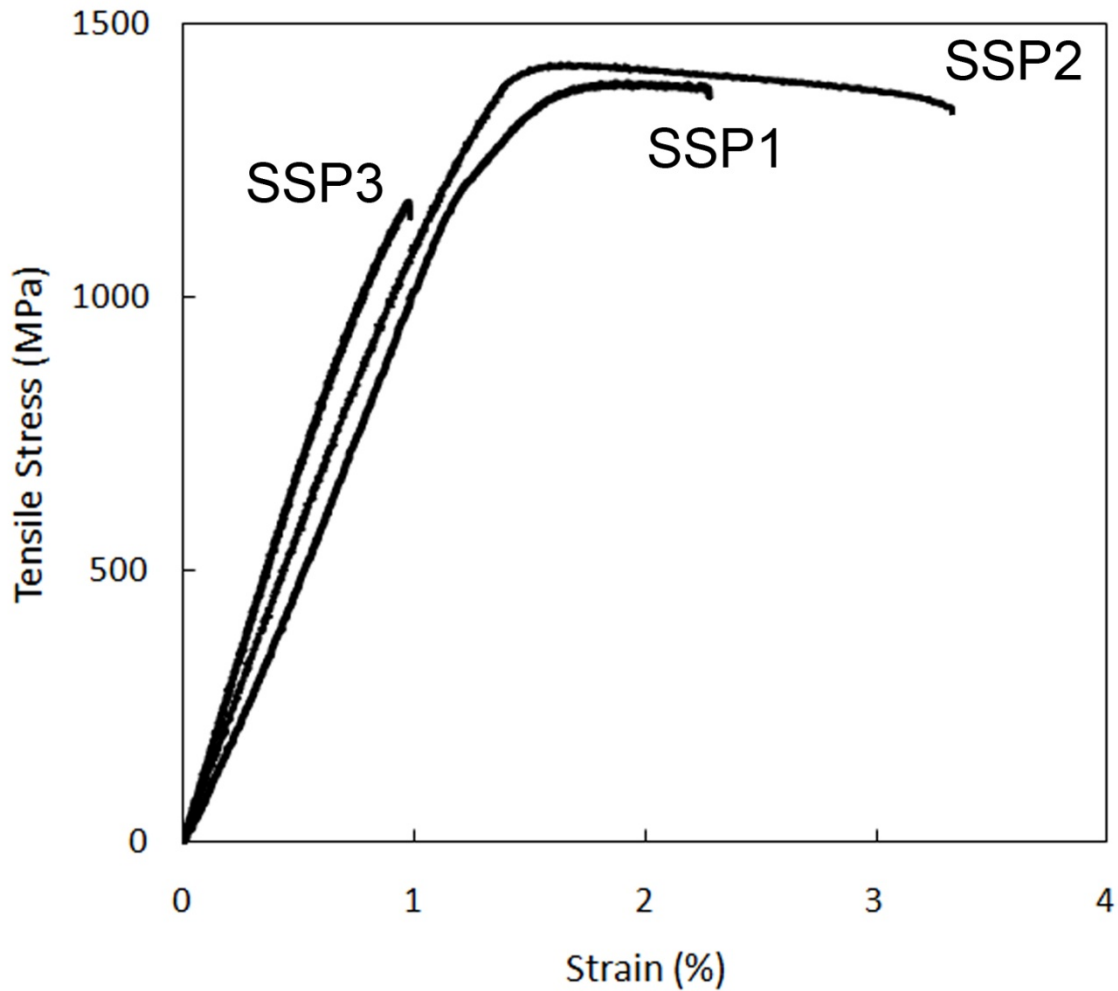


Figure 5.3.10. Tensile stress-strain curves for $\text{Ti}_{51.4}\text{Ni}_{42.4}\text{Si}_{3.9}\text{Mo}_{2.3}$ processed according to three different processing conditions to yield alloys SSP1, SSP2, and SSP3. Only alloys featuring an amorphous matrix exhibited tensile ductility (SSP1 and SSP2). Greater tensile ductility has been observed in SSP2 because the larger β -Ti microstructure is better able to arrest shear band propagation compared with the finer scale β -Ti in SSP1.

5.3.4 Conclusion

Precise compositional design and novel processing techniques have permitted the design of high strength amorphous matrix composites exhibiting enhanced ductility and fracture toughness. The development of low cost alloys with large GFA across a broad compositional spectrum provided a reliable candidate to serve as a stable glass matrix in a

BMG composite material. A ductile β -Ti phase was incorporated into the glass matrix through careful compositional tuning and the addition of the β -Ti stabilizing element molybdenum. The β -Ti phase was coarsened and homogenized via semi-solid processing such that shear band extension was limited and strain was delocalized in the alloys. The resultant material demonstrates benchmark compressive ductility, and the first observation of tensile ductility in a non-beryllium containing Ti-based BMG composite, as well as fracture toughness far exceeding that of its parent glass. The enhanced mechanical properties demonstrated by these new advanced composites exceed that of current titanium alloy alternatives, and therefore represent a monumental step towards applying BMG composites as structural materials in advanced aerospace and aeronautics applications.

Chapter 6: Conclusion

This work represented a stepwise evolution towards the development of low-cost, toughened BMG composites. Through modeling, design and experiment, several new metallic glasses were developed. Thorough thermal analyses were conducted to characterize the stability of these glasses, and novel processing techniques were developed in an attempt to deploy the impressive mechanical properties of BMGs in a more useable form. The final results presented demonstrate an in depth understanding of all aspects governing metallic glass formation and BMG composite design, and introduce a material with a combination of strength and toughness rivaling the best conventional alloys currently available. The realization of low-cost toughened BMG composites was critically dependent on the lessons and knowledge gained from the experiments leading up to its development. In the following paragraphs, a brief summary of the significant findings of this work is given.

The crystallization phenomena of two new, low cost, Fe-based BMGs ($\text{Fe}_{67-x}\text{C}_{10}\text{B}_9\text{Mo}_{7+x}\text{Cr}_4\text{W}_3$ and $\text{Fe}_{57}\text{C}_9\text{B}_{11}\text{Mo}_{12}\text{Cr}_8\text{W}_3$) have been extensively studied. Devitrification experiments have unveiled a dependence of mechanical hardness on free volume annihilation in structurally relaxed glass. Furthermore, these heating experiments have led to identification of the phases nucleating from the destabilized glass, and a correlation between hardness enhancement and phase composition has been established. It has been determined through cooling rate experiments that a $\text{Fe}_{57}\text{C}_9\text{B}_{11}\text{Mo}_{12}\text{Cr}_8\text{W}_3$ amorphous alloy cooled slowly from the molten state exhibits the same exact phase

nucleation as $\text{Fe}_{57}\text{C}_9\text{B}_{11}\text{Mo}_{12}\text{Cr}_8\text{W}_3$ devitrified above its highest crystallization temperature.

A novel processing technique called semi-solid processing was developed to precisely tune the microstructure of the composites. Power-modulated induction melting coupled with variety of quenching geometries permit the versatility to coarsen second phase particles while maintaining a glassy or nanocrystalline matrix.

The low cost iron-based glass presented in this work exhibits tremendously high strength, however the high metalloid content leads to carbide and boride formation in all Fe-based composites. The stability of these crystalline phases presents an insurmountable obstacle to global ductility because they are such brittle phases. Even when a ductile phase was successfully incorporated into the alloy, the crack propagates through the brittle phases without deforming the ductile phase. Tuning the microstructure in these Fe-based glasses through power-modulated induction heating did result in marginal gains in fracture toughness, as well as a significant enhancement in mechanical hardness.

The low cost titanium based glass, $\text{Ti}_{48}\text{Ni}_{32}\text{Cu}_8\text{Si}_8\text{Sn}_4$ presented in this work was successfully utilized to form a β -Ti reinforced amorphous matrix composite in small geometries. As the sample size increases, the glass becomes destabilized, and a nanocrystalline matrix results. The nanocrystalline matrix, β -Ti reinforced BMG composite exhibits significantly enhanced plasticity, as well as dislocation-slip-derived work hardening behavior. The nanocrystalline matrix, however is extremely brittle, and does not facilitate enhanced tensile ductility or fracture toughness.

A Ti-Ni-Si-Mo glass was also developed, with the intent of simplifying the crystallization mechanism at the matrix-dendrite interface, thus promoting the retention of amorphous structure. This simplified glass still demonstrates good glass stability, and led to the successful development of an amorphous matrix composite through semi-solid processing. This new BMG composite represents the first non-Be, non-Zr containing alloy of its kind. Extensive studies detailing the deformation mechanism reveal a marked jump in compressive plasticity over nanocrystalline matrix, BMG-derived composites, as well as a nearly 400% increase in fracture toughness over the monolithic glass, up to 40 MPa*m^{1/2}. This alloy also demonstrates 3.5% tensile ductility, due to the optimization of microstructural and mechanical length scales. The microstructure must be designed to optimally arrest and deflect shear bands, thus delocalizing the strain and allowing global ductility. The size and spacing of the reinforcing ductile phase has a profound effect on mechanical properties, and this spacing is dependent upon the composition of the glass. The achievement of enhanced ductility and fracture toughness in low-cost BMG composites without sacrificing strength represents the dawn of a new, and potentially useful class of structural materials unrivaled by current alternatives.

Chapter 7: References

1. Klement, W.J., R.H. Willens, and P. Duwez, *Nature*, 1960. **187**: p. 869-870.
2. Inoue, A., in *Trans Tech Publications*. 1998: Switzerland.
3. Johnson, W.L., *Materials Science Forum*, 1996. **225-227**: p. 35-50.
4. Inoue, A., B.L. Shen, and C. C.T., *Intermetallics*, 2006. **14**: p. 936-944.
5. Wang, H., C. Dong, and C.H. Shek, *Materials Science & Engineering R*, 2004. **44**: p. 45-89.
6. Johnson, W.L., in *Metastable phase*. 1994, John Wiley & Sons.
7. Johnson, W.L., 1999. **24**: p. 42-56.
8. Geng, J.-y., et al., *Transactions of Nonferrous Metals Society of China*, 2007. **17**(5): p. 907-912.
9. Jiang, Q.K., et al., *Acta Materialia*, 2007. **55**(13): p. 4409-4418.
10. Pemberton-Pigott, N., et al., *Journal of University of Science and Technology Beijing, Mineral, Metallurgy, Material*, 2007. **14**(Supplement 1): p. 26-30.
11. Wang, Z.X., R.J. Wang, and W.H. Wang, *Materials Letters*, 2006. **60**(6): p. 831-833.
12. Wei, Y.X., et al., *Materials Letters*, 2005. **59**(8-9): p. 945-947.
13. Oak, J.-J. and A. Inoue, *Journal of Non-Crystalline Solids*, 2008. **354**(17): p. 1828-1832.
14. Komatsu, T., *Journal of Non-Crystalline Solids*, 1995. **185**: p. 199-202.
15. Peker, A., in *Materials Science and Engineering*. 1994, Caltech: Pasadena, CA.
16. Hu, Y., et al., *Materials Science and Engineering A*, 2006. **375-377**: p. 297.
17. Busch, R., Y.J. Kim, and W.L. Johnson, *J. Appl. Phys.*, 1995. **77**(8): p. 4039-4043.
18. Duwez, P. and R.H. Willens, *Trans. Met. Soc. AIME*, 1963. **227**: p. 326.
19. Lu, I.R., et al., *Journal of Non-Crystalline Solids*, 1999. **250-252**(Part 2): p. 577-581.

20. Inoue, A., *Acta Materialia*, 2000. **48**: p. 279-306.
21. Cheney, J. and K. Vecchio, *Materials Science and Engineering: A*, 2007. **471**(1-2): p. 135-143.
22. Cowley, J.M., ed. *Diffraction Physics*. 1995, Elsevier Science, B.V.
23. Miracle, D.B. and O.N. Senkov, *Materials Science and Engineering A*, 2003. **347**(1-2): p. 50-58.
24. Miracle, D.B., et al., *Materials Science and Engineering A*, 2004. **375-377**: p. 150-156.
25. Cohen, M.H. and D. Turnbull, *Nature*, 1961. **189**: p. 131-132.
26. Turnbull, D., *Contemporary Physics*, 1969. **10**: p. 473.
27. Cheney, J. and K. Vecchio, *Materials Science and Engineering: A*, 2008. **492**(1-2): p. 230-235.
28. Khalifa, H.E., J.L. Cheney, and K.S. Vecchio, *Materials Science and Engineering: A*, 2008. **490**(1-2): p. 221-228.
29. Senkov, O.N. and D.B. Miracle, *Journal of Non-Crystalline Solids*, 2003. **317**(1-2): p. 34-39.
30. Desre, P.J. in *Materials Research Society*. 1999.
31. Marcus, M. and D. Turnbull, *Materials Science*, 1976. **23**: p. 211.
32. Ma, H., et al., *Applied Physics Letters*, 2005. **87**: p. 181915.
33. Davies, H.A. and B.G. Lewis, *Scripta Metall.*, 1975. **9**: p. 1107.
34. Fan GJ, L.J., Wunderlich RK, Fecht HJ, *Acta Materialia*, 2004. **52**: p. 667-674.
35. Fu, H.M., et al., *Journal of Alloys and Compounds*, 2008. **458**(1-2): p. 390-393.
36. Lu, Z.P., et al., *Scripta Materialia*, 2000. **42**(7): p. 667-673.
37. Egami, T., *Journal of Alloys and Compounds*, 2007. **434-435**: p. 110-114.
38. Argon, A.S., *Acta Metallurgica*, 1979. **27**: p. 47-58.
39. Masuhr, A., et al., *Phys Rev Lett*, 1999. **82**: p. 2290.
40. Mukherjee, S., et al., *Acta Materialia*, 2004. **52**(12): p. 3689-3695.

41. Egry, I., et al., Applied Physics Letters, 1998. **73**: p. 462.
42. Tsang, K.H., S.K. Lee, and H.W. Kui, J. Appl. Phys., 1991. **70**: p. 4837.
43. Cohen, M.H. and G.H. Grest, Phys. Rev. B, 1979. **20**: p. 1077.
44. Chow, K.C., S. Wong, and H.W. Kui, J. Appl. Phys., 1993. **74**: p. 5410.
45. Lu, I.R., G.P. Gorler, and R. Willnecker, Applied Physics Letters, 2002. **80**: p. 4534.
46. Ohsaka, K., et al., Applied Physics Letters, 1997. **70**: p. 726.
47. Angell, C.A., Science, 1995. **267**: p. 1924.
48. Fan, G.J., H. Choo, and P.K. Liaw, Journal of Non-Crystalline Solids, 2005. **351**(52-54): p. 3879-3883.
49. Hammond, H., M. Houtz, and J. O'Reilly, Journal of Non-Crystalline Solids, 2003. **325**: p. 179-186.
50. Haruyama, O. in *Advanced Intermetallic Alloys and Bulk Metallic Glasses, 6th International Workshop on Advanced Intermetallic and Metallic Materials*. 2007.
51. Haruyama, O., et al. in *Materials Science and Engineering: A. Proceedings of the 12th International Conference on Rapidly Quenched & Metastable Materials*. 2007.
52. Kissinger, H.E., Journal of Research of the National Bureau of Standards, 1956. **57**(4): p. 2712.
53. Chen, Q.J., et al., Journal of Alloys and Compounds, 2006. **407**(1-2): p. 125-128.
54. Inoue, A., et al., Acta Materialia, 2001. **49**(14): p. 2645-2652.
55. Flores, K.M. and R.H. Dauskardt, Acta Materialia, 2001. **49**(13): p. 2527-2537.
56. Spaepen, F., Acta Metallurgica, 1977. **25**(4): p. 407-415.
57. Inoue, A., B.L. Shen, and C.T. Chang, Acta Materialia, 2004. **52**(14): p. 4093-4099.
58. Steif, P.S., F. Spaepen, and J.W. Hutchinson, Acta Metallurgica, 1982. **30**(2): p. 447-455.
59. Choi-Yim, H., et al., Acta Materialia, 1999. **47**(8): p. 2455-2462.
60. Zhang, W.G., et al., Materials Science and Engineering A, 2009. **516**: p. 148-153.

61. Conner, R.D., et al., *Acta Materialia*, 2004. **52**: p. 2429.
62. Sergueeva, A.V., et al., *Materials Science and Engineering A*, 2004. **383**(2): p. 219-223.
63. Keryvin, V., *Acta Materialia*, 2007. **55**(8): p. 2565-2578.
64. Jana, S., et al., *Materials Science and Engineering A. Eleventh International Conference on Rapidly Quenched and Metastable Materials*, 2004. **375-377**: p. 1191-1195.
65. Schroers, J. and W.L. Johnson, *Phys Rev Lett*, 2004. **93**: p. 255506.
66. Nieh, T.G. and J. Wadsworth, *Scripta Materialia*, 2006. **54**(3): p. 387-392.
67. Inoue, A., Y. Kawamura, and Y. Saotome, *Materials Science Forum*, 1997. **233-234**: p. 147.
68. Flores, K.M., W.L. Johnson, and R.H. Dauskardt, *Scripta Materialia*, 2003. **49**(12): p. 1181-1187.
69. Hess, P.A. and R.H. Dauskardt, *Acta Materialia*, 2004. **52**(12): p. 3525-3533.
70. Suh, D. and R.H. Dauskardt, *Scripta Materialia*, 2000. **42**(3): p. 233-240.
71. Hess, P.A., B.C. Menzel, and R.H. Dauskardt, *Scripta Materialia*, 2006. **54**(3): p. 355-361.
72. Wang, G.Y., et al. in *Intermetallic: Intermetallic and Advanced Metallic Materials - A Symposium Dedicated to Dr. C.T. Liu, 3-6 March 2003, San Diego, CA, USA*. 2004.
73. Lowhaphandu, P., S.L. Montgomery, and J.J. Lewandowski, *Scripta Materialia*, 1999. **41**: p. 19.
74. Zhang, Z.F., J. Eckert, and L. Schultz, *Metallurgical and Materials Transactions A*, 2004. **35A**.
75. Menzel, B.C. and R.H. Dauskardt, *Acta Materialia*, 2006. **54**(4): p. 935-943.
76. Chen, M., et al., *Physical Review Letters*, 2006. **96**(24): p. 245502-4.
77. Hays, C.C., C.P. Kim, and W.L. Johnson, *Physical Review Letters*, 2000. **84**(13): p. 2901 LP - 2904.
78. Conner, R.D., R.B. Dandliker, and W.L. Johnson, *Acta Materialia*, 1998. **46**(17): p. 6089-6102.

79. Wang, J., et al., *Advanced Engineering Materials*, 2008. **10**: p. 46.
80. Courtney, M.H., *Mechanical Behavior of Materials*, ed. I. McGraw-Hill Company. 2000.
81. Hofmann, D.C., et al., *Nature*, 2008. **451**: p. 1085.
82. Liang, J.Z. and R.K.Y. Li, *Journal of Applied Polymer Science*, 2000. **77**: p. 409-417.
83. Long, Z.L., et al., *Intermetallics*, 2007. **15**: p. 1453.
84. Pang, S.J., et al., *Corrosion Science*, 2002. **44**: p. 1847.
85. Makino, A. and A. Inoue, *JIM*, 2000. **41**: p. 1471.
86. Evteev, A.V., A.T. Kosilov, and E.T. Levchenko, *Acta Materialia*, 2003(51): p. 2665.
87. Chen, Q.J., et al., *Materials Science and Engineering: A*, 2005. **402**(1-2): p. 188-192.
88. Lu, Z.P., C.T. Liu, and W.D. Porter, *Applied Physics Letters*, 2003. **83**(13): p. 2581-3.
89. Lu, Z.P., et al., *Physical Review Letters*, 2004. **92**(24): p. 245503/1-4.
90. Ponnambalam, V., S.J. Poon, and G.J. Shiflet, *Journal of Materials Research*, 2004. **19**(5): p. 1320-1323.
91. Ponnambalam, V., et al., *Applied Physics Letters*, 2003. **83**(6): p. 1131-1133.
92. Poon, S.J., et al., *Journal of Non-Crystalline Solids*, 2003. **317**(1-2): p. 1-9.
93. Shen, T.D. and R.B. Schwarz, *Applied Physics Letters*, 1999. **75**(1): p. 49-51.
94. Hu, Y., et al., *Materials Letters*, 2006. **60**: p. 1080-1084.
95. Gan, Z.H., et al., *Scripta Materialia*, 2003. **48**: p. 1543-1547.
96. Soliman, A., et al., *Thermochimica Acta*, 2004. **413**: p. 57-62.
97. Yang, Y.J., et al., *Journal of Alloys and Compounds*, 2006. **415**: p. 106.
98. Stoica, M., et al., *Journal of Alloys and Compounds*, 2007. **434**: p. 171.
99. Zhang, T. and T. Masumoto, *Journal of Non-Crystalline Solids*, 1993(473): p. 156-158.

100. Schroers, J., et al. in *Proceedings of the 12th International Conference on Rapidly Quenched & Metastable Materials*. 2007: Materials Science and Engineering: A.
101. Wall, J.J., et al., Materials Science and Engineering: A, 2007. **445-446**: p. 219-222.
102. Yamasaki, T., et al., Intermetallics, 2006. **14**: p. 1102-1106.
103. Grabias, A., et al., Materials Science and Engineering A, 2006.
104. Li, H.X., K.B. Kim, and S. Yi, Scripta Materialia, 2007. **56**(12): p. 1035-1038.
105. Cullity, B.D. and S.R. Stock, *Elements of X-Ray Diffraction, Third Edition*. 2001: Prentice Hall.
106. Shapaan, M., et al., Materials Science and Engineering A, 2004(375-377): p. 785-788.
107. Shapaan, M., et al., Materials Science and Engineering A, 2004(375-377): p. 789-793.
108. Iqbal, M., et al., Materials Letters, 2006(60): p. 662-665.
109. Dmowski, W., et al., Materials Science and Engineering A, 2007.
110. He, G., et al., Acta Materialia, 2004. **52**(10): p. 3035-3046.
111. Szuecs, F., C.P. Kim, and W.L. Johnson, Acta Materialia, 2001. **49**(9): p. 1507-1513.
112. Olofinjana, A.O. and K.S. Tan. in *Journal of Materials Processing Technology Advances in Materials and Processing Technologies, July 30th - August 3rd 2006, Las Vegas, Nevada*. 2007.
113. Loser, W., et al. in *Intermetallics Bulk Metallic Glasses III*. 2004.
114. Zhang, Y., et al., Acta Materialia, 2005. **53**(9): p. 2607-2616.
115. Wang, W.H., et al., Applied Physics Letters, 2001. **79**: p. 1106.
116. Sun, X., et al., Physica B: Condensed Matter, 2000. **291**(1-2): p. 173-179.
117. Busch, R., et al., Applied Physics Letters, 1995. **67**: p. 1544.
118. Marion, R.H. American Society of Testing and Materials, ed. S.W. Frieman. 1979, Philadelphia.

119. Lewandowski, J.J., W.H. Wang, and A.L. Greer, *Phil. Mag. Lett.*, 2005. **85**: p. 77-87.
120. Zhao, S., et al., *International Journal of Refractory Metals and Hard Materials*, 2009. **27**(6): p. 1014-1018.
121. Duan, G., et al., *Scripta Materialia*, 2008. **58**(6): p. 465-468.
122. Calin, M., L.C. Zhang, and J. Eckert, *Scripta Materialia*, 2007. **57**: p. 1101.
123. Jiang, F., et al., *Metallurgical and Materials Transactions A*, 2008. **39A**: p. 1817.
124. Guo, F.Q., et al., *Applied Physics Letters*, 2005. **86**: p. 091907.
125. Patterson, A.L., *Physical Review*, 1939. **56**: p. 978.
126. Ichitsubo, T., E. Matsubara, and H. Numakura, *Materials Science and Engineering: A. Proceedings of the 12th International Conference on Rapidly Quenched & Metastable Materials*, 2007. **449-451**: p. 506-510.
127. Lasocka, M., *Journal of Materials Science*, 1976. **11**: p. 1770.
128. Busch, R., E. Bakke, and W.L. Johnson, *Acta Materialia*, 1998. **46**(13): p. 4725-4732.
129. Mitrovic, N., S. Roth, and J. Eckert, *Applied Physics Letters*, 2001. **78**: p. 2145.
130. Inoue, A., et al., *Materials Transactions, JIM*, 1994. **35**: p. 95.
131. Revesz, A., *Journal of Thermal Analysis and Calorimetry*, 2008. **91**: p. 879.
132. Zhuang, Y.X., et al., *Applied Physics Letters*, 1999. **75**: p. 2392.
133. Chen, L. and F. Spaepen, *Nature*, 1988. **336**: p. 366.
134. Avrami, M., *Journal of Chemical Physics*, 1941. **9**: p. 177.
135. Christian, J.W., *The Theory of Transformations in Metals and Alloys*. 1965, Oxford, England: Pergamon Press.
136. Porter, D.A. and K.E. Easterling, *Phase Transformations in Metals and Alloys, 2nd Edition*. 1992, Cheltenham, United Kingdom: Chapman and Hall.
137. Huang, J.M. and F.C. Chang, *Journal of Polymer Science Part B: Polymer Physics*, 2000. **38**: p. 934.
138. Das, J., F. Ettinghausen, and J. Eckert, *Scripta Materialia*, 2008. **58**: p. 631.

139. Das, J., et al., Journal of Alloys and Compounds, 2007. **434-435**: p. 28.
140. He, G., et al., Nature Materials, 2003. **2**: p. 33.
141. Louzguine, D.V., H. Kato, and A. Inoue, Journal of Alloys and Compounds, 2004. **375**(1-2): p. 171-174.
142. Hofmann, D.C., et al., PNAS, 2008. **105**: p. 1073.
143. Das, J., et al., Applied Physics Letters, 2003. **82**(26): p. 4690-4692.
144. Bian, Z., et al., Acta Materialia, 2005. **53**(7): p. 2037-2048.
145. Ma, H., J. Xu, and E. Ma, Applied Physics Letters, 2003. **83**(14): p. 2793-2795.
146. Davis, J.R., *Stainless Steels*. 1994, ASM, Materials Park, USA.
147. Schutz, R.W., in *TMS*. 1994: Warrendale, USA. p. 295.
148. Ma, E., Nature Materials, 2003. **2**: p. 7.
149. Lütjering, G. and J.C. Williams, *Titanium*. Second ed. Engineering Materials and Processes, ed. B. Derby. 2007: Springer.
150. Cheney, J., H. Khalifa, and K. Vecchio, Materials Science and Engineering: A, 2009. **506**(1-2): p. 94-100.
151. Hansen, M., *Constitution of Binary Alloys*. 2nd ed. Metallurgy and Metallurgical Engineering. 1958, New York: McGraw-Hill.
152. Eckert, J., et al., Journal of Alloys and Compounds, 2007. **434-435**: p. 13.
153. Eckert, J., et al., Materials Science and Engineering A, 2008. **493**: p. 71.
154. Das, J., et al., Scripta Materialia, 2003. **49**(12): p. 1189-1195.
155. Kim, K.B., et al., Applied Physics Letters, 2005. **86**(17): p. 171909-3.
156. Schutz, R.W. and D.E. Thomas, *Corrosion*. 9th ed. Metals Handbook. Vol. 13. 1987, ASM, Metals Park, USA.
157. Lütjering, G. and J.C. Williams, *Corrosion Behavior, in Titanium*, B. Derby, Editor. 2003, Springer: New York. p. 47-50.
158. Peter, W.H., et al., Intermetallics, 2002. **10**(11-12): p. 1157-1162.
159. Qin, C., et al., Acta Materialia, 2005. **53**(14): p. 3903-3911.

160. Lee, M.L., Y. Li, and C.A. Schuh, *Acta Materialia*, 2004. **52**: p. 4121-4131.
161. Conner, R.D., *J. Appl. Phys.*, 2003. **94**: p. 904-911.
162. Conner, R.D., et al., *Acta Materialia*, 2004. **52**(8): p. 2429-2434.
163. Ravichandran, G. and A. Molinari, *Acta Materialia*, 2005. **53**: p. 4087-4095.
164. Evans, A.G., et al., *Acta Metallurgica*, 1986. **34**(1): p. 79-87.
165. Khalifa, H.E. and K.S. Vecchio, *Journal of Non-Crystalline Solids*. **In Press, Corrected Proof**.
166. Khalifa, H. and K. Vecchio, *Advanced Engineering Materials*, 2009. **9999**(9999): p. NA.
167. Lebrun, N., *Nickel-Silicon-Titanium*, in *Light Metal Systems. Part 4*. 2006, Springer Berlin Heidelberg. p. 435-445.
168. Miedema, A.R., F.R. de Boer, and R. Boom, *Calphad* 1, 1977: p. 341.
169. Hofmann, D.C., et al., *Acta Materialia*, 2008. **59**: p. 684-687.
170. He, G. and M. Hagiwara, *Materials Science and Engineering: C*, 2006. **26**(1): p. 14-19.
171. Plummer, J.D., et al., *Journal of Non-Crystalline Solids*, 2009. **355**(6): p. 335-339.
172. Jiang, F. and K. Vecchio, *Metallurgical and Materials Transactions A*, 2007. **38**(12): p. 2907-2915.
173. Ming-Yuan, H. and J.W. Hutchinson, *International Journal of Solids and Structures*, 1989. **25**(9): p. 1053-1067.
174. Adharapurapu, R., et al., *Metallurgical and Materials Transactions A*, 2005. **36**(6): p. 1595-1608.
175. Lin, A.Y.M., M.A. Meyers, and K.S. Vecchio, *Materials Science and Engineering: C*, 2006. **26**(8): p. 1380-1389.
176. Zhang, L.C., et al., *Scripta Materialia*, 2007. **57**(2): p. 101-104.
177. Hertzberg, R.W., *Deformation and Fracture Mechanics of Engineering Materials*. Second ed. 1976, New York: John Wiley & Sons.
178. Huang, Y.J., et al., *Journal of Alloys and Compounds*, 2007. **427**(1-2): p. 171-175.

179. Park, J.M., et al., Scripta Materialia, 2005. **53**(1): p. 1-6.
180. Zhang, T. and A. Inoue, Materials Science and Engineering A, 2001. **304-306**: p. 771-774.
181. Pampillo, C.A., J. Appl. Phys., 1975. **10**: p. 1194.